UNIVERSITY OF SOUTHAMPTON

Faculty of Engineering and the Environment
Institute of Sound and Vibration Research

Investigation of sound transmission in lightweight structures using a waveguide finite element/boundary element approach

by

Iwan Prasetiyo

Thesis for the degree of Doctor of Philosophy

November 2012

UNIVERSITY OF SOUTHAMPTON

ABSTRACT

FACULTY OF ENGINEERING AND THE ENVIRONMENT
Institute of Sound and Vibration Research

Doctor of Philosophy

INVESTIGATION OF SOUND TRANSMISSION IN LIGHWEIGHT STRUCTURES USING A WAVEGUIDE FINITE ELEMENT/BOUNDARY ELEMENT METHOD

by

Iwan Prasetiyo

The use of lightweight construction in building applications offers flexibility in use and ease of construction but often goes hand in hand with reduced sound insulation. Regarding this issue, this thesis investigates sound transmission behaviour of such structures. A numerical model is developed using a coupled waveguide finite element-boundary element (WFBE) method to predict the transmission loss (TL) of more complex structures and is applied to double panel systems.

Initially, analytical waveguide models for a plate strip are developed. These models are used to gain insight into the vibro-acoustic behaviour of such a structure, particularly compared with an infinite system, as well as for validating the WFBE method.

Compared with results for an infinite double panel system, the finite extent in one direction of the waveguide system introduces some features in its TL. One of them is the presence of lateral cavity modes. These introduce additional stiffness to the air in the cavity so that the mass-air-mass resonance frequency of the waveguide structure shifts to higher frequency. Such additional stiffness reduces the overall transmission loss. This tendency is confirmed by measurement results. Another aspect related with the finite width is the presence of internal coincidence phenomena which cause dips that are not related with cavity resonance and are also independent of incidence angles. Moreover, a higher TL is found for the waveguide double panel partition at low frequencies as the finite width system radiates less efficiently than the infinite plate model. The results obtained also confirm that the dissipative mechanism behaviour found in the structure originates from the cavity rather than from the panel as postulated by London.

The effect of studs connecting the two leaves of the double panel system is also investigated. The effect of the air in the cavity becomes less significant with increasing frequency for the case of stiff studs so that the stud behaviour is predominant at high frequency. However, for more flexible studs lateral cavity modes and the internal coincidence effect become more significant and reduce the sound transmission loss. Therefore, for the case of elastic steel studs where no sound absorbent material in the cavity, both the transmission paths need to be handled carefully in order to achieve a good prediction of TL.

Comparisons of the numerical model results and measurements suggest that inclusion of an appropriate cavity loss factor is important to achieve accurate results particularly when sound absorbing material is absent from the cavity. A reduced air stiffness also needs to be considered to account for practical considerations. Moreover, it is of importance to include the detail in terms of elastic stud geometry in order to have a more representative stiffness. The comparison results also indicate that numerical models based on the WFBE method are able to produce good prediction results.

Contents

Contents ..... **iii**
List of figures ..... **vii**
List of tables ..... **xvii**
Declaration of authorship ..... **xix**
Acknowledgements ..... **xxi**
Abbreviations ..... **xxiii**
Nomenclature ..... **xxv**
Chapter 1. Introduction **1**
1.1 Background **1**
1.2 Literature review **3**
1.2.1 Prediction models for single panel 3
1.2.2 Double panel partition with air cavity 4
1.2.3 Double panel partition with studs 7
1.2.4 Numerical models 10
1.3 Objectives and scope of the thesis **12**
1.4 Thesis outline **13**
1.5 Thesis contributions **14**
Chapter 2. Vibro-acoustic behaviour for an infinite plate strip **17**
2.1 Vibration of a plate strip **17**
2.1.1 Undamped free vibration 18
2.1.2 Inclusion of damping 23
2.2 Response due to a point force **24**
2.2.1 Formulation 24
2.2.2 Convergence 26
2.2.3 Results 27
2.2.4 Effect of plate thickness 28
2.2.5 Effect of excitation position 29
2.2.6 Effect of damping loss factor 29
2.2.7 Average response of plate 30
2.3 Sound radiation of a plate strip **34**
2.3.1 Infinite plate 35
2.3.2 Plate strip 37

2.3.3 Radiation due to point force 38
2.3.4 Effect of finite width and point force excitation on the plate strip 41
2.3.5 Effect of damping loss factor 44
2.3.6 Effect of plate thickness 46
2.3.7 Inclusion of the cross-terms 47
2.4 Sound transmission loss of a plate strip 49
2.4.1 Pressure and velocity functions 49
2.4.2 Transmission coefficient 56
2.4.3 Diffuse sound field 66
2.5 Summary 67
Chapter 3. Waveguide Finite Element-Wavedomain Boundary Element (WFBE) method 71
3.1 Waveguide Finite Element method 71
3.1.1 Plate elements 72
3.1.2 Solid elements 73
3.1.3 Fluid element 74
3.1.4 Free wave solution 75
3.1.5 Forced response 76
3.1.6 Residue calculus method 77
3.1.7 Numerical integration 79
3.2 Wavenumber Boundary Element method 80
3.2.1 Wavenumber domain 80
3.2.2 Mixed boundary condition 82
3.3 Coupling between WFE and WBE models 82
3.3.1 Radiated sound power 84
3.3.2 Sound transmission 86
3.4 Summary 88
Chapter 4. Validation of WFBE for a plate strip 89
4.1 Point mobility of a plate strip 90
4.1.1 Effect of element size 93
4.1.2 Effect of wavenumber range and step size on accuracy of mobility calculation 94
4.2 Sound radiation of a plate strip 97
4.2.1 Effect of baffle width 99
4.2.2 Effect of enclosed boundary thickness 102

4.3 Sound transmission loss of a plate strip 103
4.3.1 Normal incidence case 105
4.3.2 Oblique incidence case 106
4.3.3 Effect of plate thickness 108
4.3.4 Effect of damping loss factor 108
4.3.5 Diffuse sound field 109
4.4 Substitution of plate elements by solid elements 110
4.4.1 Element density 111
4.4.2 Effect of restrained nodes 112
4.4.3 Point mobility 113
4.4.4 Radiated sound power 114
4.4.5 Sound transmission loss 116
4.4.6 Diffuse sound field 117
4.5 Summary 118
Chapter 5. Waveguide double panel system 121
5.1 Transmission loss of infinite double panel partition 121
5.2 Waveguide double panel partition with air cavity 128
5.2.1 Problem statement 129
5.2.2 Features found in the waveguide double panel results for normal incidence 131
5.2.3 Effect of finite cavity 133
5.2.3.1 Lateral cavity mode effect 134
5.2.3.2 Internal coincidence frequency 141
5.2.3.3 Effect of cavity loss factor 144
5.2.4 Panel loss factor 147
5.2.5 Effect of edge condition 149
5.2.6 Coincidence frequency behaviour 152
5.2.7 Radiation ratio 155
5.2.8 Effect of asymmetrical structures 156
5.2.9 Diffuse sound field 159
5.3 Summary 162
Chapter 6. Waveguide double panel system with steel studs 163
6.1 Problem statement 163
6.2 *In-vacuo* model 165
6.3 Origin of peaks and dips 166
6.4 Dispersion relations 167

6.5 Effect of air in the cavity **169**
6.6 Effect of stud parameters **171**
6.6.1 Effect of stud spacing 171
6.6.2 Effect of stud stiffness 174
6.6.3 Effect of stud loss factor 175
6.6.4 Effect of stud geometric form 177
6.7 Diffuse sound field excitation: comparison with measurement **179**
6.7.1 Effect of cavity loss factor 179
6.7.2 Effect of simplified cross-section stud shape 181
6.7.3 Effect of limiting angle 182
6.7.4 Effect of air stiffness 183
6.8 Summary **186**
Chapter 7. Experimental validation **189**
7.1 Experimental setup and procedure **189**
7.1.1 Reverberation chamber 189
7.1.2 Test specimen parameter 190
7.1.3 Measurement procedure 193
7.2 Preliminary test **194**
7.3 Effect of air cavity dimensions **197**
7.4 Effect of steel stud **203**
7.5 Summary **205**
Chapter 8. Conclusions **207**
8.1 Infinite plate strip **207**
8.2 Waveguide Finite Element-Boundary Element **207**
8.3 Waveguide double panel system **209**
8.4 Recommendations for further work **210**
Appendix A. Out-of plane displacement of a plate strip due to a point force **213**
Appendix B. Modulus squared of plate velocity in wavenumber domain **217**
Appendix C. Stiffness and mass matrices of WFE method **219**
Appendix D. Mobility of single panel system and double panel system with steel studs **223**
Appendix E. Cavity loss factor **227**
References **229**

List of figures

Figure 1.1. Typical lightweight structures for building application.....1
Figure 2.1. A simply-supported plate strip. 18
Figure 2.2. The dispersion curves in the $x-$direction of an undamped simply-supported plate strip with parameters in Table 2.1: (a) $k_{x1,m}$; (b) $k_{x2,m}$. 21
Figure 2.3. Complex wavenumber evolution against frequency (— real components; --- imaginary components). 24
Figure 2.4. The point mobility of the plate strip excited at position $(0, 0.433l_y)$. The dashed line indicates the mobility of an infinite plate. 27
Figure 2.5. Effect of plate thickness on the point mobility excited at (0, $0.433\,l_y$) 28
Figure 2.6. Modulus and phase of point mobility for an infinite plate strip (—at $\left(0, l_y/2\right)$; – • – at $\left(0, l_y/4\right)$). 29
Figure 2.7. Effect of damping loss factor on the point mobility of plate strip with parameters in Table 2.1 (--- $\eta = 0.01$; — $\eta = 0.1$).....30
Figure 2.8. Average response of the plate strip with different damping loss factor η for unit excitation at $\left(0, 0.433l_y\right)$ (— η = 0.01; ---η = 0.03; • – • – • η = 0.1).....33
Figure 2.9. Average response of the plate strip due to different thickness with damping loss factor equal to 0.1 and excited by unit point force at (0, $0.433\,l_y$) (---h = 3 mm; — h = 6 mm; – • – h = 9 mm). 34
Figure 2.10. Transverse wave in a plate in contact with a fluid.....35
Figure 2.11. (a) Sound power radiation of the plate strip due to a unit point force at (0, $0.433\,l_y$); (b) its associated radiation ratio. 40
Figure 2.12. Dispersion curve of the plate strip (— bending wavenumbers for different mode orders (k_{x1}) and wavenumber for each mode m (k_y); --- acoustic wavenumbers). ..43
Figure 2.13. Radiated power of plate strip and infinite plate excited at position $\left(0, 0.433l_y\right)$ with force amplitude $F_0 = 1$ (— plate strip; --- infinite plate). 44
Figure 2.14. Comparison of sound power radiation for different damping loss factors for plate strip excited at (0, $0.433\,l_y$) (— η = 0.01; ---η = 0.03; – • – η = 0.1). 45

Figure 2.15 Comparison of radiation ratio due to different damping loss factor excited at (0, $0.433 l_y$) (— η = 0.01; --- η = 0.03; – • – η = 0.1).....46

Figure 2.16. (a) Comparison of sound power radiation due to different thickness with damping loss factor equal to 0.1 and excited at (0, $0.433 l_y$); (b) its associated radiation ratio (--- h = 3 mm ; — h = 6 mm; – • – h = 9 mm) 47

Figure 2.17. Effect of the cross-terms contribution in radiated power due to a point force excitation at (0, 0.433 l_y) (— the cross-terms modal radiation incorporated along with the self-modal one ; --- only self- modal radiation considered). 48

Figure 2.18. Direction of a plane wave incident on an infinite plate strip 50

Figure 2.19. Elevation and azimuth angle convention and trace wavenumbers in the fluid. 50

Figure 2.20. Effect of neglecting of cross-term contribution on TL of plate strip (— with cross-term contribution;--- without cross-term contribution).....59

Figure 2.21. TL comparison of the plate strip and the infinite plate for normal incident case (— plate strip; --- infinite plate) 60

Figure 2.22. TL slope of plate strip in the stiffness-controlled region and the mass-controlled region.....61

Figure 2.23. TL comparison of the plate strip and the infinite plate for obliquely incident case: (a) about x axis; (b) about y axis (— plate strip; --- infinite plate). 63

Figure 2.24. Effect of changing thickness of the plate strip on the sound transmission loss: (a) normal incidence; (b) oblique incidence at angle 45° about y-axis (--- h = 3 mm ; — h = 6 mm ; – • – h = 9 mm). 64

Figure 2.25. Effect of structural loss factor of the plate strip on the sound transmission loss: (a) normal incidence; (b) oblique incidence at angle 45º about y-axis (– • – η = 0.01 ; --- η = 0.03, — η = 0.1).....65

Figure 2.26. TL of plate strip under a diffuse sound field excitation: random incidence ($0^\circ \le \theta \le 90^\circ$): (— Plate strip; --- infinite plate); field incidence ($0^\circ \le \theta \le 78^\circ$): (– • – Plate strip; ••• infinite plate). 67

Figure 3.1. A shell (or plate) strip element.....72

Figure 3.2. Path of integration in complex plane [9].....78

Figure 3.3. Integration in Eq. (3.4) is performed as a series of rectangles to approximate the area under the graph. 80
Figure 3.4. Description of incident direction in WANDS 87
Figure 4.1. Mobility of the plate strip due to force excitation at $\left(0, l_y/2\right)$ calculated using WFE model compared with analytical result (— numerical; --- analytical).....91
Figure 4.2. Relative percent difference of mobility amplitude and difference of phase in radians between numerical result and analytical one. 91
Figure 4.3. The predicted dispersion curves of a simply-supported plate strip and particular mode shapes. 92
Figure 4.4. Mobility spectrum of the plate strip at (a) 1 Hz, (b) 500 Hz and (c) 3 kHz to represent low, mid and high frequencies respectively, with associated bending wavenumber of 0.8169, 18.27 and 44.74 rad/m (— range required for 1 dB error; --- 0.1 dB error; ••• border for the region required for 1 dB error). 96
Figure 4.5. Schematic illustration of the WFBE model. 98
Figure 4.6 Comparison of the radiated power between numerical result and analytical one for excitation at the middle (0, $l_y/2$) (— numerical model with closed BE mesh; --- numerical model with open BE mesh; – • – analytical model). 99
Figure 4.7 Radiated sound power calculated using the numerical model with various baffle width on each side of the plate and compared with those obtained with the analytical model (---analytical model; — numerical model with baffle width of 2 m; --- baffle width of 1 m; – • – baffle width of 0.2 m; ••• no baffle exists) 100
Figure 4.8. The baffle width effect on the radiated power in terms of radiated power differences relative to the analytical model (— baffle width beyond plate of 2 m; ---- 1 m; – • – 0.2 m; ••• no baffle exists).....101
Figure 4.9. Effect of enclosed boundary mesh thickness (— 100 mm; --- 66 mm; 103
Figure 4.10. Schematic illustration of the plate strip excited by the acoustic plane wave.104
Figure 4.11. The difference in the transmission loss between open boundary and closed boundary mesh on the source side. 105
Figure 4.12. Comparison of transmission loss of the plate strip based on the numerical model and the analytical one (— numerical model; --- analytical model; – • – mass law). 106

Figure 4.13. Comparison of transmission loss of the plate strip and the analytical model for oblique incidence case: (a) $\theta = 45^{\circ}$; $\varphi = 90^{\circ}$ (b) $\theta = 45^{\circ}$; $\varphi = 0^{\circ}$ (— numerical model; --- analytical model). 107
Figure 4.14 Comparison of transmission loss of the plate strip based on the numerical model and analytical model for the case of the different thickness (— numerical model; --- analytical model). 108
Figure 4.15. Comparison of transmission loss of the plate strip and the analytical model for lower damping loss factor $\eta = 0.01$ (— numerical model; --- analytical model). 109
Figure 4.16. TL comparison of the numerical models and the analytical model under a diffuse sound field excitation (— numerical model using plate elements; --- analytical model). 110
Figure 4.17. Restrained node for simply supported boundary conditions in the solid element model. 111
Figure 4.18. Dispersion curve comparison of the plate element model and the solid element one (● Plate element ; ○ solid element) 111
Figure 4.19. Restrained nodes position of an solid element (● restrained node) 112
Figure 4.20 Dispersion curve comparison of configurations in Figure 4.19 (○ configuration (a); ● configuration (b) ; □ configuration (c)). 113
Figure 4.21. Mobility comparison of the solid element model and the plate element model (— solid element; --- plate element; —•— analytical model). 114
Figure 4.22. Radiated power comparison (— solid element; --- plate element; —•— analytical model). 115
Figure 4.23. Radiated power level difference between the numerical model and the analytical one (— solid element model and analytical; --- plate element model and analytical). 115
Figure 4.24. Transmission loss comparison of the model with solid element and plate element for normal incidence case (— solid element; --- plate element; —•— analytical model). 116
Figure 4.25. Transmission loss comparison of the model with solid element and plate element for oblique incidence case: (a) at angle 45º about x axis; (b) at angle 45º about y axis (— solid element; --- plate element; —•— analytical model). 117

Figure 4.26. TL comparison of the numerical models and the analytical model under a diffuse sound field excitation (— solid element; --- plate element; – • – analytical model). 118
Figure 5.1. Effect of the incident angle on TL according to the London model for parameters in Table 5.1 (— $\theta = 0^{\circ}$; --- $\theta = 45^{\circ}$; • • • $\theta = 60^{\circ}$; – • – $\theta = 80^{\circ}$).....124
Figure 5.2. Effect of the air cavity depth on standing waves/acoustic resonance for normal incidence (— $d =$ 100 mm ; --- $d =$ 200 mm).....125
Figure 5.3. Effect of incorporating the panel resistance R on the TL curve for normal incidence (— Eq. (5.1); --- Eq. (5.11), R = 2.16; – • – Eq. (5.11), R = 10.5).....126
Figure 5.4. Effect of incorporating the flexural motion of the panel and resistance panel R on the TL curve for the obliquely incident case ($\theta = 75^{\circ}$) (— Eq. (5.1); ---Eq. (5.11), R = 0 ; – • – Eq. (5.11), R = 2.16 ; • • • Eq. (5.11), R = 10.5).....127
Figure 5.5. Diffuse TL for infinite system with $R = 0$ 128
Figure 5.6. Schematic illustration of the numerical model for double panel partition with enclosed air cavity. The dashed-line on the WBE-2 mesh is to indicate the surface velocities are equal to zero.....129
Figure 5.7. TL comparison of the waveguide double panel system using 30 plate elements and London's model for normal incidence (— waveguide structure; --- London's model). 133
Figure 5.8 The change in volume and pressure due to compression and refraction in the enclosed cavity when the panels deform.....135
Figure 5.9. Operating deflection shape of the 1.218 m wide double panel partition at 173 Hz, obtained using WANDS.....136
Figure 5.10. Effect of the panel size on TL for normal incidence (waveguide structure: — 1.0 m width ; --- 1.8 m width; – • – 3.05 m width ; • • • infinite structure).....136
Figure 5.11. Effect of cavity depth for normal incidence: (a) infinite structure (b) waveguide structure with 1.8 m width (— 65 mm depth; --- 100 mm; — • — 200 mm)..137
Figure 5.12 Effect of width and cavity depth of the waveguide to f_{MAM} for normal incidence (— : 1.8 m width and 65 mm depth ; ---1.8 m width and 100 mm depth; — : 3.05m width and 65 mm depth ; --- : 3.05 m width and 100 mm depth).....138
Figure 5.13. f_{MAM} of finite cavity compared with that of infinite system with 65 mm cavity depth (— waveguide system ; --- infinite system).....140

Figure 5.14 Dispersion curve of the waveguide double panel system for $\kappa = 0$ (— free bending wave; --- acoustic wavenumber in the $y-$direction in the air cavity). 142
Figure 5.15. Pressure distribution in the cavity at internal coincidence frequency for normal incidence: (a) 2028 Hz (b) 3840 Hz. 143
Figure 5.16. Standing sound wave match standing flexural wave. 143
Figure 5.17. Effect of cavity loss factor on TL in 1/3 octave frequency bands: (a) normal incidence case; (b) oblique incidence at angle 45° about x axis; (c) oblique incidence at angle 45° about y axis (— $\eta_{cav} = 10^{-3}$; --- $\eta_{cav} = 10^{-2}$; - • - $\eta_{cav} = 10^{-1}$). 146
Figure 5.18 Damping loss factor effect on the TL behaviour for normal incidence: full spectrum (--- $\eta_{panel} = 0.6$; — $\eta_{panel} = 0.06$; - • - $\eta_{panel} = 0.006$; ••• TL slope). 147
Figure 5.19. Effect of panel loss factor in 1/3 octave frequency bands: (a) normal incidence case; (b) oblique incidence at angle 45° about x axis; (c) oblique incidence at angle 45° about y axis (--- $\eta_{panel} = 0.6$; — $\eta_{panel} = 0.06$; - • - $\eta_{panel} = 0.006$)..... 148
Figure 5.20. Effect of boundary condition on the TL behaviour: (a) normal incidence; (b) oblique incidence at angle 45° about x-axis; (c) oblique incidence at angle 45° about y-axis (— simply supported BC; --- free-free BC; ••• clamped BC). 151
Figure 5.21. TL due to oblique incidence: (a) angle about x-axis (b) angle about y-axis (— numerical model at angle 60°; — numerical model at angle 80°; --- infinite plate model). 153
Figure 5.22. Transmission loss of waveguide double panel system due to oblique incidence: (a) about the x axis; (b) about the y axis 155
Figure 5.23. Radiation ratio of waveguide structure again the incident angle as a function of incident angle compared with that of infinite structure indicated by dashed line. 156
Figure 5.24. Effect of different panel thickness on TL: (a) normal incidence; (b) oblique incidence at angle 45° about x axis; (c) oblique incidence at angle 45° about y axis (— identical 16 mm thick panels; --- combination of 8 mm and 16 mm thick panels; 158
Figure 5.25. Diffuse TL comparison of the numerical model and the infinite plate one (— numerical model; ---Infinite plate model with $R = 0$). 160
Figure 5.26. Effect of the cavity loss factor on TL for diffuse sound field in 1/3 octave frequency bands (••• $\eta_{cav} = 10^{-6}$; — $\eta_{cav} = 10^{-3}$; --- $\eta_{cav} = 10^{-2}$; — • - $\eta_{cav} = 10^{-1}$). 160

Figure 5.27. Effect of upper incidence angle on the TL behaviour in 1/3 octave frequency bands with $\eta_{cav} = 10^{-3}$:(a) Numerical model (— $\theta_{\lim} = 90^{\circ}$; --- $\theta_{\lim} = 80^{\circ}$; ••• $\theta_{\lim} = 70^{\circ}$; – • – $\theta_{\lim} = 60^{\circ}$); (b) Infinite plate model with $R = 0$ (— $\theta_{\lim} = 90^{\circ}$; --- $\theta_{\lim} = 80^{\circ}$; ••• $\theta_{\lim} = 70^{\circ}$; – • – $\theta_{\lim} = 60^{\circ}$) 161

Figure 6.1 (a) Sketch of the waveguide double panel system with steel studs (b) Schematic view of numerical model of the waveguide double panel system with steel studs. The dashed-line on the WBE-2 mesh is to indicate the surface velocities are equal to zero. ...164

Figure 6.2 TL comparison of the waveguide double panel system with stud removed, vacuum in cavity for normal incidence (— *in-vacuo* model; --- double panel system with enclosed cavity without studs) 166

Figure 6.3 Operating deflection shapes of the *in-vacuo* structure for normal incidence on lower panel: (a) 162 Hz (b) 273 Hz (c) 964 Hz (d) 1219 Hz 167

Figure 6.4. Dispersion curve of the waveguide double panel partition without existence of the air in the cavity: (a) with studs (b) without studs. 169

Figure 6.5. TL comparison of the full model and the *in-vacuo* model with the studs for normal incidence (— full model; --- *in-vacuo* model; – • – double panel system with enclosed cavity without studs). 170

Figure 6.6. Effect of stud spacing on TL of *in-vacuo* model for normal incidence (— 600 mm; --- 300 mm; – • – 200 mm). Arrows indicate a dip corresponding with fundamental natural frequency of a single bay of each system. 172

Figure 6.7 dispersion curves for different stud spacing: (a) 600 mm stud spacing; (b) 300 mm stud spacing; (c) 200 mm stud spacing. 173

Figure 6.8. Effect of stud stiffness on TL of *in-vacuo* model: (a) normal incidence; (b) oblique incidence (— $E = 2\times10^{11}$ N/m^2; --- $E = 2\times10^{10}$ N/m^2; ••• $E = 2\times10^{9}$ N/m^2; – • – $E = 2\times10^{8}$ N/m^2). 175

Figure 6.9. Effect of loss factor on TL of *in-vacuo* model for normal incidence: (a) $E = 2\times10^{11}$ N/m^2; (b) $E = 2\times10^{8}$ N/m^2 (--- $\eta_{stud} = 0.1$; — $\eta_{stud} = 0.01$; • — • $\eta_{stud} = 0.001$). 176

Figure 6.10. Cross-sectional shape of the studs: (a) simplified stud; (b) C-stud; (c) acoustic stud. 177

Figure 6.11. Effect of stud geometric form for normal incidence case (--- simplified C-stud; — C-stud; — • — acoustic stud). 178

Figure 6.12. TL comparison between *in-vacuo* and full model with C-stud (— full model; --- *in-vacuo* model). 179

Figure 6.13. TL comparison of measured result and numerical results (WANDS) for different cavity loss factor η_{cav} (— $\eta_{cav}=10^{-3}$; --- $\eta_{cav}=10^{-2}$; - • - $\eta_{cav}=10^{-1}$; •••frequency-dependent cavity loss factor; - ○ - measurement TL-93-057 [38]). 180
Figure 6.14. TL comparison of numerical results (WANDS) and measured one for the case of 65 mm cavity depth (C-stud: — $\eta_{cav}=2.7\times10^{-2}$, --- $\eta_{cav}=10^{-3}$; ••• simplified stud with $\eta_{cav}=10^{-3}$; - ○ - measurement TL-93-057 [38]). 182
Figure 6.15. TL comparison of measured result and numerical results (WANDS) for different upper limit angle $\theta_{\lim}$ (— $\theta_{\lim}=90^{\circ}$; --- $\theta_{\lim}=80^{\circ}$; - • - $\theta_{\lim}=70^{\circ}$; ••• $\theta_{\lim}=60^{\circ}$; - ○ - measurement TL-93-057 [38]). 183
Figure 6.16. TL comparison of measured result and numerical results (WANDS) for different air stiffness with cavity loss factor of 10^{-2} (— ρ_{air} = 0.6 kg/m^3; --- ρ_{air} = 1.21 kg/m^3; - ○ - measurement TL-93-057 [38]). 184
Figure 6.17. TL comparison of measured result and numerical results (WANDS) and for half air stiffness with different cavity loss factor (— $\eta_{cav}=2.7\times10^{-2}$; --- $\eta_{cav}=10^{-2}$; ••• $\eta_{cav}=10^{-1}$ and $\rho_{air}=1.21$ kg/m^3; - ○ - measurement TL-93-057 [38]). 185
Figure 6.18 TL comparison of numerical result (WANDS) and measurement one for the case of 90 mm cavity depth (— Numerical result for $\rho_{air}=0.6$ kg/m^3 and $\eta_{cav}=2.7\times10^{-2}$; --- Numerical result for $\rho_{air}=0.6$ kg/m^3 and $\eta_{cav}=10^{-2}$; - ○ - measurement TL-93-418 [38]). 186
Figure 7.1. Sketch of test specimens considered in the measurement. 192
Figure 7.2. Timber cavity blocker 192
Figure 7.3. Measurement setup in the reverberation chamber 194
Figure 7.4. Sketch of filler wall during preliminary test. 195
Figure 7.5. TL of filler wall. 196
Figure 7.6. Sound pressure level at receiver room and compared with that of background noise when the filler wall or each test specimen fitted into the aperture. 196
Figure 7.7. Transmission loss comparison between filler wall and TS1 197
Figure 7.8. Transmission loss of TS1, TS2 and TS3 198

Figure 7.9. TL comparison of numerical results and measurements ones in 1/3 octave frequency bands (--- TS1; --- TS2; — numerical model for TS1; — numerical model for TS2).....199
Figure 7.10. TL comparison of numerical result and measurements one for TS2 in narrow bands (--- measurement; — numerical model). 200
Figure 7.11. The difference in the transmission loss between TS1 and TS2 (— Numerical model; --- Measurement).....200
Figure 7.12. TL comparison of numerical results and measured ones: (a) TS1 (b) TS2 (--- measurement ; — numerical model ; – • – numerical model with ρ_o = 0.6 kg/m^3).....201
Figure 7.13. TL comparison of numerical results and measured ones for the case of TS3 202
Figure 7.14. The difference in the transmission loss between TS2 and TS3 (— Numerical model; --- Measurement).....202
Figure 7.15. Effect of steel stud on transmission loss.....203
Figure 7.16. TL comparison of numerical results and measurements ones (--- TS3; --- TS4; — numerical model for TS3; — numerical model for TS4).....204
Figure 7.17. The difference in the transmission loss between TS3 and TS4 (— Numerical model; --- Measurement).....204
Figure 7.18. TL comparison of numerical results and measured one for TS4 (--- measurement ; — numerical model; – • – numerical model with ρ_o = 0.6 kg/m^3).....205

List of tables

Table 2.1. Material properties and dimensions of the plate strip (unless otherwise stated).22
Table 2.2. Cut-on frequencies for each mode m in Hz. 22
Table 2.3. Relation between frequency, number of cut-on modes m and upper limit M for 1% difference in $|Y|$. 27
Table 4.1. Material properties of the plate strip (unless otherwise stated). 90
Table 4.2. Cut-on frequency f_{m}: comparison between numerical results and analytical ones. 93
Table 4.3. Mobility comparison based on analytical results and numerical ones based on residue calculus. 94
Table 4.4. Relative error of numerical results compared with analytical results for certain frequencies. 94
Table 4.5. Wavenumber ranges and step sizes required for 1 dB error and 0.1 dB error. ...95
Table 4.6. Effect of baffle width on the lowest frequency limit for 1 m width structure .101
Table 4.7. Cut-on frequencies f_m corresponding with configurations in Figure 4.19. 113
Table 5.1. Material properties of the gypsum plasterboard 123
Table 5.2. Material properties and dimensions of the double panel partition (unless otherwise stated).....129
Table 5.3. Modified f_{MAM} of the waveguide structure $f_{MAM,WG}$ 139
Table 6.1 Material properties and dimensions of the double panel partition.....165
Table 7.1. Parameters of test specimens 191
Table 7.2. Material properties used in numerical models (unless otherwise stated).....198

Declaration of authorship

I, Iwan Prasetiyo

declare that the thesis entitled

Investigation of sound transmission in lightweight structures using a waveguide finite element/boundary element approach

and the work presented in the thesis are both my own, and have been generated by me as the result of my own original research. I confirm that:

- this work was done wholly or mainly while in candidature for a research degree at this University;
- no part of this thesis has previously been submitted for a degree or any other qualification at this University or any other institution;
- where I have consulted the published work of others, this is always clearly attributed;
- where I have quoted from the work of others, the source is always given. With the exception of such quotations, this thesis is entirely my own work;
- I have acknowledged all main sources of help;
- where the thesis is based on work done by myself jointly with others, I have made clear exactly what was done by others and what I have contributed myself;
- Parts of this work have been published as:
    1. Prasetiyo, I. and Thompson, D. *Vibration response, sound radiation and sound transmission of an infinite plate strip*, ISVR Technical Memorandum, November 2011, University of Southampton, UK.
    2. Prasetiyo, I. and Thompson, D., *Study of the effect of finite extent on sound transmission loss of single panel using a waveguide model*, Acoustics 2012, Nantes, France.
    3. Prasetiyo, I. and Thompson, D., *Effect of finite air cavity and steel studs on sound transmission loss of lightweight double panel system*, Euronoise 2012, Pague, Czech Republic
    4. Prasetiyo, I., D.J. Thompson, and J. Ryue, *Validation of coupled Waveguide Finite Element-Wavedomain Boundary Element (WFBE) method for case of an infinite plate strip*, ISVR Technical Memorandum, October 2012, University of Southampton: Southampton

Signed: ……..
Date:…….

Acknowledgements

First and foremost, I would like to express my sincere gratitude to my supervisor, Prof. David Thompson for his guidance, encouragement, immense knowledge and great supervision in this research. He gave me optimism throughout this study to deal with things in a proper way even when they appeared naturally out of my control in regard to the completion of this research.

I am deeply grateful to Dr. Christopher Jones for providing assistance with using the software WANDS. This research was also made easier with the help from Dr. Jungsoo Ryue and Dr. Qingsong Feng in updating the software WANDS voluntarily so that it was more applicable for this research. A special thanks is also extended to Dr. Anand Thite for useful discussions particularly for developing a numerical model using WANDS.

I am also indebted to the Institute of Sound and Vibration Research (ISVR) staff and technicians. Among them, I would like to give a special credit to Phil Oxborrow and John Fithyan who have helped me a lot during measurements. My colleagues in the Dynamics Group for a great friendship and atmosphere. Appreciation is also expressed to my Indonesian and Malaysian friends for their supports and kindness during my life in the UK of which they are too many to mention individually.

My sincere thank also goes to Directorate General of Higher Education (DGHE), Department of National Education of Indonesia for providing a postgraduate scholarship. I also thank Institute Teknologi Bandung (ITB) for their supports during my study.

Last but not the least, I would like to thank my beloved wife Yeny for her understanding, love and sacrifices during my study in UK. And also for my son Wiksa who has coloured and cheered up my days. I wish also to express my gratitude to all my family to whom this thesis is lovingly dedicated.

Abbreviations

DOF	Degree of freedom
MAM	Mass-air-mass
TL	Transmission loss
WFE	Waveguide finite element
WBE	Wavenumber boundary element
WFBE	Waveguide finite element/boundary element
WANDS	Wavenumber domain software

Nomenclature

a	Ratio of mass impedance to acoustic impedance
$A_{1,m}$, $A_{2,m}$, $A_{3,m}$, $A_{4,m}$	Wave amplitudes of transverse displacement
$\mathbf{A}_j$	Matrix of stiffness
c	Sound velocity
d	Cavity depth of double panel system
D	Bending stiffness
D'	Complex bending stiffness
E	Young's modulus
f	Force per unit area
f_c	Critical frequency
f_{ll}	Lowest frequency limit
f_x, f_y	x and y dependent force
F	Force amplitude
F_m	Fourier coefficients
$\mathbf{F}$	A vector of nodal force amplitudes
h	Plate thickness
$i = \sqrt{-1}$	Imaginary unit
J	Jacobian
k_B	Free bending wavenumbers of plate
k_x, k_y, k_z	Acoustic wavenumber in x, y and z directions
$k_{x1,m}, k_{x2,m}$	Wavenumber in x-direction for each mode order m
$\mathbf{K}_n$	Stiffness matrices
l_y	Plate strip width
m	Mode order across width of plate
m''	Mass per unit area
M	Total number of orders considered
$\mathbf{M}$	Mass matrices
$\mathbf{M_f}$	Fluid mass matrices
n	Number of half waves across cavity depth

$\mathbf{n}$	Unit direction vector
p	Acoustic pressure
p_i	Incident sound pressure
p_{rad}	Radiated pressure
$\tilde{P}$	Fourier transform of p
r	Panel resistance
R	Normalized panel resistance
$R_{mm'}$	Inter-modal coupling which couples structural mode m with the radiated pressure in other modes
s	Stiffness per unit area
S_m	Shear force per unit width
v	Vibration velocity
$\left\langle \overline{v(x,y)^2} \right\rangle_{\inf}$	Spatial 'average' mean-square velocity
$\tilde{V}$	Fourier transform of v
V_0	Nodal surface velocity
w	Out-of-plane displacement
W_{rad}	Radiated power
$\mathbf{W}$	Vector of nodal displacement amplitudes at nodes in $y-z$ plane
$\tilde{\mathbf{W}}$	Fourier transform of displacement
w_m	Complex amplitude of the m^{th} component
W_{rad}	Sound power radiation
$x,\ y,\ z$	Cartesian coordinates
Y	Structural mobility
z_a	Acoustic impedance
Z_w	Wall impedance
α	Acoustic wavenumber in $y-z$ plane
β	Phase of pressure wave
γ	Wavenumber in y direction
η	Damping loss factor
θ	Elevation angle

Γ	Perimeter of the cross-section
κ	Structural wavenumber in x-direction
λ	wavelength of vibration
ν_p	Poisson's ratio
ρ_0	Mean fluid density
ρ	Plate strip density
τ	Transmission coefficient
τ_d	Diffuse transmission coefficient
φ	Azimuth angle
ϕ	Angle about x axis
χ	Angle about y axis
ψ	Velocity potential
ω	Angular frequency
ω_m	m^{th} cut-on frequency

Chapter 1. Introduction

1.1 Background

Lightweight structures are widely used in vehicles and buildings. In buildings lightweight walls, such as shown in Figure 1.1, have become commonplace due to their flexibility of use and ease of construction. In order to meet the stipulations of building regulations as in [1], such lightweight structures have to meet a certain sound reduction performance without increasing their weight unnecessarily. Hence, it is of importance to have a fundamental understanding of the vibro-acoustic behaviour as well as a good prediction model in the design process to ensure that such structures can comply with such requirements.

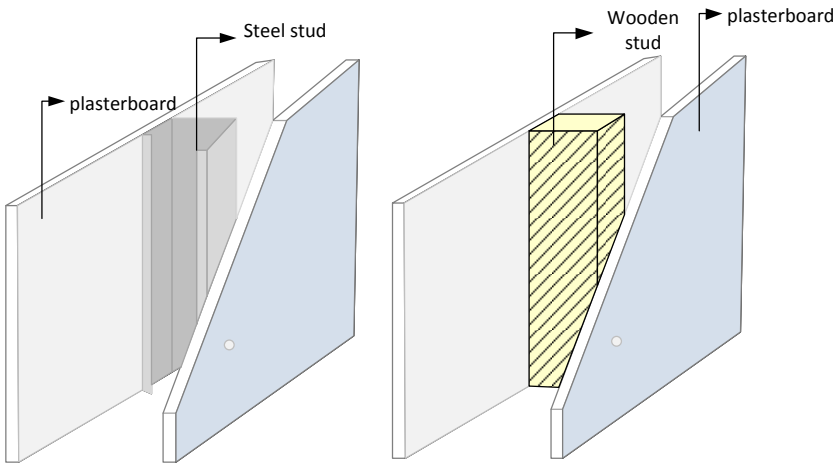

Figure 1.1. Typical lightweight structures for building application.

In general, the reduction in sound across a partition increases with its mass. As the weight of the structures is critical, and considerable transmission losses are required, an appropriate construction is required in order to suppress their acoustic deficiencies. Double panel partition structures are often used in practice to deal with such requirements as they have a higher transmission loss (TL) performance than that of single panels for the same overall mass. However, double panel partitions introduce other complexities in their sound reduction mechanism that are not found in the single panel case, due to the air-cavity and acoustic material inserted within it as well as structural connections [2, 3]. Therefore, for a

good prediction model, it is not sufficient simply to consider the mass of the panels in order to calculate the sound reduction obtained but there is also a need to take account of the other relevant aspects of the system.

A fundamental understanding of the vibro-acoustic behaviour of lightweight structures is of importance to investigate key parameters affecting the structure-borne and air-borne sound transmissions of such systems. This aim, however, is not always easily achieved as the most common models usually include some simplifications in their formulation, e.g. using infinite panel theory and limp panel theory where the bending stiffness effect of panel is disregarded [4, 5], using an infinite cavity [6], assuming infinite stiffness for the studs [2, 7] and so on, which are not always justified in practice. Under such circumstances, a parameter study and prediction for more realistic structures is restricted accordingly and may give rise to a misleading conclusion due to limitations in portraying their true physical behaviour. Moreover, it is found that existing prediction models do not yet cover all possible variations found in practice [8]. Hence, a more versatile prediction model is still required.

For waveguide structures which have a constant cross-section in a particular direction, the waveguide finite element/boundary element (WFBE) method is a numerical tool that is able to provide a flexible approach in representing the structure in detail in terms of its geometry for a wide frequency range as well as allowing for fluid-structure interaction [9]. WFBE method allows an efficient model to be produced for situations where the geometry is effectively two-dimensional but the wave field is three dimensional. Hence, this method requires less computational time and memory compared with conventional FE/BE.

As a typical double panel system has an arbitrary cross section with constant properties in one direction and therefore forms a waveguide, the WFBE method is expected to be useful for investigating its transmission loss behaviour as well as suitable to develop prediction models for such structures by taking into account the finite width of the panel and of the air cavity explicitly. Moreover, steel studs can also be included into the model as mechanical connectors between the panels. In the next section, literature on transmission loss particularly from single and double panel systems is reviewed.

1.2 Literature review

1.2.1 Prediction models for single panel

The transmission loss (TL) is a decibel quantity of the ratio of the incident power W_{inc} impinging on a structure to resulting transmitted power W_{trans} as

$$R = 10\log_{10}\left(\frac{W_{inc}}{W_{trans}}\right) \qquad (1.1)^{1}$$

This quantity is used to indicate the reduction in sound energy across the structure. Hence, a higher TL means a lesser amount of sound energy can be transmitted through the structures and vice versa. The TL prediction of a panel has been carried out for many years under the fundamental assumption that the panel is infinitely extended and excited by a random incidence sound field [4]. This enables the TL of the panel to be predicted conveniently, assuming perfectly diffuse conditions where the incident energy is distributed equally in all directions. The use of a limp panel has the implication that the prediction is only dependent on the mass of the panel per unit area, not on its stiffness. This leads to a formulation known as the mass law which corresponds to 'non-resonant transmission'. Accordingly, it is inadequate to explain resonant transmission in which the coincidence phenomenon is present. Moreover, compared with experimental results, this approach gives rise to some discrepancy where field incidence [10] is usually used as an empirical correction to get better prediction results.

The coincidence phenomenon in sound transmission occurs when the trace wavenumber of sound excitation equal to a free wavenumber of structure [11]. Under such a condition, the sound energy is transmitted almost unattenuated as the wave impedance of structure becomes zero. The coincidence in the TL curve can be found at different frequencies as it depends on the incident angle and the lowest coincidence appears at grazing incident angle which is equal to the critical frequency.

London [5], developed a model for the sound transmission loss prediction of an unbounded single panel by considering the effect of mass, dissipation and flexural motion.

[1] For consistency throughout this thesis, R is used instead of TL to denote sound reduction index or transmission loss formula.

The average TL for a diffuse sound field was obtained by integrating the transmission coefficient over the incident angles. This study concluded that neither normal incidence theory nor the mass law were adequate to explain the behaviour of single panel in a diffuse sound field.

As the panel is finite in practice, a number of researchers have addressed some problems that are not present in the infinite case, i.e. effect of the finiteness and mounting (or boundary) conditions which introduce peaks and dips in the TL curve over a particular range of frequency. For the finite panel, Sewell [12] developed a formula to predict the sound transmission loss of a single-leaf partition which was set in an infinite rigid baffle by means of a modal expansion approach. This study produced a correction to the TL prediction of the infinite plate, leading to an improvement in the prediction accuracy relative to the mass law.

Leppington [13] investigated the resonant and non-resonant transmission of panels. Analytical formulae for the problem with two-dimensional geometry where a panel is mounted in an infinite rigid baffle were then developed. The formulae obtained can particularly improve the non-resonant transmission calculation which leads to better agreement with experimental results when combined with the resonant transmission. This corrects the non-resonant formulae proposed by Sewell [12] as well as providing further explanation for issues corresponding with the non-resonant transmission and field incidence that is commonly introduced in transmission prediction using infinite panel theory.

1.2.2 Double panel partition with air cavity

Some efforts to formulate the TL prediction of double panel partitions have been conducted over the years. Initially, simple models were developed for an infinite double panel partition without structural connections, for example the model proposed by Beranek and Work [14]. This was developed using the transfer impedance method based on continuity of the acoustic velocity at the interfaces. For simplicity only the mass reactance of the panel was initially considered. Moreover, this model did not include the effect of a diffuse incident sound field. Fahy [2] and London [15] used the progressive-wave method to develop a prediction model for a similar case by considering forward and reverse travelling waves between panels. From these models, the double panel partition may have

a lower TL than that of a single panel due to the presence of a dip at low frequency. Such a dip is present when the panels move out-of phase due to excitation in the normal direction and referred to as the mass-air-mass resonance. In the London model, a complex impedance consisting of the resistance and reactance term was introduced for the panels. Moreover, compared with the model in [14], the inclusion of the flexural motion of the panel allows the coincidence effect in the sound transmission problem to be evaluated and the panel response due to a diffuse field excitation to be investigated. Using this approach with an appropriate value of the panel resistance, the prediction results and measured ones can be aligned.

In comparison with measurement results, however, the results from the infinite prediction model differ to some degree. To overcome these differences, various correction factors are commonly introduced to obtain an improved fit with the measurement results. The most classic way is by limiting the maximum incident angle for a diffuse field calculation; the limit typically varies between 70° and 85° [16]. For example Beranek et al. [10] found an upper incident angle of 78° leads to a good fit between the prediction results and the measurement ones. It should be noted that these limiting incident angle values were obtained empirically from the best fit between the prediction results and the experimental ones. The resulting model is then termed “field incidence”. In physical terms, it is reasonable as the incident sound at grazing incidence is hard to realize in practice. Mulholland et al. [17] support this by observing a relation between the room mode density and the incident angle. It is found that above the limiting angle the number of modes decreases significantly hence justifying the absence of sound in this region. Therefore, it is suggested that the introduction of the upper limit angle actually deals with imperfections in the diffuse sound field found in practice that might be caused by the properties of the measurement facility. Moreover, such an upper limit angle can minimize the “niche” effect at frequencies below the critical frequency; this corresponds to the shielding effect due to the depth of aperture in which the specimen is mounted [18] where such an effect is also evident at low frequency as discussed in [19]. Sewell [12] indicated in his theory that the limiting angle of incidence varies and is not limited to a fixed value; instead the exact value depends on frequency and on the panel size. This indicates that the form of the incident sound field is not the only cause of the discrepancy. Despite all that, Kang et al. [20] found that a Gaussian distribution function over incident angle offers a better

directional distribution of the incident energy than the field incidence theory for the case of multi-layered panels.

The effect of finiteness of the structure on the transmission problem in double panel partitions is also considered through rigorous mathematical formulations among others by Sewell [6]. This was based on a multimodal analysis of the panels in order to get a solution for a finite double panel mounted in an infinite rigid baffle. Compared with the infinite models, his formulation for a fully diffuse incident field behaves similarly to those with a limiting angle of incidence, although such a limitation is not incorporated in his model. Instead, this behaviour is related to the cavity depth rather than the characteristic of the measurement facilities introduced as the limiting angle. Cummings and Mulholland [21] developed a prediction model for the same case by introducing absorption at the edges of the cavity. By using the multiple-reflection theory [17], the prediction model considers absorption effects in the air cavity by tracing the incoming sound in which the amplitude of reflected sound reduces as it undergoes successive reflections. However, it requires an absorption coefficient equal to 1 to allow the results to become close to the experimental ones and that is not realistic in practice. Xin et al. [22] developed a model which is applicable for a double panel system of finite extent. It differs from Sewell's model since the solutions are derived for a double panel system with clamped boundary conditions instead of the simply supported boundary.

A spatial windowing technique has been developed to deal with issues arising from the finiteness of the panel [23, 24]. A theoretical radiation ratio of a baffled finite sized panel is introduced to address the diffraction characteristics at the edges of the bounded structure. Compared with the infinite plate model, this increases the TL values, particularly at low frequency. However, in this approach, the modal characteristics of the panel due to its finiteness are not taken into account. More recently, Vigran [25] developed a prediction model based on a simplified spatial windowing technique in which a one-dimensional "window" was used rather than a two-dimensional one.

Other methods used for sound transmission through finite structures, include SEA (statistical energy analysis) [26], FEM (finite element method) or BEM (boundary element method) [27, 28]. These are discussed further in section 1.2.4 below.

Apart from numerical models, prediction models dealing with finite structures do not necessarily treat the air cavity as a finite system, e.g [6, 23]. Moreover, although a

finite cavity is considered in a model in [22], this was focused to investigate the effect of the boundary condition of the panel rather than discussing specifically the effect of the finite cavity on the transmission loss, particularly where no sound absorption is present in the cavity.

1.2.3 Double panel partition with studs

In a typical double panel wall, structural links or studs are commonly present between the two panels. They are used to increase the stiffness of the structure as well as to provide a structural support and stability to the panels attached to them. However, this leads to a degraded sound insulation performance as the studs act as an additional path for sound transmission. Some models have been proposed in order to evaluate such a structure. Sharp [7] considered double panel systems with the studs having an infinite stiffness that rigidly connects the panels. In this model, the vibration velocity of both panels is equal at the stud positions. The results obtained would be suitable for studs which have a high transverse stiffness, e.g. wooden studs. A primary positive aspect of Sharp's model is that it is simple and easy to implement, hence it is very attractive for practical purposes. However, for the case of a double panel system with elastic studs, the resulting TL prediction would be underestimated due to the omission of the flexibility which reduces vibration transmission. For this reason, Gu and Wang [29] proposed a model in which flexible studs were included. They aimed to take account of the lateral resilient effect of the metal studs when under compression. The flexible studs were represented by a spring having equivalent stiffness K_t so that the vibration velocity of both panels at the stud is no longer equal. However, owing to assumptions made concerning the stud vibration velocity ratio of the two panels, their formulation should be used with caution for a lightweight partition regarding the frequency range under consideration.

Fahy [2] proposed a model for the same system using assumptions similar to Sharp's, i.e. the stud possesses infinite stiffness and each stud is assumed to have an independent dynamic behaviour. Moreover, the studs are considered to move in the translational direction only. However, it differs from Sharp's model as Fahy also considered the mass per unit length of the studs in calculating the vibration velocity of the stud due to excitation of the first panel. It should be noted that this model was derived to illustrate the general behaviour of the double panel system with studs rather than to give an

accurate solution to the stud-panel system for practical purposes. Nevertheless, this model gives a basic idea about how the stud connections transmit sound energy. By considering the ratio of transmission via the stud and via the cavity, assuming that the line impedance of both panels is equal, this formulation suggests that the sound transmission through the studs would be more dominant for panels with low critical frequencies. The stud transmission is then multiplied by a factor which expresses the ratio of sound power radiated by the whole panel and by the excitation region around the studs in order to get the overall transmission coefficient.

Following Fahy's model [2], Davy [30, 31] developed a prediction model with some extensions. It allows different line impedances for the panels involved in the system and flexible studs may be considered. Moreover, compared with the models in Refs. [2, 7, 29], it also considers resonant components of the panel vibration besides the non-resonant ones, as proposed in [26]. This basic model actually consists of approximation equations to the numerical model proposed by Sato [32] to deal with bounded partitions. Among the established models, it delivers a better prediction for double panel cases than other models [8, 33]. However, this model seems to be difficult to understand in physical terms as various ad-hoc corrections are employed in order to get the results closer to the measurement ones rather than solving the vibro-acoustic governing equations as in e.g. Refs. [6, 34, 35]. Therefore, optimization of design may not be easy to perform using this formulation.

The prediction models developed in Refs. [2, 7, 29, 31] use a decoupled approach to predict the sound transmission loss of the double panel system with studs. It is termed as such as the prediction models calculate the energy transmitted through the structure and the cavity separately and then add them up to obtain the total transmission of the system. More recently, a similar approch was also proposed by Nakanishi et al. [36] with a weighting factor introduced to each transmission path in order to get a better fit between the prediction result and the experimental ones.

The frequency at which the stud and the air in the cavity have equal contributions to the total response if considered separately is termed the bridge frequency f_B [7, 29]. Below this frequency the air in the cavity contributes most to the total transmission of the system while above this frequency, the stud starts to dominate in the overall transmission. This frequency is clearly seen for cases where sound absorbing material is present in the

cavity as in calculations [7, 29] and measurement [37] where the cavity and stud dominant regions in TL curves is clearly seen. Without sound absorbing material in the cavity, however, such a frequency would be different. Such a tendency is indicated by measurement results, e.g. in Ref. [38], where the inclusion of sound-absorbing material in the cavity in order to suppress undesirable cavity modes was found to increase the TL of a double panel system with C-studs for frequencies up to 6.3 kHz where the critical frequency was around 2.5 kHz. This indicates that the transmission through the air cavity is also significant at high frequency.

Due to the periodic spacing of studs a periodic approach has been considered. Lin and Garrelick [39] developed an analytical model for an infinite double panel system with rigid studs treated as a periodic structure. By means of a Fourier transform, the solution for the system was obtained and then the relative contributions of the structural and cavity paths in such a system were obtained. However, as indicated by Urusovskii [40], the basic formulation of Lin and Garrelick has some shortcomings with regard to the phase factor and mass reactance of the stud as well as the acoustical influence of the cavity. These were remedied by the model proposed by Urusovskii [40].

With the help of a space harmonic expansion and the principle of virtual work, Wang et al. [41] developed a model in which the studs were assumed to be periodically distributed along the gap between the panels. This is actually an extension of Mead and Pujara's model [42, 43] for the case of a double panel system with flexible studs. For this, compressional and torsional springs were used to cover the resilient characteristics of the studs. Subsequently, Legault and Atalla [33] reviewed some models that were developed using both the decoupled approach and the periodic one. By exploiting the important features of each model, a periodic model was developed for thin lightweight panels with mechanical connectors and sound absorbing material in the air cavity. Meanwhile, Brunskog [34] investigated the finite cavity effect of the same system using the Fourier transform to solve the vibro-acoustic problem. The cavity was treated as finite due to the presence of the wooden studs rather than being transparent to the studs as assumed in [33, 41] but the system was otherwise infinite in extent.

Instead of using a constant compressional stiffness to represent a resilient channel as in [29, 33, 41], some models used a frequency-dependent equivalent stiffness. Poblet-Puig [44] calculated such an equivalent stiffness by approximating the results of the FE

model of elastic studs by simpler models consisting of compressional and rotational springs. Vigran [45] developed a model by including the best fit to the equivalent stiffness data in [44] to simplify calculations in his model. Compared with measurement results, his model produces a good agreement. More recently, Davy et al. [46] used a similar approach but with different data for best fitting based on NRCC sound insulation measurement data [38].

A numerical aproach can be an alternative method in modelling such cases without introducing many simplifications as found in [7, 29] which can give rise to restrictions to the prediction models in their use. Sound-structure interaction between panels and air in the cavity and surrounding medium can also be established in more rigorous way so that mutual effects can be taken account which are absent in the decoupled approach. This allows the total transmission to be obtained rather than calculating each transmission individually. This means that the use of weighting factors to the contribution of each transmission path [2, 7, 29, 31, 36] is no longer required. Moreover, the geometric form of studs can be expressed as they are (or closer to their true shape) and the stud parameters can be varied easily as well. This allows investigation of the physical origin of phenomena associated with the effect of steel studs on the TL to be performed more intensively, not limited for typical studs found in practice but also for new ones, where such advantages may be difficult to be inferred directly from some existing models, e.g. [45, 46].

1.2.4 Numerical models

Since the exact solution is not always available, numerical approaches can be an alternative way to solve vibro-acoustic problems. This is beneficial for calculating the transmission loss for complex structures, e.g. geometrical complexity, where the analytical approach becomes impractical. For this, a coupled FEM/BEM approach can be used to calculate the sound transmission loss, where FEM is used for modelling the structural and internal fluid behaviour whilst the fluid domain outside the structure is efficiently handled by BEM especially for radiation problems [27, 28, 47]. The drawback of these numerical tools is that the computer resources required become excessive for high frequencies when the number of elements required increases. Therefore, it is more suitable for investigations at low frequencies [28].

Conversely, Statistical Energy Analysis (SEA) can be used for mid-high frequency cases, depending on the modal density over a certain frequency band, but the results lack detail due to the statistical nature of the approach. The use of SEA for the TL calculation can be found for a homogeneous panel in [48] where coupling of the panel and rooms was considered. The concept of resonant transmission and the non-resonant transmission were introduced, the latter being associated with the mass of panel and introduced in SEA scheme as a direct coupling between the two rooms. This model was then extended for double panel systems in [26]. However, after comparing with experimental results, Elmallawany [49, 50] found inaccuracy or disagreement of the SEA results at low frequency and around and above the critical frequency. Moreover, for the double panel system case, such disagreement was also found at the dip frequency associated with the mass-air-mass resonance. With regard to the latter issue some extensions to improve the SEA model have been developed, e.g. Brekke [51] included a non-resonant coupling component for the panel and the air stiffness in the cavity while the problem related with the low frequency performance still remained as a consequence of nature of this method. The implementation of SEA for more complex structures can be found for double panel systems with mechanical connections in [52, 53] and sandwich panels in [54].

A numerical approach offers flexibility in modelling but a high computational resource is required as well as long computation times. As an alternative numerical tool, the spectral finite element (SFE) method [55] can be considered. This method is efficient as the solution can be expressed as a combination of cross-section mode shapes and exponential functions for propagation in the other direction so that the number of the degrees of freedom is reduced. For an infinite length waveguide system with arbitrary cross-section, an exact wave solution is utilized in the infinite direction. Hence, this method needs 2D modelling of the cross section with special elements that allow for wave propagation in the third dimension. This technique is also referred to as the waveguide finite element (WFE) method. It can be coupled with wavenumber boundary element (WBE) method to form a coupled waveguide finite element/wavenumber boundary element (WFBE) method. This numerical approach can provide results in detail and cover a wide frequency range compared with conventional FEM/BEM and SEA. It has been applied for example to railway tracks [56-58], pipes [55], cylindrical shells [59] and tyres

[9, 60]. The use of WFBE to calculate the sound transmission loss for an example extruded panel is reported in [61].

As this numerical method requires specific elements that need to be developed on a case-by-case basis, another approach in modelling waveguides based on the finite element method can be found [62]. By applying a periodicity condition, dynamic behaviour of a section with particular segment length Δ cut from a structure can be used to predict the response of the whole structure. Using similar approaches, Mace et al. [63] has developed a method without necessarily requiring new elements where the element library of a conventional FE package can be employed. The advantage of these apparoches, however, contains some inherent weaknesses in regard with accuracy as the effects of spatial discretisation and periodicity as well as machine rounding error exist. Hence, the segment length Δ must be selected carefully in order to avoid being comparable to the shortest wavelength in the structure as well as not too small where round-off error is present in which the value of the stiffness matrices is too large compared with the inertial term [64].

1.3 Objectives and scope of the thesis

The main objective of this thesis is to investigate the sound transmission behaviour of lightweight structures. For this, a physically based model using the WFBE method is developed that allows a parameter study to be carried out for "waveguide" structures which have constant geometry in one dimension.

The double panel system is the main application considered. The investigation is focussed on the effect of the finite cavity and finite panel width where sound absorbing material is not present. For more complex structures, the effect on sound transmission of mechanical connectors in the form of steel studs is also investigated. All results are expressed in terms of transmission loss (TL). The results are discussed by comparing them with those of an infinite system (London model). It means that the numerical model implicitly is used to assess the London model which uses infinite plate theory and introduces a complex impedance mass in order to get better prediction results. In this study, measurement results are also presented to validate the numerical ones and some findings related with issue of the finite cavity in double panel systems.

The WFBE method allows the vibro-acoustic behaviour of complex structures to be evaluated. Using this method, the numerical model of the double panel system can be

realized with various parameters of interest to represent the physical structure including details that are usually simplified in analytical models. Hence, the WFBE approach allows flexibility in expressing the stud geometry with various cross-section shapes and material properties. The numerical model proposed assumes the structures are mounted in a rigid baffle. Moreover, room effects and flanking transmission that may exist in practice or measurements are not considered. In order to verify the WFBE approach, an analytical solution for a plate strip is developed as a benchmark solution.

1.4 Thesis outline

The structure of the thesis as follows:

Chapter 2 is devoted to a systematic procedure for obtaining solutions for the vibro-acoustic behaviour of a plate strip using the Fourier transform method with emphasis on how the fluid and structure interact with each other. Moreover, a detailed discussion of the implication of varying several parameters of the plate strip is also provided. The resulting solutions, which are exact apart from their numerical evaluation, can be used as a benchmark solution for validating the waveguide finite element/boundary element approach.

Chapter 3 introduces the basic concept of the waveguide finite element/boundary element (WFBE) method. It starts with a description of plate elements and solid elements used in the WFBE method. Solutions for free and forced response using this method are also presented. Subsequently, the Wavenumber Boundary Element (WBE) method is explained to underline the way in which it differs from the conventional BE method. The coupling of these two methods is provided in terms of matrices and the procedure of calculating the radiated power and transmission loss is described including the diffuse sound field case.

In Chapter 4 validation of the numerical model is conducted by comparing the results obtained with those from the analytical models in Chapter 2 for a finite width plate strip. Comparisons of the results of the two methods as well as various methods for evaluating the integral in the inverse Fourier transform are discussed in detail. This latter step is important in order to know the effect of discretization in wavenumber space in terms of step size and wavenumber range. As the numerical model is implemented with a

finite width baffle, the effect of baffle width on the accuracy of the radiated power calculation is also investigated. Moreover, the effect of the thickness (i.e. depth) of the WBE mesh is considered to ensure the WBE method does not produce unreliable results [65] owing to a close distance between the opposite sides of the mesh.

In Chapter 5 a numerical model of the transmission loss for a double panel system is developed using the WFBE method. At first, the general behaviour of a double panel system is illustrated using the model proposed by London [15] in which the system is considered to be infinite in extent. The numerical WFBE model is then used to investigate the effect of finite cavity and panel width on the transmission loss. The results obtained are compared with those of the infinite system to draw some important conclusions.

In Chapter 6 the elastic studs are introduced in the waveguide double panel system which has been developed in Chapter 5. The dimensions of the structure in general are chosen to follow specimens measured by NRCC [38] which are used for comparison. The case is investigated initially using a simplified stud model where only the web part is included in the numerical model. This is then extended to include the flanges. A parameter study is presented to investigate further the elastic stud behaviour.

In Chapter 7 new experimental results are provided to validate some findings, particularly in Chapter 5 and 6. In this chapter, the general specification of test specimens is presented as well as the measurement setup and procedure. The cavity dimension and elastic stud effect become a central issue in this measurement. Results are compared with the prediction model.

Chapter 8 contains conclusions and suggestions for futher work.

1.5 Thesis contributions

The main contributions that have been achieved from this study can be outlined as follows:

a. Analytical models based on a wave method have been developed to calculate the vibration response, sound radiation and sound transmission of an infinite plate strip. Compared with those obtained by infinite plate theory, it is shown that ‘edge modes’ contribute to the radiated power below the critical frequency for a point force excitation.

b. It is shown that the slope of sound transmission loss curve for an infinite plate strip at low frequency is modified from the results for an infinite plate.
c. Numerical integration and discretization effects in the wavenumber domain have been assessed and simple rules proposed to avoid losing information when implementing the coupled Waveguide Finite Element-Wavedomain Boundary Element (WFBE) method.
d. The width of the finite rigid baffle used in the WBE method is shown to be important to the accuracy of the numerical model results at low frequency. The width of baffle required at a given frequency has been determined.
e. It is found that the total response of the waveguide double panel system is the sum of the stiffness dependent response and acoustic lateral cavity modes as a consequence of the finite extent of the cavity. Measurement results validate such a tendency.
f. Internal coincidence effects are found to be a source of TL degradation in the waveguide double panel system. The frequency of these phenomena is independent of the direction of incoming waves.
g. It is confirmed that the stiffness of an elastic stud is a critical parameter to determine the overall response of the double panel system with mechanical connectors.
h. Compared with measurement results, appropriate values of the cavity loss factor and air stiffness are also required to achieve better prediction results for cases where no sound-absorbing material is present in the air cavity.

Chapter 2. Vibro-acoustic behaviour for an infinite plate strip

A plate strip is considered here which is assumed to be infinite in length but have a finite width, where it is confined by parallel boundaries. Such structures can also be considered as waveguides [2]. Since such plate strips form a basic element of more complex lightweight structures, they will be discussed first before proceeding to more complex waveguide structures.

The framework for deriving the exact solutions for the vibro-acoustic problem for this structure is readily available in some references, e.g. in Ref.[2, 4]. In those references, the structural vibration response and its interaction with the surrounding fluid are discussed from a wave phenomenon point of view. This wave approach has been applied to obtain solutions by utilizing a spatial Fourier transform for solving many basic cases e.g. beams, plates, pipes (or cylindrical structures), etc. For the case of a plate strip, some results have also been found for particular cases but with a limited discussion.

The focus of this chapter is to understand the vibro-acoustic behaviour of a plate strip in terms of its point mobility, sound radiation and sound transmission loss. For this, an analytical model is developed using a wave approach in order to find waves propagating freely along the waveguide. By combining this wave approach with a modal solution in the transverse direction, the response of the plate strip is obtained in the wavenumber domain using the Fourier transform method. This solution is then extended in order to solve cases in which the interaction of the plate strip and the surrounding fluid is considered, i.e. for the case of radiated sound power and sound transmission loss.

2.1 Vibration of a plate strip

For a waveguide structure an analytical wave approach can be considered. This is used in this section to find the free waves in an infinite plate strip, and in the next section its point mobility. The sound radiation of the structure due to a point force excitation is considered in section 2.3 and the sound transmission due to acoustic excitation is studied in section 2.4. Simply supported boundaries on the two parallel edges will be considered throughout for simplicity.

2.1.1 Undamped free vibration

The plate strip under consideration is illustrated in Figure 2.1. It has width l_y in the $y-$direction and is infinite in the $x-$direction. It is assumed to be simply supported (pinned) along the edges $y=0$ and $y=l_y$. This condition allows the response to be written in a separable form. A travelling wave solution is used to describe the dependence of the displacement on the $x-$direction while, for the $y-$direction, a modal solution can be utilized to describe the structural response. Only the out-of-plane response w is considered here.

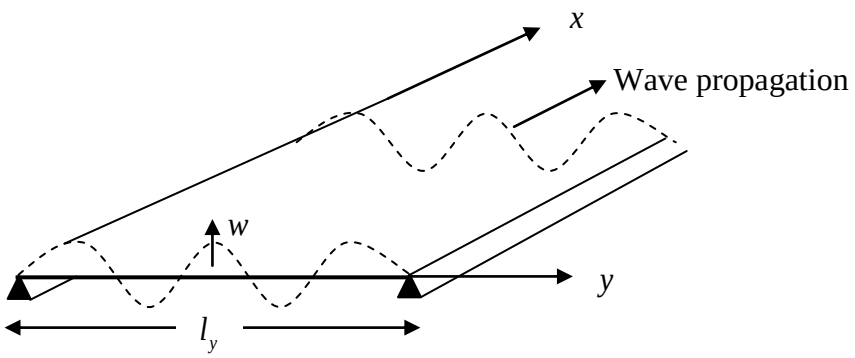

Figure 2.1. A simply-supported plate strip.

For a thin undamped plate, the out-of-plane displacement $w(x,y,t)$ in the absence of external forces satisfies the following differential equation [2]

$$D\left(\frac{\partial^4 w}{\partial x^4}+2\frac{\partial^4 w}{\partial x^2\partial y^2}+\frac{\partial^4 w}{\partial y^4}\right)+(\rho h)\frac{\partial^2 w}{\partial t^2}=0 \tag{2.1}$$

where $D=\dfrac{Eh^3}{12(1-\nu_p^2)}$ is the bending stiffness, E is Young's modulus, h is the plate thickness, ν_p is Poisson's ratio, and ρ is the mass density of the plate.

Harmonic motion is assumed at the angular frequency ω, with a time dependence $e^{i\omega t}$ which is omitted for brevity. Due to the use of simply supported boundaries, the response amplitude w of the plate at position (x,y) may be separated into its x and y

components and written as a summation over components with m half-sine waves across the width l_y

$$w(x,y) = \sum_{m=1}^{\infty} w_m(x) \sin\left(\frac{m\pi y}{l_y}\right) \tag{2.2}$$

where $w_m(x)$ is the complex amplitude of the m^{th} component that depends on the excitation. This series forms a complete set of functions which satisfy the boundary conditions on $y = 0$ and $y = l_y$. Considering one term in the series, substituting this into Eq. (2.1) yields

$$\left(\frac{d^4 w_m}{dx^4} - 2\left(\frac{m\pi}{l_y}\right)^2 \frac{d^2 w_m}{dx^2} + \left(\frac{m\pi}{l_y}\right)^4 w_m\right) - \frac{\rho h}{D}\omega^2 w_m = 0 \tag{2.3}$$

Seeking solutions of the form $w_m(x) = e^{-ik_{x,m}x}$ gives

$$\left(k_{x,m}^4 + 2\left(\frac{m\pi}{l_y}\right)^2 k_{x,m}^2 + \left(\frac{m\pi}{l_y}\right)^4\right) - \frac{\rho h}{D}\omega^2 = 0 \tag{2.4}$$

which can be written as

$$\left(k_{x,m}^2 + \left(\frac{m\pi}{l_y}\right)^2\right)^2 = {k_B}^4 \tag{2.5}$$

where $k_B = \sqrt{\omega}\left(\frac{\rho h}{D}\right)^{1/4}$ is the free bending wavenumber of the plate. Eq. (2.5) has four solutions which can be divided into two fundamentally different wave-type solutions for each m

$$k_{x1,m} = \pm\sqrt{k_B{}^2 - \left(\frac{m\pi}{l_y}\right)^2}$$
$$k_{x2,m} = \pm\sqrt{-k_B{}^2 - \left(\frac{m\pi}{l_y}\right)^2} \qquad (2.6)$$

Real wavenumbers represent propagating waves; the wavenumber is the phase change per unit distance, equal to $2\pi/\lambda$, where λ is the wavelength of vibration. Imaginary wavenumbers represent evanescent waves which decay with distance. At low frequency, $k_B < m\pi/l_y$ and all four wavenumbers in Eq. (2.6) are imaginary so that all four waves behave as evanescent or nearfield waves. In contrast, when $k_B > m\pi/l_y$, $k_{x1,m}$ is real but $k_{x2,m}$ remains imaginary. Therefore, both propagating and nearfield waves are present for the latter case. It may be noted that real positive or negative imaginary values of the wavenumber $k_{x1,m}$ and $k_{x2,m}$ correspond to waves travelling or decaying in the positive $x-$direction while the opposite sign corresponds to those travelling or decaying in the negative $x-$direction. The frequency at which $k_B = m\pi/l_y$ is referred to as the m^{th} cut-on frequency ω_m and is given by

$$\omega_m = \left(\frac{m\pi}{l_y}\right)^2 \left(\frac{D}{\rho h}\right)^{1/2} \qquad (2.7)$$

The relation between the wavenumbers $k_{x1,m}$ and frequency ω from Eq. (2.6) can be observed from the dispersion curves shown in Figure 2.2. These are calculated for the example parameters listed in Table 2.1 corresponding to a 6 mm aluminium plate. A damping loss factor of 0.1 is considered in order to give a smooth response. Although this value does not represent the typical internal loss factor of aluminium, it is useful to look at its behaviour clearly particularly at high frequency. It can be seen that the presence of the boundary constraint has modified the dispersion curves so that $k_{x1,m} < k_B$. For each mode m , as frequency increases, the wavenumbers $k_{x1,m}$ change from imaginary values into real

ones at the cut-on frequencies at which $k_{x1,m}$ = 0. Conversely, all the wavenumbers $k_{x2,m}$ are negative imaginary with zero real part. Both $k_{x1,m}$ and $k_{x2,m}$ have the same values $-im\pi/l_y$ at $\omega = 0$.

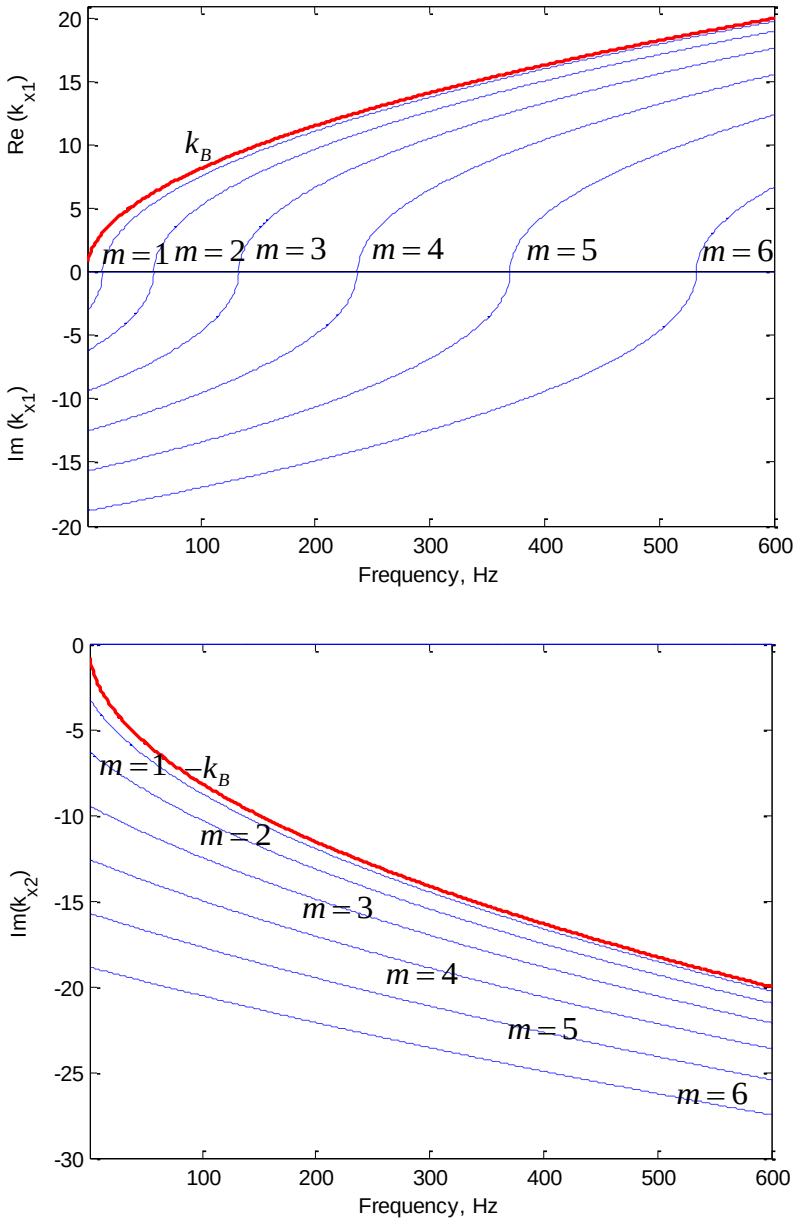

Figure 2.2. The dispersion curves in the $x-$direction of an undamped simply-supported plate strip with parameters in Table 2.1: (a) $k_{x1,m}$; (b) $k_{x2,m}$.

Table 2.1. Material properties and dimensions of the plate strip (unless otherwise stated).

Properties	Dimension
Young's modulus, E ($\mathrm{N/m^2}$)	7.1×10^{10}
Poisson's ratio, ν_p	0.332
Thickness, h (mm)	6.0
Width, l_y (m)	1.0
Density, ρ ($\mathrm{kg/m^3}$)	2.7×10^{3}
Damping loss factor (if used), η	0.1

The cut-on frequencies for this plate are listed in Table 2.2. It is noticeable that they are proportional to m^2 as indicated in Eq. (2.7).

Table 2.2. Cut-on frequencies for each mode m in Hz.

m	f_m
1	14.8
2	59.2
3	133
4	237
5	370
6	533
7	725
8	947
9	1198
10	1479
11	1790
12	2130
13	2500
14	2899
15	3328

2.1.2 Inclusion of damping

Up to this point, the equations have been derived for an undamped structure. In practice, however, all structures experience damping. In order to incorporate this, a damping loss factor η is included in the formulation by making the Young's modulus complex. The bending stiffness becomes

$$D' = \frac{E(1+i\eta)h^3}{12(1-\nu_p^2)} \tag{2.8}$$

From now on, this complex bending stiffness D' will be used.

Due to the introduction of the complex bending stiffness, the wavenumbers in Eq. (2.6) become complex. Therefore, there are no purely propagating waves or purely evanescent waves in this case as both of them are decaying oscillatory waves. Moreover, since Eq. (2.6) produces wavenumber values in which the imaginary part can be either positive or negative, in the calculation process it must be ensured that the complex wavenumbers have imaginary values less than zero for positive-going waves in order to obtain waves that decay as $x \to \infty$. Figure 2.3 shows examples of complex wavenumbers for $\eta = 0.1$ and the same parameters as previously, see Table 2.1. Results are shown for $m = 1$ to $m = 6$. The wavenumbers $k_{x1,m}$ can be seen to be predominantly imaginary at low frequency and then to become predominantly real above the cut-on frequency. However, this transition around the cut-on frequencies is more gradual than for the undamped case. The wavenumbers $k_{x2,m}$ are negative imaginary with a small negative real part.

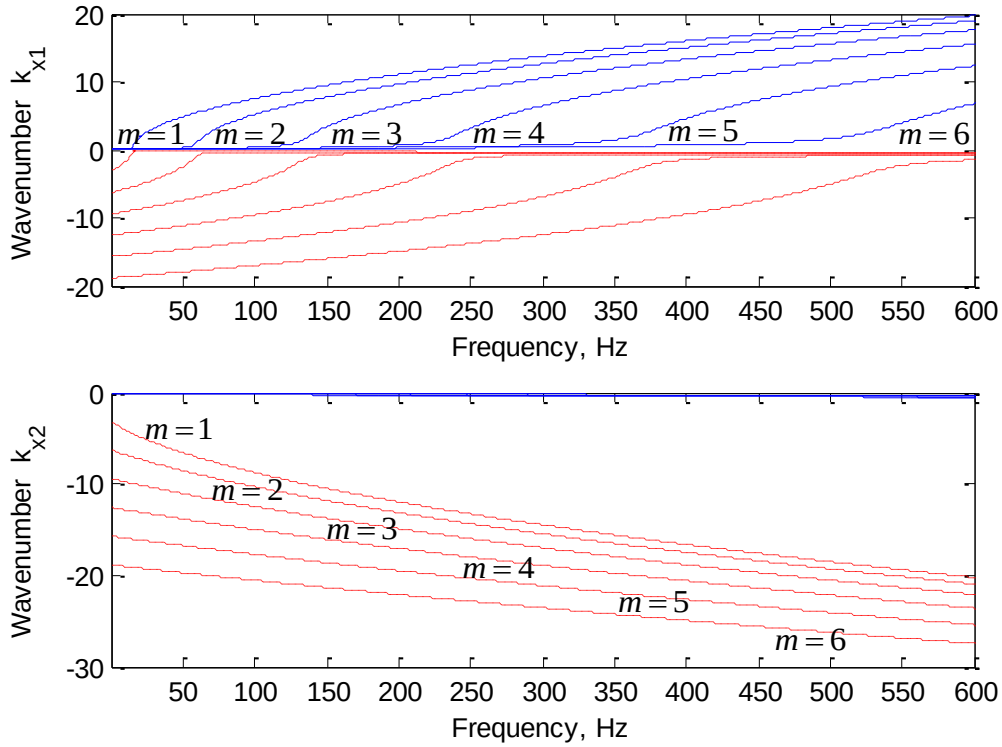

Figure 2.3. Complex wavenumber evolution against frequency (— real components; --- imaginary components).

2.2 Response due to a point force

2.2.1 Formulation

There are four wave solutions for each m in Eq. (2.6), allowing the complete solution to be written as

$$w(x,y)=\sum_m \left\{A_{1,m}e^{ik_{x1,m}x}+A_{2,m}e^{ik_{x2,m}x}+A_{3,m}e^{-ik_{x1,m}x}+A_{4,m}e^{-ik_{x2,m}x}\right\}\sin\left(\frac{m\pi y}{l_y}\right) \tag{2.9}$$

In order to determine the constants $A_{1,m}$, $A_{2,m}$, $A_{3,m}$ and $A_{4,m}$, boundary conditions are required. For a force applied at $x=0$ it should be noted that, to ensure that waves decay in both directions, $A_{1,m}$ and $A_{2,m}$ are zero in the region $x\geq 0$ while $A_{3,m}$ and $A_{4,m}$ are zero in the region $x\leq 0$. The external force can be written as a pressure $f(x,y)$

$$f(x,y) = f_x(x) f_y(y) \tag{2.10}$$

where $f_x(x) = \delta(x-0)$ and $f_y(y) = F\delta(y-y_0)$ for a point force at $(0, y_0)$. Since the Fourier transform of $f_x(x) = \delta(x-0)$ into the wavenumber domain is unity at all wavenumbers, it is sufficient to consider only $f_y(y)$. Due to the finite width of the plate and the simply supported boundary conditions, this can be expressed as a Fourier sine series as follows

$$f_y(y) = \sum_{m=1}^{\infty} F_m \sin\left(\frac{m\pi}{l_y} y\right) \tag{2.11}$$

where F_m are the Fourier coefficients which are given by

$$F_m = \frac{2}{l_y} \int_0^{l_y} f_y(y) \sin\left(\frac{m\pi}{l_y} y\right) dy \tag{2.12}$$

Recalling $f_y(y) = F\delta(y-y_0)$, Eq. (2.12) becomes

$$F_m = \frac{2F}{l_y} \sin\left(\frac{m\pi}{l_y} y_0\right) \tag{2.13}$$

where F is the force amplitude.

Considering the continuity of displacement, rotation and bending moment and the force equilibrium condition at $x = 0$, the solution may be written as follows (see Appendix A for its derivation)

$$\begin{aligned} w(x \le 0, y) &= \sum_{m=1}^{\infty} \frac{-iF_m}{2D' k_{x1,m}\left(k_{x1,m}^2 - k_{x2,m}^2\right)} \left[e^{ik_{x1,m}x} - \frac{k_{x1,m}}{k_{x2,m}} e^{ik_{x2,m}x} \right] \sin\left(\frac{m\pi y}{l_y}\right) \\ w(x \ge 0, y) &= \sum_{m=1}^{\infty} \frac{-iF_m}{2D' k_{x1,m}\left(k_{x1,m}^2 - k_{x2,m}^2\right)} \left[e^{-ik_{x1,m}x} - \frac{k_{x1,m}}{k_{x2,m}} e^{-ik_{x2,m}x} \right] \sin\left(\frac{m\pi y}{l_y}\right) \end{aligned} \tag{2.14}$$

From this, the mobility $Y = i\omega w / F = \dot{w} / F$ for the infinite plate strip can be derived as

$$\frac{\dot{w}(x,y)}{F} = i\omega \sum_{m=1}^{\infty} \frac{-i(2/l_y)\sin(m\pi y_0/l_y)}{2D'k_{x1,m}\left(k_{x1,m}^2 - k_{x2,m}^2\right)} \left[e^{-ik_{x1,m}|x|} - \frac{k_{x1,m}}{k_{x2,m}} e^{-ik_{x2,m}|x|} \right] \sin\left(\frac{m\pi y}{l_y}\right) \tag{2.15}$$

The point mobility for the structure can be found by setting $x = 0$ and $y = y_0$

$$Y(\omega) = \sum_{m=1}^{\infty} \frac{\omega}{D'l_y k_{x1,m}\left(k_{x1,m}^2 - k_{x2,m}^2\right)} \left[1 - \frac{k_{x1,m}}{k_{x2,m}} \right] \sin^2\left(\frac{m\pi}{l_y} y_0\right) \tag{2.16}$$

Note that as an alternative formulation it is possible to apply the residue calculus method to obtain the point mobility Y [66].

2.2.2 Convergence

Theoretically, the response amplitude of the plate strip is obtained from an infinite number of the wave components. In practice, the summation in Eq. (2.2), (2.9), (2.14) and (2.16) is performed for $m = 1$ to M, where the upper limit M is determined based on some convergence criterion. In order to find a suitable criterion, the mobility was calculated for the example parameters in Table 2.1 at various representative frequencies (30 Hz, 200 Hz, 400 Hz, 1 kHz, 2 kHz, and 3 kHz) for different values of M with excitation at the position (0, 0.433 l_y). Table 2.3 shows that the relation between frequency, the number of cut-on modes and the upper limit M associated with a 1% relative difference in $|Y|$ compared with $M = 400$. From this, it can be concluded that M = 82 will give results within 1% for 3 kHz which is the highest frequency considered. The required upper limit M decreases for lower frequencies but the ratio of this to the number of waves that have cut-on at each of these frequencies tends to be roughly constant. From this convergence study, a ratio of 6 (i.e. M is taken as 6 times the number of cut-on modes) is found to be sufficient to estimate the mobility to within 1% for a particular frequency of interest.

Table 2.3. Relation between frequency, number of cut-on modes m and upper limit M for 1% difference in $|Y|$.

Frequency (Hz)	m	M
30	1	6
200	3	22
400	5	30
1 k	8	42
2 k	11	66
3 k	14	82

2.2.3 Results

Figure 2.4 shows the point mobility of a plate strip with properties as in Table 2.1 for excitation at position $(0, 0.433l_y)$. The mobility of an infinite plate with the same properties is shown for comparison. This is given by $Y = 1/8\sqrt{D(\rho h)}$ [67].

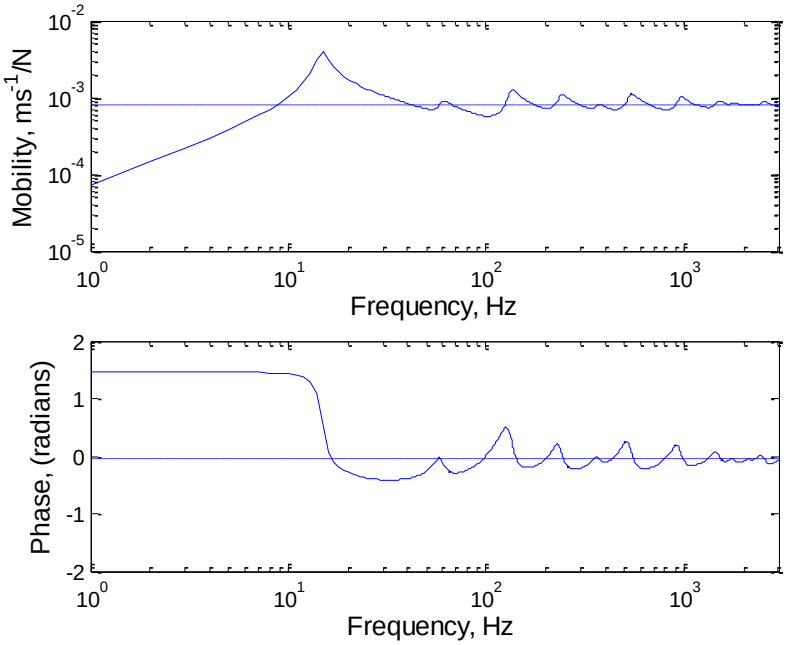

Figure 2.4. The point mobility of the plate strip excited at position $(0, 0.433l_y)$. The dashed line indicates the mobility of an infinite plate.

The features of the plate strip mobility in Figure 2.4 can be identified as follows:

1. At low frequencies, below the first cut-on frequency, the mobility is clearly stiffness-controlled as indicated by the phase of nearly $\pi/2$ radians and the

amplitude which increases in proportion to frequency. Note that the phase is less than $\pi/2$ radians due to the presence of the damping loss factor which makes the stiffness complex. It is also seen from the point mobility formula, where $k_B \ll \left(m\pi/l_y\right)$ in this frequency region, so that Eq. (2.16) reduces to

$$Y(\omega) = i\sum_{m=1}^{\infty} \frac{\omega}{2D'm\pi}\left(\frac{\sin\left(m\pi y_0/l_y\right)}{m\pi/l_y}\right)^2 \tag{2.17}$$

2. Peaks occur at each of the cut-on frequencies (see Table 2.2).
3. At high frequencies, when a lot of waves have cut on, the mobility tends to converge to that of an infinite plate.

2.2.4 Effect of plate thickness

It is instructive to study the point mobility behaviour due to changes in the plate thickness. Three different plate thicknesses are considered, 3 mm, 6 mm and 9 mm. The results are shown in Figure 2.5. It is clear that reducing the plate thickness leads to a higher mobility and a reduction in the cut-on frequencies.

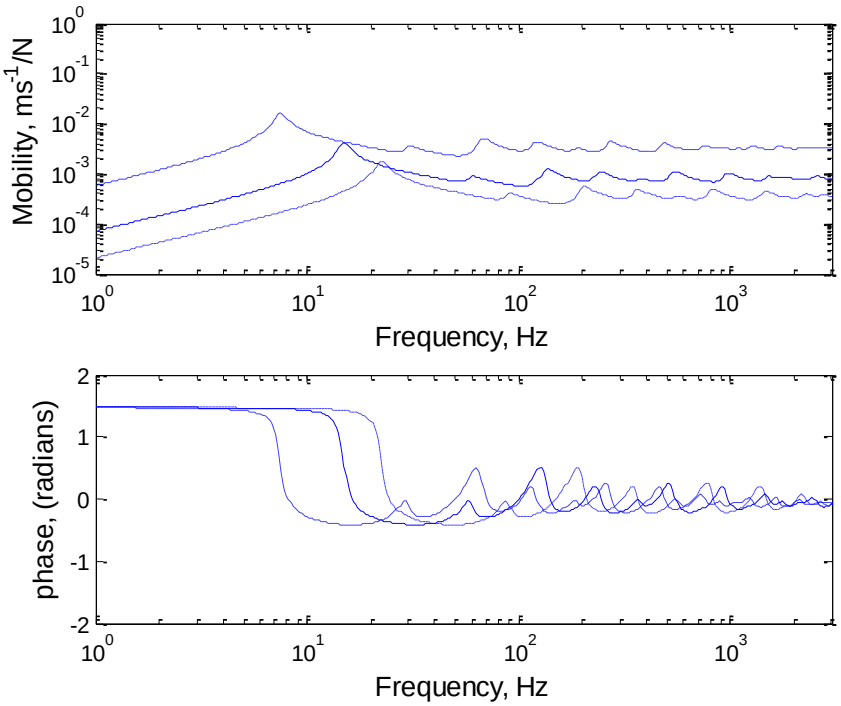

Figure 2.5. Effect of plate thickness on the point mobility excited at (0, 0.433 l_y)

(- - - h = 3 mm; — h = 6 mm; – • – h = 9 mm).

2.2.5 Effect of excitation position

The peaks at the cut-on frequencies have magnitudes that are determined by the term $\sin^2\left(m\pi y_0/l_y\right)$ in Eq. (2.16). Figure 2.6 shows the point mobility for $y_0 = l_y/4$ and $y_0 = l_y/2$. For the case of excitation at the centre position ($y_0 = l_y/2$), the peaks only exist when $m =$ 1, 3, 5,…etc, as for the even ones $\sin\left(m\pi y_0/l_y\right) = 0$. Meanwhile, for the case of $y_0 = l_y/4$ the peaks are found for $m = 1$, 2, 3, 5, 6, 7 etc while those for $m = 4$, 8, etc are missing. Again, the term $\sin\left(m\pi y_0/l_y\right) = 0$ for these values of m. For the latter case, the low frequency stiffness-like behaviour corresponds to a higher stiffness (lower mobility) because this position is closer to the edge.

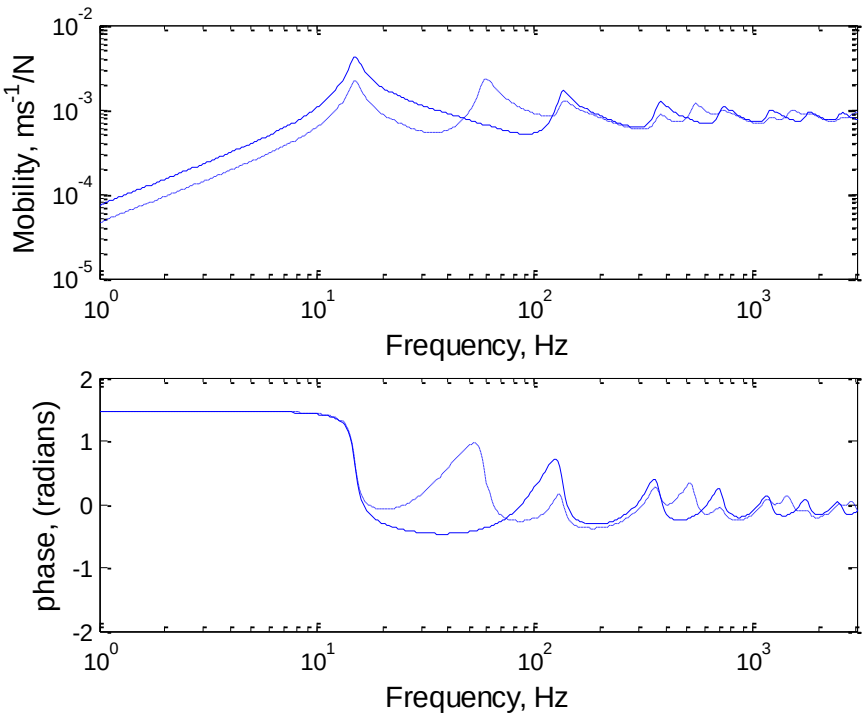

Figure 2.6. Modulus and phase of point mobility for an infinite plate strip (—at $\left(0, l_y/2\right)$; – • – at $\left(0, l_y/4\right)$).

2.2.6 Effect of damping loss factor

To show the effect of the damping loss factor on the mobility, Figure 2.7 compares results with $\eta = 0.01$ and $\eta = 0.1$ for excitation at the centre position. This figure shows that a lower damping loss factor causes a higher amplitude at the peaks, whereas a higher

damping suppresses the peak amplitude. Away from the peaks, the response is similar. So, it is clear that the greatest damping effect on the point mobility can be seen in the region of the peaks which correspond to the cut-on frequencies.

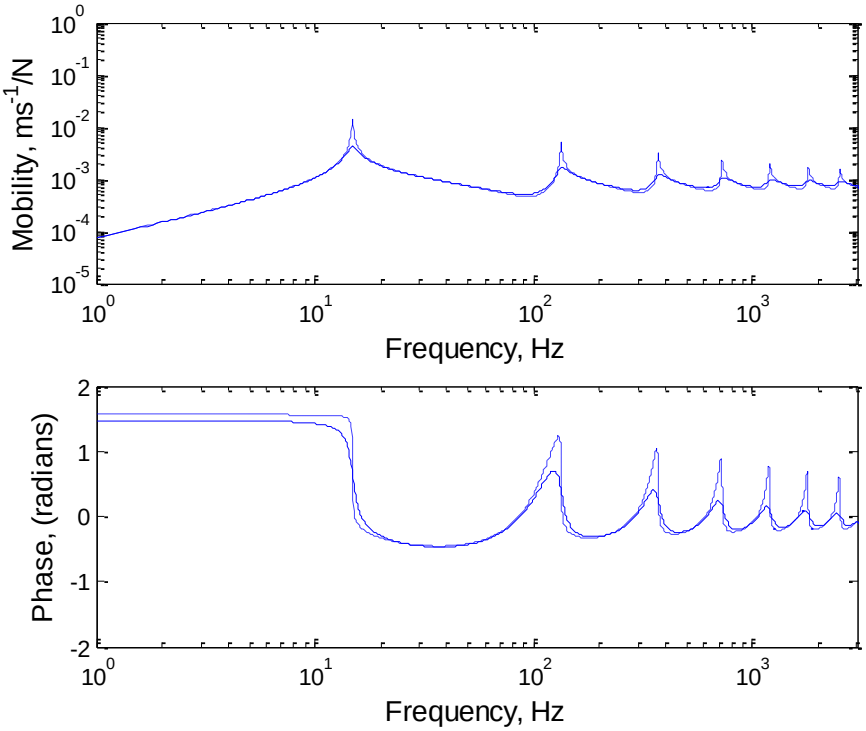

Figure 2.7. Effect of damping loss factor on the point mobility of plate strip with parameters in Table 2.1 (--- $\eta = 0.01$; — $\eta = 0.1$).

2.2.7 Average response of plate

In this section the spatially averaged response of the plate is determined. The vibration of the plate surface in Eq. (2.15) can be expressed as a two dimensional Fourier transform pair as follows

$$\tilde{V}(k_x, k_y) = \int_{-\infty}^{-\infty} \int_{-\infty}^{\infty} v(x, y) e^{i(k_x x + k_y y)} dxdy \tag{2.18}$$

$$v(x, y) = \frac{1}{4\pi^2} \int_{-\infty}^{\infty} \int_{-\infty}^{\infty} \tilde{V}(k_x, k_y) e^{-i(k_x x + k_y y)} dk_x dk_y \tag{2.19}$$

Thus, the wavenumber transform of $v(x, y)$ as given by Eq. (2.14) for a unit point force and a single mode m is

$$\tilde{V}_m(k_x,k_y)=\frac{\omega F_m}{2D'k_{x1,m}\left(k_{x1,m}^2-k_{x2,m}^2\right)}\left[\int_{-\infty}^{0}\left(e^{i(k_{x1,m}+k_x)x}-\frac{k_{x1,m}}{k_{x2,m}}e^{i(k_{x2,m}+k_x)x}\right)dx\right.$$
$$\left.+\left(\int_{0}^{\infty}e^{-i(k_{x1,m}-k_x)x}-\frac{k_{x1,m}}{k_{x2,m}}e^{-i(k_{x2,m}-k_x)x}\right)dx\right]\left[\int_{0}^{l_y}\left(\frac{e^{i(m\pi/l_y+k_y)y}-e^{-i(m\pi/l_y-k_y)y}}{2i}\right)dy\right] \tag{2.20}$$

where the integration limit $\pm\infty$ in the $y-$direction is replaced by 0 to l_y because it is assumed that the velocity is zero outside this range (for a plate set in a baffle). Eq. (2.20) has the following solution

$$\tilde{V}_m(k_x,k_y)=\frac{i\omega F_m}{D'\left(k_{x1,m}^2-k_x^2\right)\left(k_{x2,m}^2-k_x^2\right)}\frac{(m\pi/l_y)[(-1)^m e^{ik_y l_y}-1]}{[k_y^2-(m\pi/l_y)^2]} \tag{2.21}$$

The mean-square response $\overline{v(x,y)^2}$ at a given point is the integration of the squared velocity over time. For harmonic motion with complex velocity amplitude $v(x,y)$, this is equal to $\left|v(x,y)\right|^2/2$. It can also be written in terms of the product of the complex velocity amplitude $v(x,y)$ and its conjugate $v^*(x,y)$. A spatial 'average' mean-square response can then be obtained by integrating $\overline{v(x,y)^2}$ over the plate strip area

$$\left\langle\overline{v(x,y)^2}\right\rangle_{\text{inf}}=\frac{1}{l_y}\int_0^{l_y}\int_{-\infty}^{\infty}\overline{v(x,y)^2}dxdy \tag{2.22}$$

where $\langle\cdots\rangle_{\text{inf}}$ denotes a spatial 'average' over the width. Note that this is actually an integral over the length direction rather than an average. Due to the infinite extent of the plate strip, where damping is included in the calculation the average would tend to zero whereas the integral is finite. An index inf is added to the angle brackets to indicate this. Recalling the definition of the mean-square response and substituting Eq. (2.19) into Eq. (2.22), this yields

$$\left\langle \overline{v(x,y)^2} \right\rangle_{\inf} = \sum_{m=1}^{\infty}\sum_{m'=1}^{\infty} \frac{1}{l_y}\frac{1}{32\pi^4} \int_{-\infty}^{\infty}\int_{-\infty}^{\infty} \mathrm{Re}\left\{ \left[\int_{-\infty}^{\infty}\int_{-\infty}^{\infty} \tilde{V}_m(k_x,k_y)\, e^{-i(k_x x + k_y y)} dk_x dk_y \right. \right. \\ \left. \left. \times \int_{-\infty}^{\infty}\int_{-\infty}^{\infty} \tilde{V}^*_{m'}(k_x^{'},k_y^{'})\, e^{i(k_x^{'} x + k_y^{'} y)} dk_x^{'} dk_y^{'} \right] \right\} dxdy \tag{2.23}$$

where k_x' and k_y' are introduced to distinguish between the integration over k_x and k_y related to $\tilde{V}_m$ and $\tilde{V}^*_{m'}$ respectively. If the integration order is changed so that integration is first performed over x and y, use can be made of the Dirac delta function as follows

$$\int_{-\infty}^{\infty}\int_{-\infty}^{\infty} e^{i(k_x' - k_x)x} e^{i(k_y' - k_y)y} dxdy = 4\pi^2 \delta(k_x' - k_x)\delta(k_y' - k_y) \tag{2.24}$$

where the integral is zero for $k_x \neq k_x^{'}$ or $k_y \neq k_y^{'}$ and is infinite if $k_x = k_x^{'}$ and $k_y = k_y^{'}$.

Thus, the average mean-square response can be obtained in terms of the surface velocity in the wavenumber domain as follows

$$\left\langle \overline{v(x,y)^2} \right\rangle_{\inf} = \sum_{m=1}^{\infty} \frac{1}{l_y}\frac{1}{8\pi^2} \int_{-\infty}^{\infty}\int_{-\infty}^{\infty} \left| \tilde{V}_m(k_x,k_y) \right|^2 dk_x dk_y \tag{2.25}$$

where $\left| \tilde{V}_m(k_x,k_y) \right|^2$ is given by

$$\left| \tilde{V}_m(k_x,k_y) \right|^2 = \left| \frac{\omega F_m}{D'\left(k_{x1,m}^2 - k_x^2\right)\left(k_{x2,m}^2 - k_x^2\right)} \right|^2 \left[\frac{2\pi m / l_y}{k_y^2 - (m\pi/l_y)^2} \right]^2 \sin^2\left(\frac{k_y l_y - m\pi}{2} \right) \tag{2.26}$$

which reflects the energy spectrum of $\tilde{V}_m(k_x,k_y)$. The derivation of Eq. (2.26) is given in Appendix B. In determining the squared-amplitude of the surface velocity for each mode order in Eq. (2.26) the cross-term contributions have been neglected.

Figure 2.8 presents the average response of the plate strip with different damping loss factors for a unit point force, $F = 1$. It is clear that the damping loss factor has a

significant impact above the first cut-on frequency, with the largest influence found around the cut-on frequencies. In this frequency region, away from the cut-on frequencies, it can be seen that the average response is inversely proportional to the damping loss factor. Hence, increasing the damping loss factor gives a reduction in the average response. Below the cut-on frequency, the response is largely unaffected by the damping since all waves in the $x-$direction are evanescent in nature.

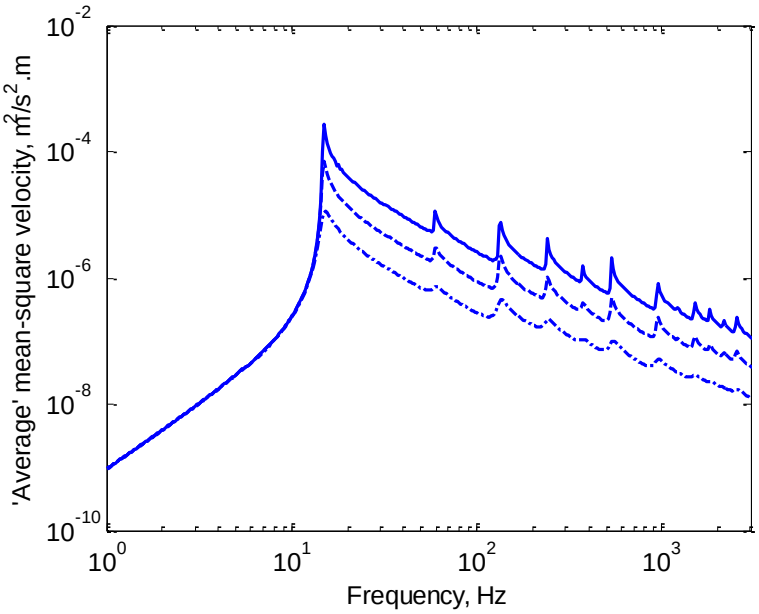

Figure 2.8. Average response of the plate strip with different damping loss factor η for unit excitation at $\left(0, 0.433 l_y\right)$ (— η = 0.01; - - - η = 0.03; • – • – • η = 0.1)

The effect of plate thickness on the average response can be observed from Figure 2.9. In general, a thinner plate has a higher average response compared with a thicker one. The peak associated with the first cut-on frequency shifts to a lower frequency as the thickness of the plate strip is reduced. The implication of these results will be discussed further in section 2.3 where the radiation ratio, which is the sound radiation normalized to the average response of the plate, is investigated.

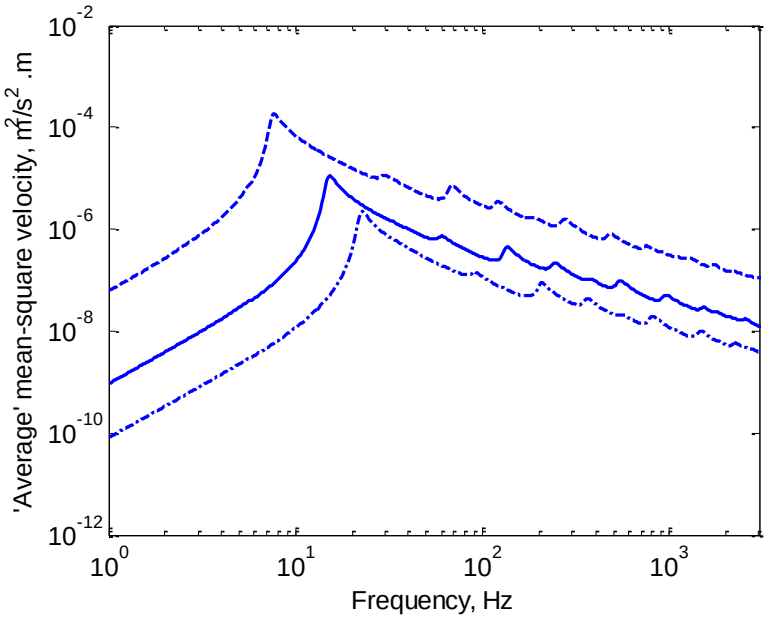

Figure 2.9. Average response of the plate strip due to different thickness with damping loss factor equal to 0.1 and excited by unit point force at (0, 0.433 l_y) (- - - h = 3 mm; — h = 6 mm; – • – h = 9 mm).

2.3 Sound radiation of a plate strip

A vibrating plate in contact with a fluid will radiate sound by producing acoustic waves that propagate away from the plate surface. In this section, the sound radiation from the plate strip is evaluated by means of an analytical model. The analytical model uses a wave-domain approach.

In order to understand the sound radiation mechanism for an infinite plate strip, a two-dimensional spatial (or wavenumber) Fourier transform is used for predicting the sound radiated in the wavenumber domain. In this evaluation, a wave approach as above is used to determine the velocity distribution of the plate strip in the infinite direction. The basic concept of using the wavenumber domain approach for the sound radiation is introduced through an infinite plate case. It is then extended to the plate strip case by imposing simply supported boundaries on the two parallel edges while assuming that the plate strip is set in an infinite rigid baffle. A detailed explanation of the radiated power calculation in the wavenumber domain can be found in [2, 4, 68].

In this section fluid loading is neglected, i.e. the velocity response of the plate strip to the applied forces is taken from the *in-vacuo* response calculated in the previous section.

2.3.1 Infinite plate

Consider first an infinite, uniform plate which is in contact with a semi-infinite fluid domain $z > 0$, as shown in Figure 2.10. A plane transverse wave is assumed to travel in the plate in the x-direction with arbitrary frequency ω and wavenumber κ. The velocity amplitude with the implicit time dependence $e^{i\omega t}$ is expressed by

$$v(x) = Ve^{-i\kappa x} \tag{2.27}$$

Subsequently, sound is radiated by the vibrating plate into the fluid with the same wavenumber component in the $x-$direction.

In terms of the acoustic field, a plane wave propagates with a component in the $x-$direction and a component in the $z-$direction

$$p(x,z) = Pe^{-i(k_x x + k_z z)} \tag{2.28}$$

The acoustic plane waves must have a wavenumber component in the x- direction equal to that of the wave in the plate $k_x = \kappa$. This leads to the wavenumber in the $z-$direction being given by

$$k_z = \pm(k^2 - \kappa^2)^{1/2} \tag{2.29}$$

where $k = \omega/c$ is the acoustic wavenumber in the fluid at frequency ω and c is the wave speed in the fluid.

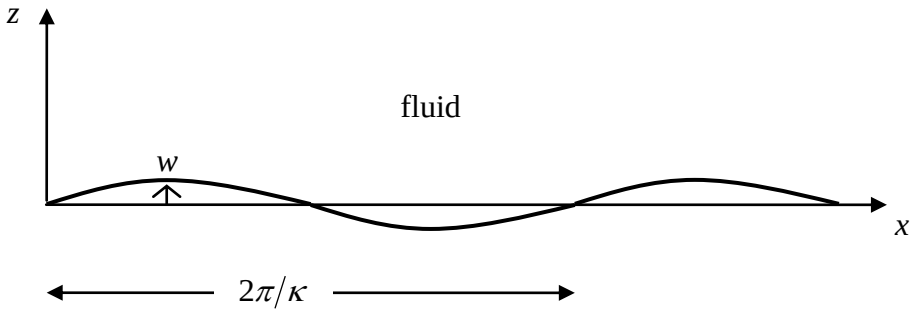

Figure 2.10. Transverse wave in a plate in contact with a fluid.

The appropriate sign of the square root in Eq. (2.29) depends on the values of k and κ. For the case $\kappa \le k$, a real k_z is obtained and plane sound waves will travel away from the plate surface with $k_z \ge 0$. Meanwhile for the case $\kappa > k$ an imaginary k_z is obtained which can be conveniently expressed as $k_z = -i(\kappa^2 - k^2)^{1/2}$. In the latter case, the disturbance of the fluid decays exponentially with the distance normal to the plate. For the opposite sign it would grow exponentially which is not allowed as a solution. Therefore in the plate-fluid interaction, propagating sound waves only exist due to the plate wave when $\kappa < k$. In other words the bending wave phase speed must be greater than the sound wave phase speed (supersonic velocity) in order to radiate energy into the far field.

The radiated pressure field caused by the plate vibration can then be calculated by the use of the specific acoustic wave impedance z_a which is defined as the ratio of the complex amplitudes of pressure and normal particle velocity. At the plate-fluid interface, the particle velocity in the $z-$direction v_z is equal to the surface normal velocity of the plate v. Hence [2]

$$z_a = \left(\frac{p}{v_z} \right)_{z=0} = \frac{\omega \rho_0}{k_z} = \frac{\rho_0 c k}{(k^2 - \kappa^2)^{1/2}} \tag{2.30}$$

where p is the pressure amplitude, v_z is the particle velocity in the $z-$direction and ρ_0 is the fluid density.

Using the spatial Fourier transform, an arbitrary velocity distribution $v(x)$ can be transformed into the wavenumber domain using

$$\tilde{V}(k_x) = \int_{-\infty}^{\infty} v(x) e^{ik_x x} dx \tag{2.31}$$

and its inverse Fourier transform

$$v(x) = \frac{1}{2\pi} \int_{-\infty}^{\infty} \tilde{V}(k_x) e^{-ik_x x} dk_x \tag{2.32}$$

A similar expression can be written for the sound pressure. Therefore, from Eq. (2.30) the sound pressure at $z = 0$ can be expressed in the wavenumber domain as

$$[\tilde{P}(k_x)]_{z=0} = z_a(k_x)\tilde{V}(k_x) = \frac{\rho_0 ck}{(k^2 - k_x^2)^{1/2}}\tilde{V}(k_x) \tag{2.33}$$

2.3.2 Plate strip

Now, consider a simply supported plate strip of infinite length (in the $x-$direction) and of finite width (in the $y-$direction) vibrating harmonically in an infinite rigid baffle. The vibration of the plate surface and the resulting pressure can be written as a two dimensional Fourier transform analogous to Eq. (2.32) as follows

$$v(x,y) = \frac{1}{4\pi^2}\int_{-\infty}^{\infty}\int_{-\infty}^{\infty}\tilde{V}(k_x,k_y)e^{-i(k_x x+k_y y)}dk_x dk_y \tag{2.34}$$

$$[p(x,y)]_{z=0} = \frac{1}{4\pi^2}\int_{-\infty}^{\infty}\int_{-\infty}^{\infty}\left[\tilde{P}(k_x,k_y)\right]_{z=0}e^{-i(k_x x+k_y y)}dk_x dk_y \tag{2.35}$$

where k_x and k_y are the wavenumbers in the x and y directions.

The power radiated by the plate strip is given by

$$W_{rad} = \frac{1}{2}\mathrm{Re}\left\{\int_{-\infty}^{\infty}\int_{-\infty}^{\infty}p(x,y)v^*(x,y)dxdy\right\} \tag{2.36}$$

where $*$ indicates the complex conjugate. By substituting Eq. (2.34)-(2.35) into Eq. (2.36), this gives

$$\begin{aligned} W_{rad} = \frac{1}{32\pi^4}\mathrm{Re}\Bigg\{\int_{-\infty}^{\infty}\int_{-\infty}^{\infty}\Bigg[\int_{-\infty}^{\infty}\int_{-\infty}^{\infty}\left[\tilde{P}(k_x,k_y)\right]_{z=0}e^{-i(k_x x+k_y y)}dk_x dk_y \\ \times\int_{-\infty}^{\infty}\int_{-\infty}^{\infty}V^*(k_x',k_y')e^{i(k_x' x+k_y' y)}dk_x' dk_y'\Bigg]dxdy\Bigg\} \end{aligned} \tag{2.37}$$

where k_x' and k_y' are introduced to distinguish between the integration over k_x and k_y related to $\tilde{P}$ and $\tilde{V}$. Referring to Eq. (2.33), the surface pressure for the two dimensional case can be replaced by the plate velocity distribution in two dimensions multiplied by the wave impedance, as follows

$$W_{rad} = \frac{1}{32\pi^4}\mathrm{Re}\left\{\int_{-\infty}^{\infty}\int_{-\infty}^{\infty}\left[\int_{-\infty}^{\infty}\int_{-\infty}^{\infty}\frac{\rho_0 ck}{(k^2-k_x^2-k_y^2)^{1/2}}\tilde{V}(k_x,k_y)e^{-i(k_x x+k_y y)}dk_x dk_y \right.\right. \\ \left.\left. \times\int_{-\infty}^{\infty}\int_{-\infty}^{\infty}\tilde{V}^*(k_x',k_y')e^{i(k_x' x+k_y' y)}dk_x' dk_y'\right]dxdy\right\} \tag{2.38}$$

Further simplification can be made using the Dirac delta function in Eq. (2.24). Therefore Eq. (2.38) can be simplified as

$$W_{rad} = \frac{1}{8\pi^2}\mathrm{Re}\left\{\int_{-\infty}^{\infty}\int_{-\infty}^{\infty}\frac{\rho_0 ck}{(k^2-k_x^2-k_y^2)^{1/2}}\left|\tilde{V}(k_x,k_y)\right|^2 dk_x dk_y\right\} \tag{2.39}$$

where $\left|\tilde{V}(k_x,k_y)\right|^2$ is the square of the plate velocity in the wavenumber domain. It is possible to limit consideration to wavenumbers satisfying the necessary condition for plate waves to be able to radiate sound energy, that is $k_x^2+k_y^2 \le k^2$; elsewhere the term $(k^2-k_x^2-k_y^2)^{1/2}$ is imaginary. Therefore, the range of integration can be limited to give

$$W_{rad} = \frac{\rho_0 c}{8\pi^2}\int_{-k}^{k}\int_{-\sqrt{k^2-k_y^2}}^{\sqrt{k^2-k_y^2}}\frac{k}{(k^2-k_x^2-k_y^2)^{1/2}}\left|\tilde{V}(k_x,k_y)\right|^2 dk_x dk_y \tag{2.40}$$

2.3.3 Radiation due to point force

The normal velocity distribution $v(x,y)$ [2] due to the point force can be found from the displacement solution in section 2.2 using

[2] Note that some publications use index n for the variable v to indicate the velocity in the normal direction v_n. In this thesis, it does not appear explicitly but the velocity v is actually the velocity distribution in the z - direction so that this is the normal velocity.

$$v(x,y) = i\omega w(x,y) \tag{2.41}$$

where $w(x,y)$ is the surface displacement of the plate strip which is given by Eq. (2.14). Now the normal surface velocity is

$$v(x,y) = \sum_{m=1}^{\infty} \frac{\omega F_m}{2D' k_{x1,m}\left(k_{x1,m}^2 - k_{x2,m}^2\right)} \left(e^{-ik_{x1,m}|x|} - \frac{k_{x1,m}}{k_{x2,m}} e^{-ik_{x2,m}|x|} \right) \sin\left(\frac{m\pi y}{l_y}\right) \tag{2.42}$$

For a given value of *m*, the modulus squared $\left|\tilde{V}(k_x,k_y)\right|^2$ of Eq. (2.21), which reflects the energy spectrum of $\tilde{V}(k_x,k_y)$, is given by

$$\left|\tilde{V}_m(k_x,k_y)\right|^2 = \left| \frac{\omega F_m}{D'\left(k_{x1,m}^2 - k_x^2\right)\left(k_{x2,m}^2 - k_x^2\right)} \right|^2 \left[\frac{2\pi m / l_y}{k_y^2 - (m\pi/l_y)^2} \right]^2 \sin^2\left(\frac{k_y l_y - m\pi}{2}\right) \tag{2.43}$$

For the time being, it is assumed that each transverse order *m* of the velocity $\tilde{V}(k_x,k_y)$ radiates sound independently, i.e. cross terms are ignored for simplicity. This allows the radiated power of the plate strip due to a point force excitation to be expressed as

$$W_{rad} = \frac{\rho_0 c}{8\pi^2} \sum_{m=1}^{\infty} \int_{-k}^{k} \int_{-\sqrt{k^2-k_y^2}}^{\sqrt{k^2-k_y^2}} \frac{k}{(k^2 - k_x^2 - k_y^2)^{1/2}} \left| \frac{\omega F_m}{D'\left(k_{x1,m}^2 - k_x^2\right)\left(k_{x2,m}^2 - k_x^2\right)} \right|^2 \left[\frac{2\pi m / l_y}{k_y^2 - (m\pi/l_y)^2} \right]^2 \sin^2\left(\frac{k_y l_y - m\pi}{2}\right) dk_x dk_y \tag{2.44}$$

The effect of this assumption will be considered in section 2.3.7 below.

Note that the radiated sound power can be determined using a different approach, e.g. Junger and Feit [69] and Sakagami et al. [70] use a far-field solution to calculate the radiated power of a plate strip or waveguide structure.

The radiation ratio σ is used to indicate how much sound power is radiated from the vibrating surface compared with an infinite flat surface vibrating in phase with the same mean-square velocity. It is thus defined as [2, 4, 71, 72]

$$\sigma = \frac{W_{rad}}{\rho_0 c S \left\langle \overline{v^2} \right\rangle} \tag{2.45}$$

where ρ_0 is the fluid density, c is the sound velocity, S is the surface area and $\left\langle \overline{v^2} \right\rangle$ is the spatially averaged mean-square velocity. For the plate strip case, the 'average' is an integral over the x - direction so the area is replaced by the width l_y:

$$\sigma = \frac{W_{rad}}{\rho_0 c l_y \left\langle \overline{v^2} \right\rangle_{\inf}} \tag{2.46}$$

where $\left\langle \overline{v^2} \right\rangle_{\inf}$ now represents the integral of the mean-square velocity over the length and the average over the width.

Figure 2.11 presents the radiated sound power and radiation ratio of the plate strip considered in the previous section due to a point force excitation at position (0, 0.433 l_y). The total number of modes $M = 82$ is the same as used in the mobility calculation in section 2.2. The radiated power has peaks at the various cut-on frequencies. The critical frequency is 2 kHz at which the radiation ratio reaches its maximum value.

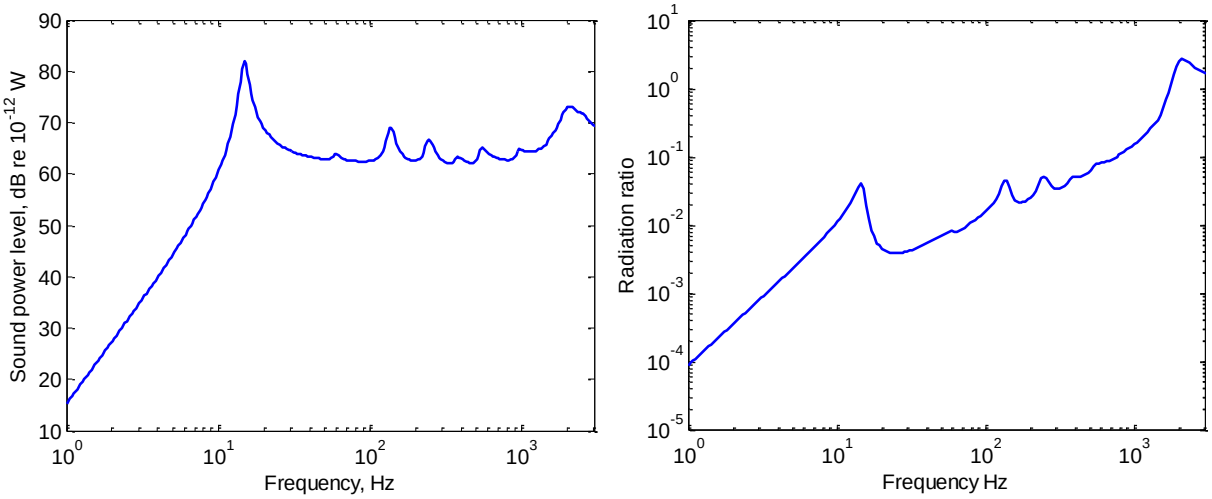

(a) (b)

Figure 2.11. (a) Sound power radiation of the plate strip due to a unit point force at (0, 0.433 l_y); (b) its associated radiation ratio.

2.3.4 Effect of finite width and point force excitation on the plate strip

It is interesting to see the effect of the finite plate width and the effect of the point force excitation in the case of the plate strip. The plate strip differs from an infinite plate, on the one hand, and a finite plate on the other hand. In the infinite plate, above the critical frequency f_c, sound is radiated effectively by the plate vibration. However, as seen in section 2.3.1 there is no radiated power from a plane wave in an infinite plate below the critical frequency because of acoustic short-circuiting. For a point force excitation, some radiation will occur from the nearfield in the vicinity of the forcing point. In contrast, a finite plate experiences non-zero radiation below the critical frequency due to the influence of edges and corners [10]. The plate strip has a finite width but infinite length which makes the problem more complex, especially for the case below the critical frequency.

In principle, referring to [2, 4], whenever the trace wavenumber in a particular direction in a structure is higher than the acoustic wavenumber k at the same frequency, acoustic short-circuiting will occur. In the case under consideration, the acoustic short-circuiting occurs when the characteristic wavenumber in the y direction $k_y = m\pi/l_y$ is higher than the acoustic wavenumber k, i.e. $m\pi/l_y > k$. Under this circumstance, because the adjacent anti-nodal regions in the plate strip are separated by much less than the acoustic wavelength in the surrounding medium, the fluid displaced outward by one region will compensate for the inward motion in the adjacent region [10]. However, the finite width of the structure means that the acoustic short-circuiting is incomplete at the edges. The combination of $\left(m\pi/l_y > k\right)$ and the structural wavenumbers in the x - direction which are smaller than the acoustic wavenumber ($k_{x1.m} < k$) would create radiating modes along the edge in the x - direction. Commonly, on a finite plate such modes are termed edge modes.

The acoustic short-circuiting is also present in the x - direction. When the condition $k_{x1,m} > k$ is fulfilled, the cancellation takes place completely along the plate as it is infinite in length. Hence only the radiating component due to the nearfield wave and the discontinuity introduced by the point force exist. This means neither edge modes nor corner modes are found in this direction. However, not all free propagating waves undergo short-circuiting because this depends on the mode order, which determines the

wavenumbers $k_{x1,m}$ and $k_{x2,m}$. As mentioned in section 2.1.1, $k_{x1,m}$ corresponds to the propagating waves which carry vibration energy above their cut-on frequencies while $k_{x2,m}$ corresponds to the nearfield waves. As shown by the dispersion curves of the plate strip in Figure 2.12, in this example only the first five propagating waves have wavenumbers higher than the acoustic wavenumber k. The rest of the modes have wavenumbers that are always lower than the acoustic wavenumbers ($k_{x1,m} < k$) and hence contribute to the sound power radiation. Peaks in the radiated power (see Figure 2.11) are associated with the cut-on frequency behaviour for every mode order m as all the dispersion curves start below the diagonal line representing k.

To provide a visual description of the radiation components of the plate strip, a classification can be made intuitively by considering the wavenumber distribution over the frequency range of interest. Figure 2.12 presents dispersion curves corresponding to the wavenumbers in the $x-$direction $k_{x1,m}$ and primary wavenumber components[3] in the $y-$direction $k_y = m\pi/l_y$ in the absence of damping. The acoustic wavenumber values and an indication of the critical frequency are added to each graph to help identify the various regions where the radiation components can be described based on their values relative to the acoustic wavenumber k. Regions A and B indicate regions in which $k_{x1,m} > k$ and $k_{x1,m} < k$ respectively. Meanwhile, regions C and D are assigned for the corresponding wavenumber areas for k_y. Hence, $k_y > k$ occupies the region C and $k_y < k$ can be found in region D. Following the explanations from the previous paragraphs, some combinations of these regions can thus be identified as follows:

1. The combination of regions A and C causes a zero radiation ratio as there are no corner modes present due to the complete acoustic short-circuiting along the infinite direction.
2. The combination of regions A and D leads to a similar situation. The structural wavenumber in the $y-$direction is smaller than the acoustic one which would

[3] It should be borne in mind that the finite extent over width produces modal wavenumber spectra with the spectrum peaks found at $\left(m\pi/l_y\right)$ rather than single wavenumber as found in an infinite plate. Therefore, in this study, $k_y = m\pi/l_y$ is termed the primary wavenumber. The same terminology is also found in [2].

result in radiation. However, there is a complete short-circuiting along the $x-$direction, hence zero radiation occurs.

3. The combination of regions B and C clearly leads to the edge modes along the $x-$direction where the acoustic short-circuiting takes place along the direction normal to this axis.
4. The combination of regions B and D is related to surface radiation component where the radiation ratio tends to unity at high frequency. Note that region B and D can occur below f_c but mostly occurs above this frequency.

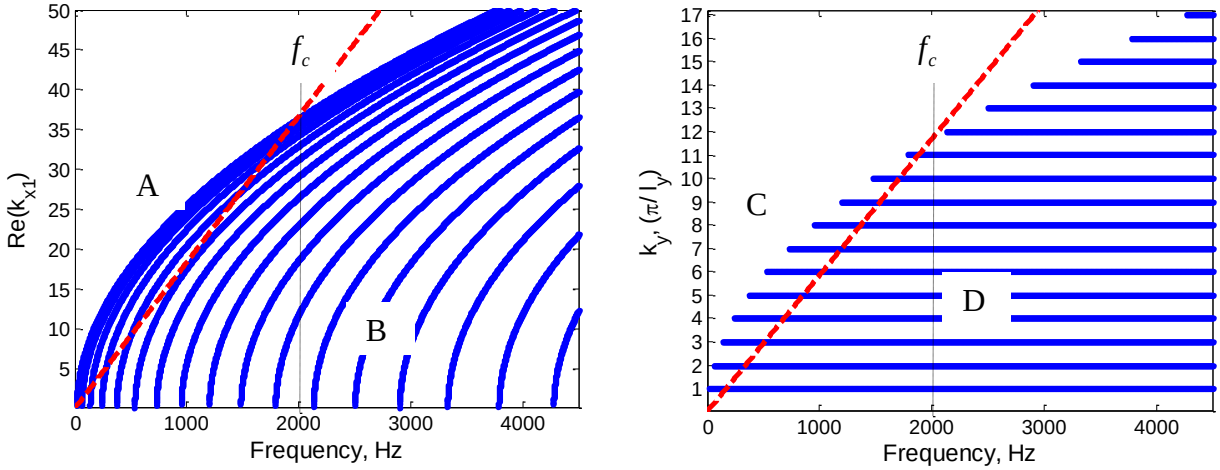

Figure 2.12. Dispersion curve of the plate strip (— bending wavenumbers for different mode orders (k_{x1}) and wavenumber for each mode m (k_y); --- acoustic wavenumbers).

Figure 2.13 compares the radiated power of the plate strip and the infinite plate. The radiated power of the infinite plate due to a point force W_{inf} was calculated based on a formulation proposed in [4] but neglecting the fluid loading contribution as follows

$$W_{\text{inf}} = \frac{F_0^2 \rho_0 c k}{4\pi} \int_0^k \frac{k_r dk_r}{\sqrt{k^2 - k_r^2}\left[\left(\omega\rho h\right)^2 \left(1 - k_r^4 / k_B^4\right)^2\right]} \tag{2.47}$$

where $k_r^2 = k_x^2 + k_y^2$. If the frequency range of interest is limited to well below the critical frequency ($k_r \ll k_B$) so that $\left(1 - k_r^4 / k_B^4\right) \approx 1$, this gives

$$W_{\inf} = \frac{F_0^2 \rho_0 c k}{4\pi (\omega \rho h)^2} \int_0^k \frac{k_r dk_r}{\sqrt{k^2 - k_r^2}} = \frac{F_0^2 \rho_0}{4\pi c (\rho h)^2} \tag{2.48}$$

which is independent of frequency.

It is clear that the radiated power of the plate strip is higher than the infinite plate result for frequencies above the first cut-on frequency and below the critical frequency. The presence of the edge mode radiation component has caused more power to be radiated compared with the infinite plate for the same amplitude of force. Conversely, only the radiated power of the nearfield around the forcing position can be found from the infinite plate for this frequency region. Below the first cut-on frequency, the radiated power of the plate strip is less than that of the infinite plate as the stiffness characteristic of the plate strip determines its radiated power whereas in this frequency region that of the infinite plate depends on the square of the mass per unit area as indicated in Eq. (2.48). Above the critical frequency the results of both models are similar.

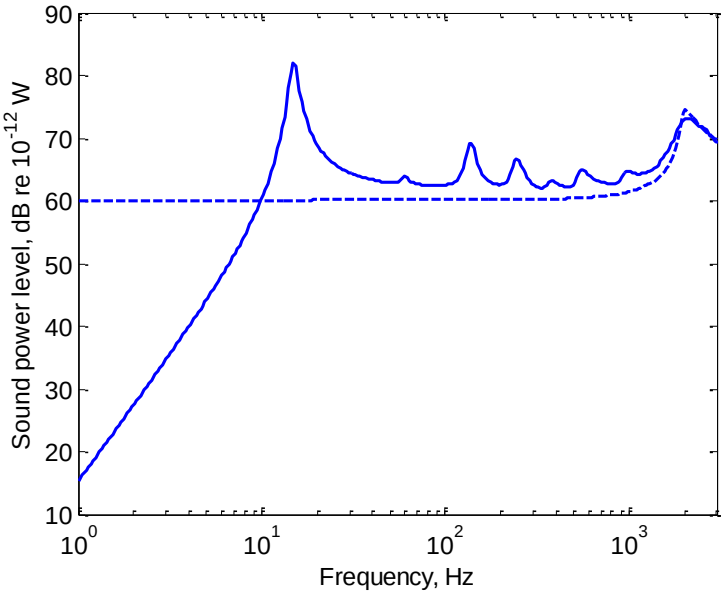

Figure 2.13. Radiated power of plate strip and infinite plate excited at position $\left(0, 0.433 l_y\right)$ with force amplitude $F_0 = 1$ (— plate strip; - - - infinite plate).

2.3.5 Effect of damping loss factor

Figure 2.14 indicates the effect of the damping loss factor on the radiated sound power. In general, its effect mostly appears at the cut-on frequencies at which the peak

amplitude increases as the damping loss factor decreases. However, the effect significantly increases at the frequencies where there are several bending wavenumbers which are lower than the acoustic wavenumbers, i.e. above about 500 Hz (see Figure 2.12). In contrast, at low frequencies where the bending wavenumbers are generally higher than the acoustic wavenumbers for most frequencies, the damping only affects the radiated power close to the cut-on frequencies. In this lower frequency region, away from the cut-on frequencies, only a small part of the vibration, which corresponds to nearfield or evanescent waves, radiates into the fluid medium. Therefore, as the nearfield is almost independent of the damping values, the damping loss factor has a negligible effect in this region except at the cut-on frequencies [4].

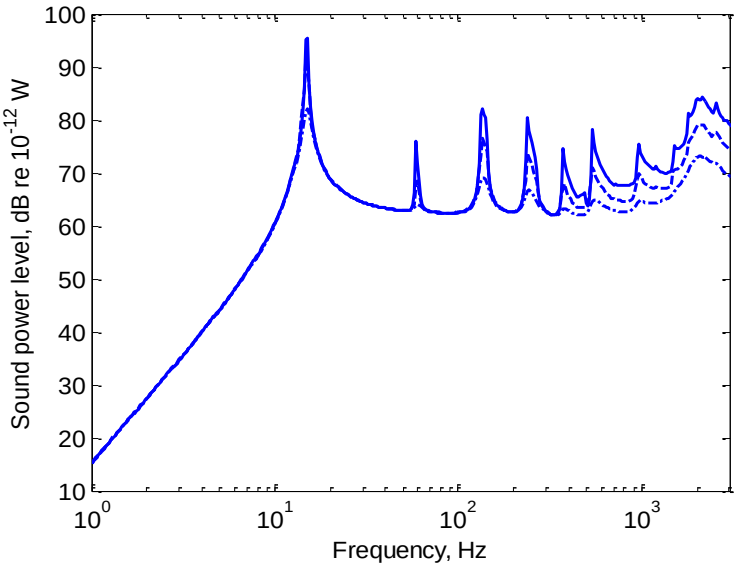

Figure 2.14. Comparison of sound power radiation for different damping loss factors for plate strip excited at (0, 0.433l_y) (— η = 0.01; - - - η = 0.03; – • – η = 0.1).

The corresponding radiation ratios are shown in Figure 2.15. The greatest damping effect is found in the acoustic short-circuiting region while the effect is negligible at frequencies below the first cut-on frequency and above the critical frequency. It is clear that the radiation ratio in the short-circuiting region is proportional to the damping value as the average mean-square velocity decreases with increasing damping (see section 2.2.7).

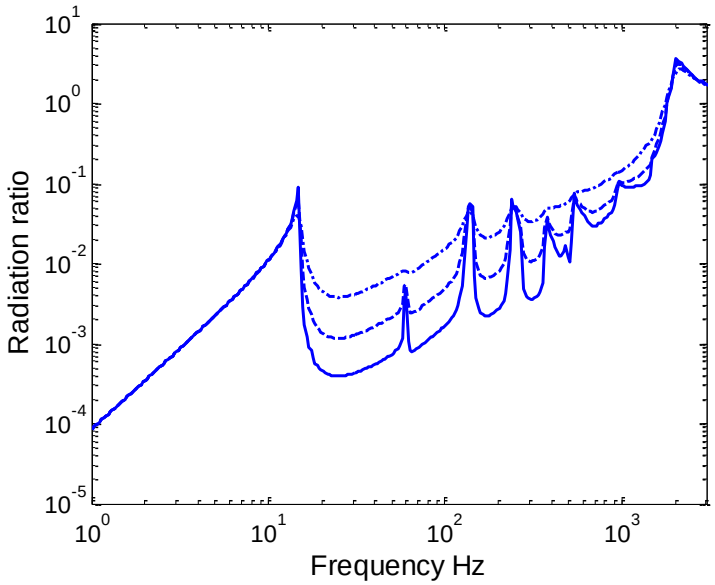

Figure 2.15 Comparison of radiation ratio due to different damping loss factor excited at $(0, 0.433 l_y)$ (— η = 0.01; - - - η = 0.03; – • – η = 0.1).

2.3.6 Effect of plate thickness

The effect of the plate thickness can be observed from Figure 2.16(a). It is clear that the sound power level increases across the frequency range considered as the thickness of the plate strip is reduced. Moreover, the first cut-on frequency is reduced and the critical frequency is increased as the thickness reduces. Therefore the frequency region between the first cut-on frequency and the critical frequency becomes wider and the acoustic short-circuiting effect is increased. This is seen in the radiation ratio which is plotted in Figure 2.16(b). The radiation ratio decreases as the thickness reduces in the acoustic short-circuit region. Below the first cut-on frequency the radiation ratio is largely unaffected.

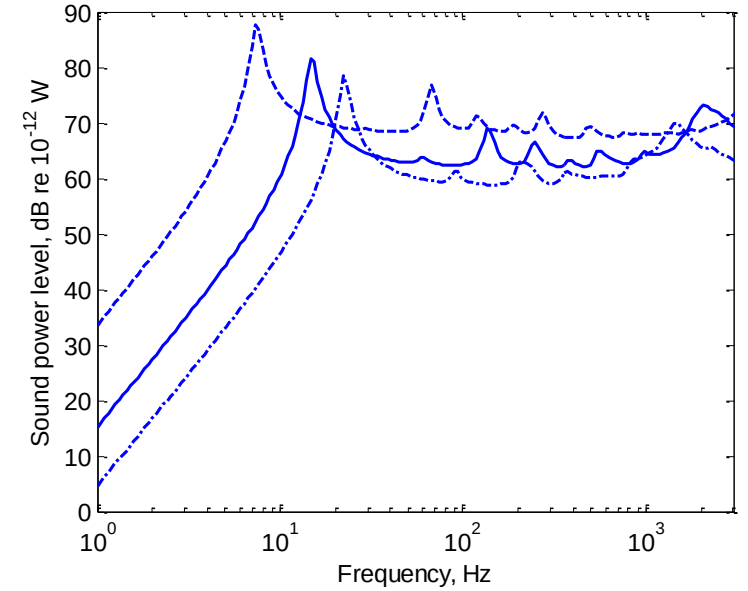

(a)

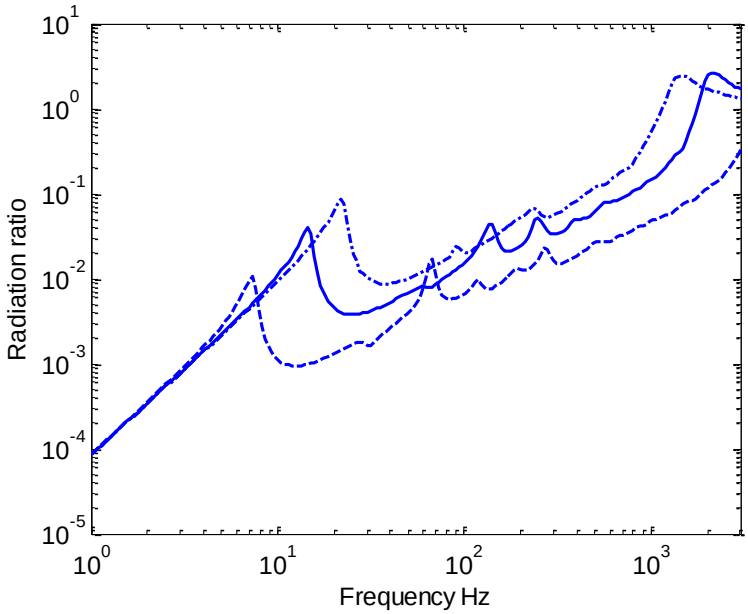

(b)

Figure 2.16. (a) Comparison of sound power radiation due to different thickness with damping loss factor equal to 0.1 and excited at (0, $0.433\,l_y$); (b) its associated radiation ratio (--- h = 3 mm ; — h = 6 mm; – • – h = 9 mm) .

2.3.7 Inclusion of the cross-terms

In the formulation of the previous section, the radiated sound power is calculated on the basis of individual modes generating sound independently. In fact, there is an interaction between the resulting pressures produced by one mode of a vibrating structure

and the vibration of other modes. Hence it is of importance to assess the cross-term contributions to the resulting radiated sound power. This has been studied in [73] for a finite plate where it is shown that neglecting the cross modal contribution can lead to under- or over-estimates of the radiated power even at resonance frequencies. They are frequently disregarded in the radiated power formulation due to the computational burden they introduce in calculation.

To include the cross-terms in the radiated sound power formulation, Eq. (2.44) needs to be modified. It becomes

$$W_{rad} = \frac{\rho_0 c}{8\pi^2} \sum_{m=1}^{\infty} \sum_{m'=1}^{\infty} \int_{-k}^{k} \int_{-\sqrt{k^2-k_y^2}}^{\sqrt{k^2-k_y^2}} \frac{k}{(k^2 - k_x^2 - k_y^2)^{1/2}} \tilde{V}_m(k_x, k_y) \tilde{V}_{m'}^*(k_x, k_y) dk_x dk_y \qquad (2.49)$$

where $\tilde{V}_m$ and $\tilde{V}_n$ are defined by Eq. (2.21) with m and m' the mode index of velocity corresponding to pressure and velocity respectively.

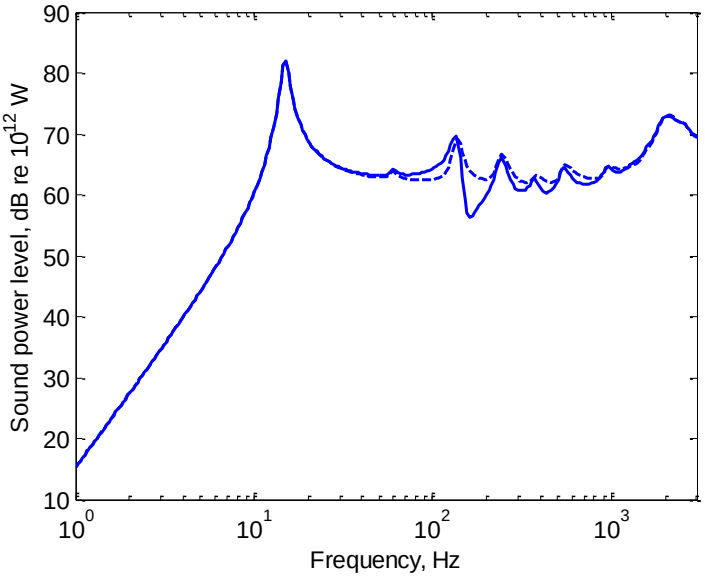

Figure 2.17. Effect of the cross-terms contribution in radiated power due to a point force excitation at (0, 0.433 l_y) (— the cross-terms modal radiation incorporated along with the self-modal one ; --- only self- modal radiation considered).

Figure 2.17 presents a comparison of the radiated power calculated with only self-modal radiation and including the cross modal radiation using the same material properties

as listed in Table 2.1 with excitation at position (0, $0.433 l_y$). It is clear that the cross-terms contribute to the radiated sound power mainly away from the cut-on frequencies in the acoustic short-circuiting region between the first cut-on frequency and the critical frequency. Below the first cut-on frequency where the radiation is dominated by first wave mode (m = 1) and around the critical frequency, both formulations agree well.

As pointed out earlier, the resulting radiated power using Eq. (2.49) to determine the radiated power increases the required calculation time considerably. Using Matlab on a personal computer powered by an Intel Pentium Quadcore 2.8 GHz processor and 4 Gbyte memory, it requires 24.6 hours to get the result. This is around 80 times the calculation time required to obtain the results where the cross-term contribution is neglected.

2.4 Sound transmission loss of a plate strip

In this section the sound transmission due to a plane acoustic wave acting on the simply supported plate strip (waveguide) is considered. The incident plane wave is assumed to impinge on the plate strip with elevation angle θ and azimuth angle φ as shown in Figure 2.18. The transmission loss (TL) is determined by considering the bending waves in the plate. The bending stiffness therefore influences the TL calculation inherently. Moreover, the finite width and the boundary conditions of the plate strip on its two edges are expected to give useful insights of those effects in the transmission loss prediction whereas they are not considered explicitly in most classical theory based on infinite plates, e.g. in Ref. [2, 5, 10].

2.4.1 Pressure and velocity functions

Since the structure is finite in the $y-$direction a modal solution can be utilized to describe the structural response in terms of y as in section 2.1. Meanwhile, for the $x-$direction, as the structure is infinite, a travelling wave solution is suitable to describe the dependence of displacement on x. Therefore, the general solution for the radiated pressure p and the plate velocity v can be decomposed into terms of the form

$$p(x,y) = p_m e^{-i\kappa x} \sin\left(\frac{m\pi y}{l_y}\right), \quad v(x,y) = v_m e^{-i\kappa x} \sin\left(\frac{m\pi y}{l_y}\right) \tag{2.50}$$

where m is an integer and κ is the (real) wavenumber in the $x-$direction.

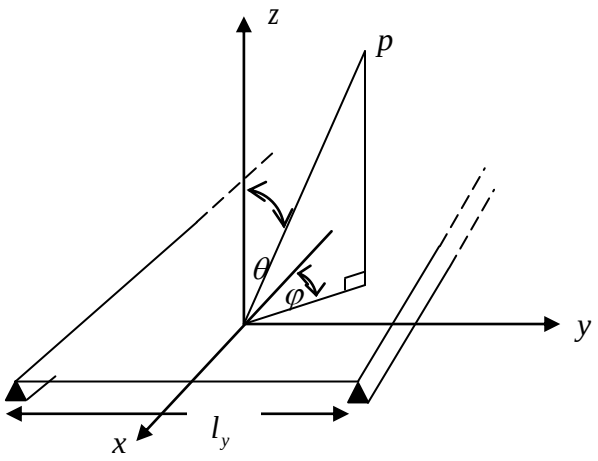

Figure 2.18. Direction of a plane wave incident on an infinite plate strip

Before proceeding to the mathematical formulation and solution for the transmission coefficient, some simplifying assumptions should be noted as follows:

1. As in previous sections, the plate strip is modelled with the thin-plate theory and it is set in a rigid baffle.
2. The thickness of the baffle and the plate is neglected in the acoustic formulation.
3. The amplitude of the reflected sound pressure is initially assumed equal to the incident sound pressure so that the blocked pressure field at the plate surface is equal to twice the incident pressure.
4. Simply supported boundaries are assumed.
5. The acoustic medium on both sides of the plate is assumed to be identical.

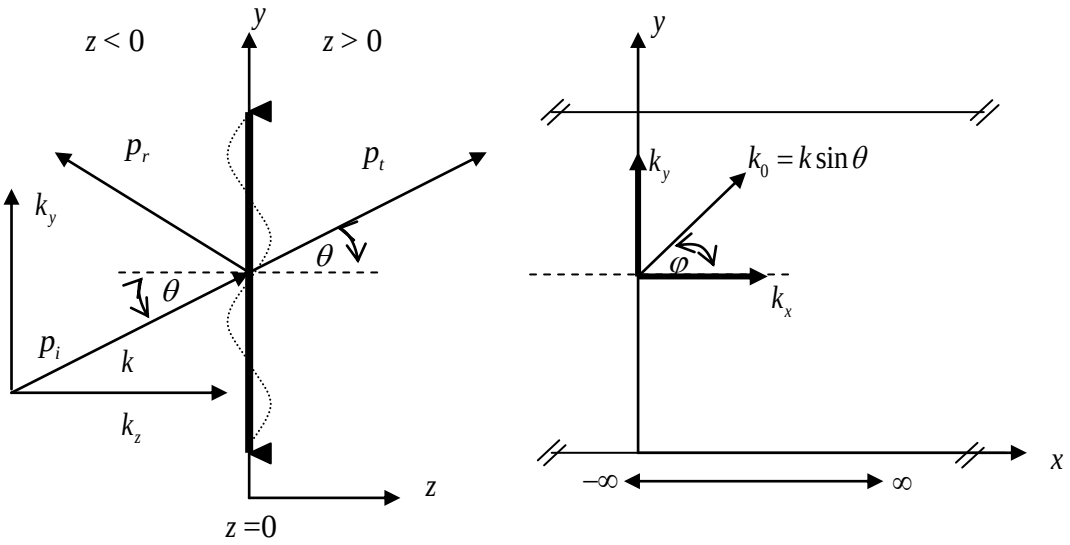

Figure 2.19. Elevation and azimuth angle convention and trace wavenumbers in the fluid.

Considering Figure 2.19 the incident sound pressure is considered as a plane wave expressed by

$$p_i(x,y,z) = p_i e^{-ik_x x} e^{-ik_y y} e^{-ik_z z} \tag{2.51}$$

where time harmonic dependence $e^{i\omega t}$ is omitted for clarity. The wavenumbers in x, y and z directions can be defined as follows:

$$\begin{aligned} k_z &= k\cos\theta \\ k_x &= k\sin\theta\cos\varphi \\ k_y &= k\sin\theta\sin\varphi \end{aligned} \tag{2.52}$$

where $k = \sqrt{k_x^2 + k_y^2 + k_z^2}$ is given by $k = \omega/c$ with ω the angular frequency and c the sound velocity.

For a rigid, uniform and infinitely extended plate, the pressure field in $z < 0$ (the source side) consists of the superposition of the incident wave and a reflected wave. At the plate surface they add in phase to give the so-called blocked pressure p_{bl}. When the plate motion is considered, the plate radiates in the negative and positive $z-$directions. The radiated pressure in the positive $z-$direction is then called the transmitted sound pressure p_t. The total pressure on the plate surface at $z = 0$ consists of the superposition of the blocked pressure field and the radiated pressure field on both sides of the plate. The radiated pressure terms in the total pressure will impose a fluid loading at the plate surface. An implication of this is that it will introduce a damping to the plate strip in addition to the internal damping loss factor. Due to the finite width, the radiated field on either side of the plate strip does not consist of a plane wave.

The two-dimensional bending wave equation in terms of velocity subject to the applied acoustic pressure field and the radiated acoustic pressure produced by the plate velocity is

$$D'\left(\left(\frac{\partial^4 v}{\partial x^4} + 2\frac{\partial^4 v}{\partial x^2 \partial y^2} + \frac{\partial^4 v}{\partial y^4}\right) - k_B^4 v\right) = i\omega\left(p_{bl} + p_{rad}^- - p_{rad}^+\right) \tag{2.53}$$

The distribution of the pressure $p(x,y)$ may be expressed by the combination of a Fourier integral and a Fourier series. This yields

$$p(x,y)=\frac{1}{2\pi}\int_{-\infty}^{\infty}\sum_{m=1}^{\infty}p_m(\kappa)e^{-i\kappa x}\sin\left(\frac{m\pi y}{l_y}\right)d\kappa \tag{2.54}$$

and

$$p_m(\kappa)=\frac{2}{l_y}\int_0^{l_y}\int_{-\infty}^{\infty}p(x,y)e^{i\kappa x}\sin\left(\frac{m\pi y}{l_y}\right)dxdy \tag{2.55}$$

where m is an integer corresponding to each mode of the pressure in the $y-$direction and κ is the (real) wavenumber in the $x-$direction.

As stated earlier, it is assumed that a blocked reflected sound pressure is generated equal to the incident sound pressure at the plate surface. The total pressure on the plate surface at $z=0$ consists of the superposition of the blocked pressure field and the radiated pressure field on both sides of the plate due to plate motion. Hence the pressure for mode m is given by

$$p(x,y)=2p_ie^{-ik_yy}e^{-ik_xx}+\left(p^-_{rad}(y)-p^+_{rad}(y)\right)e^{-ik_xx} \tag{2.56}$$

and Eq. (2.55) becomes

$$p_m=\frac{2}{l_y}\int_0^{l_y}\left(2p_ie^{-ik_yy}+p^-_{rad}(y)-p^+_{rad}(y)\right)\sin\left(\frac{m\pi y}{l_y}\right)dy\left(\int_{-\infty}^{\infty}e^{i(\kappa-k_x)x}dx\right) \tag{2.57}$$

It may be noted that $\int_{-\infty}^{\infty}e^{i(\kappa-k_x)x}dx=2\pi\delta(\kappa-k_x)$. Hence

$$p(x,y)=\sum_{m=1}^{\infty}A_m\sin\left(\frac{m\pi y}{l_y}\right)e^{-ik_xx} \tag{2.58}$$

where

$$A_m = \frac{2}{l_y}\int_0^{l_y}\left(2p_i e^{-ik_y y'} + p^-_{rad}(y') - p^+_{rad}(y')\right)\sin\left(\frac{m\pi y'}{l_y}\right)dy' \tag{2.59}$$

Similarly, because the plate strip is uniform and infinite in the $x-$direction, its transverse velocity may be written in the form

$$v(x,y) = \frac{1}{2\pi}\int_{-\infty}^{\infty}\sum_{m'=1}^{\infty} v_{m'} e^{-i\kappa x}\sin\left(\frac{m'\pi y}{l_y}\right)d\kappa \tag{2.60}$$

Using the same argument as above $\int_{-\infty}^{\infty} e^{i(\kappa-k_x)x}dx = 2\pi\delta(\kappa-k_x)$ and hence

$$v(x,y) = \sum_{m'=1}^{\infty} v_{m'}\sin\left(\frac{m'\pi y}{l_y}\right)e^{-ik_x x} \tag{2.61}$$

where m' is an integer designating each mode of the plate vibration. Eq. (2.61) can be conveniently written as

$$v(x,y) = \sum_{m'=1}^{\infty} v_{y,m'}(y)e^{-ik_x x} \tag{2.62}$$

where $v_{y,m'}(y) = v_{m'}\sin\left(m'\pi y/l_y\right)$. This expression for the transverse velocity only applies for $0 \le y \le l_y$; it is zero otherwise. Subsequently, it can be expressed in terms of an infinite set of simple harmonic waves travelling in the $y-$direction, with wavenumber denoted as γ in order to distinguish it from the incident wavenumber k_y, as follows

$$\tilde{V}_{y,m'}(\gamma) = \int_0^{l_y} v_{y,m'}(y)e^{i\gamma y}dy \tag{2.63}$$

$$v_{y,m'}(y) = \frac{1}{2\pi}\int_{-\infty}^{\infty}\tilde{V}_{y,m'}(\gamma)e^{-i\gamma y}d\gamma \tag{2.64}$$

The solution for $\tilde{V}_{y,m'}(\gamma)$ is

$$\tilde{V}_{y,m'}(\gamma) = v_{m'} a_{m'}(\gamma) \tag{2.65}$$

where $a_{m'}(\gamma) = \int_0^{l_y} \sin\left(\frac{m'\pi y}{l_y}\right) e^{i\gamma y} dy = \frac{(m'\pi/l_y)[(-1)^{m'} e^{i\gamma l_y} - 1]}{[\gamma^2 - \left(m'\pi/l_y\right)^2]}$ (see also Eq. (2.21)).

In order to solve the coupled vibration-radiation problem, some conditions must be satisfied, i.e. the fluid particle velocity must be equal to the normal plate velocity and the fluid particle velocity v and the pressure p must satisfy Euler's equation $i\omega\rho_0\vec{v} = -\vec{\nabla}p$. Therefore, the (normal) plate velocity v in Eq. (2.62) is related to the radiated pressure by

$$v = -\frac{1}{i\omega\rho_0}\left.\frac{\partial p}{\partial z}\right|_{z=0} \tag{2.66}$$

Hence the radiated pressure field, assuming the fluid on both sides is the same, is

$$\begin{aligned} p_{rad}(x,y) &= \frac{1}{2\pi}\int_{-\infty}^{\infty}\sum_{m'=1}^{\infty} V_y(\gamma) e^{-i\gamma y} e^{-i\kappa x}\left(\frac{\omega\rho_0}{k_z}\right) d\gamma \\ &= \frac{1}{2\pi}\int_{-\infty}^{\infty}\sum_{m'=1}^{\infty} v_{m'} a_{m'}(\gamma) e^{-i\gamma y} e^{-i\kappa x}\left(\frac{\omega\rho_0}{k_z}\right) d\gamma \end{aligned} \tag{2.67}$$

or as a function of y, the radiated pressure can be written as

$$p_{rad}(y) = \frac{1}{2\pi}\int_{-\infty}^{\infty}\sum_{m'=1}^{\infty} v_{m'} a_{m'}(\gamma) e^{-i\gamma y}\left(\frac{\omega\rho_0}{k_z}\right) d\gamma \tag{2.68}$$

where $k_z = \sqrt{k^2 - \kappa^2 - \gamma^2}$. Note that $p_{rad}^- = -p_{rad}^+$.

Therefore, A_m in Eq.(2.59) becomes

$$\begin{aligned} A_m &= \frac{2}{l_y}\left(2p_i a_m(k_y) - 2\left[\frac{1}{2\pi}\int_{-\infty}^{\infty}\sum_{m'=1}^{\infty} v_{m'} a_{m'}(\gamma)\left(\frac{\omega\rho_0}{k_z}\right)\left(\int_0^{l_y} e^{-i\gamma y}\sin\left(\frac{m\pi y}{l_y}\right) dy\right) d\gamma\right]\right) \\ &= \frac{2}{l_y}\left(2p_i a_m(k_y) - \frac{1}{\pi}\left(\int_{-\infty}^{\infty}\sum_{m'=1}^{\infty} v_{m'} a_{m'}(\gamma) a_m^*(\gamma)\left(\frac{\omega\rho_0}{k_z}\right) d\gamma\right)\right) \end{aligned} \tag{2.69}$$

where $a_m(-\gamma) = a_m^*(\gamma)$ as the modal displacement function is real.

Substituting Eq. (2.58) and Eq. (2.61) into Eq. (2.53), this gives

$$\sum_{m'=1}^{\infty}\left(-\frac{i}{\omega}\left[D'\left(\left(k_x{}^2+\left(m'\pi/l_y\right)^2\right)^2-k_B{}^4\right)\right]\right)v_{m'}e^{-ik_x x}\sin\left(\frac{m'\pi y}{l_y}\right)=\sum_{m=1}^{\infty}A_m e^{-ik_x x}\sin\left(\frac{m\pi y}{l_y}\right) \tag{2.70}$$

Using the orthogonality of the mode shapes

$$\int_0^{l_y}\sin\left(\frac{m\pi y}{l_y}\right)\sin\left(\frac{m'\pi y}{l_y}\right)dy=\begin{cases}0 & m\neq m'\\ \frac{l_y}{2} & m=m'\end{cases} \tag{2.71}$$

Eq. (2.70) can be written for a single term in the series; to obtain this, it is multiplied with $\sin\left(\frac{m\pi y}{l_y}\right)$ and integrated over the length l_y yielding

$$\left(-\frac{i}{\omega}\left[D'\left(\left(k_x{}^2+\left(m\pi/l_y\right)^2\right)^2-k_B{}^4\right)\right]\right)v_m=A_m \tag{2.72}$$

and substituting A_m from Eq. (2.69) into Eq. (2.72) after some simplifications, it is found that

$$\left(-\frac{i}{\omega}\left[D'\left(\left(k_x{}^2+\left(m\pi/l_y\right)^2\right)^2-k_B{}^4\right)\right]\right)v_m=\frac{2}{l_y}\left(p_i a_m(k_y)-2\sum_{m'=1}^{\infty}v_{m'}R_{mm'}\right) \tag{2.73}$$

where $R_{mm'}$ is the inter-modal coupling which couples the structural mode m with the radiated pressure in other modes as is given

$$R_{mm'}=\frac{1}{2\pi}\int_{-\infty}^{\infty}a_{m'}(\gamma)a_m^*(\gamma)\left(\frac{\omega\rho_0}{k_z}\right)d\gamma \tag{2.74}$$

where $k_z=\sqrt{k^2-\kappa^2-\gamma^2}$. Considering the solution of $a_m(\gamma)$, $R_{mm'}$ has non-zero values for the parity indices of odd-odd or even-even, otherwise its value is zero as the odd and

even modes do not interact each other. The solution of Eq. (2.73) is rather complicated as it is not mathematically orthogonal [74, 75]. For light fluid loading, the off-diagonal terms of $R_{mm'}$ can be neglected. This implies that there is no energy transfer due to two different modes hence only direct fluid loading exists. Consequently, this removes the summation sign in second term on the right hand side of Eq. (2.73). This yields

$$v_m = \frac{4}{l_y} \frac{p_i a_m(k_y)}{\left[\left(-\frac{i}{\omega}\left[D'\left(\left(k_x{}^2 + \left(m\pi/l_y\right)^2\right)^2 - k_B{}^4\right)\right]\right) + \frac{4}{l_y} R_m\right]} \tag{2.75}$$

where

$$R_m = \frac{1}{2\pi}\int_{-\infty}^{\infty} \left|a_m(\gamma)\right|^2 \left(\frac{\omega\rho_0}{k_z}\right) d\gamma \tag{2.76}$$

Despite the above simplification relating to fluid loadng, the cross-modal radiation terms can still be included as discussed in the next section.

2.4.2 Transmission coefficient

The transmission coefficient τ is defined as the ratio of the transmitted sound power W_{tran} to the incident sound power W_{inc}. The sound power transmitted through the plate strip is equal to the sound power radiated into the region $z > 0$, hereafter denoted by $W_{rad\,2}$. For clarity and consistency in defining the radiated power of the plate strip, an arbitrary length of plate strip L_x is retained in the following derivation. Thus, the radiated sound power of the plate strip $W_{rad\,2}$ per unit length in the $x-$direction is given by

$$W_{rad\,2} = \frac{1}{2}\mathrm{Re}\left\{\frac{1}{L_x}\int_{-\infty}^{\infty}\int_{0}^{L_x} p(x,y)v^*(x,y)dxdy\right\} \tag{2.77}$$

in which the range of the integration 0 to l_y has been extended to $\pm\infty$ because the form of $\tilde{V}_y(\gamma)$ ensures that v_y is zero outside $0 < y < l_y$. Substituting Eq. (2.64) and Eq. (2.67) into Eq. (2.77) for the radiated sound power per unit length, this yields

$$\begin{aligned} W_{rad\,2} &= \frac{1}{2}\mathrm{Re}\left\{ \frac{1}{L_x}\int_{-\infty}^{\infty}\int_{0}^{L_x}\frac{1}{2\pi}\int_{-\infty}^{\infty}\frac{\rho_0 ck}{\sqrt{k^2-k_x^2-\gamma^2}}\tilde{V}_y(\gamma)e^{-i\gamma y}e^{-ik_x x}d\gamma \right. \\ &\left. \times\frac{1}{2\pi}\int_{-\infty}^{\infty}\tilde{V}_y^*(\gamma')e^{i\gamma' y}e^{ik_x x}d\gamma' dx dy \right\} \\ &= \frac{1}{4\pi}\mathrm{Re}\left\{ \int_{-\infty}^{\infty}\frac{\rho_0 ck}{\sqrt{k^2-k_x^2-\gamma^2}}\tilde{V}_{y,m}(\gamma)\tilde{V}_{y,m'}^*(\gamma)d\gamma \right\} \end{aligned} \tag{2.78}$$

where $\tilde{V}_{y,m}(\gamma)$ as defined in Eq. (2.65).

Hence the total radiated sound power with the necessary condition $k_x^2+\gamma^2 \le k^2$ is

$$W_{rad\,2} = \frac{1}{4\pi}\sum_{m=1}^{\infty}\sum_{m'=1}^{\infty}\left\{ \int_{-\sqrt{k^2-k_x^2}}^{\sqrt{k^2-k_x^2}}\frac{\rho_0 ck}{\sqrt{k^2-k_x^2-\gamma^2}}v_m a_m(\gamma)a_{m'}(\gamma)v_{m'}d\gamma \right\} \tag{2.79}$$

where the product of $a_m(\gamma)$ and $a_{m'}(\gamma)$ corresponds to the cross-modal radiation coupling. For the case where the cross-term contribution is neglected, Eq. (2.79) reduces to

$$W_{rad\,2} = \frac{1}{4\pi}\sum_{m=1}^{\infty}\left\{ \int_{-\sqrt{k^2-k_x^2}}^{\sqrt{k^2-k_x^2}}\frac{\rho_0 ck}{\sqrt{k^2-k_x^2-\gamma^2}}|v_m|^2\left[\frac{2\pi m/l_y}{\gamma^2-(m\pi/l_y)^2}\right]\sin\left(\frac{\gamma l_y - m\pi}{2}\right)\right|^2 d\gamma \right\} \tag{2.80}$$

The incident power per unit length of the plate strip can be expressed as follows

$$W_{inc} = \frac{1}{2}\frac{|p_i|^2\cos\theta}{\rho_0 c}l_y \tag{2.81}$$

The transmission coefficient is given by

$$\tau = \frac{W_{rad\,2}}{W_{inc}} \tag{2.82}$$

Substituting Eq. (2.80) and (2.81) into Eq. (2.82) gives

$$\tau = \frac{\left(\rho_0 c\right)^2}{2\pi \left|p_i\right|^2 l_y \cos\theta} \left\{ \sum_{m=1}^{\infty} \int_{-\sqrt{k^2-k_x^2}}^{\sqrt{k^2-k_x^2}} \frac{k}{\sqrt{k^2-k_x^2-\gamma^2}} \left|v_m\right|^2 \left| \left[\frac{2\pi m / l_y}{\gamma^2 - (m\pi / l_y)^2} \right] \sin\left(\frac{\gamma l_y - m\pi}{2} \right) \right|^2 d\gamma \right\} \tag{2.83}$$

The sound reduction index or transmission loss R is found from

$$R = 10 \log_{10}\left(\frac{1}{\tau}\right) \quad \text{dB} \tag{2.84}$$

Figure 2.20 presents results for normal incidence for the plate strip considered in the previous sections (see Table 2.1). From Figure 2.20, it can be seen that the results of the analytical model with and without including the cross-term contribution in the calculation are very similar except between 80 and 200 Hz. Hence, for this case, the model without the cross-term contribution can be considered to achieve a sufficient accuracy, except in this frequency region, without requiring such a high computational time. Using Matlab on a personal computer powered by an Intel Pentium Quadcore 2.8 GHz processor and 4 Gbyte memory, it is found that this approach allows obtaining the results in 1/67 times the calculation time required by the model with the cross-term contributions. Due to this fact, without losing the generality of this model, the cross-term contribution will be neglected in the calculations for investigating the TL behaviour of the plate strip in next paragraphs.

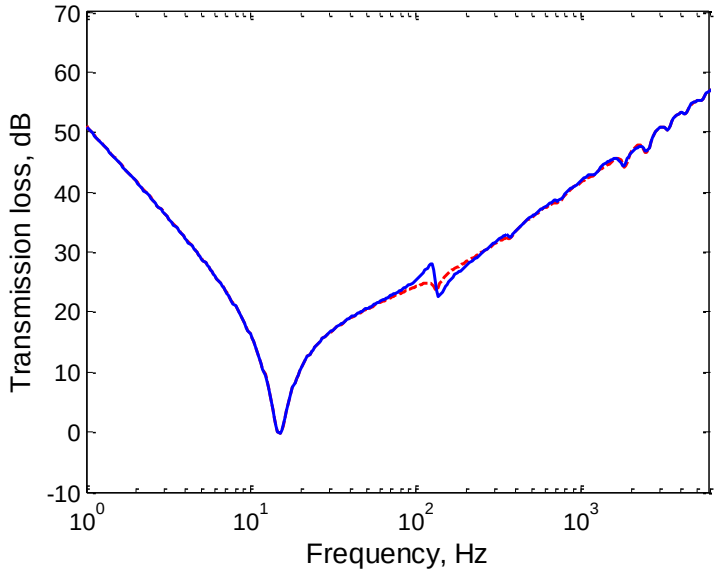

Figure 2.20. Effect of neglecting of cross-term contribution on TL of plate strip (— with cross-term contribution;--- without cross-term contribution).

The above model was used to evaluate the effect of changing the incident angle, thickness and structural loss factor with a total number of modes M = 150 taken into account in calculation. In the present case, the number of the modes is increased from that considered in section 2.1 as the frequency range is extended to 10 kHz where 25 waves have cut-on in the plate strip.

Figure 2.21 presents a comparison of the predicted transmission loss calculated using the transmission coefficient in Eq. (2.83) and the transmission coefficient of an infinite plate for normal incidence which is calculated using Eq. (5.14) of [2]

$$\tau = \frac{4}{\left[\left(\omega\rho h - s/\omega\right)/\rho_0 c\right]^2 + \left(\omega_0 \rho h \eta/\rho_0 c + 2\right)^2} \tag{2.85}$$

where s is the stiffness per unit area and $\omega_0 = \sqrt{s/(\rho h)}$.

In general, at frequencies above 100 Hz, the TL of the plate strip tends to the infinite plate result which typically follows the mass-law behaviour $\tau = \left(2\rho_0 c/\omega\rho h\right)^2$. Hence, for this region the TL of the plate strip is mass-controlled. Some dips or ripples in the curve are related to cut-on frequencies and the corresponding modal behaviour while such features are not present in the infinite plate model. At low frequency, or $\omega \ll \omega_1$, a

stiffness-controlled behaviour appears where a slope of -30 dB/decade occurs rather than -20 dB/decade as indicated by the infinite plate model. At the first cut-on frequency ω_1, the transmission loss has a negative value rather than zero as the lowest value which appears for the infinite plate model. This happens as a consequence of the normalization area introduced in the transmission coefficient. In particular only the incident power falling within the width of the plate strip is consideted. Hence the ratio of radiated sound power and incident power can be greater than unity for the case of the plate strip which has a finite dimension (in one direction). A more detailed discussion on this issue is given in [76].

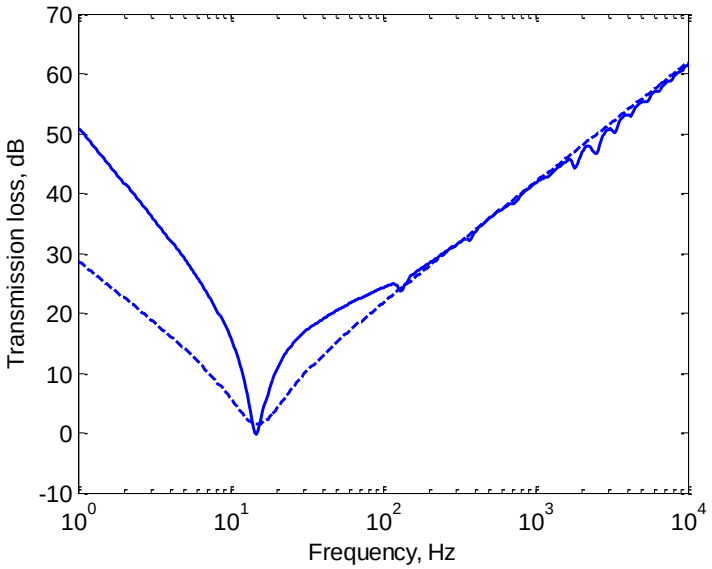

Figure 2.21. TL comparison of the plate strip and the infinite plate for normal incident case (— plate strip; --- infinite plate)

The slope of -30 dB/decade in the stiffness-controlled region can be demonstrated by considering $\omega \ll \omega_1$ in Eq. (2.75). Hence v_m reduces to

$$|v_m| = \frac{4}{l_y} \frac{p_i |a_m(k_y)| \omega}{D'\left(k_x{}^2 + \left(m\pi/l_y\right)^2\right)^2 \sqrt{\eta^2+1}} \tag{2.86}$$

In this frequency range $k_x^2 \ll \left(m\pi/l_y\right)^2$ so that the transmission coefficient in Eq. (2.83) is finally proportional to the cube of frequency, $\tau \propto \omega^3$, which results in a slope of -30

dB/decade. If $\omega \gg \omega_1$, where the mass-controlled region is found, v_m in Eq. (2.75) becomes

$$|v_m| = \frac{4}{l_y} \frac{p_i |a_m(k_y)|}{\rho_0 h \omega} \tag{2.87}$$

Accordingly, the transmission coefficient in Eq. (2.83) now is inversely proportional to frequency, $\tau \propto \omega^{-1}$. This indicates that a slope of 10 dB/decade applies in this frequency range. However, above the subsequent cut-on frequencies it is found that $\left|a_m\left(k_y\right)a_m\left(\gamma\right)\right|$ in $\left|\tilde{V}_y\left(\gamma\right)\right|$ is proportional to $1/\sqrt{\omega}$ or $\left|a_m\left(k_y\right)a_m\left(\gamma\right)\right| \approx 1/\sqrt{\omega}$ hence causing $\tau \propto \omega^{-2}$. Thus, the slope of the TL curve increases to 20 dB/decade at high frequency. It should be noted that the transition from 10 dB/decade to 20 dB/decade depends on the incident angle and the width of the plate strip as both variables are contained in the a_m term. For example for the normal incidence case, it is found that the transition occurs at about 340 Hz for 0.5 m width, 170 Hz for 1 m width and 85 Hz for 2 m width. Hence, comparing this with the acoustic wavelength it can be identified as $\lambda \approx 2l_y$. A comparison of the TL curve and these slopes is given in Figure 2.22.

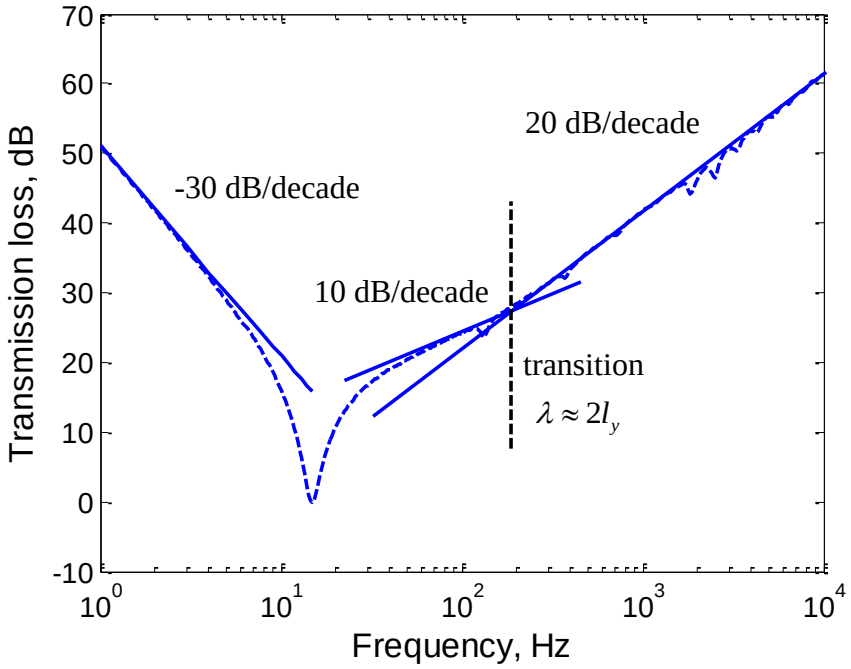

Figure 2.22. TL slope of plate strip in the stiffness-controlled region and the mass-controlled region.

Figure 2.23(a) shows results for different angles of incidence about the $x-$axis. The coincidence frequency depends on the incident angle, with a higher angle corresponding to a lower coincidence frequency. These results have a similar tendency as those obtained by the infinite plate model where the transmission coefficient is calculated using Eq. 7.74 of [4]

$$\tau = \left| \frac{1}{1 + i\omega\rho h \cos\theta \left(1 - \left(k \sin\theta / k_b\right)^4\right) \Big/ 2\rho_0 c} \right|^2 \tag{2.88}$$

However, in the area close to the coincidence frequency the TL of the infinite plate tends to be higher than that of the plate strip. This difference is affected by the presence of edge mode radiation and cut-on frequencies in the plate strip response. Conversely, for increasing incident angle and for frequencies below the coincidence frequency, it can be seen that the TL of the infinite plate is lower than that obtained by the plate strip model. This is caused by the radiation ratio of the infinite plate which is given by $\sigma_{\text{inf}} = 1/\cos\theta$, which increases when the incident angle increases and becomes infinite when $\theta = 90^\circ$ while that of a finite structure remains finite [77]. Meanwhile, above the coincidence frequency, the results of both models are in good agreement. Similar trends are also observed from the case of oblique incidence about the $y-$axis as shown in Figure 2.23(b). Compared with the former case, however, the modal behaviour effect is less apparent for this case.

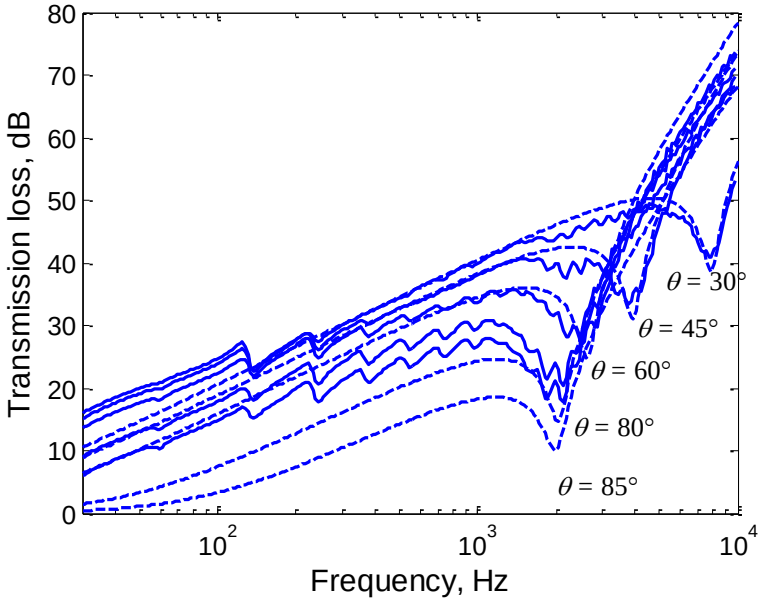

(a)

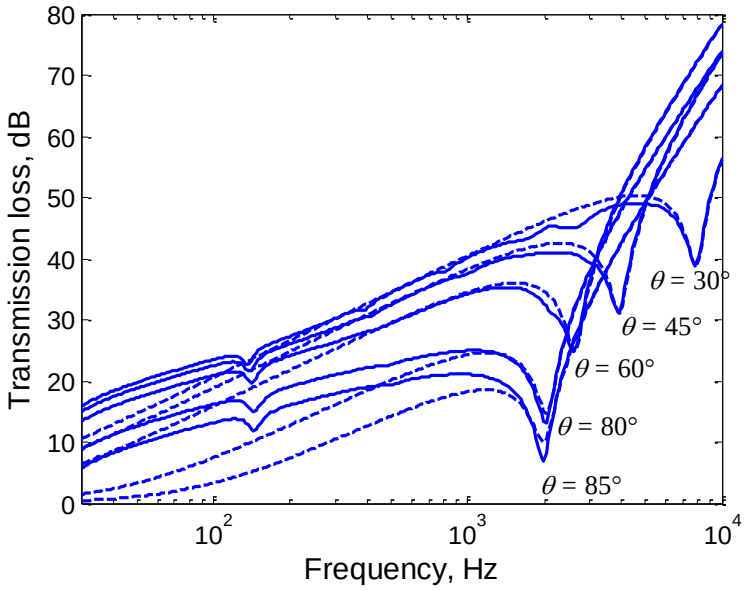

(b)

Figure 2.23. TL comparison of the plate strip and the infinite plate for obliquely incident case: (a) about x axis; (b) about y axis (— plate strip; --- infinite plate).

Results for different thicknesses for normal incidence are shown in Figure 2.24(a). Here the analytical model again behaves as expected with the first panel resonance (cut-on frequency) becoming lower and the TL values reducing when the thickness reduces. The same situation also appears when the plate strip is obliquely excited as can be seen from

Figure 2.24(b). However, the corresponding coincidence frequency now also exists and this shifts to a lower frequency with increasing thickness.

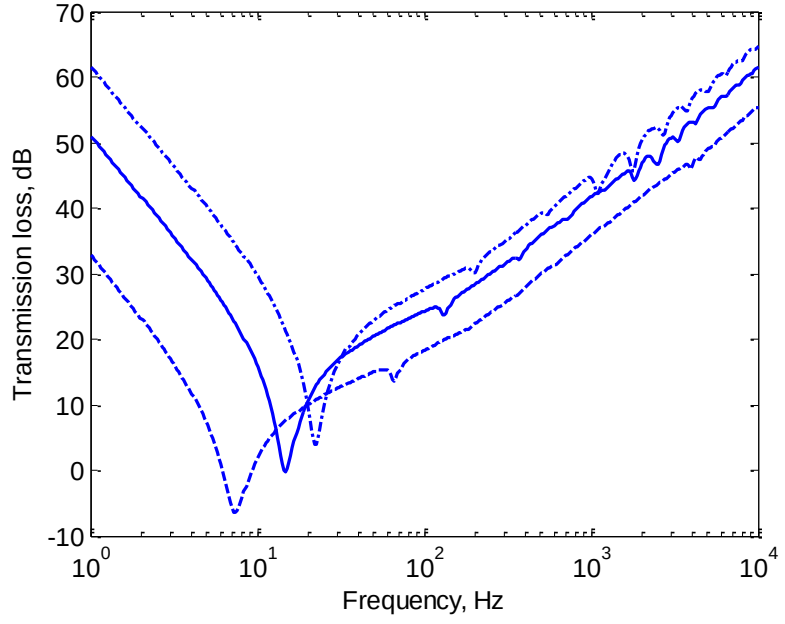

(a)

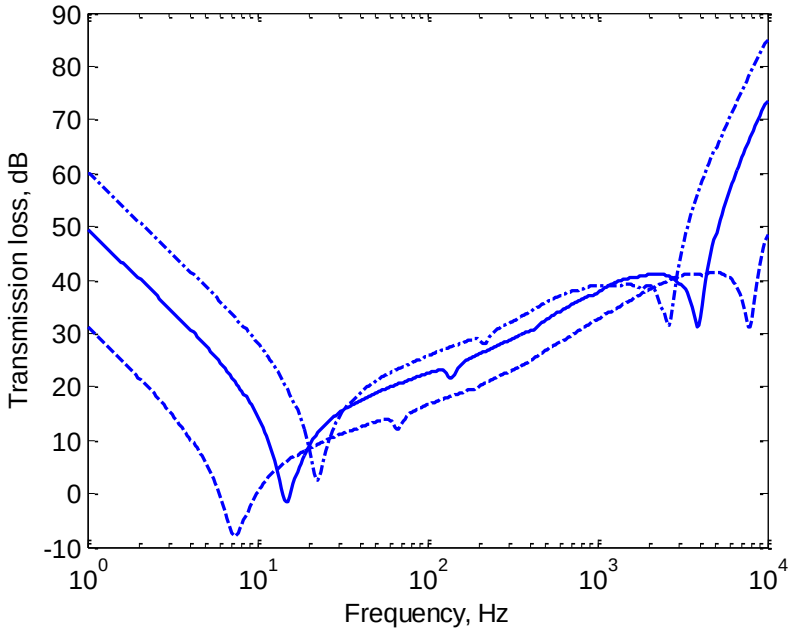

(b)

Figure 2.24. Effect of changing thickness of the plate strip on the sound transmission loss: (a) normal incidence; (b) oblique incidence at angle 45° about y-axis (- - - h = 3 mm ; ——— h = 6 mm ; – • – h = 9 mm).

Figure 2.25(a) presents the effect of the structural damping loss factor on the sound transmission loss values for normal incidence. It is clear that the loss factor has a large influence at the cut-on frequencies but negligible effect elsewhere. The same tendency is also found for oblique incidence as shown in Figure 2.25(b).

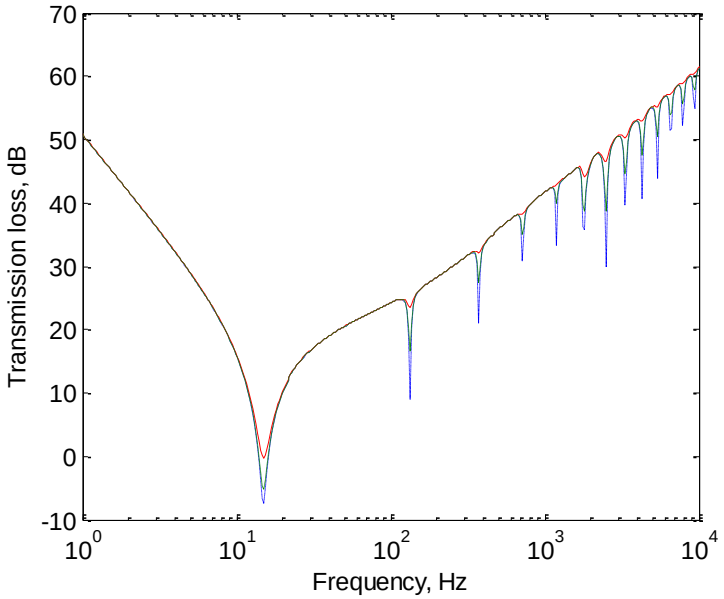

(a)

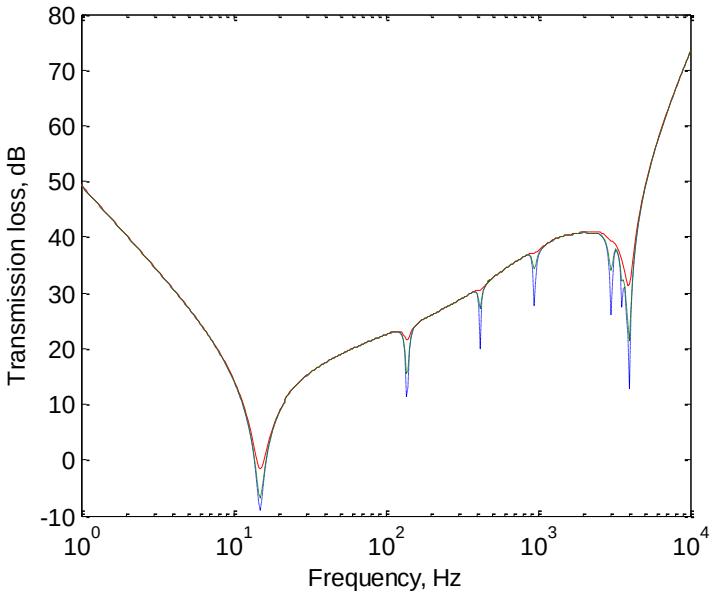

(b)

Figure 2.25. Effect of structural loss factor of the plate strip on the sound transmission loss: (a) normal incidence; (b) oblique incidence at angle 45° about y-axis (– • – $\eta = 0.01$; --- $\eta = 0.03$, — $\eta = 0.1$)

2.4.3 Diffuse sound field

The diffuse sound field excitation is formulated as the superposition of uncorrelated plane waves with equal amplitude in all direction. The sound transmission is then obtained by integrating the response of all incident plane waves over the incident angle and weighting them with the solid angle to account for the directional distribution. Therefore, the sound transmission loss for a diffuse field excitation is expressed as

$$\tau_d = \frac{\int_0^{2\pi}\int_0^{\theta_{\lim}} \tau(\theta,\varphi)\sin\theta\cos\theta d\theta d\varphi}{\int_0^{2\pi}\int_0^{\theta_{\lim}} \sin\theta\cos\theta d\theta d\varphi} \tag{2.89}$$

where $\theta_{\lim}$ is the upper elevation angle which is typically taken equal to 78º for the field incidence case and which is 90º for the full random incidence case [10].

Figure 2.26 presents a comparison of the sound transmission loss between the plate strip and the infinite plate for the diffuse field case. Here only a quarter of hemisphere is considered due to the symmetrical properties of the structures hence the limit of the azimuth angle is reduced from 2π to $\pi/2$. In practical calculation, the infinite plate are calculated using 36 incident angles under the random incidence excitation ($0^\circ \le \theta \le 90^\circ$) and the field incidence one ($0^\circ \le \theta \le 78^\circ$) while 36 incident angles for the random and field incidence excitations and 18 ones over the azimuth angles are used for the plate strip. It is clear that the dip at around 2 kHz is associated with the critical frequency. Above this frequency, the plate strip and the infinite plate produce a similar result. However, below this frequency the TL of the plate strip is higher by 6.5 dB at low frequency than that of the infinite plate. This difference reduces with increasing frequency; for example a difference of 2.7 dB is found at around the critical frequency. This difference comes about because a finite extent in one dimension of the plate strip introduces a spatial windowing effect on the infinite baffle [23]. Accordingly, the radiation ratio of the infinite plate is modified to remain finite for increasing incident angle rather than becoming infinite. This leads to a higher TL for the plate strip. This situation is also illustrated in Figure 2.23 in section 2.4.2 for oblique incidence. The relation of radiation ratio on incident angles for various parameter *kL* where *k* is the acoustic wavenumber and *L* is the panel dimension was presented in [23] for the case of a finite plate. When the plate strip is calculated using the

field incidence method, below the critical frequency, its TL is getting closer to that obtained for the infinite plate particularly close to the critical frequency. Above the critical frequency, a similar curve is seen for both models.

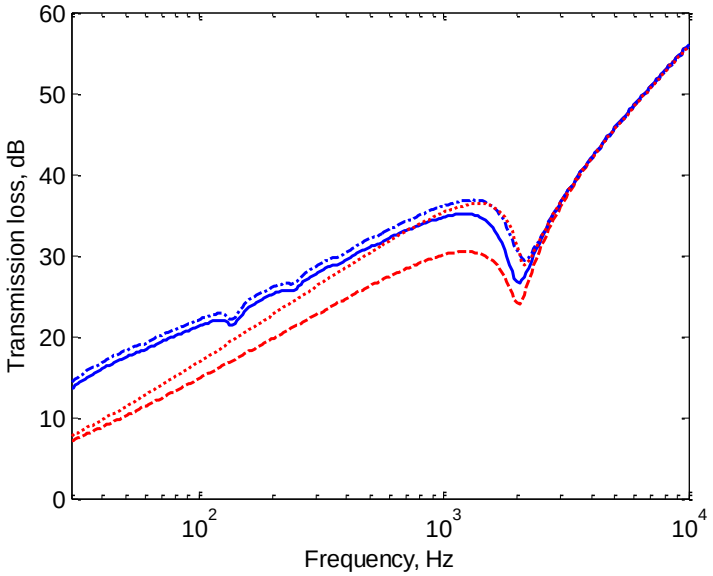

Figure 2.26. TL of plate strip under a diffuse sound field excitation: random incidence ($0^\circ \le \theta \le 90^\circ$): (— Plate strip; --- infinite plate); field incidence ($0^\circ \le \theta \le 78^\circ$): (– • – Plate strip; • • • infinite plate).

2.5 Summary

In this chapter, analytical models of the vibration and sound radiation of a plate strip have been presented. The point mobility behaviour of the plate strip is stiffness-controlled at low frequency and then tends to the mobility of an infinite plate at high frequencies. Peaks are found in the mobility curve associated with the cut-on frequencies while their magnitude is determined by the term $\sin^2\left(m\pi y_0/l_y\right)$. The damping has a significant effect at the cut-on frequencies while in other areas it has little effect on the point mobility. However the spatially averaged response is affected by the damping at all frequencies above the first cut-on frequency. Moreover, the average response is also affected by the thickness of the plate strip.

To get an acceptable accuracy, a sufficient number of waves should be incorporated in the calculation, indicated by the upper limit M. It has been shown that the ratio of M

to the number of waves that have cut-on should be at least 6 to obtain the response within 1%.

Unlike an infinite plate, a plate strip still radiates sound at frequencies below its critical frequency due to the finite extent in one dimension. Therefore, edge modes effectively contribute to the radiated sound power even though the wavenumbers in the y-direction, k_y, are higher than the acoustic wavenumber in this frequency region. In the infinite dimension, that is in the x- direction, the radiated power is also present at frequencies below the critical frequency when $k_{x1,m} < k$. For the opposite condition sound radiation occurs which is only significant in the area close to the excitation position. Peaks found in the radiated power curve are associated with the cut-on frequencies at which it is always the case that $k_{x1,m} \ll k$.

The greatest effect of damping on the radiated sound power appears at the cut-on frequencies. The damping also has a broadband effect for higher frequencies at which the bending wavenumbers $k_{x1,m}$ are lower than the acoustic wavenumbers k. Considering the related radiation ratio, it is clear that the damping loss factor affects the results significantly in the acoustic short-circuiting region between the first cut-on frequency and the critical frequency. A thicker plate strip will radiate less power as the average mean-square velocity reduces for a thicker plate. On the other hand it will reduce the frequency range of the acoustic short-circuiting region which increases the radiation ratio.

An analytical solution for sound transmission through a plate strip has been derived by considering acoustic plane wave excitation, internal and acoustic damping. Comparing the results with that of the infinite plate, some differences occur. For the normal incidence case, it is found that at high frequency, the TL of the plate strip converges to that of the infinite plate while at low frequency a slope of -30 dB/decade is found rather than the -20 dB/decade that is normally found in the TL of an infinite plate. Dips are found corresponding to the cut-on frequencies. The effect of neglecting cross-modal coupling has been shown to be small.

For the oblique incidence case, the analytical model behaves as expected considering the coincidence frequencies when the incidence angle is varied. These match with the infinite plate results. However, well below the coincidence frequency, the TL of the plate strip is greater than that of the infinite plate due to its finite width.

The internal damping loss factor effectively determines the TL values around the cut-on frequencies and the coincidence frequencies. Elsewhere, the damping has a negligible effect. Meanwhile, varying the thickness will shift the first cut-on frequency and the coincidence frequency while the TL values increase as the thickness increases.

Under random incidence, the plate strip model produces the same results as an infinite plate above the critical frequency. Below this frequency, the TL values of the plate strip are higher than those obtained using the infinite plate model. Closer results are found around the critical frequency and just below this frequency when both the plate strip and the infinite plate are excited by the field incidence limited to 78°.

The analytical models of the plate strip developed in this chapter will be used in Chapter 4 to validate WFBE results. First, however, the WFBE method is introduced in the next chapter.

Chapter 3. Waveguide Finite Element-Wavedomain Boundary Element (WFBE) method

A "waveguide structure" is one which is long (or infinite) in one (or more) dimensions and has a constant cross-section perpendicular to this axis. The Waveguide Finite Element (WFE) method [9] is a useful numerical approach to calculate the dynamic behaviour of such a waveguide structure in an efficient way. This approach uses a two-dimensional finite element mesh with special elements that allow for wave propagation in the third dimension. The general three-dimensional solution can be obtained from an inverse Fourier transform over wavenumber. For the case of sound radiation predictions, the coupled Waveguide Finite Element-Boundary Element (WFBE) method can be used to calculate the interaction with the acoustic field [58, 61]. In the present thesis, the existing software WANDS [78] is used to implement the WFBE approach. For completeness, the basis of this approach is described in this chapter, largely following Ref. [78] particularly for the equations of motion of each element. The post-processing methods for forced response and transmission loss have been specifically developed in this thesis as these are not developed in Ref. [78].

3.1 Waveguide Finite Element method

A structure with uniform geometrical and material properties along one direction taken here as the x direction, but arbitrary cross-section can be modelled numerically using the waveguide finite element (WFE) method [61, 79, 80]. Under this formulation, the structural behaviour is treated as a two-dimensional problem in which the waveguide cross-section in the $y-z$ plane is discretized into a number of finite elements. In the other dimension, the $x-$direction, the structure has homogeneous properties and harmonic wave solutions of the form $e^{-ik_x x}$ are assumed. Therefore, a solution is obtained which is three-dimensional in nature, without requiring a three-dimensional model as would be required using conventional finite elements for a similar outcome. This offers a versatile and numerically efficient method for such structures, especially when they are long (or effectively infinite) in the $x-$direction.

3.1.1 Plate elements

Consider a plate strip element with translational displacements u, v and w in the x, y and z directions and a rotational displacement ϕ about the x axis, as shown in Figure 3.1. The element is defined by node points in the $y-z$ plane which become lines in the $x-$direction. This basic element is employed in the WFE formulation to build up any thin-walled complex structure. Derivation of the equations of motion for each element under the WFE formulation can be found in [61, 80, 81]. Harmonic motion at frequency ω is assumed throughout. For a structure assembled of a number of elements, the overall equation can be written in the form

$$\left[\sum_{n=0}^{4}\mathbf{K}_n\frac{\partial^n}{\partial x^n}-\omega^2\mathbf{M}\right]\mathbf{W}(x)=\mathbf{F}(x) \tag{3.1}$$

where $\mathbf{K}_n$ and $\mathbf{M}$ are stiffness and mass matrices which correspond to elastic energy in the system and kinetic energy of the structure respectively. $\mathbf{W}$ is the vector of nodal displacement amplitudes at nodes in the $y-z$ plane which is sought as the solution and $\mathbf{F}$ is a vector of nodal force amplitudes. $\mathbf{W}$ is also a function of ω (suppressed for clarity). In the numerical implementation, the plate strip element includes in-plane and out-of plane motion so that the displacements are given by $\mathbf{W}(x)=\left[u_1 \quad v_1 \quad w_1 \quad \phi_1 \quad u_2 \quad v_2 \quad w_2 \quad \phi_2\right]^{\mathbf{T}}$.

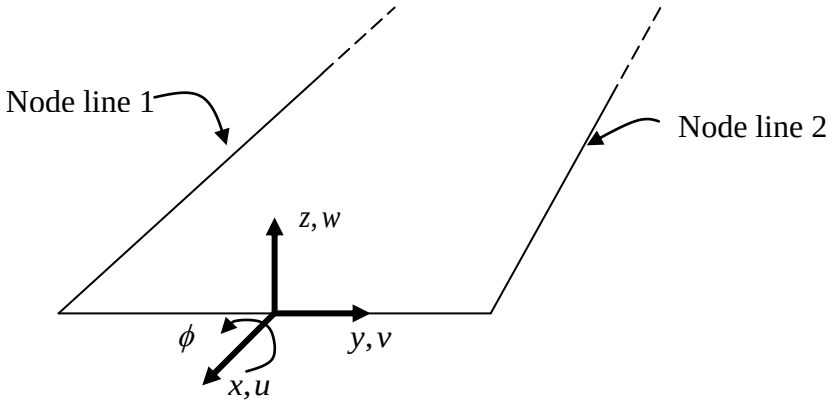

Figure 3.1. A shell (or plate) strip element

For clarity, Eq. (3.1) can be expanded as follows

$$\left[\mathbf{K}_4\frac{\partial^4}{\partial x^4}+\mathbf{K}_2\frac{\partial^2}{\partial x^2}+\mathbf{K}_1\frac{\partial}{\partial x}+\mathbf{K}_0-\omega^2\mathbf{M}\right]\mathbf{W}(x)=\mathbf{F}(x) \tag{3.2}$$

Note that the term $\mathbf{K}_3$ is not usually present. The matrices $\mathbf{K}_4$, $\mathbf{K}_2$, $\mathbf{K}_0$ and $\mathbf{M}$ are symmetric while $\mathbf{K}_1$ is skew-symmetric. Plate out-of-plane bending motion contributes terms in $\mathbf{K}_4$, $\mathbf{K}_2$ and $\mathbf{K}_0$ while in-plane motion contributes terms in $\mathbf{K}_2$, $\mathbf{K}_1$ and $\mathbf{K}_0$. The matrices $\mathbf{K}_n$ and $\mathbf{M}$ and given in Appendix C in terms of the dimensions and material properties of the element.

For the case of an infinite waveguide structure, a spatial Fourier transform in the longitudinal direction enables the response of the structure to be obtained. The following Fourier transform pair is used

$$\tilde{\mathbf{W}}(\kappa)=\int_{-\infty}^{\infty}\mathbf{W}(x)e^{i\kappa x}dx \tag{3.3}$$

$$\mathbf{W}(x)=\frac{1}{2\pi}\int_{-\infty}^{\infty}\tilde{\mathbf{W}}(\kappa)e^{-i\kappa x}d\kappa \tag{3.4}$$

and a similar transform for $\mathbf{F}$. Taking the Fourier transform of Eq. (3.2) to transform it from the spatial domain into the wavenumber domain, yields

$$\left[\mathbf{K}_4(-i\kappa)^4+\mathbf{K}_2(-i\kappa)^2+\mathbf{K}_1(-i\kappa)+\mathbf{K}_0-\omega^2\mathbf{M}\right]\tilde{\mathbf{W}}(\kappa)=\tilde{\mathbf{F}}(\kappa) \tag{3.5}$$

where κ is the wavenumber in the $x-$direction.

3.1.2 Solid elements

Similarly a solid element can be defined by four (or more) node points. Nodes in the solid elements have 3 degrees of freedom corresponding to three translational displacements. Using the same principle as presented in section 3.1.1, the overall motion of a structure built up of solid elements can be written as follows [78]

$$\left[\mathbf{K}_2\frac{\partial^2}{\partial x^2}+\mathbf{K}_1\frac{\partial}{\partial x}+\mathbf{K}_0-\omega^2\mathbf{M}\right]\mathbf{W}(x)=\mathbf{F}(x) \tag{3.6}$$

where again **W** is also a function of ω (suppressed for clarity). Taking Fourier transforms, this gives

$$\left[\mathbf{K}_2(-i\kappa)^2+\mathbf{K}_1(-i\kappa)+\mathbf{K}_0-\omega^2\mathbf{M}\right]\tilde{\mathbf{W}}(\kappa)=\tilde{\mathbf{F}}(\kappa) \tag{3.7}$$

where κ is the wavenumber in the $x-$direction. The matrices $\mathbf{K}_2$, $\mathbf{K}_1$, $\mathbf{K}_0$ and **M** are stiffness and mass matrices as before, and are given in Appendix C.

3.1.3 Fluid element

Since fluid in the cavity is presumed to be ideal in the numerical model, the flow is irrotational, i.e. the vorticity ($\nabla\times\mathbf{v}$) is equal to zero [82]. That allows the particle velocity to be written as

$$\mathbf{v}=-\nabla\psi \tag{3.8}$$

where $\psi=\psi(x,y,z,t)$ is the velocity potential. The use of the velocity potential is effective for this modelling as all components of the fluid velocity can be obtained. Moreover, the pressure can be also defined by this scalar quantity as

$$p=\rho_0\frac{\partial\psi}{\partial t} \tag{3.9}$$

The assembling of the fluid elements can be formulated by integrating their weak form (see Ref. [78] page 87) and this gives

$$\mathbf{K_2}\frac{\partial^2\hat{\boldsymbol{\psi}}}{\partial x^2}+\mathbf{K_0}\hat{\boldsymbol{\psi}}-\omega^2\mathbf{M_f}\hat{\boldsymbol{\psi}}=0 \tag{3.10}$$

where $\mathbf{K}_2$, $\mathbf{K}_0$ and $\mathbf{M_f}$ are stiffness and fluid mass matrices. These matrices are given in Appendix C.

Applying Fourier transforms to Eq. (3.10) as defined in Eq. (3.3) yields

$$\left[\mathbf{K_2}\left(-i\kappa\right)^2+\mathbf{K_0}-\omega^2\mathbf{M_f}\right]\tilde{\boldsymbol{\psi}}=0 \tag{3.11}$$

which is the waveguide FE model for a fluid in the wavenumber domain. The manner in which it is coupled to the structure us described in section 3.3 below.

3.1.4 Free wave solution

Setting the external force $\tilde{\mathbf{F}} = \mathbf{0}$ in Eq. (3.5) leads to the free vibration case, which results in a twin-parameter eigenvalue problem where both wavenumber κ and frequency ω are unknown:

$$\left[\mathbf{K}_4(-i\kappa)^4 + \mathbf{K}_2(-i\kappa)^2 + \mathbf{K}_1(-i\kappa) + \mathbf{K}_0 - \omega^2\mathbf{M}\right]\tilde{\mathbf{W}} = \mathbf{0} \tag{3.12}$$

This is a linear eigenvalue problem in squared frequency ω^2 for a given wavenumber κ. Alternatively the polynomial eigenvalue problem in wavenumber κ can be solved for a given frequency ω. The solution obtained can then be used to describe the dispersion characteristics of the structure while the corresponding eigenvectors represent the cross-section deformation modes. For the case of $\kappa = 0$, the eigenvalue problem reduces to

$$\left[\mathbf{K}_0 - \omega^2\mathbf{M}\right]\tilde{\mathbf{W}} = \mathbf{0} \tag{3.13}$$

where the frequencies that are the solution of Eq. (3.13) are the cut-on frequencies of the various waves in the waveguide. Otherwise, however, Eq. (3.12) is a non-standard eigenvalue problem in wavenumber which can be more efficiently solved if it is transformed into a standard form. This can be achieved by transforming Eq. (3.12) so that the unknown eigenvalue κ does not appear in the system matrix. The following procedure is used for solving such an eigenvalue problem by transforming it into a standard eigenvalue problem form for $(-i\kappa)^{-1}$ as given by Gavric [80]. The procedure starts by inverting the part of Eq. (3.12) which does not depend on wavenumber, $\left(\mathbf{K}_0 - \omega^2\mathbf{M}\right)$. Eq. (3.12) is then multiplied by the inverted matrix and divided by $-i\kappa$ to give the following relation

$$\left(\mathbf{A_1}+(-i\kappa)\mathbf{A_2}+(-i\kappa)^3\mathbf{A_4}\right)\tilde{\mathbf{W}}=\frac{1}{(-i\kappa)}\tilde{\mathbf{W}} \tag{3.14}$$

where $\mathbf{A}_j=-\left(\mathbf{K_0}-\omega^2\mathbf{M}\right)^{-1}\mathbf{K}_j$, $j=1,\ 2,\ 4$. Eq. (3.14) can then be converted to a simple eigenvalue problem by adding three identities $(-i\kappa)^{j-1}\tilde{\mathbf{W}}=(i/\kappa)(-i\kappa)^j\tilde{\mathbf{W}}$ for $j=1,\ 2,\ 3$ to yield the square matrix system

$$\begin{pmatrix}\mathbf{A_1} & \mathbf{A}_2 & \mathbf{0} & \mathbf{A}_4\\ \mathbf{I} & \mathbf{0} & \mathbf{0} & \mathbf{0}\\ \mathbf{0} & \mathbf{I} & \mathbf{0} & \mathbf{0}\\ \mathbf{0} & \mathbf{0} & \mathbf{I} & \mathbf{0}\end{pmatrix}\begin{pmatrix}\tilde{\mathbf{W}}\\ (-i\kappa)\tilde{\mathbf{W}}\\ (-i\kappa)^2\tilde{\mathbf{W}}\\ (-i\kappa)^3\tilde{\mathbf{W}}\end{pmatrix}=\frac{1}{(-i\kappa)}\begin{pmatrix}\tilde{\mathbf{W}}\\ (-i\kappa)\tilde{\mathbf{W}}\\ (-i\kappa)^2\tilde{\mathbf{W}}\\ (-i\kappa)^3\tilde{\mathbf{W}}\end{pmatrix} \tag{3.15}$$

where $\mathbf{I}$ is the identity matrix. The dimension of the unknown eigenvector is four times the dimension of the original finite element model. The eigenvalues are the inverse of the wavenumbers $(-i\kappa)^{-1}$. Eq. (3.15) satisfies the standard eigenvalue problem form. For the case of $\mathbf{K}_4=\mathbf{0}$, e.g. only solid elements, Eq. (3.15) reduces to

$$\begin{pmatrix}\mathbf{A_1} & \mathbf{A}_2\\ \mathbf{I} & \mathbf{0}\end{pmatrix}\begin{pmatrix}\tilde{\mathbf{W}}\\ (-i\kappa)\tilde{\mathbf{W}}\end{pmatrix}=\frac{1}{(-i\kappa)}\begin{pmatrix}\tilde{\mathbf{W}}\\ (-i\kappa)\tilde{\mathbf{W}}\end{pmatrix} \tag{3.16}$$

where $\mathbf{A}_j=-\left(\mathbf{K_0}-\omega^2\mathbf{M}\right)^{-1}\mathbf{K}_j$, $j=1,\ 2$.

3.1.5 Forced response

In order to predict the forced response of a structure, all the wave solutions including nearfield waves are required. Hence, Eq. (3.15) and Eq. (3.16) have to be solved to obtain all wavenumbers and mode shapes at a given frequency ω.

For the case of forced vibration due to a concentrated load at a given frequency ω, the force can be represented using a delta function in the spatial domain as follows

$$\mathbf{F}(x)=\hat{\mathbf{F}}\delta\left(x\right) \tag{3.17}$$

where $\hat{\mathbf{F}}$ represents the nodal force vector. The response of the structure is then given as the solution to

$$\left[\mathbf{K}_4\frac{\partial^4}{\partial x^4}+\mathbf{K}_2\frac{\partial^2}{\partial x^2}+\mathbf{K}_1\frac{\partial}{\partial x}+\mathbf{K}_0-\omega^2\mathbf{M}\right]\mathbf{W}(x)=\hat{\mathbf{F}}\delta\left(x\right) \tag{3.18}$$

Using Fourier transforms as in Eq. (3.3), Eq. (3.18) is subsequently written as

$$\left[\mathbf{K}_4(-i\kappa)^4+\mathbf{K}_2(-i\kappa)^2+\mathbf{K}_1(-i\kappa)+\mathbf{K}_0-\omega^2\mathbf{M}\right]\tilde{\mathbf{W}}(\kappa)=\tilde{\mathbf{F}}(\kappa) \tag{3.19}$$

where

$$\tilde{\mathbf{F}}\left(\kappa\right)=\int_{-\infty}^{\infty}\hat{\mathbf{F}}\delta(x)e^{i\kappa x}dx=\hat{\mathbf{F}} \tag{3.20}$$

and $\tilde{\mathbf{W}}(\kappa)$ is the displacement of the cross-section at wavenumber κ. By inverting the dynamic stiffness matrix in square brackets in Eq. (3.19), the displacement of the structure in the wavenumber domain can be obtained as

$$\tilde{\mathbf{W}}(\kappa)=\left[\mathbf{K}_4(-i\kappa)^4+\mathbf{K}_2(-i\kappa)^2+\mathbf{K}_1(-i\kappa)+\mathbf{K}_0-\omega^2\mathbf{M}\right]^{-1}\tilde{\mathbf{F}}(\kappa) \tag{3.21}$$

Subsequently, the displacement in the spatial domain can be recovered through the inverse Fourier transform, Eq. (3.4). This equation can be solved by several methods as discussed below.

3.1.6 Residue calculus method

Using the residue calculus method, as presented in [9, 58, 81, 83], the integral in Eq. (3.4) with limits $\pm\infty$ can be replaced by a contour integral in the complex plane. Two such curves are shown in Figure 3.2. For $x\leq 0$ the integral in Eq. (3.4) is performed over the upper half plane because the integrand will approach zero in this plane as $R\to\infty$.

Similarly for $x>0$ the integral is performed over the lower half plane. The integral is equal to $\pm 2\pi i$ times the sum of the residues at the poles of the integrand [84]

$$\oint \frac{f(z)}{q(z)} dz = 2\pi i \sum_p \frac{f(z)}{q'(z)} \tag{3.22}$$

where $f(z)$ and $q(z)$ are finite functions of the complex variable z and the sign depends on the direction in which the poles are encircled. Eq. (3.22) has poles, where the dynamic stiffness has zero determinant, at precisely the solutions to Eq. (3.12), i.e. the free wave solutions. It is assumed that each of them is a simple pole hence there are no duplicate wave solutions.

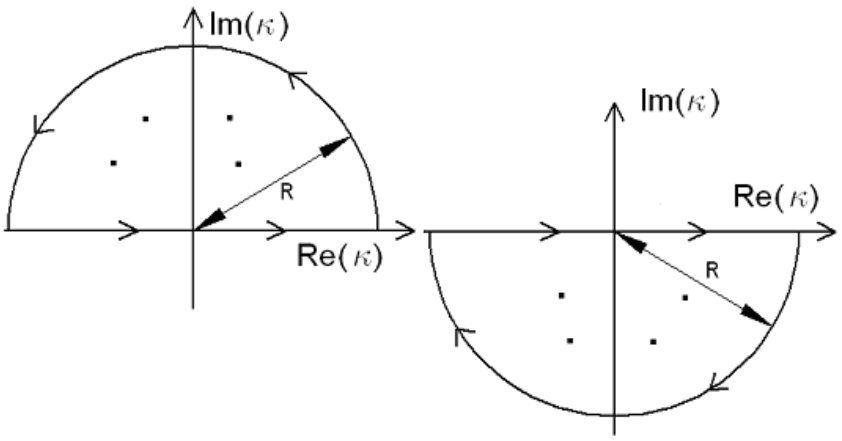

Figure 3.2. Path of integration in complex plane [9].

The response in the spatial domain is then calculated as a sum of residues as follows [9, 81]

$$W_{DOF}(x) = i\sum_q \frac{\tilde{\mathbf{W}}_{q,L}^T \tilde{\mathbf{F}}}{\tilde{\mathbf{W}}_{q,L}^T \left[\frac{\partial}{\partial \boldsymbol{\kappa}} \left(\sum_j \mathbf{K}_j (-i\boldsymbol{\kappa})^j \right)_{\boldsymbol{\kappa}=\boldsymbol{\kappa}_p} \right]_q \tilde{\mathbf{W}}_{q,R}} \tilde{W}_{DOF,q,R} \tag{3.23}$$

where q is an index over the waves in the structure under consideration at a given frequency. $\tilde{\mathbf{W}}_L$ and $\tilde{\mathbf{W}}_R$ are referred to as the left and right eigenvectors of Eq. (3.12) respectively for the eigenproblem evaluated at $\kappa = \kappa_p$. The DOF subscript is an index

indicating the degree of freedom at which the displacement is required while $\tilde{W}_{DOF,q,R}$ is the component of the right eigenvector $\tilde{\mathbf{W}}_R$ corresponding to index DOF.

The differential term in the denominator of Eq. (3.23) can be derived as follows

$$\frac{\partial}{\partial \kappa}\left(\sum_j \mathbf{K}_j(-i\kappa)^j\right)_{\kappa=\kappa_p} = -i\left(4\mathbf{K}_4(-i\kappa)^3 + 2\mathbf{K}_2(-i\kappa) + \mathbf{K}_1\right)_{\kappa=\kappa_p} \tag{3.24}$$

For the case of the solid elements, where $\mathbf{K}_4$ is absent, Eq. (3.24) becomes

$$\frac{\partial}{\partial \kappa}\left(\sum_j \mathbf{K}_j(-i\kappa)^j\right)_{\kappa=\kappa_p} = -i\left(2\mathbf{K}_2(-i\kappa) + \mathbf{K}_1\right)_{\kappa=\kappa_p} \tag{3.25}$$

3.1.7 Numerical integration

Aside from the residue calculus approach, the integration in Eq. (3.4) can also be solved for a limited wavenumber range by using a simple numerical integration technique such as the rectangle method [84]. This method works by dividing the area under the graph of Eq. (3.21) into r rectangles. The area of each is the product of height and width. Thus the integral in Eq. (3.4) becomes

$$\mathbf{W}(x) = \frac{1}{2\pi}\int_{-\kappa_{\max}}^{\kappa_{\max}} \tilde{\mathbf{W}}(\kappa)e^{-i\kappa x}d\kappa \approx \frac{1}{2\pi}\sum_r \underset{(1)}{\tilde{\mathbf{W}}(\kappa)}\, e^{-i\kappa x}\, \overset{(2)}{\Delta\kappa} \tag{3.26}$$

where term (1) determines the height of the rectangles and term (2) $\Delta\kappa$ is the step size which is taken as an equal sub-division of the length. Figure 3.3 illustrates how this method works. The key point here is to determine suitable values for $\kappa_{\max}$ and $\Delta\kappa$ which will be considered in section 4.1.2.

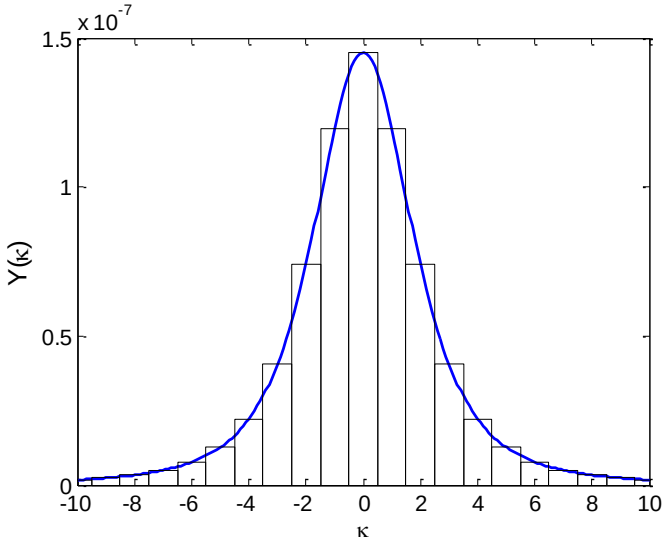

Figure 3.3. Integration in Eq. (3.4) is performed as a series of rectangles to approximate the area under the graph.

3.2 Wavenumber Boundary Element method

3.2.1 Wavenumber domain

For the boundary element method, the acoustic domanin is discretized around its boundary. The boundary variables, acoustic pressure p and fluid particle velocity in the direction $\mathbf{n}$, v_n, are conveniently expressed through the velocity potential ψ (see Eq. (3.8) and (3.9)). This gives

$$v_n = -\frac{\partial \psi}{\partial \mathbf{n}} \tag{3.27}$$

and

$$p = \rho_0 \frac{\partial \psi}{\partial t} \tag{3.28}$$

where $\mathbf{n}$ is a unit direction vector normal to the surface and ρ_0 is the mean fluid density.

The Kirchoff-Helmholtz integral equation for the radiated acoustic field is given by [78]

$$\rho_0 \int_V \left(\delta\psi^* \nabla^2 \psi + k^2 \delta\psi^* \psi \right) dV + \rho_0 \int_S \left(\delta\psi^* \frac{\partial \psi}{\partial \mathbf{n}} - \psi \frac{\partial \delta\psi^*}{\partial \mathbf{n}} \right) dS = 0 \tag{3.29}$$

where $\delta\psi^*$ is the Green's function of the system with $*$ denoting complex conjugate and S is a closed surface enclosing the volume V. For unbounded region S includes an integral over a surface at infinity.

Taking a spatial Fourier transform in the $x-$direction leads to the volume and surface integrals in Eq. (3.29) becoming surface and line integrals when the integral over wavenumber is dropped, hence

$$\rho_0 \int_S \delta\tilde{\psi}^* \left(\nabla_{2D}^2 \tilde{\psi} + \left(k^2 - \kappa^2 \right) \tilde{\psi} \right) dS + \rho_0 \int_\Gamma \left(\delta\tilde{\psi}^* \frac{\partial \tilde{\psi}}{\partial \mathbf{n}} - \tilde{\psi} \frac{\partial \delta\tilde{\psi}^*}{\partial \mathbf{n}} \right) d\Gamma = 0 \tag{3.30}$$

where $\nabla_{2D}^2 = \partial^2/\partial y^2 + \partial^2/\partial z^2$, κ is the wavenumber in the $x-$direction, S is the cross-section area of the acoustic domain and Γ is the perimeter of the boundary. It can be seen that the first term of Eq. (3.30) is similar to the normal 2D Helmholtz equation in the conventional BE method but with k^2 replaced by $\alpha^2 = (k^2 - \kappa^2)$.

Now consider the presence of a point source at $\mathbf{r_0}$. The first integral of Eq. (3.30) is required to be zero except at the source position. Meanwhile, the second integral of this equation over the source constitutes $C(\mathbf{r})\delta\psi^*(\mathbf{r})$ where $|\mathbf{r} - \mathbf{r_0}| \to 0$. The integral over the far-field boundary also disappears owing to Sommerfeld's radiation condition. Hence, the boundary integral equation becomes

$$C(\mathbf{r})\delta\tilde{\psi}^*(\mathbf{r}) = -\int_\Gamma \left(\delta\tilde{\psi}^* \frac{\partial \tilde{\psi}}{\partial \mathbf{n}} - \tilde{\psi} \frac{\partial \delta\tilde{\psi}^*}{\partial \mathbf{n}} \right) d\Gamma \tag{3.31}$$

The result from the BE model gives a relation between the boundary variables that may be written as

$$\mathbf{H}\tilde{\boldsymbol{\psi}} - \mathbf{G}\frac{\partial \tilde{\boldsymbol{\psi}}}{\partial \mathbf{n}} = \frac{\mathbf{P_{in}}}{i\omega} \tag{3.32}$$

where $\tilde{\boldsymbol{\psi}}$ and $\partial\tilde{\boldsymbol{\psi}}/\partial\mathbf{n}$ are vectors of the respective variables at the nodes of the BE model and $\mathbf{n}$ is the unit vector normal to the surface of the boundary. To allow excitation by an incident wave field, $\mathbf{P}_{\mathbf{in}}$ is introduced as the pressure amplitude of the incoming wave evaluated on the boundary nodes. $\mathbf{H}$ and $\mathbf{G}$ are generally full, non-symmetric, complex-valued matrices that are obtained by discretising terms on the right-hand side of Eq. (3.31).

3.2.2 Mixed boundary condition

In addition to Eq.(3.32), another relation between the boundary pressure and the velocity vector is also required. This relation is given to cover specific conditions of the boundary, i.e. specifying a coupling to another system, for example nodes on the boundary which are not on the FE/BE interface (or 'wetted' surface). This is then referred to as a mixed boundary condition and can be written as

$$\mathbf{C}_A\tilde{\mathbf{P}} + \mathbf{C}_B\tilde{\mathbf{V}}_n = \mathbf{c}_c \tag{3.33}$$

where $\mathbf{C}_A$ and $\mathbf{C}_B$ are diagonal matrices and $\mathbf{c}_c$ is a vector corresponding to pressure sources and moving boundaries. Note that this boundary condition is also known as a Robin (or impedance) boundary condition. This kind of boundary condition is imposed in the case of a baffled plate to enforce zero velocity on the baffle and at the edges of the plate.

3.3 Coupling between WFE and WBE models

A complex structure can be developed by combining sub-models of waveguide finite elements and wavenumber boundary elements through a suitable coupling mechanism. In this section, an overview on this is provided, while detailed explanations are given in [78].

At the wetted surface there are two types of boundary conditions along the surface, namely Dirichlet (or Essential) and Neuman (or Natural). The Neuman boundary conditions are implicitly included in the equation for Hamilton's principle in which relation between force and displacement or pressure and particle velocity have already been defined [78].

For plate FE or solid FE coupled with fluid FE, the virtual work from fluid motion needs to be included. Hence, Eq. (3.5) or (3.7) in the absence of external force now becomes

$$\left[\mathbf{K}+i\omega\mathbf{M}_1-\omega^2\mathbf{M}_2\right]\tilde{\bar{\mathbf{W}}}=\mathbf{0} \tag{3.34}$$

where $\tilde{\bar{\mathbf{W}}}=\begin{bmatrix}\tilde{\mathbf{W}} & \tilde{\boldsymbol{\psi}}\end{bmatrix}^{\mathbf{T}}$, $\mathbf{M}_1$ is the coupling matrix to account for virtual work on the solid by the fluid and vice versa, which can be seen as a gyroscopic coupling matrix , and $\mathbf{M}_2$ is the mass matrix defined as follows

$$\mathbf{M}_2=\begin{bmatrix}\mathbf{M_j} & \mathbf{0}\\ \mathbf{0} & \mathbf{M_f}\end{bmatrix} \tag{3.35}$$

where index $\mathbf{j}$ is $\mathbf{p}$ or $\mathbf{s}$ to indicate plate or solid.

For plate FE or solid FE coupled with fluid BE, the Dirichlet boundary conditions that must be fulfilled for coupled FE-BE at the wetted surface are that the velocity of the structure must match that of the fluid. Therefore, in terms of velocity potential, this can be expressed as

$$\mathbf{I_2}\frac{\partial\tilde{\boldsymbol{\psi}}}{\partial\mathbf{n}}-i\omega\mathbf{C_2}\tilde{\mathbf{W}}=0 \tag{3.36}$$

where $\mathbf{I}_2$ is a matrix containing terms which are unity or zero and $\mathbf{C}_2$ is a transformation matrix transforming FE-displacements $\tilde{\mathbf{W}}$ to the equivalent normal displacement at the boundary.

From Eq. (3.36) $\partial\tilde{\boldsymbol{\psi}}/\partial\mathbf{n}$ can be written as

$$\frac{\partial\tilde{\boldsymbol{\psi}}}{\partial\mathbf{n}}=i\omega\mathbf{I}_2^{-1}\mathbf{C_2}\tilde{\mathbf{W}} \tag{3.37}$$

where the vector $\tilde{\mathbf{W}}(\kappa)$ is the displacement from the FE model. The velocity potential is obtained by substituting Eq. (3.37) into Eq. (3.32). This gives

$$\tilde{\boldsymbol{\psi}} = \mathbf{H}^{-1}\mathbf{G}\frac{\partial\tilde{\boldsymbol{\psi}}}{\partial\mathbf{n}} \tag{3.38}$$

Having obtained $\partial\tilde{\boldsymbol{\psi}}/\partial\mathbf{n}$ and $\tilde{\boldsymbol{\psi}}$, the particle velocity $\tilde{\mathbf{V}}_n(\kappa)$ and the pressure $\tilde{\mathbf{P}}(\kappa)$ and can be found from the Fourier transforms of Eq.(3.27) and Eq. (3.28).

Due to presence of the fluid BE on the boundary, the pressure from the fluid is now added to Eq. (3.34) so that the virtual work $\mathbf{C}_1\tilde{\mathbf{P}}$ produced by the WBE model can be included in the WFE model. This gives

$$\left[\mathbf{K} + i\omega\mathbf{M}_1 - \omega^2\mathbf{M}_2\right]\tilde{\mathbf{W}} - \mathbf{C}_1\tilde{\mathbf{P}} = \mathbf{0} \tag{3.39}$$

where $\mathbf{C}_1\tilde{\mathbf{P}}$ is the force from the fluid acting on the plate in which $\mathbf{C}_1$ is the coupling matrix that projects the pressure of the fluid onto the structure and $\tilde{\mathbf{P}}$ is the pressure.

Considering all relationships in Eq.(3.32)-(3.33) and Eq.(3.36)-(3.39), the combined system is obtained as follows

$$\begin{bmatrix} \mathbf{H} & -\mathbf{G}_n & \mathbf{0} \\ -i\omega\rho\mathbf{C}_1 & \mathbf{0} & \mathbf{K} + i\omega\mathbf{M}_1 - \omega^2\mathbf{M}_2 \\ i\omega\rho\mathbf{C}_A & \mathbf{C}_B - \mathbf{I}_2 & i\omega\mathbf{C}_2 \end{bmatrix} \begin{bmatrix} \tilde{\boldsymbol{\psi}} \\ \dfrac{\partial\tilde{\boldsymbol{\psi}}}{\partial\mathbf{n}} \\ \tilde{\mathbf{W}} \end{bmatrix} = \begin{bmatrix} \tilde{\mathbf{P}}_{in} \\ \tilde{\mathbf{F}}_e \\ \mathbf{c}_c \end{bmatrix} \tag{3.40}$$

where $\mathbf{G}_n = \dfrac{1}{i\omega\rho}\mathbf{G}$ and $\tilde{\mathbf{F}}_e$ contains the other external forces.

3.3.1 Radiated sound power

The radiated power W_{rad} due to a vibrating waveguide structure is given by

$$W_{rad} = \frac{1}{2}\mathrm{Re}\left(\int_{-\infty}^{\infty}\int_{\Gamma} p(x)v_n^*(x)d\Gamma dx\right) \tag{3.41}$$

where Γ is the perimeter of the cross-section in the $y-z$ plane and $d\Gamma$ is an infinitesimal segment of the perimeter of the cross-section. By using Parseval's formula, Eq. (3.41) can be written in the wavenumber domain to give

$$W_{rad} = \frac{1}{4\pi}\mathrm{Re}\left(\int_{-k}^{k}\int_{\Gamma}\tilde{P}(\kappa)\tilde{V}_n^{*}(\kappa)d\Gamma d\kappa\right) \tag{3.42}$$

where the integral is restricted to $-k \le \kappa \le k$, with k the acoustic wavenumber, since elsewhere no radiated power is produced.

The integration process over Γ in Eq. (3.42) is actually performed element-by-element with the boundary variable $\tilde{P}_j$ and $\tilde{V}_j$ of each element j given by

$$\tilde{P}_j = \sum_{i=1}^{n} p_i N_i(\xi) \tag{3.43}$$

$$\tilde{V}_j = \sum_{i=1}^{n} V_i N_i(\xi) \tag{3.44}$$

where j is the element number, i is the node number of element j and $N_i(\xi)$ is the shape function with local coordinate $-1 \le \xi \le 1$.

The length of the infinitesimal segment itself can be evaluated by [65]

$$d\Gamma = \sqrt{(dy)^2 + (dz)^2} = \sqrt{\left(\frac{dy}{d\xi}\right)^2 + \left(\frac{dz}{d\xi}\right)^2}\, d\xi = J d\xi \tag{3.45}$$

where J is the Jacobian and

$$\frac{dy}{d\xi} = \sum_{i=1}^{n} y_i \frac{dN_i}{d\xi} \tag{3.46}$$

$$\frac{dz}{d\xi} = \sum_{i=1}^{n} z_i \frac{dN_i}{d\xi} \tag{3.47}$$

Therefore, the integration over the perimeter for each κ can be performed numerically. Here standard Gaussian quadrature [85] is used for this. This gives

$$\begin{aligned}\int_{\Gamma}\tilde{P}\tilde{V}_n^{\,*}d\Gamma &= \sum_{j=1}^{m}\int_{\Gamma_j}\tilde{P}_j\tilde{V}_{n,j}^{\,*}d\Gamma \\ &= \sum_{j=1}^{m}\int_{-1}^{1}\sum_{i=1}^{n}p_iN_i(\xi)\left(\sum_{i=1}^{n}V_iN_i(\xi)\right)^{*}Jd\xi \\ &= \sum_{j=1}^{m}\sum_{k=1}^{g}w_k f(\xi_k)\end{aligned} \tag{3.48}$$

where m is the number of elements, g is the number of Gaussian points used on the element, ξ_k is the k^{th} Gaussian point, w_k is the corresponding weight and $f(\xi_k)=\sum_{i=1}^{n}p_iN_i(\xi)\left(\sum_{i=1}^{n}V_iN_i(\xi)\right)^{*}Jd\xi$.

3.3.2 Sound transmission

For an incident plane wave at angle θ to the normal (about the $x-$axis), the incident power per unit length in the $x-$direction is defined as

$$W_{inc}=\frac{1}{2}\int_{\Gamma}\frac{|p_i|^2\cos\theta}{\rho_0 c}d\Gamma \tag{3.49}$$

where $|p_i|$ is the incident pressure amplitude. The incident angle about the y - axis is determined by the wavenumber κ in the $x-$direction. By using the radiated sound power W_{rad} as defined by Eq. (3.42), the transmission coefficient is given by

$$\tau=\frac{W_{rad}}{W_{inc}} \tag{3.50}$$

The sound reduction index or transmission loss R is found from

$$R=10\log_{10}\left(\frac{1}{\tau}\right)\quad \text{dB} \tag{3.51}$$

In practice, structures are often subjected to a diffuse sound field rather than a plane wave. The diffuse sound field excitation is formulated as the superposition of uncorrelated plane waves with equal amplitude. The response of the structure is then obtained by integrating the response due to all incident plane waves over the incident angle and weighting them with the corresponding solid angle to account for the directional distribution.

Using the same principle, the diffuse field can be defined in WANDS but with a different convention owing to the way the acoustic response is calculated in WANDS. The acoustic response of the waveguide structure is calculated based on the wavenumber α instead of k as follows (see section 3.2.1)

$$\alpha = \sqrt{k^2 - \kappa^2} = \sqrt{k_y^2 + k_z^2} \tag{3.52}$$

The incident direction in WANDS can thus be described by two respective angles ϕ and β which cover the directional distribution of the acoustic intensity, as illustrated in Figure 3.4.

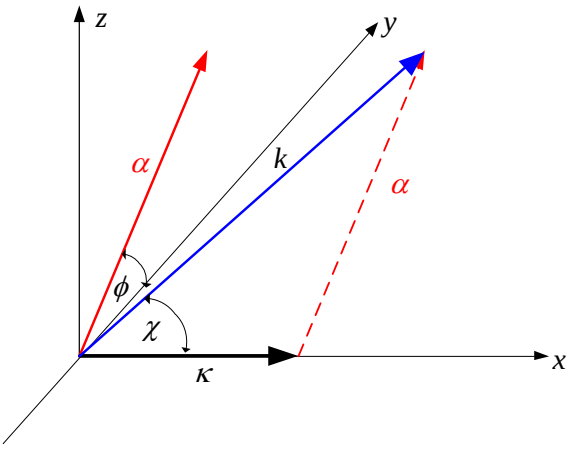

Figure 3.4. Description of incident direction in WANDS

Here ϕ is the angle within the $y-z$ plane (about the x axis) and χ is the angle between the vectors of the acoustic wavenumber and propagating wavenumber in the x – direction (for $\phi = \pi/2$ it corresponds to a rotation about the y axis). Note that the angle χ is dependent on κ while the angle ϕ is discretised from 0 to 90º.

As a consequence of the convention adopted in Figure 3.4, the wavenumbers in each direction can be defined as

$$k_x = \kappa = k\cos\chi \tag{3.53}$$

$$k_y = \alpha\cos\phi = \sqrt{k^2 - \kappa^2}\cos\phi = k\sin\chi\cos\phi \tag{3.54}$$

$$k_z = \alpha\sin\phi = \sqrt{k^2 - \kappa^2}\sin\phi = k\sin\chi\sin\phi \tag{3.55}$$

Following the Paris' formula [86], the diffuse field transmission coefficients can thus be expressed as

$$\tau_d = \frac{\int_0^{\pi/2}\int_0^{\pi/2}\tau(\chi,\phi)\sin\chi\sin\phi d\Omega}{\int_0^{\pi/2}\int_0^{\pi/2}\sin\chi\sin\phi d\Omega} = \frac{4}{\pi}\int_0^{\pi/2}\int_0^{\pi/2}\tau(\chi,\phi)\sin\chi\sin\phi d\Omega \tag{3.56}$$

where $d\Omega = \sin\chi d\phi d\chi$. Hence, the transmission loss for the diffuse sound field is finally expressed by

$$R_d = 10\log_{10}\left(\frac{1}{\tau_d}\right) \quad \text{dB} \tag{3.57}$$

3.4 Summary

The waveguide finite element (WFE) method can be used to calculate the free and forced response of dynamic systems. This method is able to model various waveguide structures as well as fluid with arbitrary cross section and homogeneous properties in the other direction. Coupled with the wavenumber boundary element (WBE) method, such an approach can be used to calculate the radiated sound power excited either by mechanical or acoustic excitation.

In this study, the WFBE method is implemented using a software package called WANDS [78] developed at the ISVR. All methods described in this section will be used to calculate structural response of an infinite plate strip as presented in Chapter 4.

Chapter 4. Validation of WFBE for a plate strip

For the particular case of sound radiation and transmission involving the coupling between structural components and the surrounding air, analytical models have been developed in Chapter 2 to enable validation of the WFBE approach. These are based on an infinite plate strip with simply supported boundaries. Results have been given in Chapter 2 for the mobility, the sound radiation due to a point force and the sound transmission due to an incident sound field.

A computer program has recently been developed at ISVR which implements the WFBE approach with a number of suitable element types as presented in Chapter 3. This software package called WANDS (Wave Number Domain Software) [78] is used here to model the structure of a plate strip as well as the surrounding fluid for the case where the structure-fluid interaction exists. The detailed procedure for using WANDS is given in [87][4].

In this chapter, validation of the numerical model is conducted by comparing the results with those from the analytical models. A comparison of the results of each method as well as an investigation of various methods for evaluating the integral in the inverse Fourier transform are discussed in detail. This step is important to know the effect of discretization in wavenumber space in terms of step size and wavenumber range in order to avoid losing information. The effect of baffle width on the accuracy of the radiated power calculation is also investigated considering the finiteness of the baffle width implemented in the numerical model. Moreover, the thickness (or depth) of the WBE mesh is considered in order to avoid problems corresponding with thin bodies [65] owing to a close distance between the opposite sides of the mesh. In general, the verification of the numerical result by comparison with the analytical one is of importance as a prerequisite to employing the method in more complicated cases.

In the present comparisons, an aluminium plate of width l_y and infinite length is assumed with simply supported boundaries. The material and geometric properties are identical to those used in Chapter 2 and are listed again in Table 4.1.

[4] No new developments of the WANDS software have been carried out by the author. However, the procedures to implement diffuse incidence TL were developed as part of the present thesis and issues surrounding the use of WBE-fluid were investigated in detail.

Table 4.1. Material properties of the plate strip (unless otherwise stated).

Properties	Value
Young's modulus, E ($\mathrm{N/m^2}$)	7.1×10^{10}
Poisson's ratio, v_p	0.332
Thickness, h (mm)	6.0
Width, l_y (m)	1.0
Density , ρ ($\mathrm{kg/m^3}$)	2.7×10^{3}
Damping loss factor (if used), η	0.1

4.1 Point mobility of a plate strip

In WANDS, a special two-noded element is implemented for plates consisting of a linear shape function for the in-plane motion and cubic Hermite polynomials for out-of plane motions. Here, unless otherwise stated, 30 plate elements are used to represent the cross-section of 1 m width. This corresponds to 4 elements per wavelength at the maximum frequency of 3 kHz. To simulate the simply supported boundaries, the first node of the first element and the second node of the last element are restrained in the x, y and z – directions but are free in rotation so that the model has 118 degrees of freedom (DOF) in total. A point force of unit amplitude is applied at the centre, which corresponds to the 16^{th} node.

The WANDS software itself is used for calculating the matrices $\mathbf{K}_n$ and $\mathbf{M}$. Then, the receptance of the plate strip is obtained in a separate post-processing state in Matlab using the residue calculus method as described in section 3.1.6. The mobility of the plate strip is obtained by multiplying by $i\omega$. Figure 4.1 shows the point mobility of the plate strip along with the analytical result from 0. It is clear that the numerical result agrees well with the analytical one for the parameters given. With the numerical parameters included in the calculation, the numerical model has errors in amplitude less than 1% compared with the analytical result while differences of up to 0.02 radians (1.15 degrees) in the phase occur as shown in Figure 4.2 .

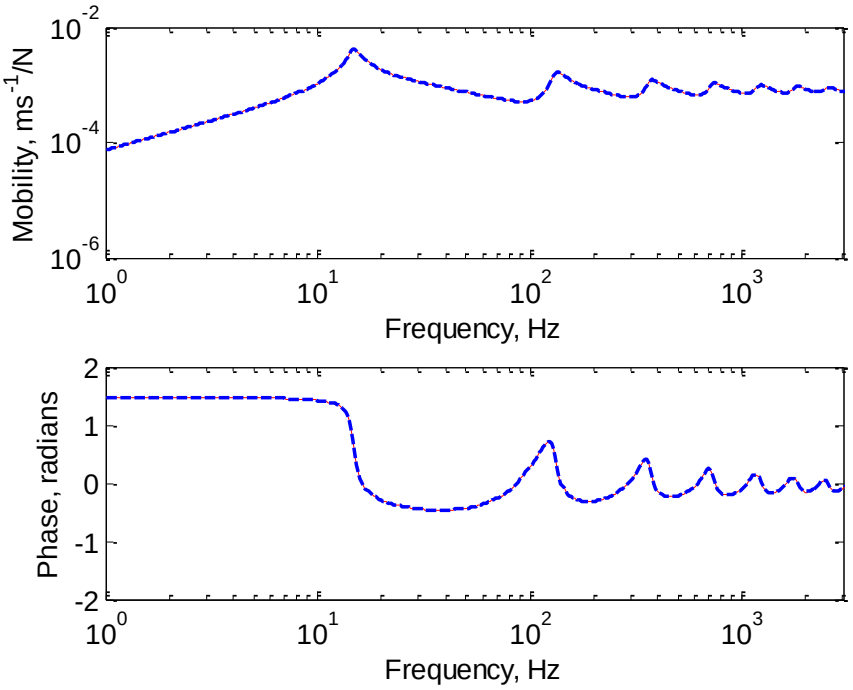

Figure 4.1. Mobility of the plate strip due to force excitation at $\left(0, l_y/2\right)$ calculated using WFE model compared with analytical result (— numerical; - - - analytical).

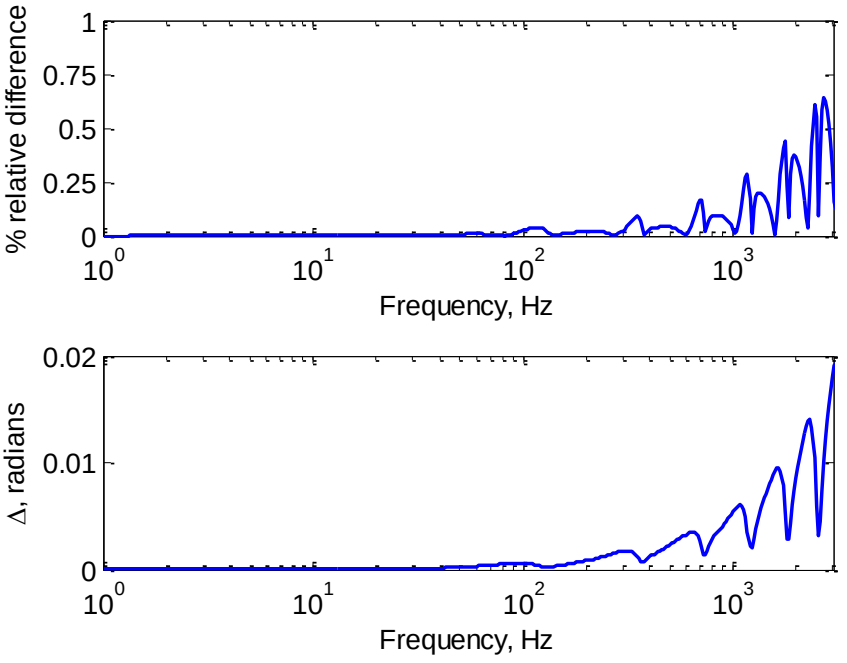

Figure 4.2. Relative percent difference of mobility amplitude and difference of phase in radians between numerical result and analytical one.

Figure 4.3 presents the predicted dispersion curves found from the free wave solutions for the undamped plate strip. Some mode shapes are also illustrated for particular cut-on frequencies. It is clear that the peaks found in the mobility are strongly related to the cut on of various waves.

In this figure, curves A and B are coupled longitudinal and shear waves resulting from in-plane displacement of the plate. These are not considered further here as this study is mainly devoted to the investigation of radiated power and sound transmission for lightweight structures. For these cases, the bending waves impose the largest normal displacement on contiguous fluid. Hence in terms of fluid-structure interaction, they are of most relevance.

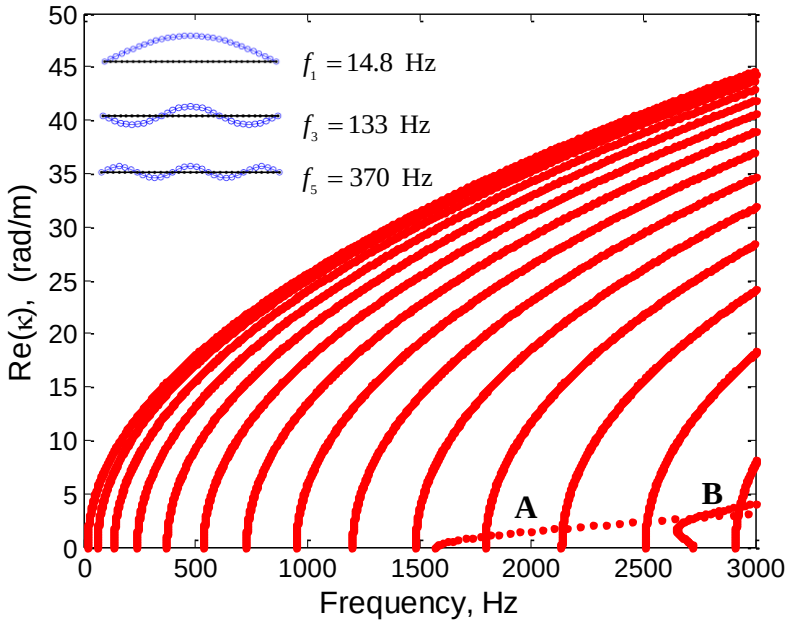

Figure 4.3. The predicted dispersion curves of a simply-supported plate strip and particular mode shapes.

Compared with the analytical results (see Figure 2.2), the discrepancy in cut-on frequency is less than 1%, as shown in Table 4.2. This discrepancy increases with increasing frequency, indicating that the element density used in the model becomes less sufficient to cover the actual structural wavelength at higher frequencies.

Table 4.2. Cut-on frequency f_m: comparison between numerical results and analytical ones.

m	f_m numerical	f_m analytical	% difference
1	14.8	14.8	0
2	59.2	59.2	0
3	133	133	0
4	237	237	0
5	370	370	0
6	533	533	0
7	725	725	0
8	947	947	0
9	1199	1198	0.08
10	1480	1479	0.07
11	1792	1790	0.10
12	2133	2130	0.14
13	2505	2500	0.20
14	2908	2899	0.30

4.1.1 Effect of element size

The required number of elements increases as frequency increases. As a rule of thumb, six finite elements or more are normally required per wavelength [88], although the element shape function also affects the accuracy. It has been seen that by including 30 elements in the model, the numerical result shows a good agreement with the analytical result up to 3 kHz. From Figure 4.3, it can be seen that at 1500 Hz 10 waves have cut on. The 10^{th} wave has 5 wavelengths across the width so that using 30 elements in the model gives 6 elements per wavelength at this frequency. By 3 kHz 14 waves have cut on and there are only 4 elements per wavelength. Table 4.3 compares the mobility results from WFE based on the residue calculus method with the analytical ones at some example frequencies. Even at 3 kHz the agreement is within 0.3% in magnitude, as shown in Table 4.4. Reducing the mesh to 10 elements, it can be seen that the results are much worse. This coarser mesh is sufficient up to 500 Hz where the error is less than 2% for the amplitude and 3 degrees for the phase. At this frequency it corresponds to 4 elements per wavelength. Hence, the results at higher frequencies are not strictly valid with this mesh.

Table 4.3. Mobility comparison based on analytical results and numerical ones based on residue calculus.

Frequency (Hz)	Analytical		WFE Residue calculus			
	Magnitude ($ms^{-1}N$)	Phase (degrees)	Magnitude ($ms^{-1}N$)		Phase (degrees)	
			30 elements	10 elements	30 elements	10 elements
1	7.402×10^{-5}	84.27	7.402×10^{-5}	7.397×10^{-5}	84.27	84.27
10	1.052×10^{-3}	81.52	1.052×10^{-3}	1.052×10^{-3}	81.52	81.52
100	5.287×10^{-4}	15.73	5.287×10^{-4}	5.268×10^{-4}	15.73	15.19
500	7.842×10^{-4}	-12.83	7.844×10^{-4}	7.969×10^{-4}	-12.88	-15.11
1000	7.194×10^{-4}	-5.73	7.196×10^{-4}	7.430×10^{-4}	-5.87	-12.13
3000	7.645×10^{-4}	-4.87	7.666×10^{-4}	8.427×10^{-4}	-5.45	-19.17

Table 4.4. Relative error of numerical results compared with analytical results for certain frequencies.

Frequency (Hz)	Relative error			
	Magnitude (%)		Phase (degrees)	
	30 elements	10 elements	30 elements	10 elements
1	0	0	0	0
10	0	0	0	0
100	0	0.36	0	0.54
500	0.03	1.62	0.05	2.28
1000	0.03	3.25	0.14	6.40
3000	0.30	10.2	0.58	14.3

4.1.2 Effect of wavenumber range and step size on accuracy of mobility calculation

When the rectangle method is used, the calculation process experiences truncation in the wavenumber domain. In order to determine correct integration parameters, the results of this approach are compared with the residue calculus ones. They are used as the reference here as they include the same effects of discretization. The comparison is therefore limited to the effect of the integration method. Various wavenumber ranges and step sizes are considered. The maximum wavenumbers and step sizes are deliberately

designed by considering them as multiples of the free bending wavenumbers k_B, as defined in Chapter 2, at the corresponding frequency.

This approach allows a more general conclusion to be reached about how many wavenumbers should be included in the calculation. The error is obtained from comparison between the numerical results based on the rectangle method and the residue calculus one, defined as

$$\text{dB error} = 20\log_{10}|Y|_{\text{rectangle}} - 20\log_{10}|Y|_{\text{residue}} \tag{4.1}$$

The residue calculus results are given in Table 4.3 above. The wavenumber range and step size required to achieve an error less than 1 dB or 0.1 dB can be observed from Table 4.5. Note that the required maximum wavenumber and step size are compared to the real part of the free bending wavenumber at the corresponding frequency in order to get a non-dimensional maximum wavenumber and step size.

Some prominent features can be deduced from Table 4.5. Firstly, for low frequencies a high maximum wavenumber ratio is needed while a lower one is sufficient for mid and high frequencies. Secondly, a large step size ratio seems to be acceptable for low frequencies but as frequency increases a smaller step size ratio is required, particularly for mid frequencies. Therefore, the largest number of integration points is found in the mid frequencies. Thirdly, as expected, in order to achieve 0.1 dB error or less, a higher maximum wavenumber ratio and a smaller step size ratio are required than for 1 dB error.

Table 4.5. Wavenumber ranges and step sizes required for 1 dB error and 0.1 dB error[5].

Frequency (Hz)	Re(k_B)	1 dB error		0.1 dB error	
		$\frac{\kappa_{\max}}{\text{Re}(k_B)}$	$\frac{\Delta\kappa}{\text{Re}(k_B)}$	$\frac{\kappa_{\max}}{\text{Re}(k_B)}$	$\frac{\Delta\kappa}{\text{Re}(k_B)}$
1	0.816	≥ 5.5	≤ 2.75	≥ 18	≤ 2.25
10	2.579	≥ 1.5	≤ 0.75	≥ 4.5	≤ 0.375
100	8.156	≥ 1.25	≤ 0.1	≥ 3.75	≤ 0.12
500	18.24	≥ 1.0	≤ 0.05	≥ 2.0	≤ 0.03
1000	25.79	≥ 0.9	≤ 0.04	≥ 1.5	≤ 0.04
3000	44.67	≥ 0.9	≤ 0.04	≥ 1.5	≤ 0.02

[5] In practical calculation , the wavenumber range and step size is implemented:
$-(\kappa_{\max} - \Delta k/2) : \Delta k : (\kappa_{\max} - \Delta k/2)$

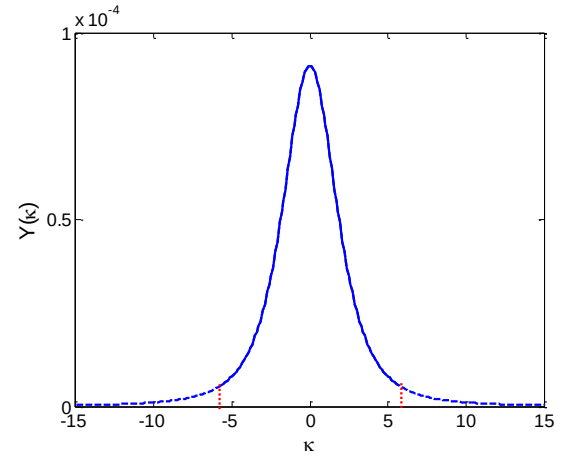

(a)

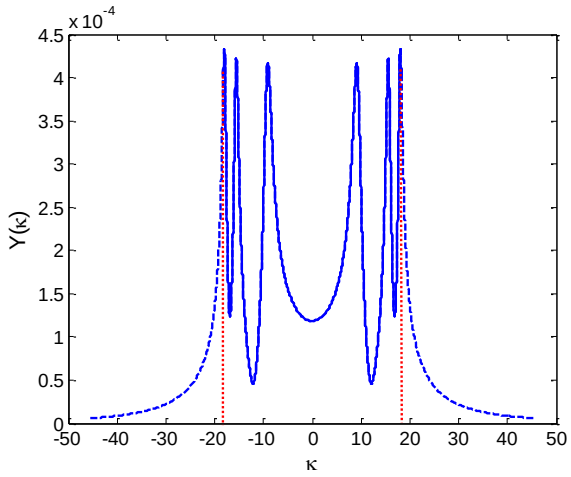

(b)

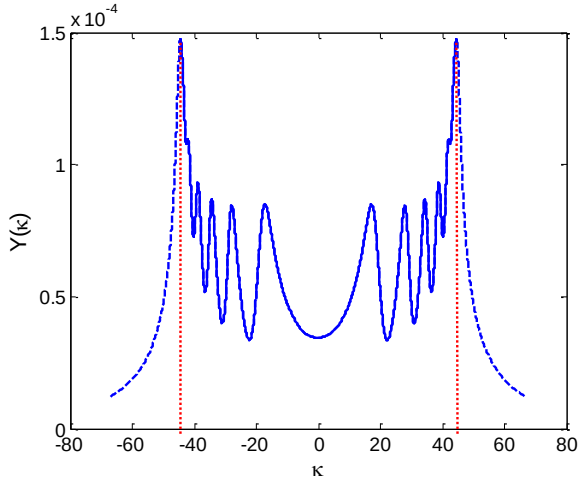

(c)

Figure 4.4. Mobility spectrum of the plate strip at (a) 1 Hz, (b) 500 Hz and (c) 3 kHz to represent low, mid and high frequencies respectively, with associated bending wavenumber of 0.8169, 18.27 and 44.74 rad/m (— range required for 1 dB error; --- 0.1 dB error; • • • border for the region required for 1 dB error).

To clarify the effect of the wavenumber range included in the calculation, Figure 4.4 portrays the mobility spectrum in the wavenumber domain for three example frequencies based on Eq. (3.26) for $\eta = 0.1$. From this figure, it is clear that a wider range of wavenumbers relative to the bending wavenumbers is required at the low frequencies due to the presence of a single broad lobe. Therefore, the tail of the curve gives an important contribution to the total integral at low frequency. Meanwhile, for the mid and high frequencies a ratio of 1 is sufficient to cover most of the lobes and achieve an agreement within 1 dB. The tail of the spectrum should be included at these frequencies in order to achieve agreement within 0.1 dB. In terms of absolute step size, the mid frequencies need a smaller step size than at low and high frequencies because the peaks are quite close together and have a narrow bandwidth. It can be expected that for lower damping a smaller step size would be required.

4.2 Sound radiation of a plate strip

The radiated sound power has also been calculated using the coupled Wavenumber Finite Element-Wavedomain Boundary Element (WFBE) method. Figure 4.5 illustrates the WFBE model schematically. The WFE parameters are the same as for the WFE model used in the mobility calculation in section 4.1 where 30 elements are used to cover 1 m wide plate strip and can cover the highest frequency up to 3 kHz. However, it is important to compare the model configuration with the acoustic wavelength as the structural wavelength is larger than this above the critical frequency of 2.0 kHz. In fact, compared with the acoustic wavelength there are only 2 elements per wavelength. To the WFE model is added a WBE model developed for an exterior problem using 30 four-noded cubic elements in all on the wetted surface. The first and last node of each element have the same coordinates as the WFE model as required in a coupled model, although the boundary elements have two intermediate nodes as well.

The analytical model used for comparison includes an infinite rigid baffle beyond the plate strip. In order to implement a rigid baffle in the numerical model, as will be shown, this must comply with the following procedure: (i) the WBE sub-model should be included as an extended boundary element mesh on either side of the plate strip with a width of at least half of the acoustic wavelength under consideration; (ii) the WBE sub-model should be closed. The nodal surface velocity V_0 is set equal to zero for all nodes outside the

wetted surface. For the current numerical model, a 1 m finite rigid baffle is included beyond both edges of the plate strip, unless otherwise stated, and this WBE mesh is 0.1 m thick. The effect of the size of this mesh is discussed in section 4.2.2. Note that the rear of the plate strip is not considered to radiate sound.

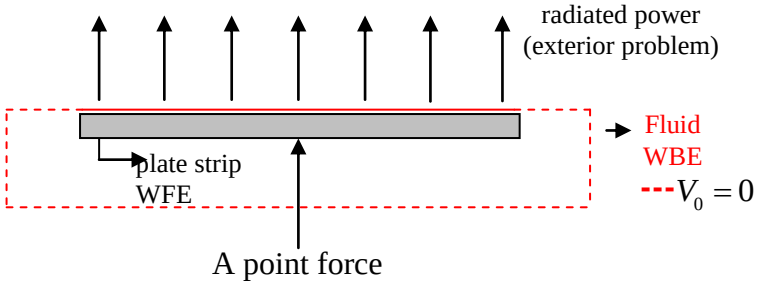

Figure 4.5. Schematic illustration of the WFBE model.

The sound power radiation from the plate strip due to the point force excitation was calculated using Eq. (3.42). Figure 4.6 presents the radiated power for excitation at the centre (0, $l_y/2$) from the numerical and the analytical models. Some discrepancies can be observed from this figure, especially at low frequencies and around 2 kHz which corresponds to the critical frequency f_c. It is likely that the finite rigid baffle length of the numerical model affects the results in the low frequency region. This effect will be studied further in the next section. Meanwhile, the difference around f_c is potentially due to difficulties in the implementation of the plate-fluid coupling in WANDS, also discussed later.

It can also be seen that a lower radiated power is obtained, where the result is not in agreement with that of the analytical model, when an open BE mesh is used. This indicates that the inclusion of a closed BE mesh in the numerical model is of importance to get a correct result. To use an open BE mesh correctly, the indirect boundary element method as in [89, 90] could be considered in future works as part of improvements to the WANDS software.

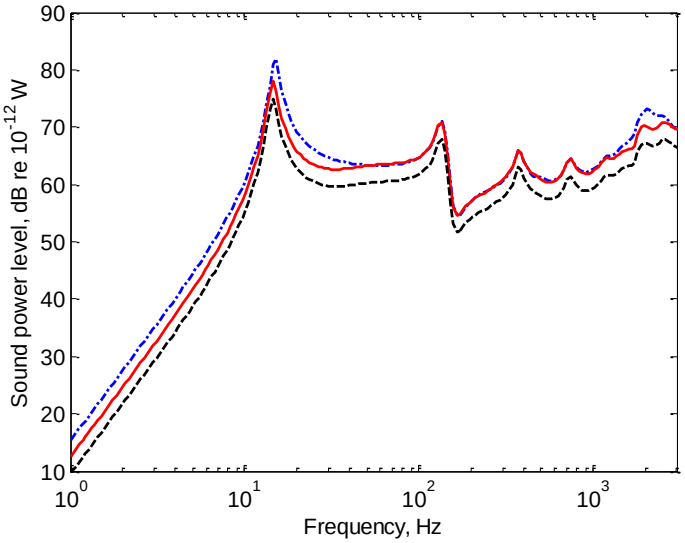

Figure 4.6 Comparison of the radiated power between numerical result and analytical one for excitation at the middle (0, $l_y/2$) (— numerical model with closed BE mesh; --- numerical model with open BE mesh; – • – analytical model).

4.2.1 Effect of baffle width

The analytical results are based on a plate strip set in an infinite baffle. In the WFBE results, this is approximated by a finite width baffle. The baffle width incorporated in the model affects the accuracy of the results, especially at low frequency. This is demonstrated here by varying the baffle width and then comparing the results with those of the analytical model. The baffle width is varied to be a 0, 0.2, 1 and 2 metre extension from either edge of the plate strip. In other words, the length of the WBE sub-model on the radiating side for the 1 metre plate-strip will be 1.0, 1.4, 3.0 and 5.0 metre in total. Compared with the acoustic wavelength at a frequency of 34 Hz, these baffle lengths correspond to 0.1, 0.14, 0.3 and 0.5 times the acoustic wavelength respectively.

The results are shown in Figure 4.7. It is clear that the sound power level results from the numerical model become closer to the analytical ones when the baffle width increases. Thus a 1.4 m width baffle gives good agreement between the numerical results and the analytical ones at frequencies above 115 Hz while the agreement is extended down to 35 Hz for a 5 m width baffle. In contrast, the numerical model does not quite agree with

the analytical one for any frequencies when the baffle is not present where the BE mesh is only 1m wide.

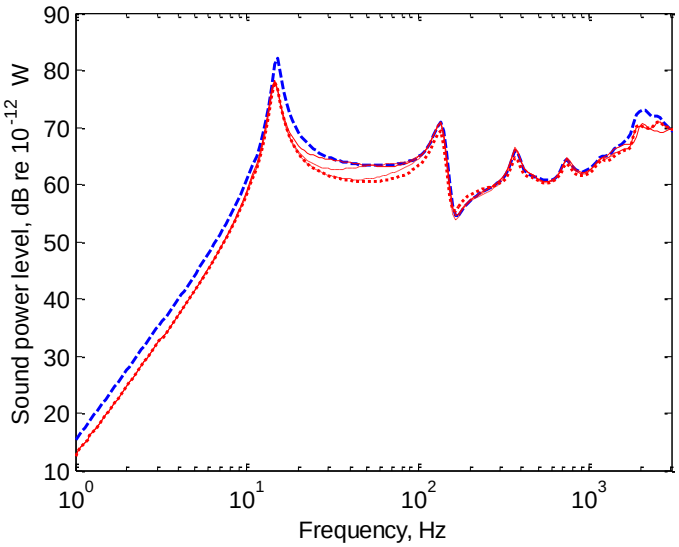

Figure 4.7 Radiated sound power calculated using the numerical model with various baffle width on each side of the plate and compared with those obtained with the analytical model (---analytical model; — numerical model with baffle width of 2 m; - - - baffle width of 1 m; – • – baffle width of 0.2 m; • • • no baffle exists)

These effects can be seen more clearly in Figure 4.8 which shows the level difference, defined as

$$\Delta W_{rad} = 10\log_{10}\left(\frac{W_{rad,numerical}}{W_{rad,analytical}}\right) \tag{4.2}$$

The value of ΔW_{rad} is approximately -3 dB at low frequency and reduces to 0 dB above a certain frequency. A large difference is found around at 15 Hz which is the first cut-on frequency. However, it should be noted that the fluid loading is neglected in the analytical model while this is considered in the numerical one. Hence, the difference greater than -3 dB at this frequency is caused by the fluid loading as well as the baffle width effect. This causes the peak at the first cut-on frequency to shift in frequency, due to mass loading. Its damping is also affected. Another large difference found at 2 kHz is related to the plate-fluid coupling issue at the critical frequency rather than the baffle width effect.

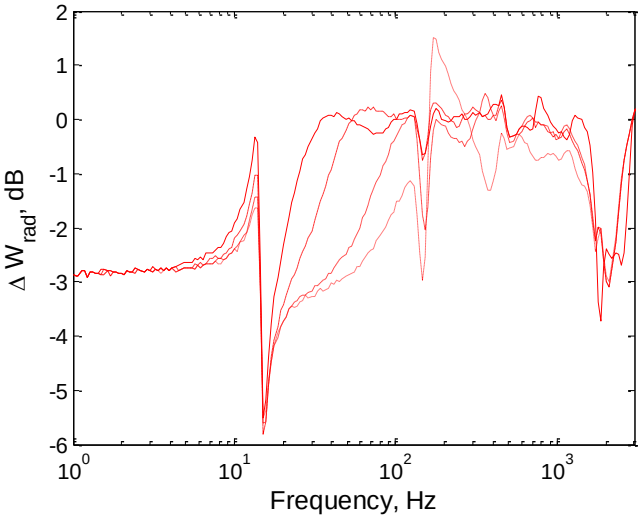

Figure 4.8. The baffle width effect on the radiated power in terms of radiated power differences relative to the analytical model (— baffle width beyond plate of 2 m; ---- 1 m; – • – 0.2 m; ••• no baffle exists)

Considering these indications, it can be further concluded that the lowest frequency that can be covered by the model depends on the baffle width. The relation between the lowest frequency limit and the total width of the WBE mesh is summarized in Table 4.6. It can be seen that the lowest frequency limit reduces with increasing baffle width. Therefore, the relation between the approximate lowest frequency of validity and the baffle width can then be shown to be

$$f_{ll} = \frac{c}{\lambda_{ll}} = \frac{c}{2l_b} \tag{4.3}$$

where f_{ll} is the lowest frequency limit and l_b is the total width of the WBE sub-model on the radiating side. Thus, in order to allow the numerical model to be used reliably down to 15 Hz, for example, l_b would need to be around 11 m. Accordingly, the 1 m wide structure would require a 5 m extension of the BE mesh beyond the structural width at both sides.

Table 4.6. Effect of baffle width on the lowest frequency limit for 1 m width structure

Baffle width (m)	Total width (m)	f_{ll} (Hz)
0.2	1.4	123
1.0	3.0	57
2.0	5.0	34

4.2.2 Effect of enclosed boundary thickness

Great care should be taken to avoid problems associated with thin bodies when developing the enclosed boundary element mesh. Otherwise, the Helmholtz integral equation in Eq. (3.31) becomes near-singular as the mesh of the surface comes too close to that of the opposite surface (or line). Under such circumstances, the required jump in the double-layer potential is not generated as both surfaces collapse to the same surface so that the pressure is zero when the field point and source point are at the same surface. Moreover, the terms $\tilde{\psi}\left(\partial\delta\tilde{\psi}^{*}/\partial\mathbf{n}\right)$ of the Helmholtz integral equation is also zero as the normal velocities are equal and opposite on each surface. Consequently the presence of the singularity is never detected by the computer program so that the Boundary Element method produces unreliable results [65].

Specifically, this can be overcome by a thin-body integral formulation, e.g. as demonstrated in [65, 91]. In this study, however, the WBE model in WANDS is tested using different boundary thicknesses in order to avoid the problem. For this, four different enclosed boundary thicknesses are used to test the WBE model in WANDS. For the WBE thickness values of 6 mm, 15 mm, 30 mm, 66 mm and 100 mm are selected. The effect of the boundary thickness is discussed in terms of the radiated power due to a point force.

Figure 4.9 shows the effect of thickness of the closed boundary WBE mesh. The results are identical for all thicknesses under consideration except for 6 mm where a 2 dB lower radiated power is found at low frequency. Therefore, the numerical model will produce good results if the thickness is 15 mm or more.

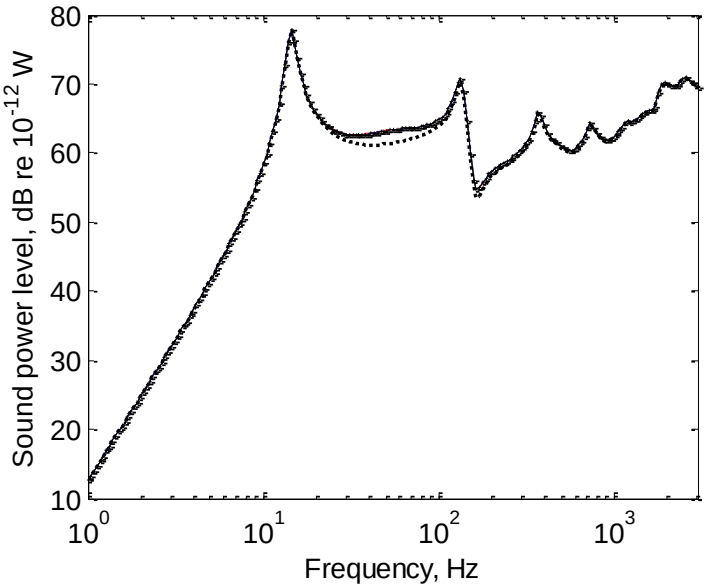

Figure 4.9. Effect of enclosed boundary mesh thickness (— 100 mm; - - - 66 mm; – • – 30 mm; –+– 15 mm; • • • 6 mm).

4.3 Sound transmission loss of a plate strip

To calculate the transmission loss for the sound transmission problem, the numerical model is similar to that used for the radiated power calculations as discussed in section 4.2. The main difference exists in the form of excitation: in the transmission loss case, a plane acoustic wave is used instead of the point force, as shown in Figure 4.10. The numerical model is developed using a coupled WFBE model consisting of one WFE region representing the plate strip structure and two WBE-fluid regions for modelling the sound pressure field on both sides of the structure. The wavenumbers of the plane waves are governed by the incidence angle, which depends on the elevation and azimuthal angles for a 3-D problem. Moreover, 50 cubic plate elements are now used to cover the 1 m width in order to extend the result to a higher frequency. Under such circumstances, the model is expected to be acceptable up to 8.5 kHz at which it corresponds to 4 elements per structural wavelength (see section 4.1.1).

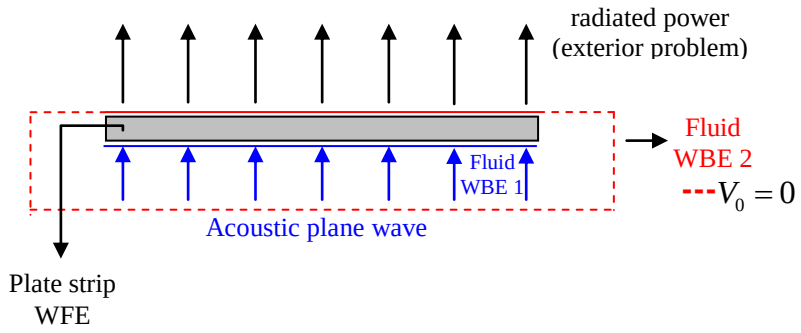

Figure 4.10. Schematic illustration of the plate strip excited by the acoustic plane wave.

For simplicity, the model differs from the WBE model of the radiation problem as the incoming plane waves are realized by an open boundary mesh. This causes differences in the scattered field on the source side. In order to assess the effect of the open boundary mesh, the result obtained is compared with that of the closed boundary one using the following formula:

$$\Delta TL = 10\log_{10}\left(\frac{\tau_{\text{closed boundary}}}{\tau_{\text{open boundary}}}\right), \qquad \text{dB} \qquad (4.4)$$

The result is presented in Figure 4.11. It is clear that the highest difference occurs at the first cut-on frequency, 14.8 Hz, at which a difference of 2.5 dB is found. As the frequency increases, the level difference reduces and it is less than 0.5 dB for frequencies above 40 Hz. This behaviour is caused by fluid loading at low frequencies which becomes negligible at higher frequencies. Hence the open boundary used in this study will not affect the accuracy of the numerical results for the current case by more than 0.5 dB for frequencies above 40 Hz.

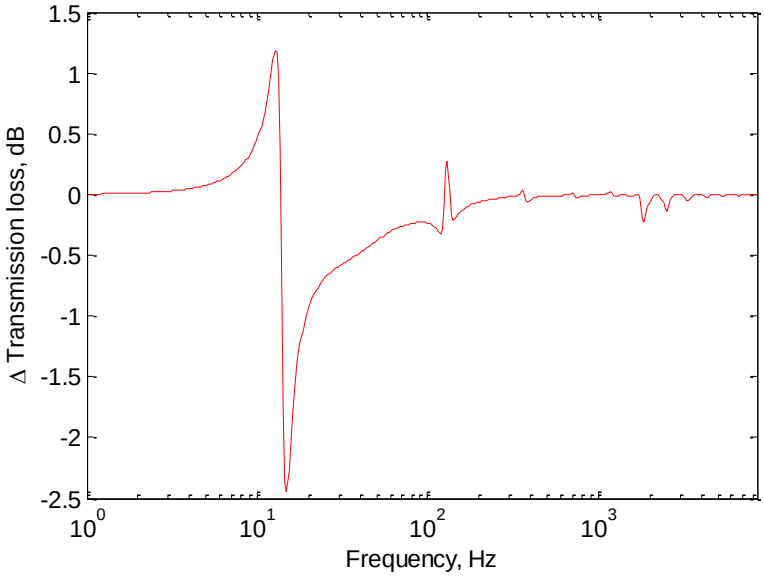

Figure 4.11. The difference in the transmission loss between open boundary and closed boundary mesh on the source side.

4.3.1 Normal incidence case

Figure 4.12 presents a comparison between the numerical result and the analytical one for normal incidence. Note that the analytical model for this case uses $W_{rad\,2}$ in Eq. (2.79) instead of Eq. (2.80) so that the cross-terms between different mode orders are included. The mass-law result is also shown for comparison.

First of all, the trend of the transmission loss in the numerical results agrees well with the analytical one. For the case under consideration, the transmission loss follows the mass law trend as frequency increases, especially above 100 Hz. Below 50 Hz, a discrepancy occurs due to the finite baffle width (see section 4.2.1); hence it will always appear below some frequency depending on the assumed baffle width considered in the numerical model. Apart from this, the numerical result agrees well with the analytical one. Various peaks and dips are seen corresponding to the cut-on frequencies of odd modes. The even modes are not excited in this case of normal incidence.

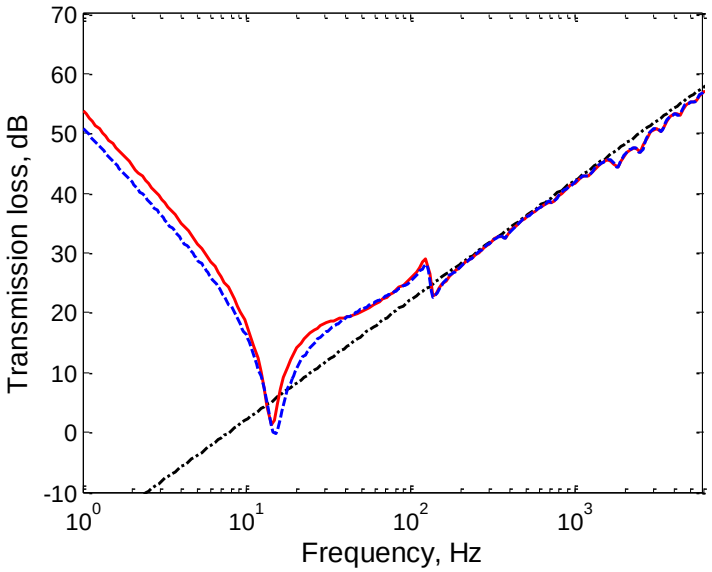

Figure 4.12. Comparison of transmission loss of the plate strip based on the numerical model and the analytical one (— numerical model; - - - analytical model; – • – mass law).

4.3.2 Oblique incidence case

A further comparison can be carried out for an oblique incidence angle. The plate strip is subject to a plane wave impinging on it at a certain angle to the normal. For the plate strip case, it is possible to construct the incident angle about the x axis or y axis, where each of them would affect the transmission loss behaviour differently due to the nature of the plate strip dimensions. Figure 4.13(a) shows the result for oblique incidence at an angle of 45º about the $x-$axis and Figure 4.13(b) is the result for the same elevation angle but about the $y-$axis. Both cases show a good agreement with the analytical result, with the dips in the curves corresponding to the cut-on frequency behaviour. Due to the finite width of the plate strip, the modal behaviour is more pronounced for the former case, where even modes as well as odd modes are excited, than it is for the latter one.

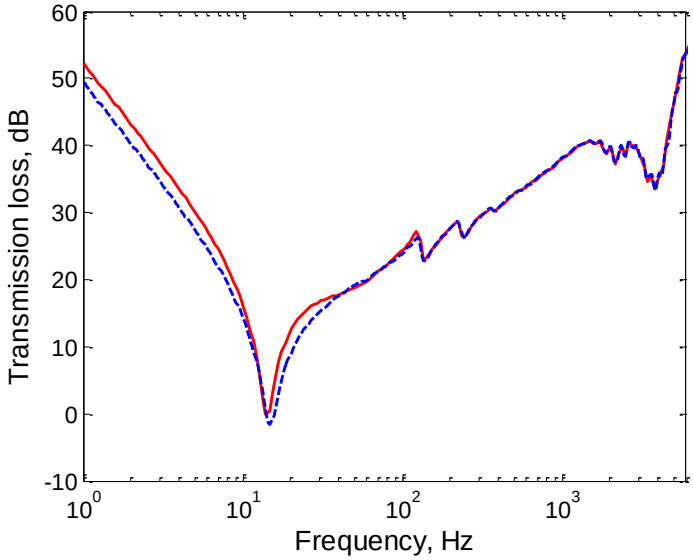

(a)

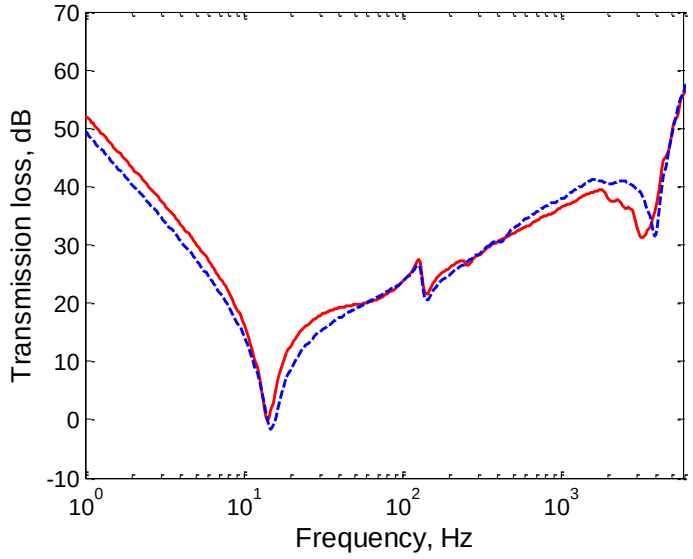

(b)

Figure 4.13. Comparison of transmission loss of the plate strip and the analytical model for oblique incidence case: (a) $\theta = 45^\circ$; $\varphi = 90^\circ$ (b) $\theta = 45^\circ$; $\varphi = 0^\circ$ (— numerical model; - - - analytical model).

Above the critical frequency, the coincidence frequency calculated by the numerical model agrees with that of the analytical model for the former case. However, it is slightly lower than the analytical one for the latter case. This unmatched coincidence frequency would lead to an erroneous result for the diffuse sound field in which the plane waves from all incident angles are evaluated in the transmission loss calculation. This discrepancy is believed to be related to the errors found in the sound radiation result

around the critical frequency (see Figure 4.6). Moreover, it has been found (not shown here) that the error increases as the incidence angle is increased.

4.3.3 Effect of plate thickness

Figure 4.14 shows results for two different plate thicknesses, 6 mm and 9 mm, for normal incidence. The numerical results show a good agreement with the analytical ones. The increasing transmission loss is as expected and the dip related to the first cut-on frequency shifts upward with increasing thickness.

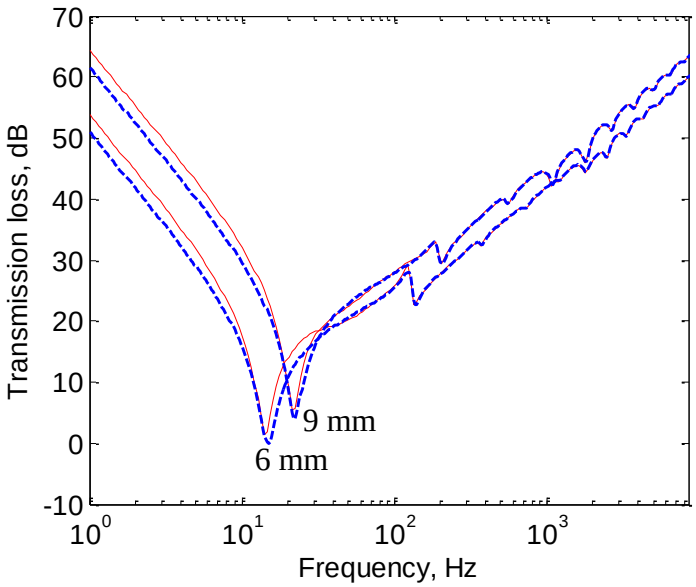

Figure 4.14 Comparison of transmission loss of the plate strip based on the numerical model and analytical model for the case of the different thickness (— numerical model; --- analytical model).

4.3.4 Effect of damping loss factor

Figure 4.15 shows results for a smaller damping loss factor η of 0.01, again for normal incidence. A good agreement is found with the analytical model, with dips in the transmission loss at the various (odd) cut-on frequencies.

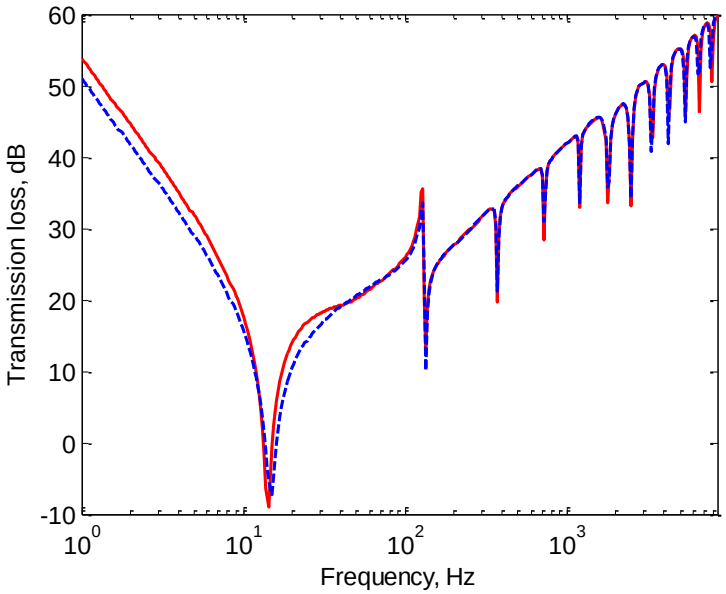

Figure 4.15. Comparison of transmission loss of the plate strip and the analytical model for lower damping loss factor $\eta = 0.01$ (— numerical model; - - - analytical model).

4.3.5 Diffuse sound field

In the previous analysis, the resulting transmission loss was calculated for excitation by an acoustic plane wave. Now the structures are subjected to a diffuse sound field excitation and the sound pressure level is calculated using the procedure described in section 3.3.2. For this, 9 incident angles ϕ about the x axis and 18 incidence angles χ are considered with an upper angle of 90º. Figure 4.16 presents a comparison of transmission loss from the numerical model and analytical one under a diffuse sound field excitation. The results of the numerical model are in a good agreement except around and above the critical frequency. Around the critical frequency, the WFBE model has a higher transmission loss than the analytical one while the dip associated with the critical frequency occurs at 2179 Hz for the numerical model instead of 2034 Hz as shown by that of the analytical model. Moreover, above this frequency the transmission loss of the plate element model starts to deviate and has lower values than the analytical results. Therefore, it is clear that the numerical model gives erroneous results in this frequency region.

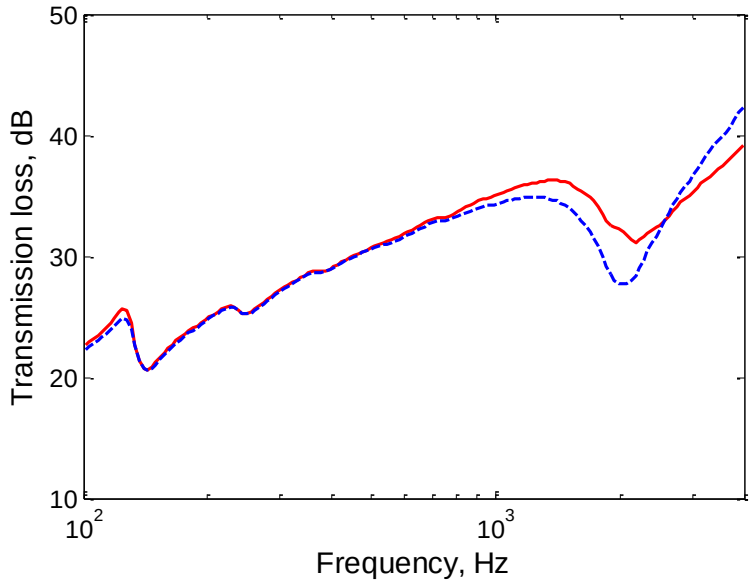

Figure 4.16. TL comparison of the numerical models and the analytical model under a diffuse sound field excitation (— numerical model using plate elements; --- analytical model).

4.4 Substitution of plate elements by solid elements

All cases considered in the previous sections will now be repeated using a model assembled using solid finite elements instead of plate elements. The results obtained will be compared with those of the plate elements and the analytical model. All procedures and formulae used for the plate element case are again used for calculating the results with the solid elements, hence the description of that is not repeated in this section. Furthermore, the material properties are the same as used for the plate element model (see Table 4.1).

To realize the WFE model using solid elements, eight-noded quadrilateral elements are used with quadratic polynomial shape functions. Three-noded boundary elements are used for the WBE fluid region with a 1 metre extension on both sides beyond the length of the plate strip in order to represent the rigid baffle. Hence the width of the BE mesh at the radiation side is 3 m in total. The elements at the edges are restrained in three directions at their mid-side points to impose simply supported boundary conditions, as shown in Figure 4.17. The effect of restraining the nodes is considered in detail in section 4.4.2.

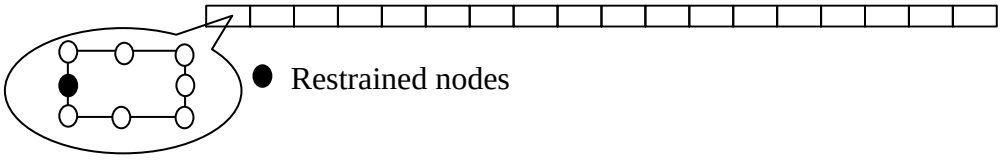

Figure 4.17. Restrained node for simply supported boundary conditions in the solid element model.

4.4.1 Element density

The element density used for the plate elements, which was 30 elements for 1 m width plate strip, is not sufficient to produce the same results up to 3 kHz for the case of the solid elements. After increasing the density up to 50 elements, the dispersion curves of this model become closer to those of the plate element model, as shown in Figure 4.18. This indicates that it requires seven elements per wavelength if the quadrilateral type of solid element is used while four elements per wavelength are sufficient for the case of the plate elements. This element density gives 0.3% difference in cut-on frequency relative to the plate element result and 0.6% compared with the analytical results at around 2.9 kHz (which is the 14th cut-on frequency). Hereafter, this element density is implemented for all comparisons considered except for particular cases where a higher maximum frequency is required.

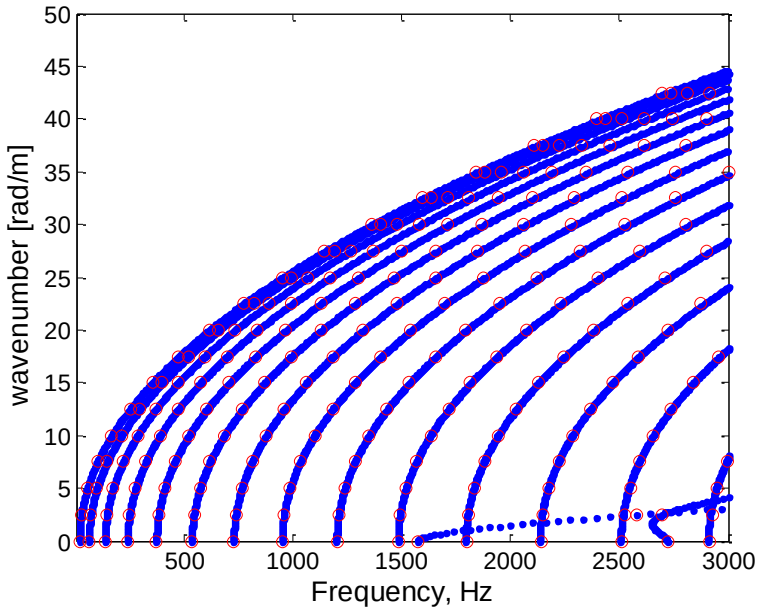

Figure 4.18. Dispersion curve comparison of the plate element model and the solid element one (● Plate element ; ○ solid element)

4.4.2 Effect of restrained nodes

Restrained nodes are of importance in realizing certain boundary conditions in the numerical model. In order to see the effect on the boundary conditions, three different configurations of restrained nodes of the solid elements are considered. This can be seen from Figure 4.19 where only a corner node is restrained in configuration (a), a midside node for configuration (b) and combination of both the corner and midside node for the configuration (c). In each case all three translations are restrained; unlike plate elements, solid elements do not have rotational degrees of freedom.

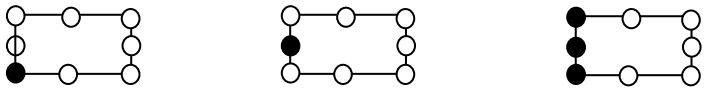

Figure 4.19. Restrained nodes position of an solid element (● restrained node)

The effect of the restrained node position is compared in terms of dispersion characteristics in Figure 4.20 and the cut-on frequencies corresponding with each configuration are listed in Table 4.7. Considering the relationship of the cut-on frequencies and the boundary conditions, it can be inferred that the cut-on frequencies of configuration (b) correspond to the simply supported boundary conditions. The corresponding analytical results are $\left(m\pi/l_y\right)^2\left(D/\rho h\right)^{1/2}$ with l_y the panel width, D bending stiffness, ρ structural density and h structural thickness. Meanwhile, configuration (c) can be inferred to correspond to the clamped boundary condition in which the cut-on frequencies equal approximately $\left[\left(m+1/2\right)\pi/l_y\right]^2\left(D/\rho h\right)^{1/2}$. For configuration (a) the results are affected by coupling with the longitudinal waves due to the asymmetrical constraint.

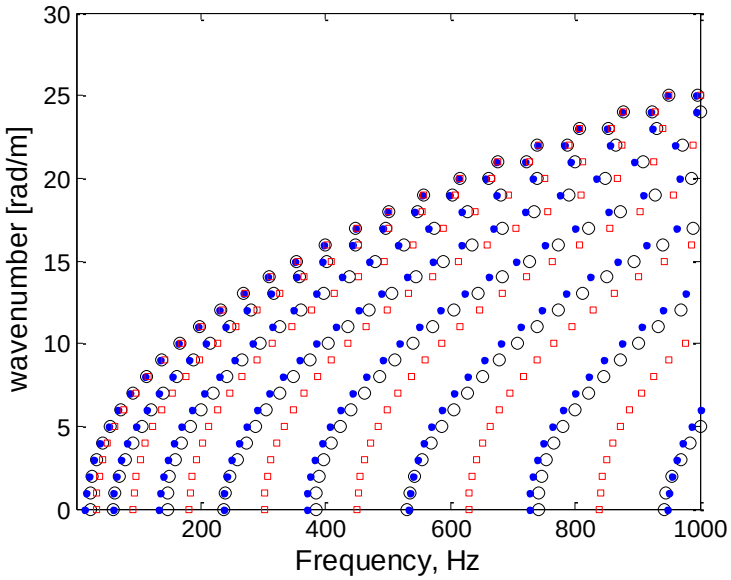

Figure 4.20 Dispersion curve comparison of configurations in Figure 4.19 (○ configuration (a); ● configuration (b) ; □ configuration (c)).

Table 4.7. Cut-on frequencies f_m corresponding with configurations in Figure 4.19.

m	f_m (Hz)				
	Numerical			Theoretical	
	a	b	c	Simply supported	Clamped
1	23.6	14.8	33.3	14.8	33.3
2	59.3	59.2	92.4	59.2	92.4
3	146.5	133	181	133	181
4	237	237	302	237	300

4.4.3 Point mobility

A point force is applied at the centre of the plate strip at position $\left(0, l_y/2\right)$. In terms of amplitude, the mobility of the solid element model is in good agreement with that obtained by the plate element model as well as the analytical model, as shown in Figure 4.21. However, the differences are found to be greater at high frequencies; e.g. at 3 kHz it is found that the mobility amplitude of the solid model is 0.4% higher than the plate element model while its phase is 0.12 radian higher than the plate element model. Compared with the analytical model, differences of 0.7% for the amplitude and of 0.13 radian for the phase are found.

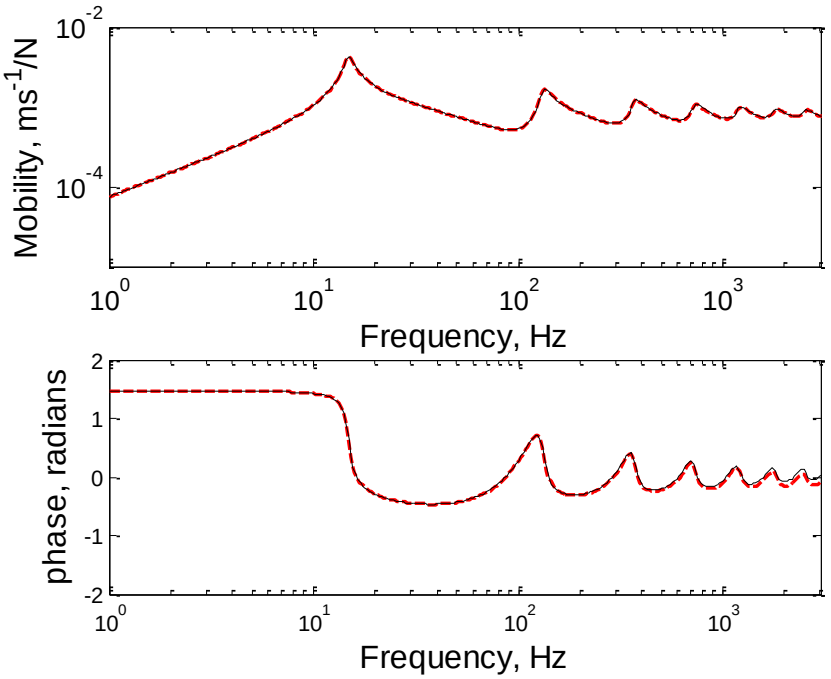

Figure 4.21. Mobility comparison of the solid element model and the plate element model (— solid element; - - - plate element; —•— analytical model).

4.4.4 Radiated sound power

It has been shown in section 4.2 that the plate element model result has a discrepancy in the radiated sound power around the critical frequency f_c. To re-evaluate the numerical model for this frequency region, the analytical results are also included along with the plate element model result. The comparison of these results for radiated sound power can be seen in Figure 4.22. It is clear that the solid element model produces a better result for the frequency range of interest, particularly around f_c, when the results are compared with those of the analytical model. At low frequency, below 50 Hz, both the numerical models produce around 3 dB lower radiated power than the analytical model as a consequence of the finite baffle width included in the models (see section 4.2.1).

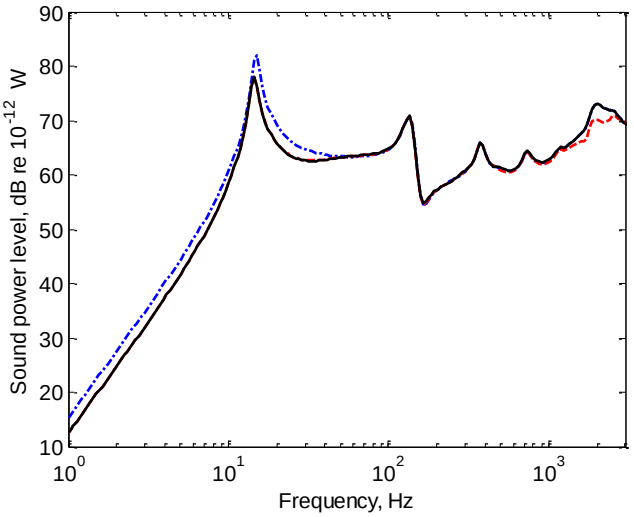

Figure 4.22. Radiated power comparison (— solid element; --- plate element; —•— analytical model).

Figure 4.23 presents the level difference of the radiated power between both the numerical models and the analytical one. It is clear that around the critical frequency a difference of up to 3 dB exists for the plate element model whereas the solid element model shows a difference of less than 0.2 dB in this frequency region. Apart from this frequency region, the difference between the numerical models and the analytical one at low frequencies is clearly due to the baffle width effect as found previously. The effect of fluid loading is again seen around the first cut-on frequency.

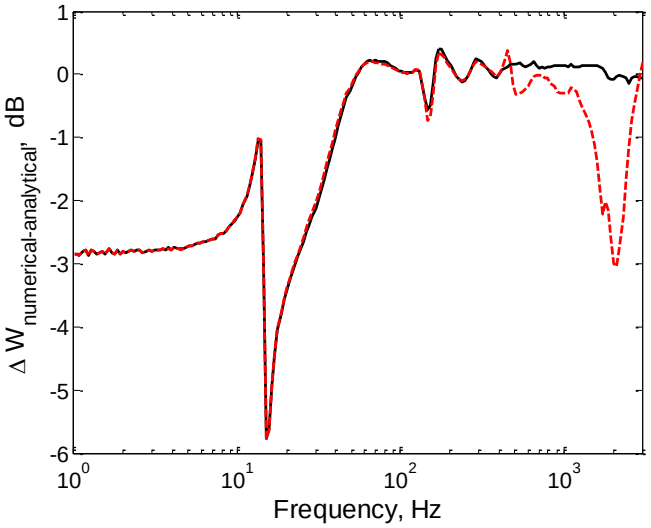

Figure 4.23. Radiated power level difference between the numerical model and the analytical one (— solid element model and analytical; --- plate element model and analytical).

Regarding the problem associated with the radiated power from plate elements at the critical frequency, it is believed that this is due to implementation of the plate-fluid coupling rather than fundamental errors in the WFBE method considering the mobility results in section 4.1 as well as an unpublished investigation of the Boundary Element implementation in WANDS which is found to work well for calculating radiated power of an oscillating cylinder[6].

4.4.5 Sound transmission loss

Next the sound transmission problem is considered using solid elements. To cover a higher frequency range up to 6 kHz, which is considered to be sufficient to include the coincidence region for oblique incidence with angle of 45°, the number of elements is increased to 70 elements covering 1 m width plate strip. At 6 kHz, there are 7 elements per structural wavelength and 4 elements per acoustic wavelength.

Figure 4.24 presents a comparison of the transmission loss for the solid element model, the plate element and the analytical one for the normal incidence case. At frequencies above 50 Hz, the results of the solid element model agree well with those of the plate element model and the analytical one. Meanwhile, the solid element model results agree with the plate element ones for all frequencies.

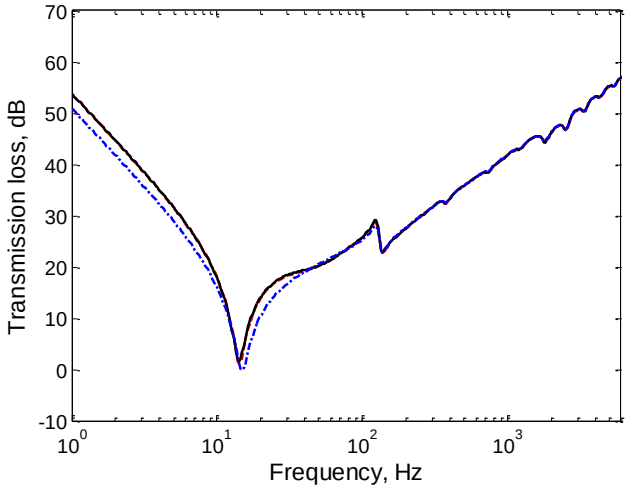

Figure 4.24. Transmission loss comparison of the model with solid element and plate element for normal incidence case (— solid element; --- plate element; —•— analytical model).

[6] Subsequent to the submission of the thesis the error in the plate element implementation has been rectified by Jungsoo Ryue

For the case of oblique incidence at an angle about the x axis, the results are shown in Figure 4.25(a). The solid element model generally produces promising results compared with the plate element model and the analytical one below the coincidence frequency at 4 kHz. Above this frequency, the transmission loss of the solid element model starts to deviate slightly from the plate element model and the analytical results. This indicates that the solid element model requires a higher element density to cover this frequency region. For the case of an incident angle about the y axis, as shown in Figure 4.25(b), it is clear that the solid element model results agree well with the analytical results whereas the plate element model results differ considerably below the coincidence frequency and at the coincidence frequency itself. Thus the discrepancy found for the plate elements appears not to occur for the solid elements.

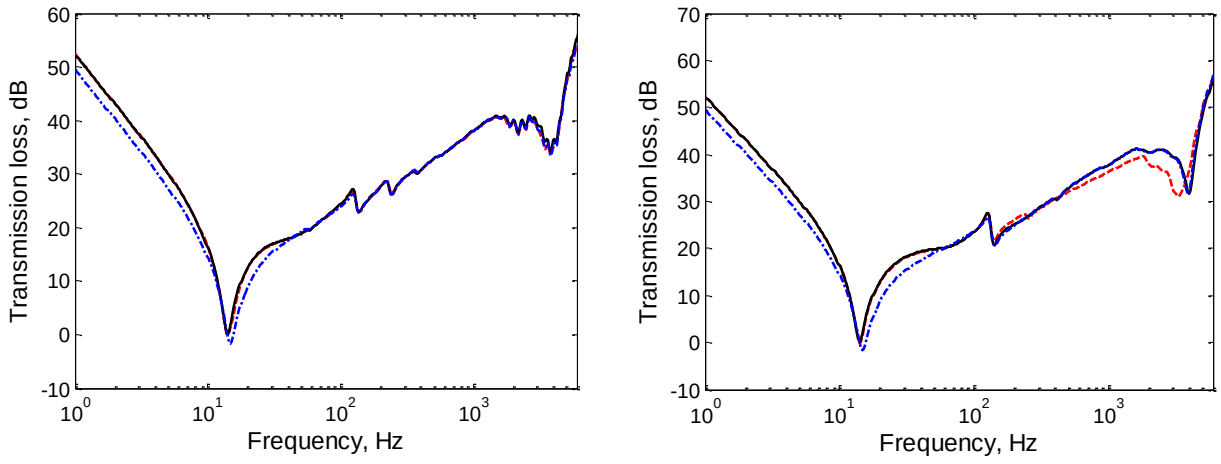

(a) (b)

Figure 4.25. Transmission loss comparison of the model with solid element and plate element for oblique incidence case: (a) at angle 45º about x axis; (b) at angle 45º about y axis (— solid element; --- plate element; —•— analytical model).

4.4.6 Diffuse sound field

As in section 4.3.5, the diffuse sound field is represented by an integral over a range of incident angles with an upper angle of 90° to represent full random incidence. These results are shown in Figure 4.26. From this, it can be seen that the solid element model gives results that are much closer to the analytical ones than the plate element model,

particularly around and above the critical frequency. This confirms the trends already observed in Figure 4.25.

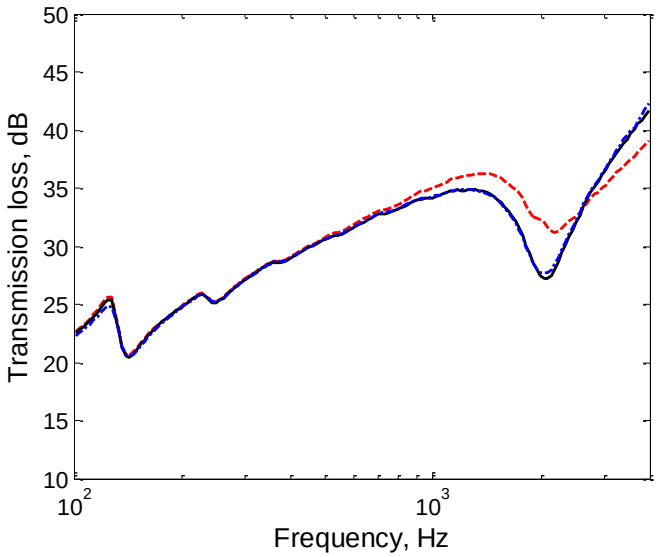

Figure 4.26. TL comparison of the numerical models and the analytical model under a diffuse sound field excitation (— solid element; --- plate element; – • – analytical model).

4.5 Summary

Comparisons of the numerical results and analytical ones were conducted to validate the WFBE method applied in this study and to determine under what circumstances the numerical model can be used to give accurate results. In terms of the mobility calculation a suitable wavenumber range and step size are determined in order to ensure errors are less than a certain value. This is expressed in terms of the maximum wavenumber ratio, relative to the associated free bending wavenumber of the plate. This study shows that the maximum wavenumber ratio decreases as frequency increases e.g. for 1 Hz $\kappa_{\max}/\mathrm{Re}(k_B) = 18$ while for 3 kHz $\kappa_{\max}/\mathrm{Re}(k_B) = 1.5$ in order to get results with an error of less than 0.1 dB.

Some practical aspects of implementing this method using the WANDS software should be borne in mind in order to obtain correct results. Firstly, the Waveguide Boundary Element (WBE) mesh should have a closed boundary rather than an open one. The thickness of the mesh should be determined carefully to avoid the thin body problem which causes misleading results. Secondly, to simulate a baffled situation a finite rigid baffle

should be included in the model by extending the width of the WBE fluid model beyond the width of the structure. The width of the finite rigid baffle is important in determining the accuracy of the numerical model results in comparison with the analytical ones, which are for an infinite baffle. The lowest frequency at which the numerical model results are still valid depends on the total width of baffle at the radiating side which should be at least half the acoustic wavelength. Thirdly, care should be taken in choosing the element type in the WANDS software. For the case of the waveguide structure considered in this study, the plate element type along with its coupling element to acoustic BE fails to calculate accurately the vibro-acoustic response of the plate strip although it gives good results for the mobility. It is found that the radiated sound power is incorrect in the critical frequency region and the sound transmission loss is incorrect around and above the coincidence frequency. Considering the mobility result, the current error found with plate elements is associated with its implementation in WANDS rather than the mathematical formulation of WFBE method. To overcome this problem, solid elements can be used to obtain the results, although a higher element density is required.

All in all, the WFBE method is applicable for the cases considered in this study. Moreover, the WANDS software can be used to develop numerical models of structures and the structure-fluid interaction provided that suitable precautions are taken. The problems associated with plate-fluid coupling require further attention in the WANDS software but this is beyond the scope of the present study. All procedures and precautions discussed in this chapter are used as a basis for the development of numerical models of a double panel system in the next chapter.

Chapter 5. Waveguide double panel system

In this chapter a numerical waveguide model of a double panel system is developed using the WFBE method, described in Chapter 3 and validated in Chapter 4. The case of a waveguide structure shares some of the features of a finite panel while also having an infinite length in one direction. It is well known that the finite extent of a bounded structure introduces structural modes which are associated with resonance frequencies. Moreover, diffraction occurs for apertures in the baffle in which the structure is mounted [2]. Therefore, theoretically, the finite width of the waveguide structure could bring some consequences in the TL behaviour. This model is intended to investigate transmisson loss behaviour of such a double panel system, particularly the effect of finiteness of the double panel system on the transmission loss rather than the single panel as discussed in section 2.4. This means the effect of finiteness of the air cavity is also studied as well as its interaction with the panels. The results are discussed for normal and oblique incidence and compared with those of an equivalent infinite system. To investigate futher the transmission loss behaviour, diffuse sound field excitation is also considered.

5.1 Transmission loss of infinite double panel partition

An analytical model of the infinite double partition is initially considered in order to give insight into the double panel partition behaviour when excited by a plane acoustic wave. On one hand, this is also intended to provide guidance in assessing the general behaviour of the numerical model as well as forming an important benchmark for the behaviour of the system of finite and infinite extent. On the other hand, the numerical model can also be useful in assessing some assumptions imposed in the infinite model. The physical behaviour is discussed by considering the normal and oblique incidence cases with several different air cavity depths.

The analytical model for the sound transmission loss of a double panel is referred to as the London model [15]. This model was chosen as the reference for benchmarking purposes throughout this study. The reasons for this are, firstly, the model is simple and can be implemented straightaway and secondly, the model is capable of evaluating possible coincidence effects due to bending waves (cf. [14]). Hence the common features of the double panel partition are readily available for the comparison considered.

Prior to discussing the formulation itself, some assumptions in the model should be noted, as follows: (I) both panels are identical and infinite in extent; (II) each panel is isolated and they are coupled only by the air space. Moreover, the infinite condition indicates that the panels have no boundary conditions or structural resonances.

By considering only the mass reactance of the wall impedance (or $Z_w = i\omega m''$ where m'' is the mass per unit area and ω is circular frequency), and excluding resistance damping and flexural motion of the panel, the inverse of the transmission coefficient of the double panel can be written as [15]

$$\frac{1}{\tau} = 1 + 4a^2 \cos^2\theta \left(\cos\beta - a\cos\theta \sin\beta\right)^2 \tag{5.1}$$

where $a = \omega m''/2\rho_0 c$ with m'' the mass of the panel per unit area, $\rho_0 c$ the characteristic impedance of air, θ is the incident angle and $\beta = kd\cos\theta$ with k the acoustic wavenumber and d the air cavity depth. By letting $\theta = 0$, Eq. (5.1) reduces to

$$\frac{1}{\tau} = 1 + 4a^2 \left(\cos kd - a\sin kd\right)^2 \tag{5.2}$$

From Eq. (5.1) , it is clear that perfect transmission (or $\tau = 1$) occurs when

$$\left(\cos\beta - a\cos\theta\sin\beta\right) = 0 \tag{5.3}$$

or

$$\cot\beta = a\cos\theta \tag{5.4}$$

In the case where β is small, which means that the air cavity is small compared with acoustic wavelength ($kd \ll 1$), $\cot\beta \simeq 1/\beta$ and hence Eq. (5.4) leads to an expression for a resonance frequency as follows

$$f_{res} = \frac{c}{2\pi\cos\theta}\sqrt{\frac{2\rho_0}{m''d}} \tag{5.5}$$

Therefore, Eq. (5.5) indicates frequencies where the incident sound at angle θ will be transmitted perfectly. For the normal incidence case, Eq. (5.5) leads to the so-called Mass-Air-Mass (MAM) resonance which occurs at

$$f_{res,0} = f_{MAM} = \frac{c}{2\pi}\sqrt{\frac{2\rho_0}{m''d}}\,. \tag{5.6}$$

At this frequency, the air in the cavity acts as a spring and the two panels move out of phase with each other on the spring. Hence the double partition suffers a poor insulation performance at this frequency. It can be further observed that the term $\cos\theta$ in Eq. (5.5) indicates that f_{MAM} is the lowest frequency at which the attenuation of the double panel system is zero; for oblique incidence f_{res} will be higher than f_{MAM}. This frequency is also known as lower London frequency.

To describe the TL behaviour relative to the frequency of mass-air-mass resonance, a normalization of Eq. (5.1) by f_{MAM} is performed. The inverse of the transmission coefficient can now be expressed as [92]

$$\frac{1}{\tau} = 1 + \left(\frac{\omega}{\omega_0}\right)^2 \left(\frac{\omega_0 m''}{\rho_0 c}\right)^2 \cos^2\theta \left(\cos\beta - \frac{1}{2}\frac{\omega}{\omega_0}\frac{\omega_0 m''}{\rho_0 c}\cos\theta\sin\beta\right)^2 \tag{5.7}$$

where $\beta = 2\dfrac{\omega}{\omega_0}\dfrac{\rho_0 c}{\omega_0 m''}\cos\theta$ and $\omega_0 = 2\pi f_{MAM}$.

In the following sections, results are given for a double panel system consisting of two panels of plasterboard and an air cavity. The properties of the system are listed in Table 5.1.

Table 5.1. Material properties of the gypsum plasterboard

Properties	Value
Young's modulus, E (N/m^2)	2.5×10^9
Poisson's ratio, v_p	0.3
Density (kg/m^3)	690
Panel thickness, h (mm)	16
Air cavity depth (mm) (unless otherwise stated)	65

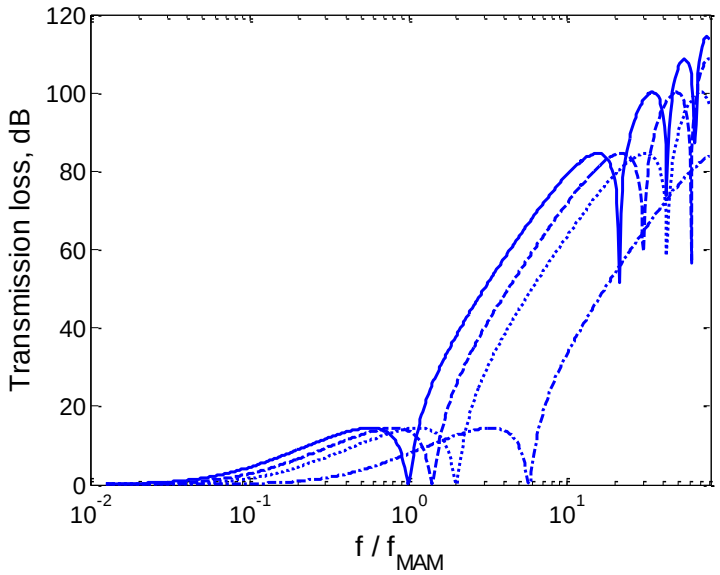

Figure 5.1. Effect of the incident angle on TL according to the London model for parameters in Table 5.1 (— $\theta = 0^\circ$; --- $\theta = 45^\circ$; • • • $\theta = 60^\circ$; – • – $\theta = 80^\circ$).

Figure 5.1 presents the TL values for various incident angles. It can be observed that the dip occurs at the frequency of the mass-air-mass resonance at angle 0°. The dip occurs at a higher frequency as the incident angle increases. It is clear that the frequency is proportional to $1/\cos\theta$ as expressed in Eq. (5.5). However, some minima also occur in the TL curves at higher frequencies above f_{MAM}. These are related to the term $\cot\beta$ in Eq. (5.4) when the transmission coefficient of the double panel system tends to 1. Since a increases with increasing frequency, at high enough frequencies this term is approximately equal to infinity, $\cot\beta \simeq \infty$ hence

$$\beta \simeq n\pi, \qquad n = 1, 2, 3, ..., \tag{5.8}$$

Under such circumstances, standing waves are present in the air cavity. These waves thus effectively connect the two panels rigidly. By recalling that $\beta = kd\cos\theta$, Eq. (5.8) gives the frequency corresponding to the standing wave as follows

$$f_n = \frac{nc}{2d\cos\theta} \tag{5.9}$$

It is clear that, if the air cavity depth increases, more minima will occur. Figure 5.2 shows the effect of doubling the air cavity depth.

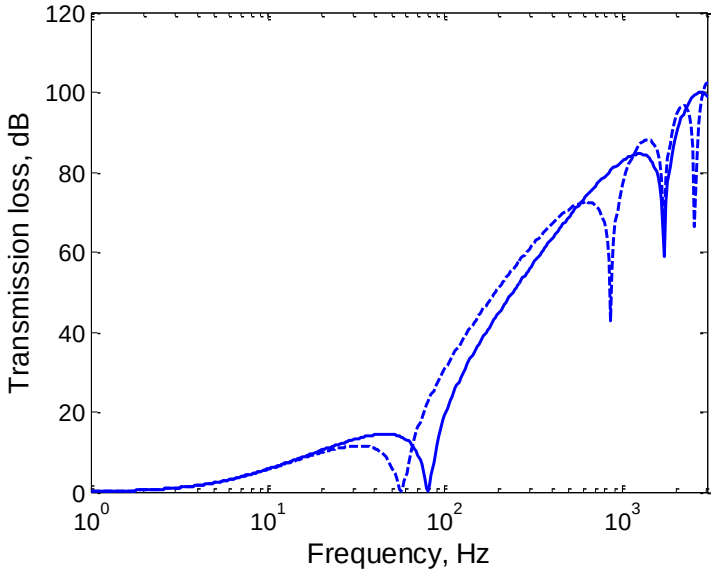

Figure 5.2. Effect of the air cavity depth on standing waves/acoustic resonance for normal incidence (— $d = 100$ mm ; --- $d = 200$ mm).

Up to this point, only the mass reactance is considered in the TL prediction. Now, the panel resistance r and the flexural motion of the plate, specified by its critical frequency, are incorporated according to London [15]. Therefore, the panel impedance becomes

$$Z_w = \frac{2r}{\cos\theta} + i\omega m''\left(1 - \frac{f^2}{f_c^2}\sin^4\theta\right) \tag{5.10}$$

where $f_c = (1/2\pi)c^2\sqrt{m''/D}$ with c the sound speed and D the bending stiffness. Considering Eq. (5.10) and performing some algebraic manipulations, the inverse of the transmission coefficient is given by [15]

$$\frac{1}{\tau} = 1 + 4\left[R(R+1) + p^2v^2\right] + 4\sin^2(bv)\left\{\left[R(R+1) + p^2v^2\right]^2 - p^2v^2\right\} - 4pv\sin(2bv)\left\{R(R+1) + p^2v^2\right\} \tag{5.11}$$

where R is the resistance of the panel r normalized by $\rho_0 c$ or $R = r/\rho_0 c$, $v = \cos\theta$, $b = kd$ and $p = a\left[1 - \left(f^2/f_c^2\right)\left(1 - v^2\right)^2\right]$. However, the postulate of the panel resistance introduced in the model does not have physical basis according to [21, 93] hence this is actually as an empirical correction to achieve a better fit to measurement results.

Figure 5.3 presents a comparison of the results calculated using Eq. (5.11) with those from the model with purely the mass reactance. It is clear that some differences exist at low frequencies due to the inclusion of the resistance. The attenuation no longer tends to zero as occurred in the previous model. Moreover, the TL value predicted using the revised model is higher at low to mid frequencies than the initial model. According to [15], this behaviour is closer to experimental results.

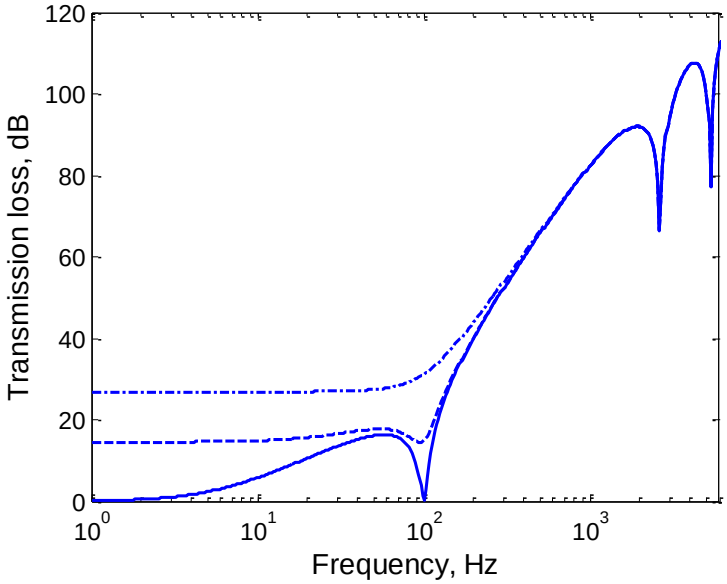

Figure 5.3. Effect of incorporating the panel resistance R on the TL curve for normal incidence (— Eq. (5.1); - - - Eq. (5.11), $R = 2.16$; – • – Eq. (5.11), $R = 10.5$).

In order to observe the effect of flexural motion on the TL curve, an oblique incidence result is presented in Figure 5.4 for an angle of 75°. It is clear that the model incorporating the flexural motion of the panel can demonstrate the coincidence phenomenon or trace-wave matching [4]. At 2.1 kHz, the component of the incident acoustic wavelength parallel to the plates matches the free flexural wavelength, hence a free propagating wave is excited in the panel. This wave is transmitted 'resonantly' and causes a considerable dip in the TL curve. In fact, this phenomenon exists at a frequency that depends on the incident angle θ. The lowest such frequency is the critical frequency f_c which occurs for $\theta = 90^\circ$ (grazing incidence). The model without these terms has the same tendency as the normal incidence result except that the MAM resonance frequency shifts upwards (see Figure 5.1). As found for the normal incidence, a similar tendency also

occurs for oblique incidence in which the inclusion of R affects the TL at low frequency and around the coincidence frequency. However, the effect of R becomes evident over a wider frequency range rather than only at low frequency as found for the normal incidence in Figure 5.1 for larger R.

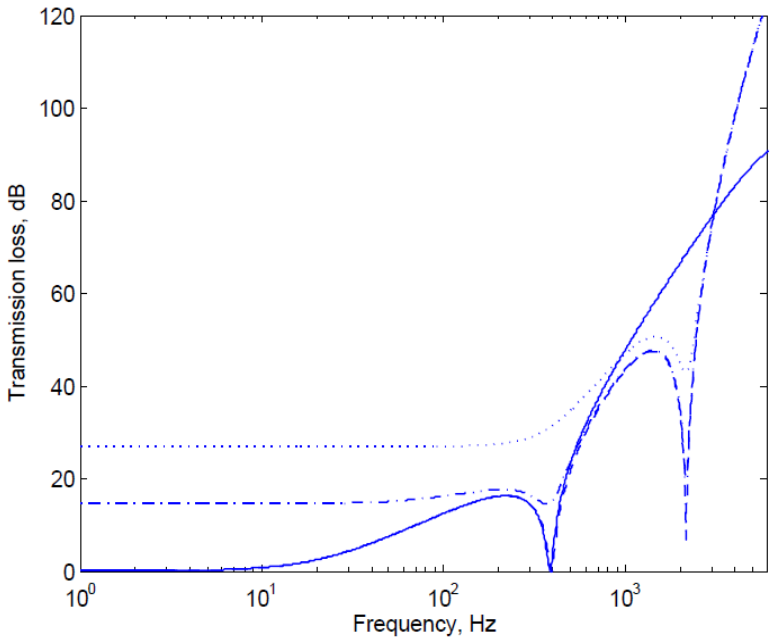

Figure 5.4. Effect of incorporating the flexural motion of the panel and resistance panel R on the TL curve for the obliquely incident case ($\theta = 75^\circ$) (— Eq. (5.1); ---Eq. (5.11), R = 0 ; – • – Eq. (5.11), $R = 2.16$; ••• Eq. (5.11), $R = 10.5$).

Figure 5.5 presents TL under diffuse sound field excitation for elevation angles ranging from 0 to $\pi/2$ calculated with $R = 0$. To achieve convergence it is found that 900 angles are required. It can be seen that the first dip at low frequency corresponds to the mass-air-mass resonance while that at high frequency corresponds to the critical frequency.

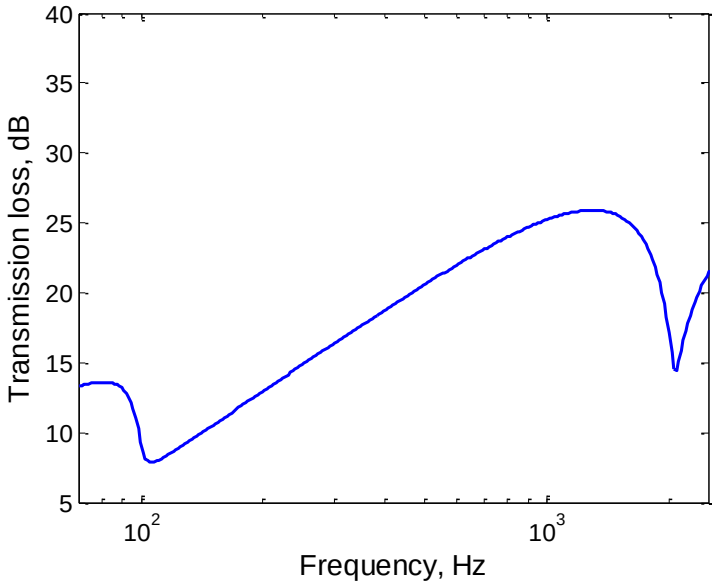

Figure 5.5. Diffuse TL for infinite system with $R = 0$.

5.2 Waveguide double panel partition with air cavity

The numerical model of the double panel partition system is now developed on the basis of a waveguide structure mounted in a finite rigid baffle using the WFBE method. As before, the double panel partition is made of two leaves of plasterboard coupled by an enclosed air cavity. The material properties and dimensions are specified in Table 5.2. Note that these properties are assumed based on typical values rather than obtained from a measurement. Most of them are similar to values given in [31, 45] which allow comparison with the same experimental data [38] as used for those studies. Hereafter, this is designated as a reference model during this study. Moreover, the system without studs is discussed separately from that with studs as it is of importance in practice: some structures have no mechanical connection, e.g. double glass or high performance double walls. Steel studs are introduced afterwards and their effect is investigated in Chapter 6.

Table 5.2. Material properties and dimensions of the double panel partition (unless otherwise stated).

Properties	Plasterboard	Air
Young's modulus, E (N/m^2)	2.5×10^9	-
Poisson's ratio, ν_p	0.3	-
Thickness (or cavity depth), h (mm)	16	65
Density, ρ (kg/m^3)	690	1.21
Damping loss factor (if used), η	0.06	10^{-3}

5.2.1 Problem statement

The waveguide double panel system model is shown schematically in cross-section in Figure 5.6. The structural response is calculated for different wavenumbers κ in the $x-$direction by solving the vibro-acoustic problem in the $y-z$ plane. In this model, a WFE fluid sub-model is included to represent the dynamic response of the air in the cavity. Thus, the model embraces three sub-models to form the whole double panel system: WFE-Solid, WFE-Fluid and WBE-Fluid. At the edges, simply supported boundaries are introduced unless otherwise stated; hence the central nodes of the solid element representing the panels here are restrained in x, y and z-directions while rotation is allowed. The wavenumbers of the incident plane wave are determined by the incidence angle θ about the x axis while the angle about the y axis depends on the wavenumbers in the x-direction.

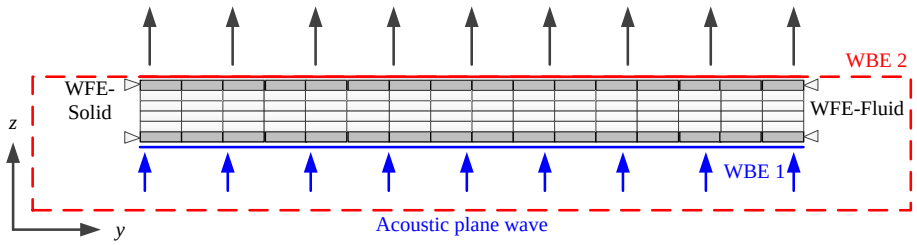

Figure 5.6. Schematic illustration of the numerical model for double panel partition with enclosed air cavity. The dashed-line on the WBE-2 mesh is to indicate the surface velocities are equal to zero.

The air in the cavity is assumed to be an ideal fluid, or close to ideal which means the fluid has low viscosity and low heat conductivity [78]. However, the formulation still permits a dissipative term to be introduced through a damping loss factor as long as the irrotational condition of the fluid particle displacement is not violated. Otherwise, care is required for example for the case of a thin air layer [94] where viscothermal effects occur which significantly increase as the air layer becomes thinner. However, a suitable loss factor for the air is still required to take account of relevant effects in the cavity as the air is trapped within the cavity. Some suggested values that are found in the literature are a loss factor $\eta = 10^{-3}$ [34] or a frequency independent power attenuation coefficient of 0.2 m^{-1} [25]. In the present study, a loss factor of 10^{-3} is initially assumed. The physical justification for this value will be discussed in detail in section 5.2.3.3. Moreover, the numerical model does not take into account the effect of possible flanking transmission that may exist in practice.

The numerical model was developed by using the software package WANDS [87]. The current version of the software restricts the maximum number of nodes or elements and coupling elements during the calculation process due to maximum allocated memory under a 32 bit Operating System environment. Accordingly, the number of elements used for each sub-model reflects this limitation considering the size of the structure, while ensuring a minimum of at least six elements per wavelength [88].

The plasterboard leaves are modelled using 8-noded solid finite elements. 48 elements are used to cover 1.218 m width which is equal to three bays of a double panel with the stud system that will be studied later. For the air in the cavity, 8-noded acoustic elements are employed where 4 layers across the depth are used to cover 65 mm depth while the same number of elements as for the solid elements is used in the direction parallel to the panels. Similarly, the boundary element mesh at the radiating side uses the same element size as the solid and acoustic elements. However, this mesh is extended by 0.60 m beyond the structure width on each side, unless otherwise stated, in order to include a finite baffle in the model. The depth of this WBE mesh is 0.13 m to form a closed boundary mesh as required. Hence, 204 elements are used to cover the whole closed boundary. Under such circumstances, the model is expected to be acceptable for a lowest frequency of around 70 Hz due to the width of the baffle and up to 3.4 kHz at high frequency at which the acoustic wavelength equals 0.1015 m. It is important to compare

the model configuration with the acoustic wavelength as the structural wavelength is larger than this above the critical frequency of 2.0 kHz. Meanwhile incoming waves with a particular pressure amplitude are defined in another WBE model (or WBE 1) which is used to apply the excitation to the system. For this, an open boundary mesh consisting of 48 acoustic boundary elements is used by considering that the fluid loading from the air is small. All these aspects have been discussed in detail in Chapter 4, sections 4.2-4.3.

It should be noted that plate elements are more convenient than solid elements but, it was found in Chapter 4 that the plate elements in WANDS give incorrect results when coupled to acoustic WBE around and above the critical frequency, as discussed in section 4.3. However, for particular cases in which a higher order element is required, e.g. to cover a wider waveguide or higher frequency, the plate elements will be used as long as such cases do not deal with results associated with the critical or coincidence frequency or a non zero wavenumber in the x direction. For these cases, at least 4 elements per wavelength will be used as this was found to be sufficient in section 4.4.1. Hence 30 plate elements can cover frequencies up to 4.2 kHz for 1.218 m width panel while that of 3.4 kHz is the upper limit for 48 solid elements. The same WBE dimensions are used as in the model assembled with the solid elements.

5.2.2 Features found in the waveguide double panel results for normal incidence

Prior to discussing the effect of various geometrical parameters on the TL behaviour, the results of the waveguide structure are first compared with those of the infinite double panel system. In this section, the numerical model is developed using plate elements. This is expected to allow observing features at higher frequency that can be found in the numerical result particularly for normal incidence. For other cases, e.g. oblique incidence, the model is based on the solid elements unless otherwise stated. The results for both the waveguide double panel structure and the infinite system are calculated using identical material properties given in Table 5.2. However, as the formulation of the London model uses the term R to account for the wall resistance instead of the loss factor of the panel, it is difficult to find an appropriate value of R to enable the results of both models to be obtained under identical dissipative conditions. Moreover, from the comparison of the results, the value of R affects the TL at low frequency whereas the damping loss factor

has little effect in this frequency region. Hence, the term R in the London model is set to zero throughout the comparison.

Figure 5.7 compares the results for the normal incidence case. This shows that the TL of the waveguide double panel system follows the general trend of the infinite double panel system at frequencies between f_{MAM} and f_c of the panel which is around 2 kHz. Hence, it increases with frequency at rate of 18 dB/octave in this frequency region [7]. At higher frequencies, the dip due to the standing wave resonance across the depth is pronounced in the TL curves of both models. The first such dip occurs in both results at 2640 Hz at which half a wavelength occurs in the cavity depth, as indicated in Eq. (5.9). However, some features appear in the waveguide results which are not found for the infinite system. Four particular frequency ranges may be considered to discuss these features:

(i) At frequencies below the mass-air-mass resonance, $f < f_{MAM}$, the TL values of the waveguide structure are higher than those of the infinite one. Some small dips are also found at frequencies below f_{MAM} which are not evident for the infinite structure.

(ii) The value of f_{MAM} for the waveguide structure is higher than that of the infinite one. For the 65 mm air cavity depth considered here, f_{MAM} of the infinite structure is around 100 Hz, calculated using Eq. (5.6), while that of the waveguide structure is 173 Hz. This suggests that the f_{MAM} formulae (Eq. (5.6)) for the infinite structure cannot be used to evaluate this parameter correctly for the case of the waveguide structure.

(iii) For $f_{MAM} \leq f < f_c$, it is clear that the TL values of the waveguide structure are lower than those of the infinite one. Significant dips are also found in the TL curve of the waveguide structure which are not coincident with the dips due to acoustic standing waves across the depth, which should be evident at 2640 Hz, 5280 Hz, etc. according to Eq. (5.9). Moreover, some considerable dips also occur around the critical frequency f_c of the panel, i.e. 2028 Hz.

(iv) For $f > f_c$, another considerable dip is also found besides that due to the cavity resonance. This can be observed at around 3840 Hz.

These features will be discussed further in the next sections. Moreover, for convenience, the case of oblique incidence angles is also skipped in this section until the loss factor and coincidence frequency issues have been discussed.

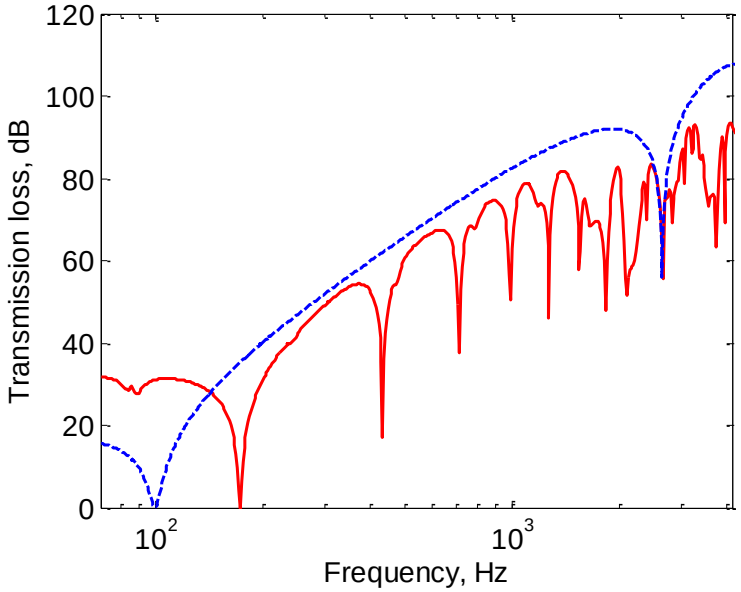

Figure 5.7. TL comparison of the waveguide double panel system using 30 plate elements and London's model for normal incidence (— waveguide structure; - - - London's model).

5.2.3 Effect of finite cavity

The London model and other double panel models, e.g. [6, 17], treat the cavity as infinite in the directions parallel to the plate. Unlike these models, the air cavity of the waveguide double panel system here is treated as finite in one direction. In this model, the edges of the cavity are assumed to be rigid, which will cause perfect acoustic reflection. From the literature, some efforts to model such a finite width cavity in double panel systems were already carried out by other workers, for example by modelling the reflected waves at the cavity boundaries using a ray tracing model [21, 95] or SEA method [26, 51]. However, these models are inherently limited at low frequencies; e.g. the geometrical approach in the ray tracing model does not allow long wavelength sound to interact with the surfaces under consideration. Likewise, the SEA method requires a sufficient modal density in order for the average response to be correctly predicted, which is not fulfilled at low frequencies. Alternatively, an analytical model is employed in [96] to solve the finite cavity with rigid walls at its edges.

It is instructive to investigate the implications of the finite cavity imposed in the double panel system in order to assess the consequences of the infinite extent which is assumed in most classical models. Moreover, some structures such as double glazing actually contain sound-absorbing material at the cavity perimeter. Therefore, the discussion of this can be beneficial for practical situations.

5.2.3.1 Lateral cavity mode effect

It is usual that the air occupying the cavity is assumed to be incompressible and have no viscosity. Hence, the cavity pressure distribution is uniform across the depth when the cavity depth d is much smaller than the acoustic wavelength (or $kd << 1$). Under such circumstances, the air effectively acts as a spring with a stiffness per unit area $\rho_0 c^2 / d$. However, when the panels exhibit flexural motion the fluid inside the cavity can experience a deformation leading to motion parallel to the plates. Under such circumstances, due to changes in the air volume in the cavity, pressure fluctuations can occur. As a consequence of this, the pressure distribution inside the cavity is not uniform but varies along the directions parallel to the panels so that air stiffness in the cavity now varies locally in the lateral direction [97]. For the case of a waveguide structure with a confined cavity, the air is trapped in the cavity and cannot escape through the edges. Hence, at certain frequencies, the pressure distribution takes the form of a standing wave pattern, as illustrated in Figure 5.8, where the acoustic wavelength is an integer fraction of twice of the width. In other words, lateral cavity modes are found in which resonant behaviour occurs across the width. These frequencies are given by

$$f_{m,y} = \frac{mc}{2l_y} \tag{5.12}$$

where l_y is the width of the waveguide structure and $m = 1, 2, 3, \ldots$. These frequencies can be seen as dips in the TL curves in Figure 5.7.

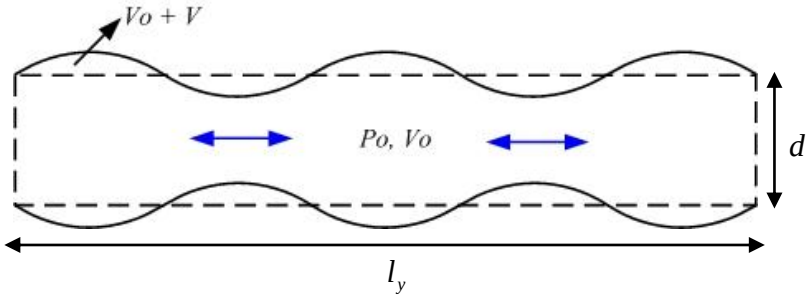

Figure 5.8 The change in volume and pressure due to compression and refraction in the enclosed cavity when the panels deform.

At the frequencies at which the lateral cavity resonances occur, the panels move out of phase. This allows the incident sound to be transmitted virtually unattenuated across the waveguide double panel system at these frequencies. This mechanism is different from the resonances due to cavity modes across the depth, in which the cavity impedance becomes infinite in the absence of dissipative terms rigidly connecting the panels. Meanwhile, for the $x-$direction, the lateral cavity modes are not present as a consequence of the infinite dimension of the waveguide structure in this direction.

Dowell and Voss [98] provided an approximate theory corresponding with flexible panel-cavity interaction. According to this theory, the discrepancy of the panel mode frequency between the *in-vacuo* panel and the one coupled with the cavity is due to coupling between cavity modes with higher-order panel modes. The effect of the cavity on the panel produces added stiffness to symmetrical modes while a negative stiffness is found for anti-symmetric panel modes. This is similar to the findings of Pretlove [99] where only "volume-displacing" modes like the fundamental panel mode is significantly affected by the cavity rather than the second mode.

To give insight into the pressure distribution inside the finite cavity, Figure 5.9 illustrates the operating deflection shape of the panels and the pressure distribution inside the cavity at 173 Hz, corresponding with the first dip in the TL of the waveguide double panel system as shown in Figure 5.7. It is clear that the lateral cavity mode is pronounced while the panels are in flexural motion at their fundamental mode. However, this does not imply the presence of the viscothermal effect as found in a thin air layer [94] as such an effect is not taken into account in the current model according to the formulation in [78].

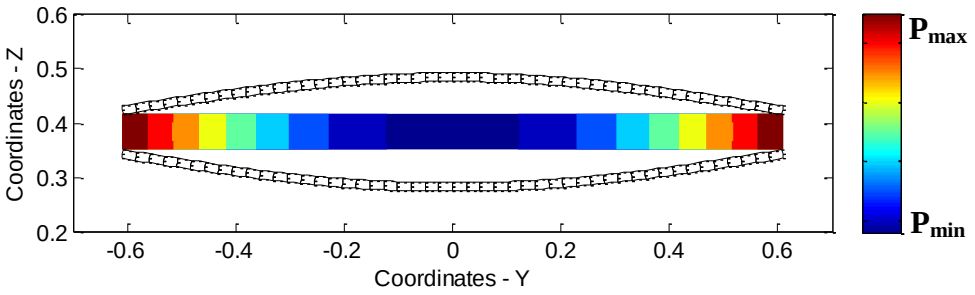

Figure 5.9. Operating deflection shape of the 1.218 m wide double panel partition at 173 Hz, obtained using WANDS.

It has been shown in section 5.1 that the first dip in the TL of the infinite double panel system corresponds to the mass-air-mass resonance frequency f_{MAM} in which no lateral cavity modes exist. To see further consequences of the presence of the lateral cavity modes in the waveguide system on this frequency, Figure 5.10 compares the transmission loss of the waveguide structure for different widths and f_{MAM} of the infinite structure for normal incidence. It is clear that the frequency of the first dip reduces as the width increases, so that for 3.05 m it is 115 Hz while for 1.8 m and 1 m it is 138 Hz and 199 Hz respectively. Therefore, the frequency of this dip becomes closer to f_{MAM} of the infinite structure as the waveguide structure becomes wider.

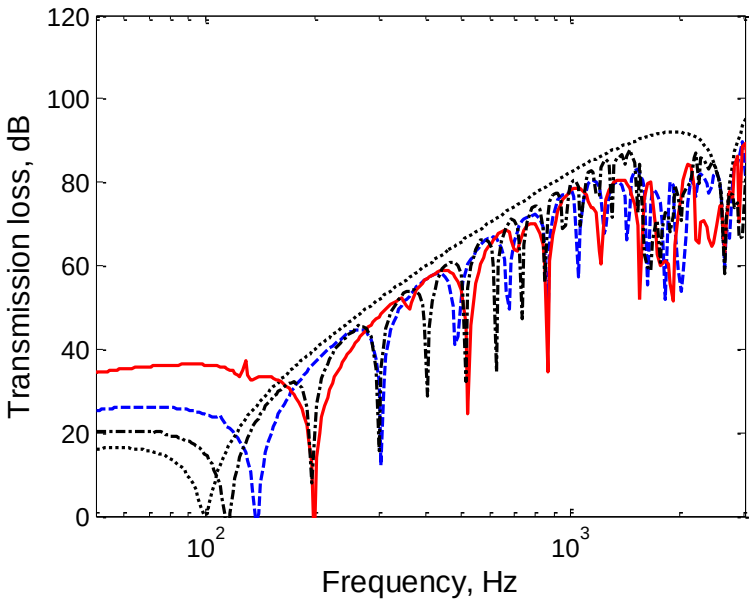

Figure 5.10. Effect of the panel size on TL for normal incidence (waveguide structure: — 1.0 m width ; --- 1.8 m width; – • – 3.05 m width ; ••• infinite structure).

It is also instructive to see the effect of the cavity depth on the frequency of the first dip of the waveguide structure, as the formulation of the London model indicates that for the infinite structure it depends on the panel mass and the air cavity depth as indicated by Eq. (5.6). For a fixed mass, according to the London model f_{MAM} is reduced as the cavity depth increases, as shown in Figure 5.11(a). The transmission loss also increases at frequencies where $f > f_{MAM}$ and $kd \ll 1$. Note that lowering f_{MAM} would be beneficial to improve overall sound reduction performance of the double panel system in the frequency range of interest, hence such an approach is frequently employed in practice.

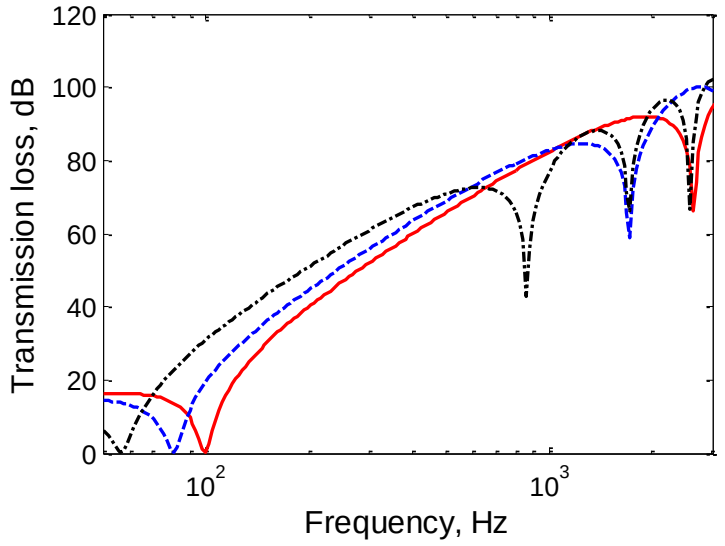

(a)

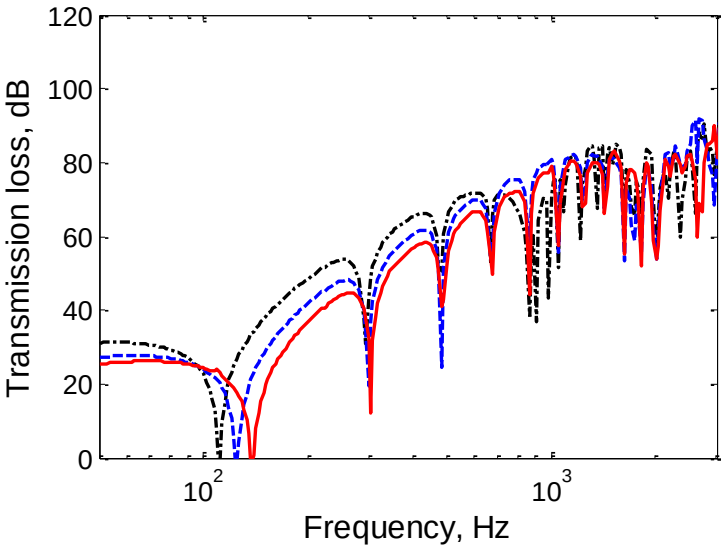

(b)

Figure 5.11. Effect of cavity depth for normal incidence: (a) infinite structure (b) waveguide structure with 1.8 m width (— 65 mm depth; - - - 100 mm; —•— 200 mm).

The same tendency is also exhibited by the waveguide structure, as shown in Figure 5.11(b). The increase in the cavity depth drives the frequency of the first dip to lower frequencies, i.e. for the present case of 1.8 m width, this resonance frequency equals 138 Hz for the cavity depth of 65 mm, reducing to 124 Hz for 100 mm cavity depth. It further reduces to 111 Hz for 200 mm cavity depth. Likewise, the standing wave resonances in the depth direction are also reduced when the cavity depth is increased. The usefulness of increasing the depth is again seen where the transmission loss below the critical frequency increases with increasing depth. Note that the standing wave resonance frequencies along the directions parallel to the panels remain virtually unchanged as long as the width of the structure is retained the same for all cases.

Considering such a tendency, the frequency of the first dip for the waveguide structure will thus be determined by two factors for a given mass, i.e. the width and depth dimensions. Figure 5.12 indicates this through a comparison of transmission loss for widths of 1.8 m and 3.05 m and depths of 65 mm and 100 mm and the results are summarized in Table 5.3 together with results from other cases.

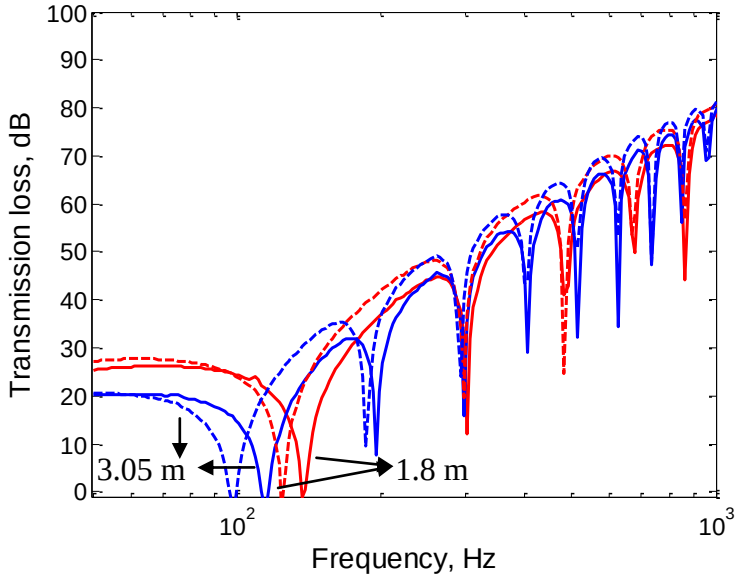

Figure 5.12 Effect of width and cavity depth of the waveguide to f_{MAM} for normal incidence (— : 1.8 m width and 65 mm depth ; ---1.8 m width and 100 mm depth; — : 3.05m width and 65 mm depth ; --- : 3.05 m width and 100 mm depth).

Following the numerical results given in Table 5.3, the first dip found for the waveguide double panel system can be considered as a modified mass-air-mass resonance

frequency where the added stiffness of lateral cavity modes is added in parallel to that of the ideal air with uniform pressure distribution which follows

$$f_{MAM,WG} = \sqrt{f_{MAM}^2 + \left(\frac{c}{2d_y}\right)^2} \tag{5.13}$$

Table 5.3. Modified f_{MAM} of the waveguide structure $f_{MAM,WG}$

		Depth		
		65 mm	100 mm	200 mm
Width	f_{MAM} , Hz / $f_{1,y}$, Hz	100	81	57
1.0 m	172	199 (199)	(190)	(181)
1.218 m	141	173 (173)	(162)	(152)
1.8 m	95	138 (138)	125 (125)	111 (111)
3.05 m	56	115 (115)	99 (99)	(80)

* Convention of the pair : Numerical (Equation (5.13))

In general f_{MAM} of the infinite system is modified for the current case and converges to that of the infinite system with increasing width of the waveguide, as shown in Figure 5.13. However, a typical double panel system is usually constructed with dimensions much less than 10 m, e.g. [100, 101]. Hence, the discrepancy in TL curve associated with f_{MAM} as indicated in this figure could be found in practice.

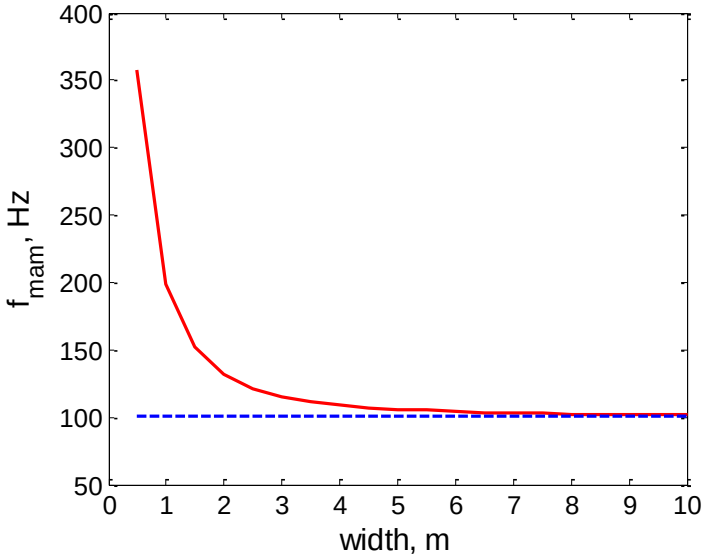

Figure 5.13. f_{MAM} of finite cavity compared with that of infinite system with 65 mm cavity depth (— waveguide system ; - - - infinite system).

Considering the numerical results obtained, it is clear that these lateral cavity resonances need to be considered where no sound-absorbing material is present to damp them. They may not be regarded as a simple continuous spring as proposed in [2, 7, 15]. Hence, the non-uniformity of the pressure distribution in the cavity causes the total response in the cavity to be the superposition of the air-stiffness dependent response across the depth and the cross-section modal response. It can be deduced further that the frequencies associated with the subsequent dips found in the transmission loss curve for $kd << 1$ can be generally formulated as

$$\bar{f}_{m,y} = \sqrt{f_{MAM}^2 + f_{m,y}^2} \tag{5.14}$$

With increasing frequency $f_{MAM} \ll f_{m,y}$ so that $\bar{f}_{m,y} \approx f_{m,y}$. Note that, for normal incidence only odd cavity modes are excited (see Figure 5.7).

For frequencies where $kd \gg 1$, the cavity modes exist in 2D form where cavity modes across the depth are also present as well as in the lateral direction. However, as previously noted, the contribution of the acoustic lateral cavity modes in this frequency range becomes smaller.

The presence of the lateral cavity modes is also discussed by Sharp in [7] where the resulting effects are considered to be similar to that of mechanical connectors such as

studs. To demonstrate the role of the lateral cavity modes in lowering the TL, he partitioned the cavity area into small parts in order to suppress the cavity modes across the width and the length. Compared with the original cavity, a higher TL amplitude was found for the partitioned cavity. For the same purpose, Sharp placed sound-absorbing material around the cavity perimeter to damp the lateral cavity modes. From this, he found that a thicker absorbent produced higher TL values than a thinner material. The same approach was used to assess the importance of the lateral cavity modes by other workers. This was discussed by London in [15] following experimental results obtained by Meyer (1935). However, this gave an opposite result where the sound-absorbing material around the cavity perimeter did not make a significant improvement in transmission loss. Nevertheless, some indications from Sharp [7] are substantiated by the present model through the presence of the cavity lateral modes. To explain the above results Utley et al. [102] argued that the insignificant improvement in transmission loss occured as absorption already existed at the edges before the sound absorption material was placed in this area. Hence, there was less additional absorption effect from the absorption material than expected.

5.2.3.2 Internal coincidence frequency

At high frequencies, acoustic standing waves across the cavity depth start to be established. Their associated frequencies can be calculated using Eq. (5.9). In this frequency region, standing waves can therefore exist in both directions. Thus, the acoustic wavenumbers in the cavity are the resultant of the acoustic wavenumbers in x, y and z-directions. For a waveguide structure, the acoustic wavenumbers in the cross-section are defined by

$$\alpha^2 = k^2 - \kappa^2 = k_y^2 + k_z^2 \tag{5.15}$$

Hence the acoustic wavenumbers along the directions parallel to the panels are given by

$$k_{y,q} = \sqrt{\alpha^2 - k_z^2} = \sqrt{\left(k^2 - \kappa^2\right) - \left(\frac{q\pi}{d}\right)^2} \tag{5.16}$$

where κ is the acoustic wavenumber along the $x-$direction and $q = 0,1,2,...$ corresponds to the number of half wavelength in the depth direction.

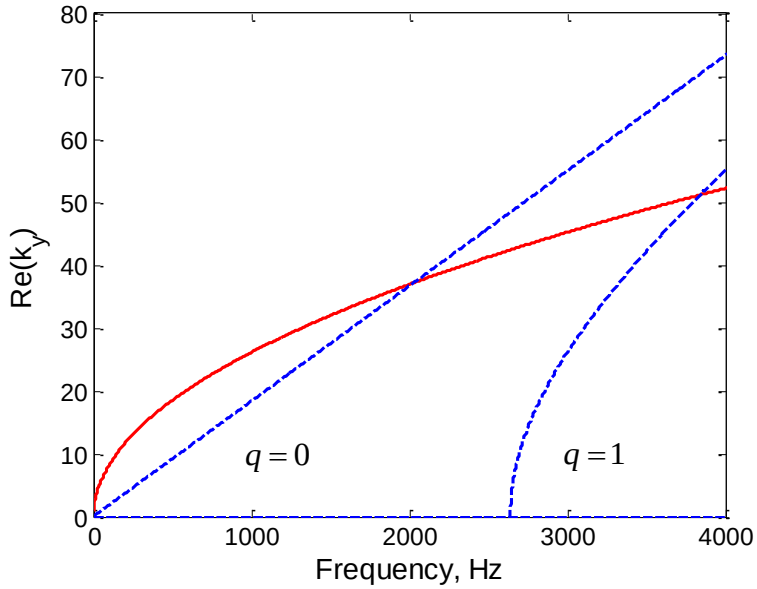

Figure 5.14 Dispersion curve of the waveguide double panel system for $\kappa = 0$ (— free bending wave; - - - acoustic wavenumber in the $y-$direction in the air cavity).

When $k_{y,q}$ coincides with the free bending wavenumbers k_B of the panel, an internal coincidence frequency is found. This can be observed from the dispersion curves in Figure 5.14 for the case of $\kappa = 0$. The curve for $q = 0$ crosses the free bending wavenumber curve at the critical frequency of 2028 Hz. This corresponds to the large dip found in Figure 5.7. This can be considered as an internal coincidence frequency in order to distinguish it from the coincidence effect proposed by Cremer [11]. Moreover, the $q = 1$ curve crosses k_B at 3840 Hz, corresponding to the further dip found in Figure 5.7. Note that these frequencies are expected to be the same for all incident angles about the x axis, although they will be different when $\kappa \neq 0$. The boundary conditions imposed on the edges also affect this (see section 5.2.5) as well as non-identical panel properties (see section 5.2.8).

The pressure distribution in the cavity associated with these frequencies can be observed in Figure 5.15 where simply supported boundaries are introduced at the edges of both the panels while the edges of the cavity are assumed to be acoustically reflective. At these frequencies, the incident energy impinging on the first panel is more easily transmitted to the second panel leading to a higher radiated power. Therefore, regarding the lower TL found for the waveguide double panel system than for the infinite system, the internal coincidence effect is another cause as well as the lateral cavity modes.

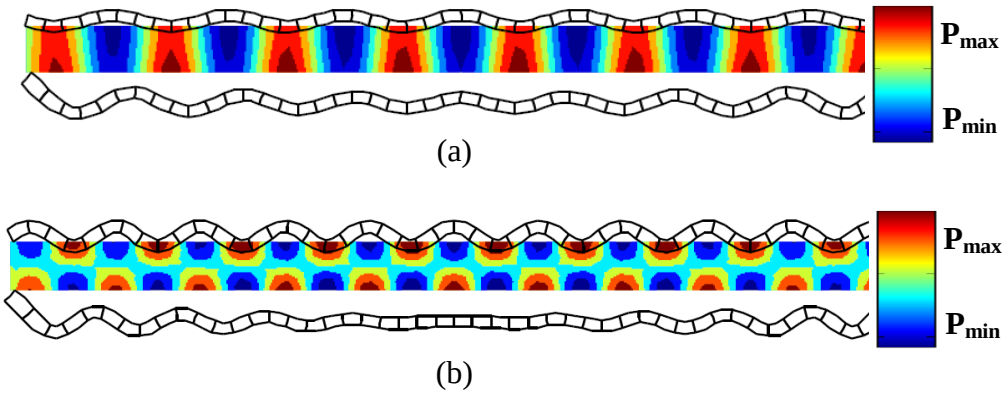

Figure 5.15. Pressure distribution in the cavity at internal coincidence frequency for normal incidence: (a) 2028 Hz (b) 3840 Hz.

Compared with the conventional coincidence phenomenon as proposed by Cremer [11], the internal coincidence occurs as progressive sound waves impinging on the panel excite standing flexural waves in the finite panel which match standing sound waves in the finite cavity. Therefore, physically, the coincidence is independent of the incident angle because the standing waves are stationary and do not depend on the trace wavenumber of the incident wave, as shown in Figure 5.16. Such indications can be seen later in section 5.2.6 where two extreme incidence angles about the $x-$axis and $y-$axis are considered. The same phenomenon was also found by Bhattacharya et al. [103] for the case of a finite flexible panel backed by a cavity.

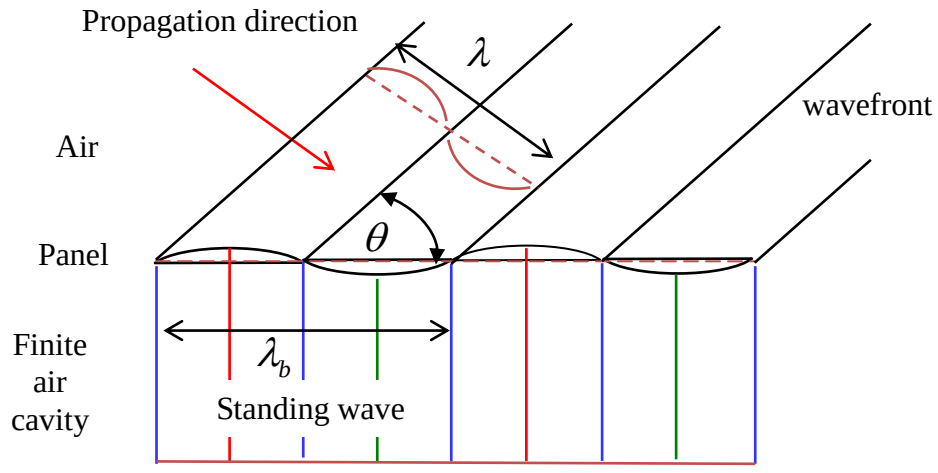

Figure 5.16. Standing sound wave match standing flexural wave.

5.2.3.3 Effect of cavity loss factor

For an air cavity without any sound-absorbing material or mechanical connections between the panels, the cavity loss factor η_{cav} becomes a crucial factor with regard to the accuracy of TL prediction results. It is also not justified to treat the air in the cavity as inviscid. The main reasons are: (I) viscous and thermal loss effects; (II) absorption will always be present even in a small quantity on the edges so sound will not be totally reflected as assumed in an ideal cavity model; (III) some sound-absorbing material is often found around the cavity perimeter, e.g. in double glazing systems. Cummings et al. [21] and Quirt [93] confirmed points (II) and (III) through their experimental results while point (I) depends on the cavity dimensions and frequency. However, in theory, it is difficult to propose an appropriate value and sometimes it becomes unrealistic in a real situation; e.g. Cummings founds that an absorption coefficient $\alpha = 1$ was required for the sound-absorbing material at the cavity perimeter [21] to get good agreement between the prediction results and the experimental ones. Price and Crocker [26] calculated the cavity loss factor based on the normal incidence absorption coefficient α_0 for sound-absorbing material introduced at the cavity perimeter for a double panel system without structural connections. They found that an average value of η_{cav} of 2.7×10^{-2} was required up to 1.25 kHz. When the sound-absorbing material is absent at the perimeter area of such a structure, it is more difficult to determine an appropriate value of the cavity loss factor. For this case, Brekke [51] found $\alpha_0 \approx 0.1$ for $d \geq 0.1$ m and $\alpha_0 \approx 0.5$ for $d \leq 0.02$ m from measurement results. Quirt [93] measured the absorption coefficient α_0 of unfinished plywood and found $\alpha_0 \approx 0.1$ for frequencies above 500 Hz while it was much lower than 0.1 for frequencies below 500 Hz. This result can be used to approximate the absorption coefficient when unfinished wood is used at the cavity perimeter. Hence, Brekke's results [51] must be used with caution depending on the material properties used at the cavity perimeter. Apart from this, Dijckmans and Vermeir [104] set the cavity loss factor to zero for the case of a double wall and multi-layered wall with cavity depth less than 30 mm using a wave based method (WBM). They found good results compared with measurement ones.

By default, $\eta_{cav} = 10^{-3}$ has been assumed in the results discussed in the previous sections. This value was chosen to represent the cavity loss factor in an attempt to cover all

aspects in points (I)-(III) above not just the damping loss factor of the air. To investigate further its effect on the waveguide double panel system, the loss factor is now varied in the range 10^{-3} to 10^{-1} for the case of normal incidence and oblique incidence at an angle of 45°. The results are shown in Figure 5.17. They are shown in 1/3 octave frequency bands to obtain a clear comparison across the frequency range of interest. For this, the sound transmission coefficient is averaged across the band to obtain the 1/3 octave value.

Figure 5.17(a) presents the effect of the cavity loss factor on the transmission loss for normal incidence in which only odd cavity modes are excited. A significant increase in TL can be seen as η_{cav} increases. For the current case, the TL around $f_{MAM,WG}$ increases by 1 dB when the loss factor is increased by a factor of 10 and by 9 dB if it is increased by a factor of 100. The effect is negligible at frequencies below f_{MAM} and above it up to around 300 Hz. At higher frequencies, where lateral cavity modes occur, the TL behaviour is affected by the cavity loss factor, increasing by 1-5 dB from $\eta_{cav}=10^{-3}$ to $\eta_{cav}=10^{-2}$ and increasing by 2-15 dB from $\eta_{cav}=10^{-3}$ to $\eta_{cav}=10^{-1}$. This trend is also evident for frequencies above f_c. A similar tendency is also exhibited in the oblique incidence cases particularly at frequencies below $f_{MAM,WG}$, as shown in Figure 5.17(b). Above this frequency, the effect of damping is greater than for normal incidence and it extends to lower frequencies. This occurs as even modes as well as odd modes are now excited. This leads to the density of the lateral cavity modes increasing when the waveguide double panel system is excited by a plane wave at an angle of 45° about the *x* axis. Hence, the mode spacing is reduced and the effect of cavity loss factor is greater. Conversely, the mode spacing is wider for the case of the oblique incidence at an angle of 45° about the y axis. Under such circumstances, the effect of the cavity loss factor is not significant up to 500 Hz as shown in Figure 5.17(c). On the other hand, an increase in TL can be found in all cases at the first internal coincidence frequency around 2 kHz.

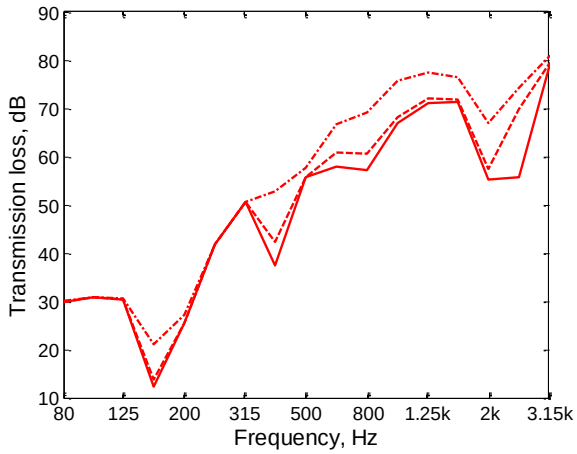

(a)

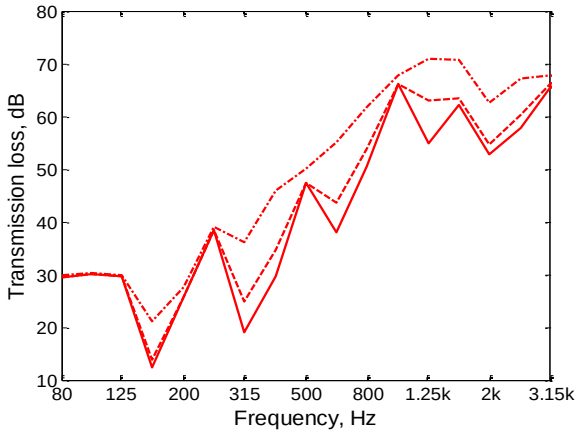

(b)

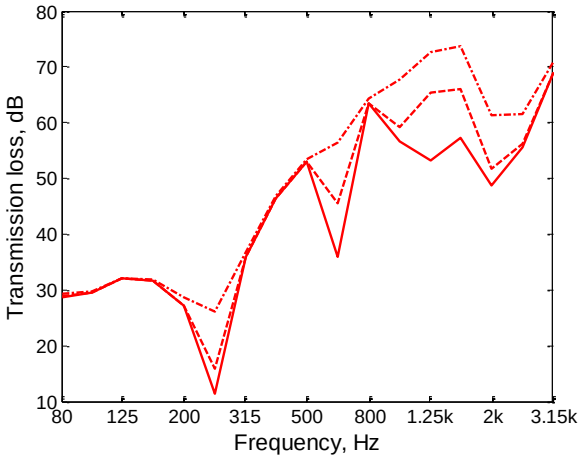

(c)

Figure 5.17. Effect of cavity loss factor on TL in 1/3 octave frequency bands: (a) normal incidence case; (b) oblique incidence at angle 45° about x axis; (c) oblique incidence at angle 45° about y axis (— $\eta_{cav} = 10^{-3}$; - - - $\eta_{cav} = 10^{-2}$; - • - $\eta_{cav} = 10^{-1}$).

5.2.4 Panel loss factor

The damping loss factor of the panel is now varied to be a factor of ten greater or smaller than its original value of $\eta = 0.06$. Figure 5.18 shows the normal incidence TL of the waveguide double panel system with different damping loss factors. For a low damping loss factor, $\eta = 0.006$, more dips are present in addition to those due to standing waves in the air cavity. It is clear that the corresponding frequencies of these dips are cut-on frequencies of waves in the panels, indicating that such dips are related to the 'resonant' transmission of the waveguide structure. For example, the dip found at 88 Hz below the mass-air-mass resonance frequency is associated with the 3rd cut-on frequency of the 1.218 m width panel and the next two dips at 244 Hz and 478 Hz are associated with the 5th and 7th cut-on frequencies. Despite the presence of these dips, the slope of the TL curve at frequencies below coincidence dip is still similar to that for the case of $\eta = 0.06$.

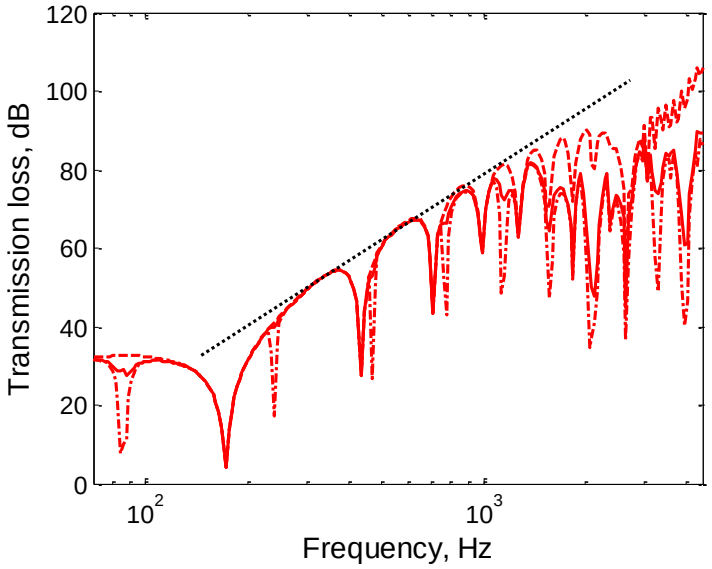

Figure 5.18 Damping loss factor effect on the TL behaviour for normal incidence: full spectrum (- - - η_{panel} = 0.6 ; ——— η_{panel} = 0.06 ; – • – η_{panel} = 0.006 ; ••• TL slope).

However, at frequencies where the internal coincidence effect takes place, around 2 kHz and 3.8 kHz, the TL is lower for the smaller damping loss factor which can be seen more clearly in 1/3 octave frequency bands as shown in Figure 5.19(a) for normal incidence. In this frequency region, the TL value is even greater when the damping loss factor is further increased to $\eta = 0.6$. Hence the considerable dips found in the previous two cases are less pronounced for this case.

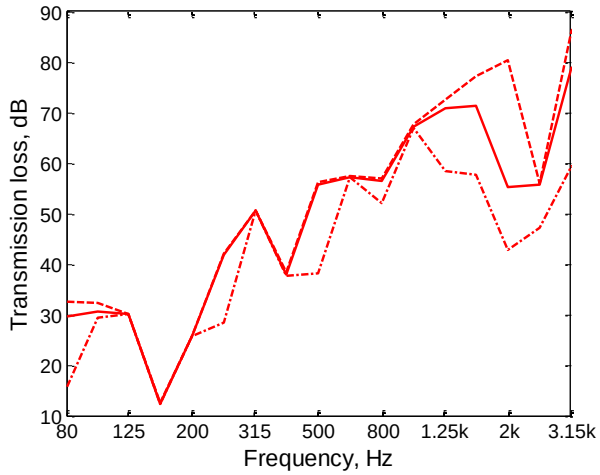

(a)

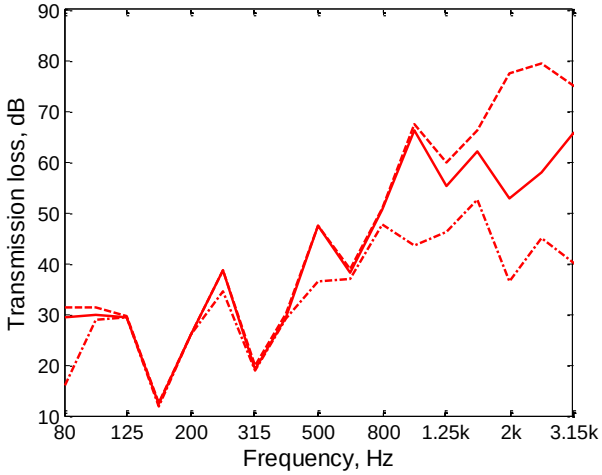

(b)

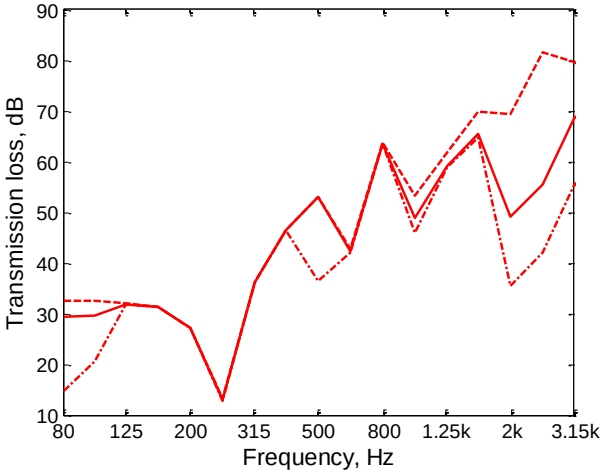

(c)

Figure 5.19. Effect of panel loss factor in 1/3 octave frequency bands: (a) normal incidence case; (b) oblique incidence at angle 45° about x axis; (c) oblique incidence at angle 45° about y axis (- - - η_{panel} = 0.6 ; ——— η_{panel} = 0.06 ; – • – η_{panel} = 0.006).

Similar indications are also found for the cases of oblique incidence at an angle of 45° about the *x* axis and *y* axis, as shown in Figure 5.19(b) and (c) respectively. It can be seen that the TL behaviour is retained even for the higher damping loss factor except around the cut-on frequencies and the internal coincidence ones.

From this comparison, the damping loss factor of the panel is effective in reducing the dips at the cut-on frequencies and the internal coincidence frequencies but not those related with the air stiffness dependent response. This differs from the London model results, in which damping is only introduced through the dissipative mechanism of the cavity. Therefore, the results do not support the existence of a resistance term in the complex impedance as postulated by London in [15]. The choice of *R* to fit measured values appears to be based on an incorrect physical principle. Similar indications to those shown in this study were also found in [21, 93].

5.2.5 Effect of edge condition

Some publications, e.g. [105, 106], discuss the effect of the edge condition of a plate specifically in terms of the radiated sound power and the radiation efficiency of the plate in response to mechanical excitation. In general, the important conclusion that is worth underlining is that a higher edge constraint does not necessarily cause additional sound radiation of the plate. However, for the case of acoustic excitation, the clamped boundary condition leads to a lower sound transmission loss than that obtained with simply supported boundaries [12, 22, 107]. Utley et al. [107] compared three boundary conditions and concluded that the real boundary condition exists between simply supported and clamped, based on comparisons with experimental results. This indicates that the real edge condition of a double panel system is not exactly known. Accordingly, the mounting method of the edge areas at the aperture potentially becomes a source of discrepancies between the prediction model results and the experimental ones. Therefore, it is of importance to clarify the TL behaviour of the waveguide double panel system in relation to the effect of the boundary conditions that are used in the numerical model.

For the waveguide structure, three different boundary conditions have been implemented and the results are compared with each other. This is done by restraining the DOF of nodes at both edges as follows:

(i) Free-free boundary: none of the DOFs are restrained.

(ii) Simply supported boundary: the DOF restrained are the x, y and z displacements of a midside node.

(iii) Clamped boundary: the DOF restrained are the x, y and z displacements of midside and corner nodes.

Additionally, for the case (i) none of the nodes at the edges of the cavity are restrained while the case (ii) and (iii) the nodes at this area are also restrained. Normal and oblique incidence are considered, while the damping loss factors are kept the same as in Table 5.2.

The effect of the boundary condition on the TL behaviour can be seen in Figure 5.20(a) for normal incidence. Ideally, the free-free boundary condition produces the same results as the infinite model since the panel is free to move without bending for normal incidence. Hence, the acoustic modes in the direction parallel to the panels are not excited in the cavity. This can be seen from the fact that f_{MAM} is 100 Hz. However, the finiteness of the system still gives rise to diffraction at the panel edges leading to non-uniform fluid loading over the panel. This causes the panels to experience a small bending and then standing waves in the cavity are excited but at a reduced amplitude compared with the other two cases. When these standing waves match the bending wave contained in the panels, internal coincidence effect occurs. This introduces some dips in the TL curve. Meanwhile, the results for the simply supported boundary conditions and the clamped ones are similar to each other. Small differences appear corresponding to the cut-on frequencies. Moreover, the TL at high frequencies, above 3 kHz, tends to be lower than that for the simply supported boundaries. Compared with the free-free boundary conditions, these results are higher at frequencies below f_{MAM} but lower above this frequency.

Figure 5.20(b) shows the equivalent results for the case of oblique incidence at an angle of 45° to the x axis. The results are now similar for all three boundary conditions. The dips are now present for the free-free boundary condition as the incoming wave at a certain angle causes bending waves in the panels. Hence, the waves with the wavenumber equal to the structural wavenumber in the $y-$direction are now found in the cavity around 2 kHz as well as 3.8 kHz. For the case of 45° incidence angle about the y axis shown in Figure 5.20(c), a similar tendency is evident except for the case of free-free boundary condition which has a similar behaviour as encountered in the normal incidence.

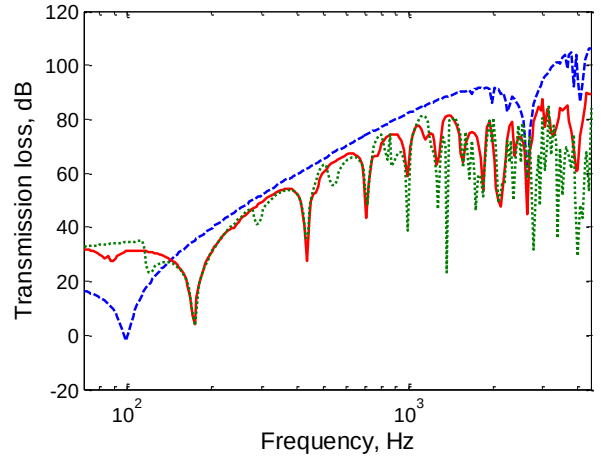

(a)

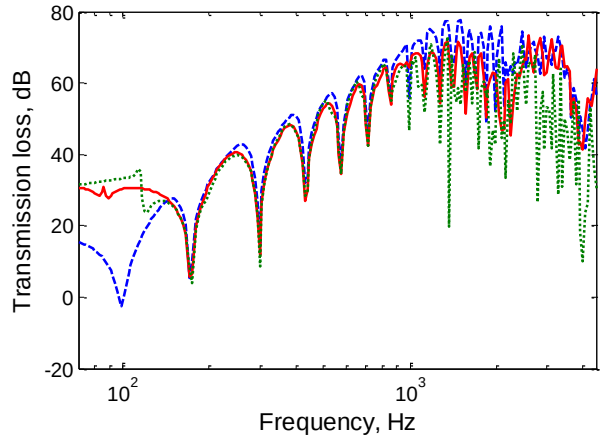

(b)

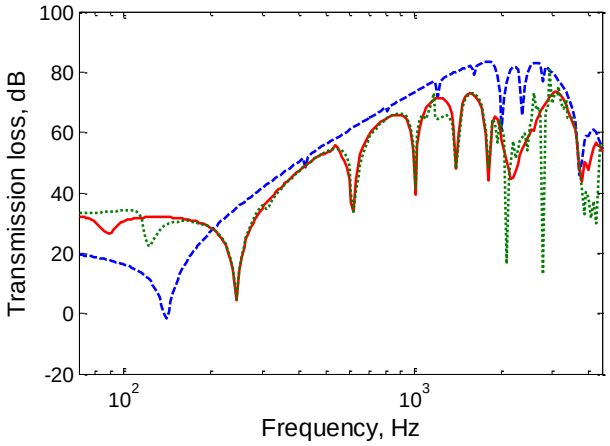

(c)

Figure 5.20. Effect of boundary condition on the TL behaviour: (a) normal incidence; (b) oblique incidence at angle 45° about x-axis; (c) oblique incidence at angle 45° about y-axis (— simply supported BC; - - - free-free BC; • • • clamped BC).

5.2.6 Coincidence frequency behaviour

The coincidence dip occurs in the TL curve of the infinite plate model if the structural wavenumber of the panel at the incoming side equals the acoustic trace wavenumber. Two different incident angle orientations are considered and discussed separately considering the presence of both finite and infinite extent in the waveguide structure. Hence, the results are presented for the case of different incident angles about the x-axis or about the y-axis; the results of the waveguide double panel system are compared with those of the infinite plate model.

For oblique incidence at an angle about the x-axis, the coincidence frequency is found to be independent of the incident angle as shown in Figure 5.21(a). Compared with the results obtained with the infinite plate model, this tendency indicates that the coincidence effect occurs by a different mechanism where the coincidence frequency is determined by standing waves along the width in the cavity rather than solely the finiteness in panel.

Conversely, different tendencies are evident for incidence at an angle about the $y-$axis as shown in Figure 5.21(b). Here, as proposed by Cremer [11], coincidence takes place if the structural wavenumber of the panel equals the acoustic trace wavenumber. The lateral cavity resonances, indicated by the dips, still occur for this case as the cavity response in the x direction cannot be completely separated from the total response considering the finiteness of the system. However, they now differ from the previous case as they shift to higher frequency by a factor of $\cos\theta$, with θ the incidence angle about the y-axis as a consequence of $\kappa \neq 0$. As the incidence angles increases, the acoustic wavenumber along the x-direction becomes larger while those in the y and z directions become smaller following the vector rules. This causes the presence of the lateral cavity modes to reduce with increasing incidence angle. Hence, the dip associated with f_{MAM} is the only one present below the coincidence frequency when the waveguide structure is acoustically excited at grazing incidence for which $k = \kappa$ while k_y and k_z are zero.

The same reasoning can explain the presence of the internal coincidences for the current case as shown in Figure 5.21(b), as indicated by the dip around 2 kHz, where they exist due to the finiteness of the system rather than being triggered by the infinite properties in the x direction. These internal coincidences will appear less with increasing

incidence angle as consequence of larger acoustic wavelengths in the y and z directions. Hence, for the case of incidence angle of 60° and 80°, the internal coincidence frequency of 3.8 kHz does not emerge as encountered in the case of oblique incidence about the x-axis.

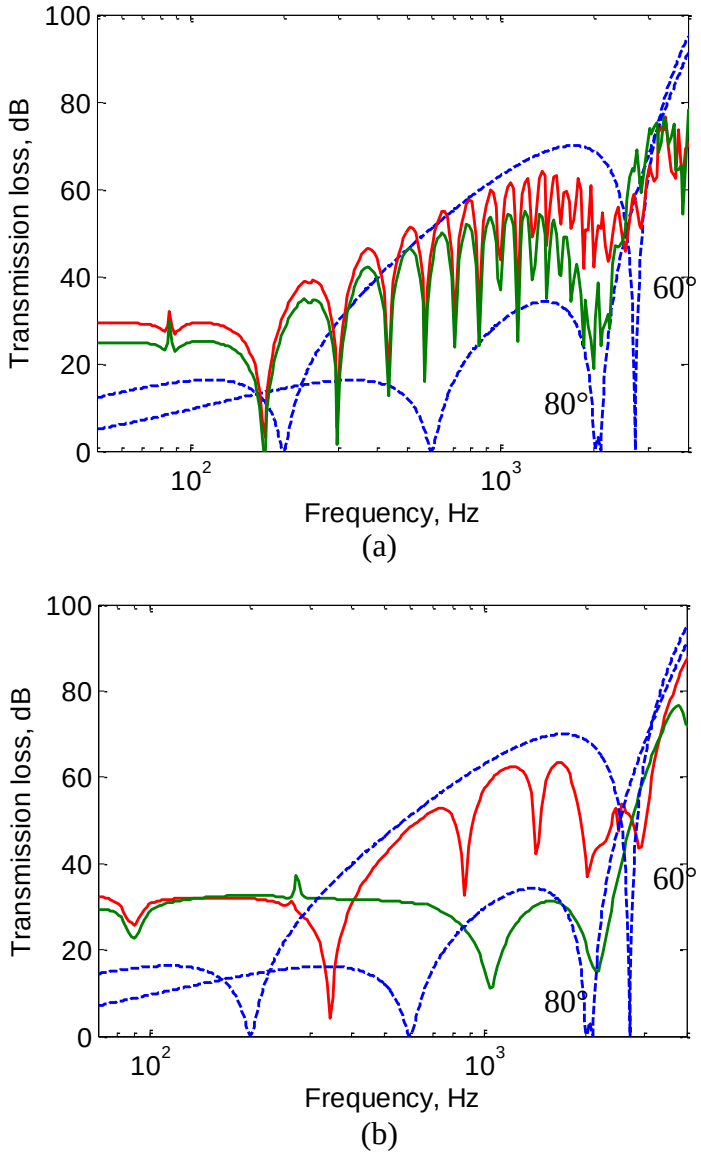

Figure 5.21. TL due to oblique incidence: (a) angle about x-axis (b) angle about y-axis (— numerical model at angle 60°; — numerical model at angle 80°; - - - infinite plate model).

Figure 5.21(a) also shows that the TL values of the waveguide structure are higher compared with the infinite structure particularly for larger incidence angles. It can be seen that the TL of the waveguide structure is dependent on the incidence angle. Hence the

incoming wave exciting the waveguide structure at an angle of 60º will cause higher TLs than if this structure is excited by the same wave at an angle of 80º to the normal. However, $f_{MAM,WG}$ is fixed at a certain frequency for all incidence angles rather than shifting toward a higher frequency with increasing incidence angle as found for the infinite plate. Conversely for the case of the oblique incidence about the y-axis as shown in Figure 5.21(b), $f_{MAM,WG}$ shifts to a higher frequency as found for the infinite model in which impedance of air in the cavity increases by $\sec\theta$ with θ incident angle. Moreover, the TL values are lower than those of the infinite system for frequencies above $f_{MAM,WG}$ for all incidence angles. For frequencies below $f_{MAM,WG}$, the TL behaviour for both incidence angles is similar to that of the normal incidence case (see Figure 5.7) where the TL of the waveguide structure is higher than the infinite structure.

In order to give a clearer comparison, the cavity loss factor is increased to 10^{-2} so that the dips due to the cavity resonances are more suppressed. Moreover, the results are presented in 1/3 octave frequency bands. For the case of incidence angle about the x-axis (or across the finite panel), the results are given in Figure 5.22(a) where the coincidence dips are fixed at a particular frequency rather than reducing with increasing incidence angle. A subsequent coincidence can be found at 4 kHz when standing waves across the depth are established. Moreover, it is clear that the incidence angle will affect the transmission loss amplitude. The case of incidence angle about y-axis (or across the finite plate) as shown in Figure 5.22(b), the coincidence frequency depends on the incidence angle along with the internal coincidence where the critical frequency is also found. For the incidence angles considered in the current case, the internal coincidence frequency of 2 kHz is present while the higher ones are not seen as lateral cavity modes become less evident as the wavenumber components in the cross-section area ($y-z$ plane) reduce.

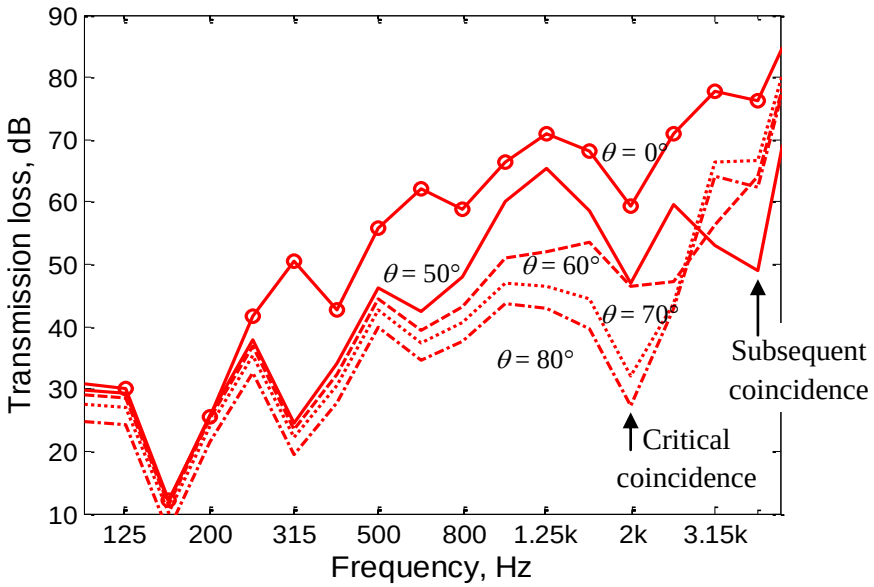

(a)

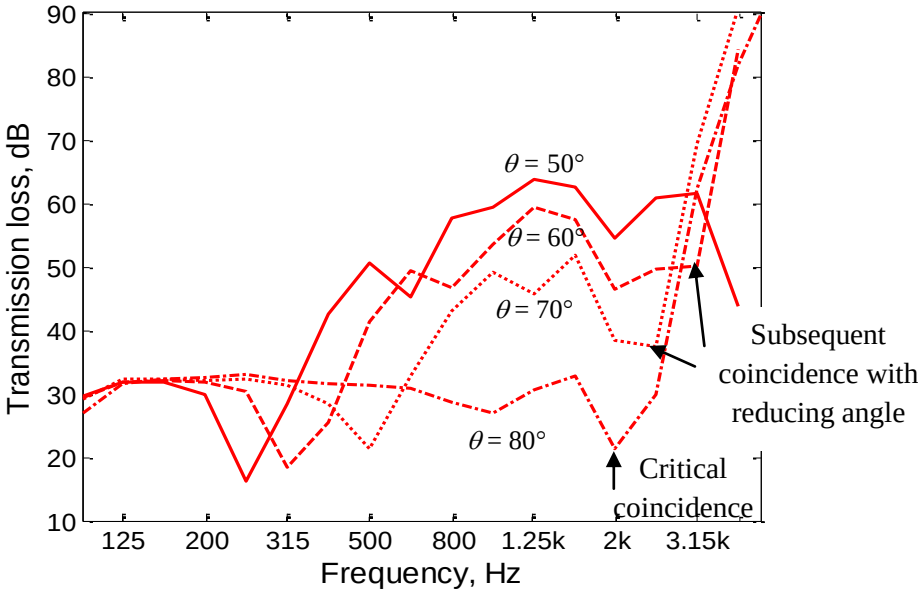

(b)

Figure 5.22. Transmission loss of waveguide double panel system due to oblique incidence: (a) about the x axis; (b) about the y axis .

5.2.7 Radiation ratio

Figure 5.23 presents the radiation ratio of the waveguide structure plotted against the incident angle for certain frequencies. This is obtained from the ratio of radiated sound power to average squared vibrational velocity due to acoustic plane wave excitation. The

corresponding result for the infinite structure is shown for comparison, which is defined for a given incident angle θ as [4]

$$\sigma_{\text{inf}} = \frac{1}{\cos\theta} \tag{5.17}$$

The orientation of the incidence angle is varied about the x-axis. At low frequencies, the radiation ratio of the waveguide is lower than the infinite structure. For mid and high frequencies, it follows the infinite results up to a certain angle, above which it tends to a finite limit instead of going to infinity as indicated for the infinite structure. Such a tendency corresponds to the presence of the windowing effect [23, 108] due to the width of the waveguide structure. These results will be useful in interpreting the diffuse sound field behaviour in the subsection 5.2.9.

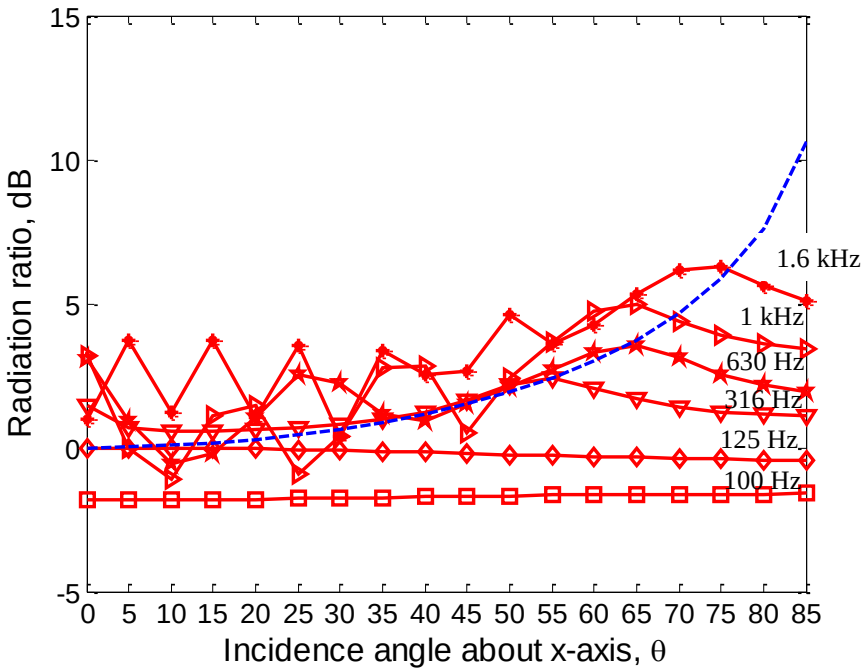

Figure 5.23. Radiation ratio of waveguide structure again the incident angle as a function of incident angle compared with that of infinite structure indicated by dashed line.

5.2.8 Effect of asymmetrical structures

Up to this point, identical panels (i.e. symmetrical structures) are considered for all cases. Now, the transmission loss of a double panel system with non-identical panels is

investigated. The thickness of one of the panels is changed by factor of 2 from their original thickness while the density and width are retained as the identical panel case. Hence, combinations of 8 mm and 16 mm thick panels and of 16 mm and 32 mm thick panels will be considered in this section in comparison with two 16 mm panels. For the non-identical panel systems, the 8 mm thick panel and the 16 mm thick panel of each system considered here are arranged to reside at the source side.

Figure 5.24 presents the results for all combinations. As expected, due to the difference of total of surface mass on each combination, the case of 16 mm and 32 mm thick panels has the highest TL for normal and oblique incidence while its mass-air-mass resonance is found at the lowest frequency. Conversely, the case of 8 mm and 16 mm thick panel has the lowest TL as well as the highest mass-air-mass resonance frequency compared with the other two systems. For these behaviours, the system with identical panels behaves between the behaviour of other two non-identical panel systems. Lateral cavity modes and cross cavity modes occur at the same frequencies for all cases as the cavity has the same width and depth while some discrepancies appear at frequencies associated with coincidence effect. It can be seen that considerable dips are found around 2 kHz and 3.8 kHz for the identical panels. For normal and oblique incidence about the $x-$ axis, see Figure 5.24(a) and Figure 5.24(b) respectively, those dips become less prominent for the case of 8 mm and 16 mm thick panels as the internal coincidence of the 8 mm thick panel is expected around 3.9 kHz. Hence, the TL associated with these coincidence frequencies is higher than for the identical panels. Likewise, for the case of 16 mm and 32 mm thick panels, a similar effect is seen. Considering the dip around 2 kHz, it further reduces in level as the internal coincidence of 32 mm thick panel is expected around 1 kHz and also the total mass is higher than for the identical panels. Hence, the TL around 2 kHz is highest compared with the other two cases. The subsequent dip is found around 3.1 kHz in addition to the dip at 3.8 kHz as now there are internal coincidences associated with the 32 mm thick panel.

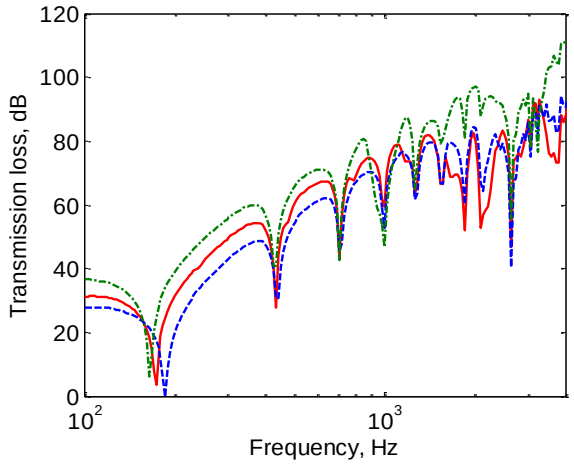

(a)

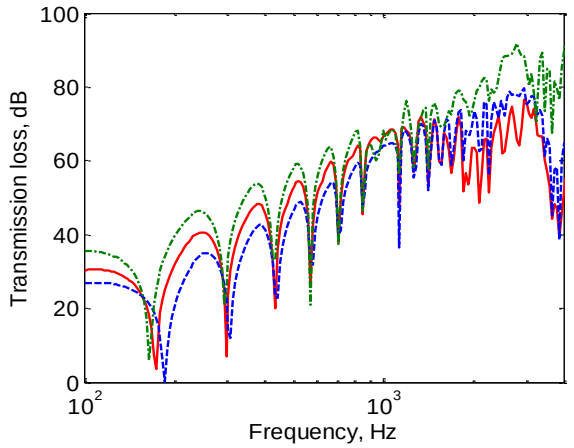

(b)

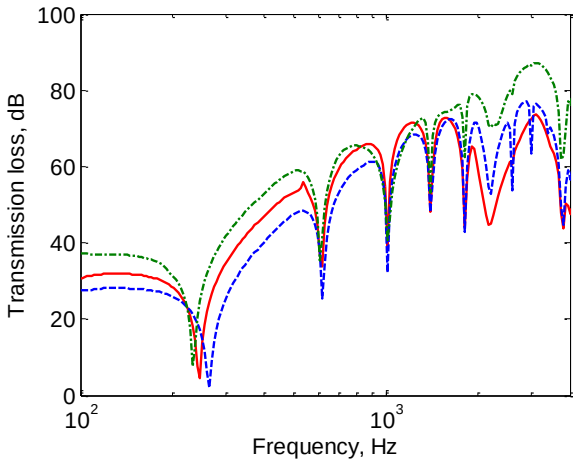

(c)

Figure 5.24. Effect of different panel thickness on TL: (a) normal incidence; (b) oblique incidence at angle 45° about *x* axis; (c) oblique incidence at angle 45° about *y* axis (— identical 16 mm thick panels; - - - combination of 8 mm and 16 mm thick panels; – • – combination of 16 mm and 32 mm thick panels).

For the case of the oblique incidence about the $y-$axis, a similar tendency is also found for coincidence effect as shown in Figure 5.24(c). At the internal coincidence around 2 kHz the non-identical panels have a higher TL than that of the identical panels while the internal coincidence of 1 kHz is also evident at which a different trend in TL curve is seen. Meanwhile, the internal coincidence related with the 8 mm panel becomes less apparent in the current case as its associated frequency is close to the dip due to the coincidence effect of a 45° incoming wave which occur around 4 kHz.

The same behaviour is found for the above non-identical panel systems with different arrangement where the 16 mm thick panel and the 32 mm thick panel of each system reside at the source side rather than at the receiver side. The results for this arrangement are not presented here.

5.2.9 Diffuse sound field

In this section, the response is presented for the waveguide double panel system with identical property panels when excited by a diffuse sound field. The diffuse sound transmission loss is calculated from nine incident angles about the x axis and eighteen incident angles about the y axis by following the procedure used for a plate strip in section 3.3.2. The results are then compared with that of the infinite plate model which has been calculated in section 5.1.

The results are shown in Figure 5.25 from which it can be seen that the waveguide double panel system has a higher TL than that of the infinite plate model. At low frequency, it is clear that the dip corresponding to the mass-air-mass resonance shifts to a higher frequency in comparison with the infinite plate model, as expected considering the finite dimension of the waveguide system. Above the critical frequency, both the waveguide double panel system and the infinite double panel one produce a similar trend. The differences are caused by the lower radiation efficiency of the waveguide double panel system as discussed in section 5.2.7. These results reinforce the elementary behaviour of the bounded system discussed in Chapter 2 and [23, 108]. Therefore, despite the fact that the damping mechanism of the infinite system is disregarded for the current case, the tendency of such higher TL is related to the finite extent of the waveguide double panel system.

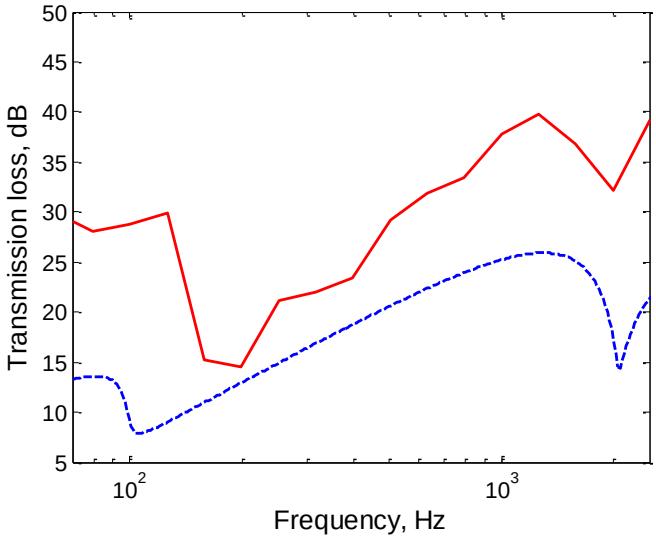

Figure 5.25. Diffuse TL comparison of the numerical model and the infinite plate one (— numerical model; - - - Infinite plate model with $R = 0$).

Figure 5.26 presents the effect of the cavity loss factor η_{cav} on the TL behaviour for diffuse incidence. It is clear that a low cavity loss factor leads to a lower TL. If η_{cav} is increased from 10^{-6} to 10^{-3}, the TL at frequencies between 500 Hz to 2 kHz is increased by 4 dB on average. However, the TL increases significantly, particularly at these frequencies, as the cavity loss factor is increased further, e.g. 8 dB for $\eta_{cav} = 10^{-2}$ and 21 dB for $\eta_{cav} = 10^{-1}$ relative to that with $\eta_{cav} = 10^{-3}$.

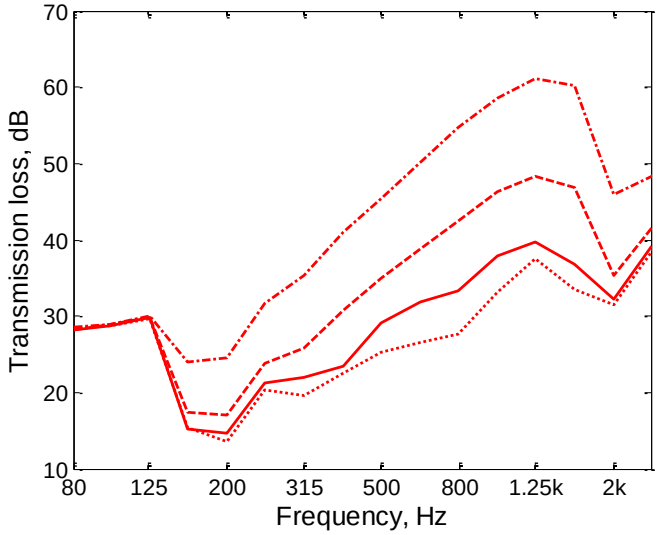

Figure 5.26. Effect of the cavity loss factor on TL for diffuse sound field in 1/3 octave frequency bands (••• $\eta_{cav} = 10^{-6}$; — $\eta_{cav} = 10^{-3}$; - - - $\eta_{cav} = 10^{-2}$; —•– $\eta_{cav} = 10^{-1}$).

The upper angle of the incident field is customarily limited to exclude the results corresponding to large angles close to grazing incidence. This is motivated by the fact that waves at grazing incidence are often not present in practice. For this study, upper limit angles of 60º up to 90º are used to demonstrate the effect of these upper angles on the TL behaviour. As the upper incident angle is reduced the TL is increased especially at frequencies around the critical frequency, as shown in Figure 5.27(a).

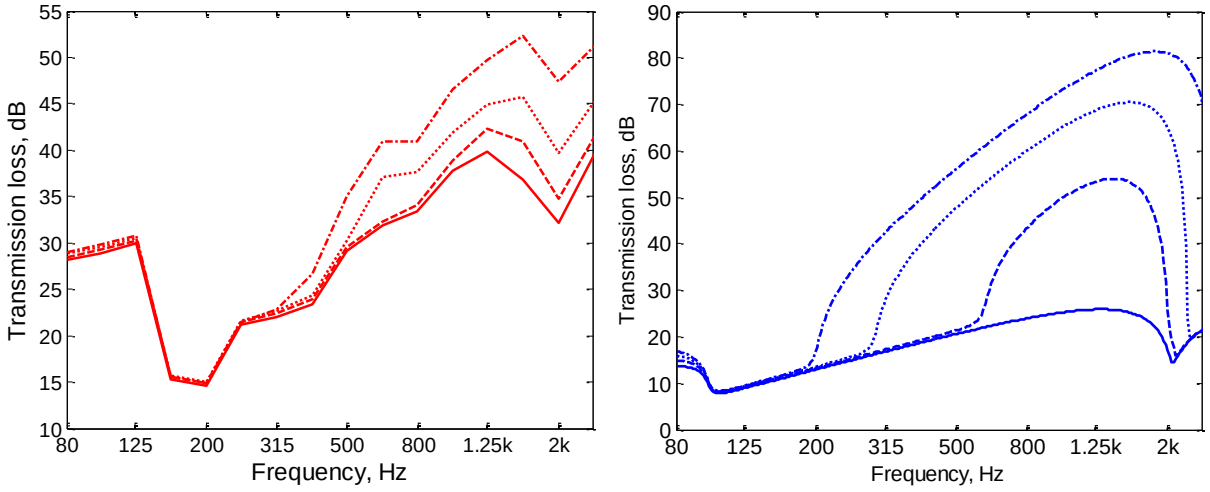

Figure 5.27. Effect of upper incidence angle on the TL behaviour in 1/3 octave frequency bands with $\eta_{cav} = 10^{-3}$:(a) Numerical model (— $\theta_{\lim} = 90^{\circ}$; --- $\theta_{\lim} = 80^{\circ}$; • • • $\theta_{\lim} = 70^{\circ}$; – • – $\theta_{\lim} = 60^{\circ}$); (b) Infinite plate model with $R = 0$ (— $\theta_{\lim} = 90^{\circ}$; --- $\theta_{\lim} = 80^{\circ}$; • • • $\theta_{\lim} = 70^{\circ}$; – • – $\theta_{\lim} = 60^{\circ}$)

Likewise for the results of the London model, similar behaviour can be seen as shown in Figure 5.27(b). It can be seen that reducing the upper angle causes a significant improvement in TL e.g. 80 º upper angle can produce 25 dB higher TL compared with that of 90º, while 60º upper angle leads to an even higher difference where 55 dB difference is evident. For the same upper angles, WFBE results only give 4 dB and 16 dB differences respectively. Therefore, excluding the response of the incoming waves close to grazing incidence can change the TL behaviour and this causes a significant change in behaviour particularly for the London model.

5.3 Summary

The comparisons presented have shown that the main features emerging in the waveguide double panel system are driven by the finite width of the panels and cavity and the coupling between the panel and the air in the cavity. In contrast, in the infinite panel theory [14, 15] such features are not considered and hence their effects are absent. Therefore, the numerical model developed in this study is able to evaluate some features caused by the finite extent in the structures, i.e. standing waves in the finite cavity, internal coincidence and finite radiation ratio caused by windowing.

Considering the non-uniformity of the pressure distribution in the finite cavity, the total response in the cavity is the superposition of the air-stiffness dependent response across the depth and the cross-section modal response. This causes the mass-air-mass frequency of the waveguide double panel system to be modified compared with the mass-air-mass resonance for normal incidence in London's model.

The cavity loss factor has a significant effect on the TL behaviour. This is due to the presence of lateral cavity modes in the direction parallel to the panels as well as the internal coincidence effect. The results obtained show that the dissipative mechanism found in the real structure actually originates from the cavity, rather than from the panel as postulated by London [15]. In the present results the damping of the panels has a more limited effect.

Non-symmetrical panel properties lead to differences in the internal resonance behaviour compared with symmetrical one. The remaining properties related with change in TL and mass-air-mass resonance are the same for both the non-symmetrical panel and symmetrical panel system.

Compared with the infinite panel for diffuse incidence, the higher TL found for the waveguide double panel partition is a consequence of the finite extent in the waveguide structure. This results in a finite radiation efficiency at grazing incidence so that the waveguide double panel system radiates less for larger angles of incidence. The cases considered in this chapter will be extended in the next chapter by introducing steel studs.

Chapter 6. Waveguide double panel system with steel studs

In Chapter 5 the transmision loss behaviour of a waveguide double panel system has been discussed. It is clear that the finite cavity brings some consequences for the transmission loss of such a structure. In this chapter, mechanical connections in the form of steel studs are introduced in the cavity and the effect of such steel studs on the transmission loss is discussed. A parameter study is carried out to give further insight into the implications of steel stud properties on the transmission loss. Finally, comparison with measurement data published by National Research Council of Canada (NRCC) [38] is provided to demonstrate the validity of the numerical model developed.

6.1 Problem statement

The waveguide double panel system model with enclosed cavity considered in section 5.2.1 is now extended to a more complex case in which a structural connection based on steel studs is introduced, as shown in Figure 6.1(a). The connection between the panels and the steel studs is regarded as a continuous line in the x direction rather than a point connection, irrespective of the fastener or screw spacing. It should be noted that point and line connection models have been considered regarding the screw spacing for the case of stiff studs, i.e. wooden studs. This affects the transmission loss behaviour as discussed in [52, 109, 110] where the transition frequency between the respective models is theoretically evident when the screw spacing is equal to a half bending wavelength. For a lightweight steel stud, this is not expected to cause a significant effect on the TL except at low frequency around the "mass-air-mass resonance" according to measurement results presented by Quirt and Warnock [101]. A measurement of the stud-panel mobility has also been carried out on various samples which supports such a tendency (see Appendix D). The stud spacing l of the model is taken as 0.406 m, unless otherwise stated, and the overall width of the structure is 1.218 m. The type of stud considered here is known as a C-stud, as shown in Figure 6.1(a). Other types of stud are also modelled for comparison purposes in section 6.6.4. The assumptions made in the previous waveguide model are

retained for this case, including the material properties, as listed in Table 6.1. The system is assumed to be symmetric with identical panels on each side.

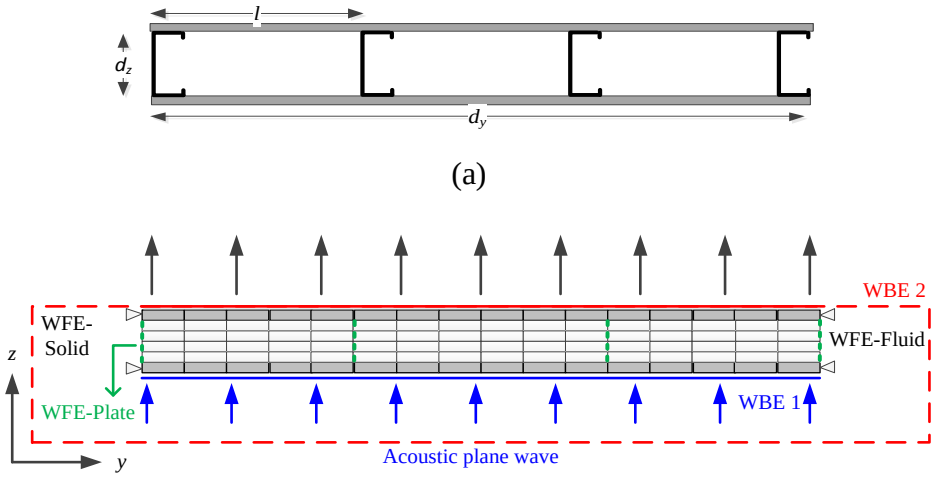

Figure 6.1 (a) Sketch of the waveguide double panel system with steel studs (b) Schematic view of numerical model of the waveguide double panel system with steel studs. The dashed-line on the WBE-2 mesh is to indicate the surface velocities are equal to zero.

Figure 6.1(b) illustrates the coupled WFBE model of the waveguide double panel system. The steel studs are represented using plate elements rather than solid elements due to their small thickness. These elements support bending, longitudinal, shear and transverse motion. As they are not coupled to the acoustic BE domain, the problem identified in Chapter 4 has no influence here. Due to different number of degrees of freedom between the plate elements and the solid ones, the node of the plate elements is coupled with two local nodes of the solid elements at the stud panel connections to ensure continuity of rotation. It should also be noted that simply supported boundaries are imposed at the edges of the panels so that the studs at this area will experience different translational constraints accordingly compared with other studs in the middle. Moreover, separate FE fluid sub-models are defined in each bay which are partitioned by the studs. This differs from the continuous fluid region as assumed in analytical work, e.g. in Ref. [33, 41]. Note that the C-stud shown in Figure 6.1(a), representing a conventional steel stud, is simplified to a line in the numerical model (see Figure 6.1(b)) rather than the full cross-section shape. Thus, the web of the stud is the only part considered, whereas the flanges and the lips of the studs

are omitted. This simplification will be further investigated when the full cross-sectional C shape is incorporated in the model later. Any holes in the studs that may be found in practice are also disregarded in this model. For brevity, the waveguide double panel system with steel studs and air in the cavity is termed a full model throughout this study while that without air in the cavity is called the *in-vacuo* model.

Table 6.1 Material properties and dimensions of the double panel partition

Properties	Plasterboard	Air	Steel
Young's modulus, E (N/m^2)	2.5×10^9	-	2×10^{11}
Poisson's ratio, v_p	0.3	-	0.28
Thickness (or cavity depth), h (mm)	16	65	0.5
Density, ρ (kg/m^3)	690	1.21	7800
Damping loss factor (if used), η	0.06	10^{-3}	0.01
Sound speed, c (m/s)	-	343	-

6.2 *In-vacuo* model

In this section, the *in-vacuo* model is initially considered before introducing the air within the bays. Figure 6.2 presents the results due to normal incidence for this model as well as the double panel system with enclosed cavity without studs. Compared with the results of the model without the studs, various dips are now found in the TL curve that are associated with the structural behaviour, e.g. around 165 Hz, 964 Hz, 2.4 kHz and so on. Moreover, above 400 Hz the TL of the *in-vacuo* model is lower than that of the model with air but without the studs.

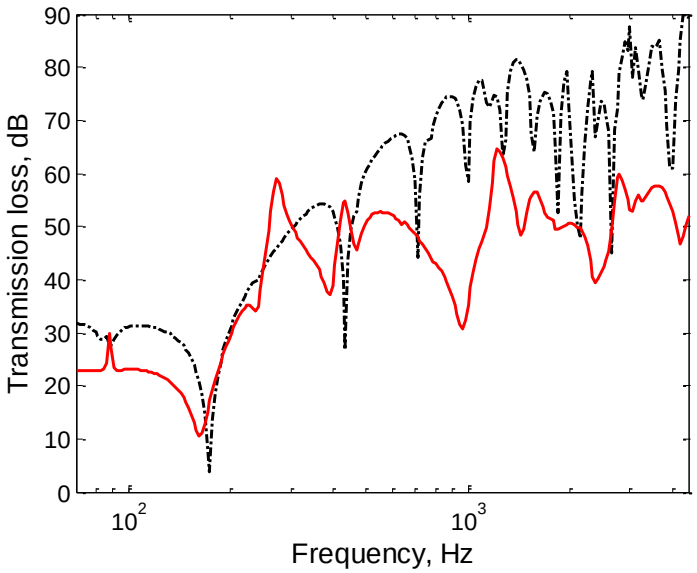

Figure 6.2 TL comparison of the waveguide double panel system with stud removed, vacuum in cavity for normal incidence (— *in-vacuo* model; --- double panel system with enclosed cavity without studs)

6.3 Origin of peaks and dips

To gain insight into the origin of the dips and peaks in the TL of the waveguide double panel system with the studs, some operating deflection shapes from the *in-vacuo* model are provided in Figure 6.3. Plots (a) and (c) correspond to dips in the TL in Figure 6.2 while plots (b) and (d) correspond to peaks. It is clear from Figure 6.3 that the dips are associated with symmetric displacement of the system while the peaks correspond to asymmetric displacement. The symmetric displacement means both that the panels vibrate out-of phase and they have symmetric displacement about the mid-plane. These mode shapes appear similar to the mass-air-mass resonance behaviour. In contrast, in the asymmetric cases the panel on the receiver side has a much smaller displacement than that on the source side. In all the plots in Figure 6.3, the studs constrain the panel in translation but allow some rotation. It is clear that the peaks occur when the deflection of the panel at the radiating side is small so that there is little disturbance to the adjacent fluid.

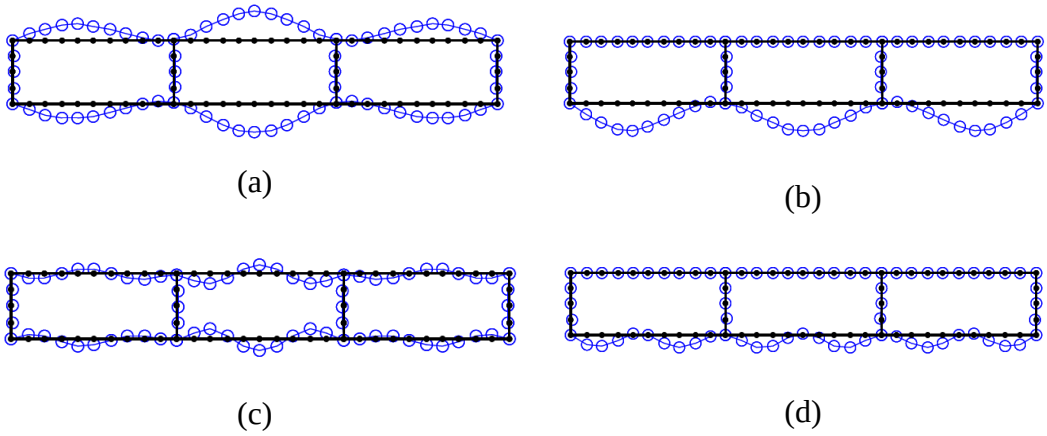

Figure 6.3 Operating deflection shapes of the *in-vacuo* structure for normal incidence on lower panel: (a) 162 Hz (b) 273 Hz (c) 964 Hz (d) 1219 Hz

6.4 Dispersion relations

The dispersion curves of the *in-vacuo* model are shown in Figure 6.4. The results in Figure 6.4(a) illustrate the effect of the studs on the propagating waves in the waveguide double panel system in the $x-$ direction. Compared with the results without studs, shown in Figure 6.4(b), it is clear that adjacent waves are now clustered into groups of dispersion curves when the studs are present in the double panel system. This dispersion characteristic is dictated by the wave characteristic in the $y-$ direction in which waves are travelling over a repetitive panel-stud system (or periodic structure). The positive interference of the free waves and the reflected ones in the $y-$direction will cause the presence of panel resonances within a bay. Following harmonic spatial expansion [43], the relation of the wavenumbers in the $x-$direction, the $y-$direction to the free bending wavenumber is given by

$$k_B = \sqrt{\kappa^2 + \left(\frac{\mu + 2n\pi}{l}\right)^2} \tag{6.1}$$

where μ is the propagation constant in the $y-$direction and l is the stud spacing. Hence, for the current case, these groups of dispersion curves approach the dispersion curves of a 0.406 m width panel (corresponding to the stud spacing) as indicated by black lines. Such

features will be seen more clearly in section 6.6.1 in which the effect of stud spacing on the TL is investigated.

From a periodic structure theory point of view, it is well known that stop and pass band frequency characteristics can lead to a series of dips and peaks in structural response [111]. A frequency band in which no energy is transmitted in the system is called a stop band. Under such circumstances the vibration is attenuated very quickly in the structure. The opposite situation occurs in the pass bands in which the vibrational energy is transmitted freely. Hence, the dispersion characteristics in Figure 6.4(a) are related to the presence of peaks and dips in the TL in Figure 6.2 as the stop and pass band characteristics across the width mean that only certain waves can exist in the $x-$direction. For the current case, only the odd wave modes are excited for normal incidence so that the corresponding groups of dispersion curves, for example around 165 Hz, 964 Hz, 2.4 kHz and so on, are associated with the dips.

Meanwhile, two steeper dispersion curves cut on at around 640 Hz and 1780 Hz. These correspond to bending waves propagating in the studs. These cut-on frequencies are proportional to $(s+1/2)^2$ with s the s^{th} wave. Thus, for the current case, they correspond to waves in the stud with clamped boundary conditions at the stud-panel connection. However these waves do not appear as features in the TL curves as they are not excited by the incident acoustic field.

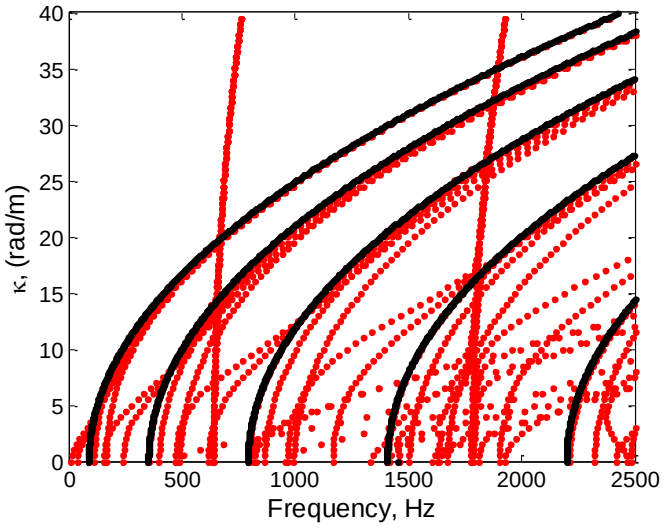

(a)

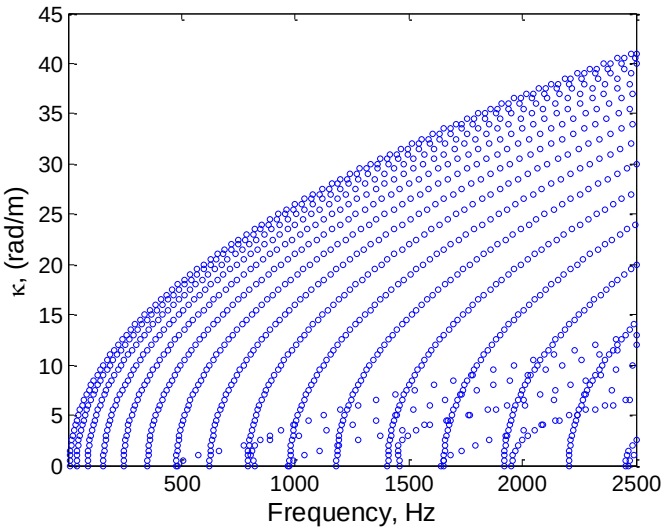

(b)

Figure 6.4. Dispersion curve of the waveguide double panel partition without existence of the air in the cavity: (a) with studs (b) without studs.

6.5 Effect of air in the cavity

For the case of the waveguide double panel system with enclosed air cavity, the sound energy is transmitted from the first panel, at the source side, to the second panel through the air cavity or airborne path. An additional transmission path exists in the system after introducing the studs which act as structural connectors between the panels. This is termed the structure-borne path.

The TL of the full model is compared with the results for the *in-vacuo* system and the system without studs in Figure 6.5 to assess the relative importance of the transmission paths found in the waveguide double panel system. This is of importance in seeking ways to improve the sound reduction performance of the double panel system.

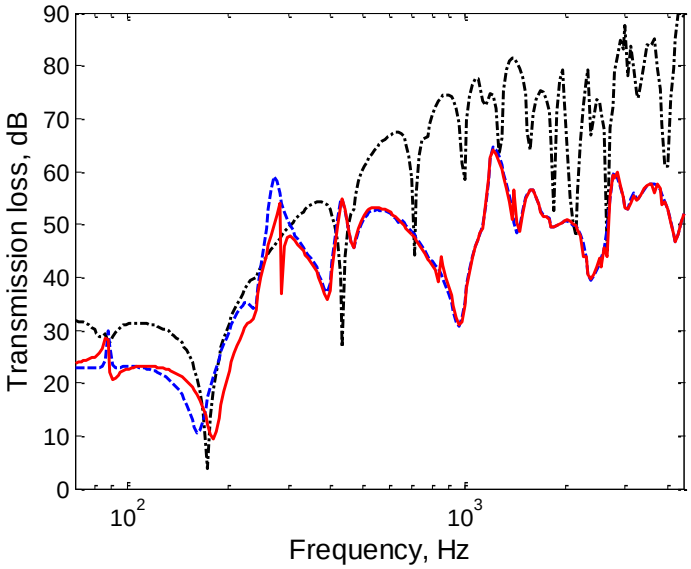

Figure 6.5. TL comparison of the full model and the *in-vacuo* model with the studs for normal incidence (— full model; - - - *in-vacuo* model; – • – double panel system with enclosed cavity without studs).

It can be seen that the TL of the full model is very similar to the *in-vacuo* one for frequencies above 390 Hz. Meanwhile, compared with the results of the model without the studs, the dips due to the standing waves in the cavity are less pronounced in the full model. It can be seen that most of the dips found in the TL curve are now associated with the structure-borne path. Likewise, peaks present in this TL curve also match those in the *in-vacuo* model for the same frequency range. Thus, this shows that the structural path is predominant over the cavity path for the current case. Moreover, the TL of such a system tends to be lower than that obtained without the studs. This indicates that the presence of the studs reduces the TL of the double panel system.

Although the structure-borne path is dominant for the case of the double panel system with the studs, a slightly different behaviour is seen from the comparison at low frequency. As shown in Figure 6.5, it can be identified that below 390 Hz the peaks and dips in the TL curve of the full model are no longer coincident with those found in the *in-vacuo* model. For the current case, this frequency can be identified as the bridge frequency

where the stud starts to be dominant in determining the overall TL behaviour. Nevertheless, it should be borne in mind that such a dominance depends on various parameters that are mainly related to the stiffness of the stud and the air cavity depth. For example, for a less stiff stud transmission through the cavity will become more evident, as will be seen later in section 6.6.4. Hence the result in this section cannot be considered to be general but is case-dependent.

Following the mode coupling method [112] for forced response, the characteristics of interaction of the air in the cavity and panels depend on their resonance frequencies and the excitation frequency. However, in most cases, according to [99, 113] only the zeroth cavity mode is of importance in changing the panel resonance as this mode can couple efficiently with the fundamental mode of panel. Such a situation can be seen from the results of the waveguide double panel system in Figure 6.5. At low frequency the lowest dip of the full model occurs at 180 Hz which is higher than for in the *in-vacuo* model where it is found at 161 Hz. This suggests that the air in the cavity exerts an additional stiffness on the panels. Compared with the case of the double panel system without studs (see Figure 6.2), the frequency associated with this dip is not too far from $f_{MAM,WG}$. Hence, the presence of the studs does not always mean that the structural resonance is dominant over the mass-air-mass resonance but the response in this frequency region is the superposition of the structural and the cavity response. Bradley and Birta discussed in [114] that the structural resonance is dominant in such a system so that the mass-air-mass resonance frequency no longer appears. This seems to be valid only for very stiff studs, i.e. wooden studs, but is not the case here despite the fact that these simplified steel studs are also quite stiff.

6.6 Effect of stud parameters

This section aims to assess the behaviour of the *in-vacuo* model when several parameters associated with the studs are varied. These include the stud spacing, stud stiffness, damping loss factor, geometric form and dimensions of the studs.

6.6.1 Effect of stud spacing

The stud spacing is varied for the same overall panel width, which is now set to 1.8 m. Stud spacing of 600 mm, 300 mm and 200 mm are considered. Hence, there are 3, 6

and 9 bays respectively. All the structures are compared for normal incidence. The height of the stud remains 65 mm.

The effect of the stud spacing can be observed from Figure 6.6. The considerable dip corresponding to the lowest TL increases in frequency as the stud spacing is reduced. The corresponding values are 74.4 Hz, 345 Hz and 790 Hz as indicated by the arrows in the figure. These are approximately equal to the fundamental natural frequency of a single bay of plasterboard with clamped boundary conditions. Moreover, the distance between the dips due to the pass and stop band behaviour also gets wider as the stud spacing is reduced. This is related with the wavenumber distribution in the *y* direction which is inversely proportional to the stud spacing. These results are consistent with the hypothesis of pass and stop band behaviour in the waveguide structure.

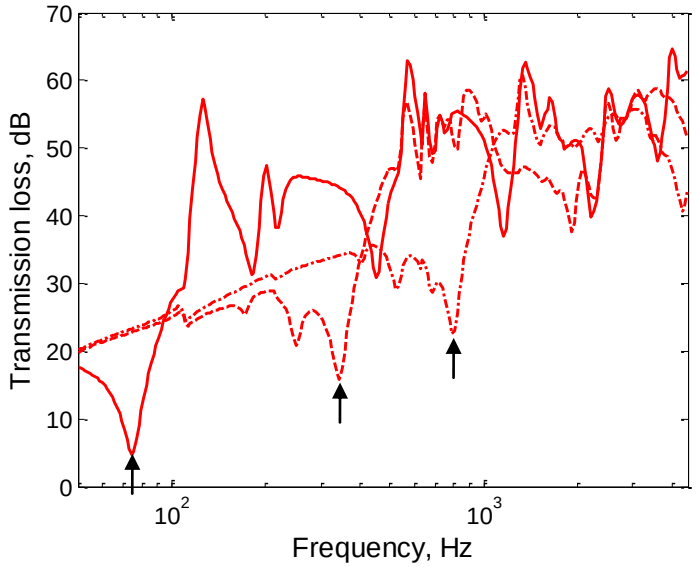

Figure 6.6. Effect of stud spacing on TL of *in-vacuo* model for normal incidence (— 600 mm; - - - 300 mm; – • – 200 mm). Arrows indicate a dip corresponding with fundamental natural frequency of a single bay of each system.

The corresponding dispersion curves for each case are shown in Figure 6.7. It is clear that the number of wave groups reduces as the stud spacing reduces but the number of waves in each group increases. Moreover, as previously stated, the various wave groups also shift toward higher frequency, approaching the dispersion behaviour of a panel with width equal to the stud spacing. The number of waves in each wave group corresponds to the number of bays across the width. Therefore, the stud spacing and the number of the bays influences the TL behaviour of the double panel system.

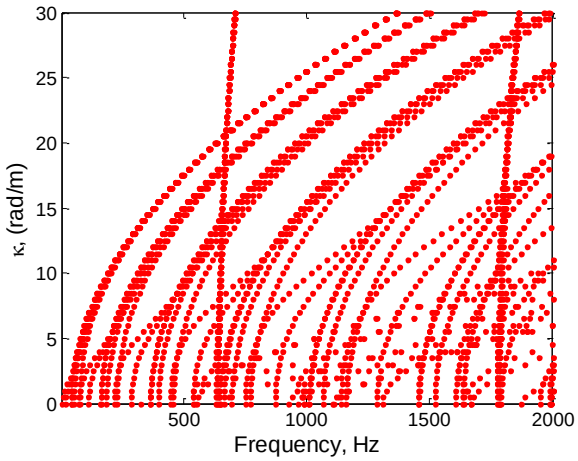

(a)

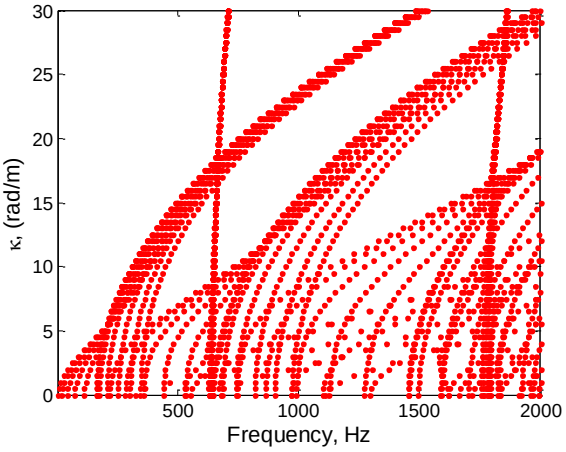

(b)

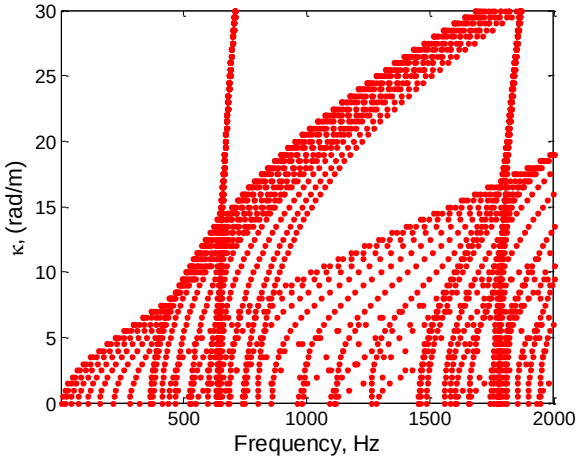

(c)

Figure 6.7 dispersion curves for different stud spacing: (a) 600 mm stud spacing; (b) 300 mm stud spacing; (c) 200 mm stud spacing.

Apart from peak and dips corresponding with the stud spacing, ripples are also found in the TL curve as shown in Figure 6.6 as a consequence of the finite number of bays. They do not appear for infinite structures, e.g. as in Ref. [41].

6.6.2 Effect of stud stiffness

Hongisto [37] found that the stud stiffness affects the TL of a double panel partition. The same tendency is also indicated in [44] where less stiff studs lead to a higher TL. In practical terms, a change in the stiffness can be achieved by modifying the cross-section shape of the stud. For example an "acoustic" stud has a lower stiffness due to the shape of the web which introduces higher flexibility.

In this section, the effect of the stud stiffness is assessed for the waveguide double panel system. For convenience, this is achieved by varying the Young's modulus of the stud material rather than modifying the cross-section shape. A lower Young's modulus means lower stiffness. The rest of the parameters included in the model are unchanged, including the stud spacing of 406 mm.

The effect of the stud stiffness on the TL of the *in-vacuo* model is shown in Figure 6.8(a) for normal incidence. From these results, it can be seen that lower stiffness causes a higher TL. Moreover, the periodic response found previously for $E = 2\times10^{11}$ N/m^2 is retained even with a lower Young's modulus although as the stiffness reduces, this effect becomes less clear. The results are considerably different for the lowest Young's modulus considered ($E = 2\times10^{8}$ N/m^2) where the dip at low frequency reduces to 148 Hz compared with around 180 Hz for the other results. Analogous to the mass-air-mass resonance, this frequency is strongly influenced by the stiffness of the stud. Hence, the lower Young's modulus leads to a lower structural resonance. The same tendency is also seen for the case of oblique incidence at 45° as shown in Figure 6.8(b).

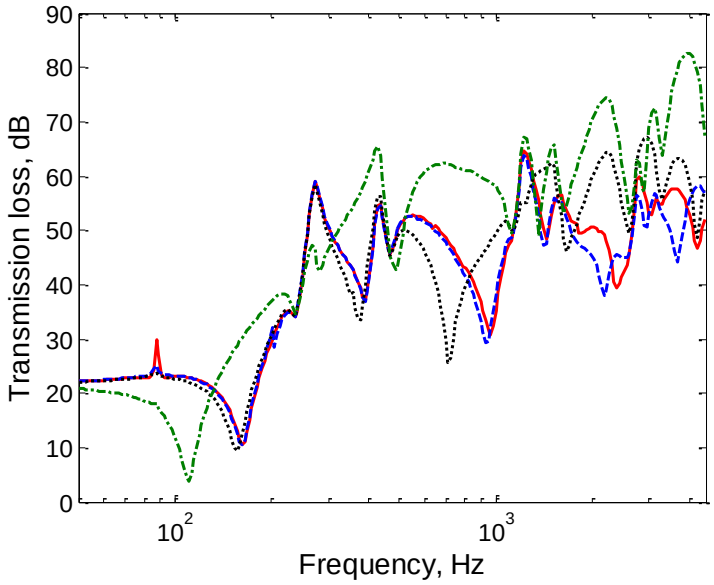

(a)

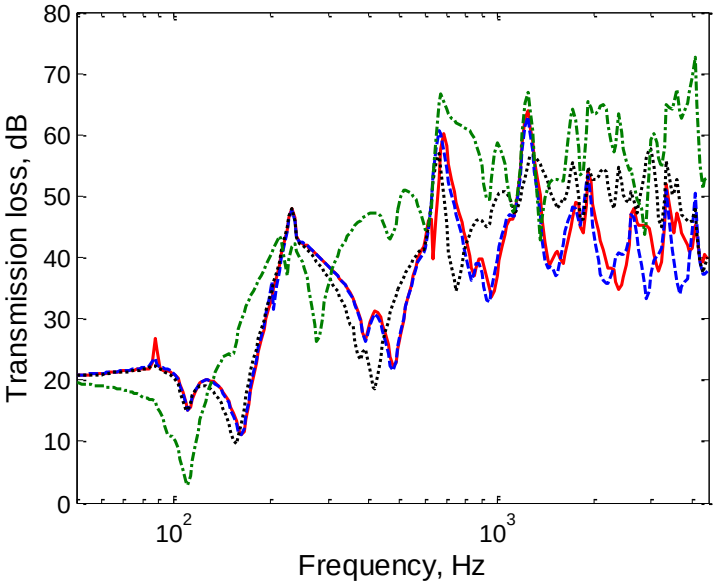

(b)

Figure 6.8. Effect of stud stiffness on TL of *in-vacuo* model: (a) normal incidence; (b) oblique incidence (— $E = 2\times10^{11}$ N/m^2; --- $E = 2\times10^{10}$ N/m^2; ••• $E = 2\times10^{9}$ N/m^2; – • – $E = 2\times10^{8}$ N/m^2).

6.6.3 Effect of stud loss factor

In this section, the damping loss factor of the stud is varied to study its effect on the TL behaviour. For this comparison, three different loss factors are considered which are

factors of ten are larger and smaller than the reference value of 0.01. Meanwhile, the loss factor of the panel is unchanged for all cases.

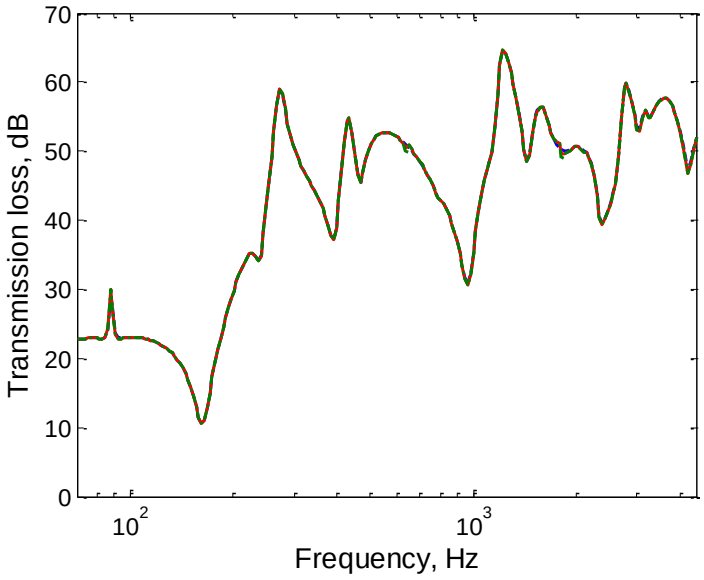

(a)

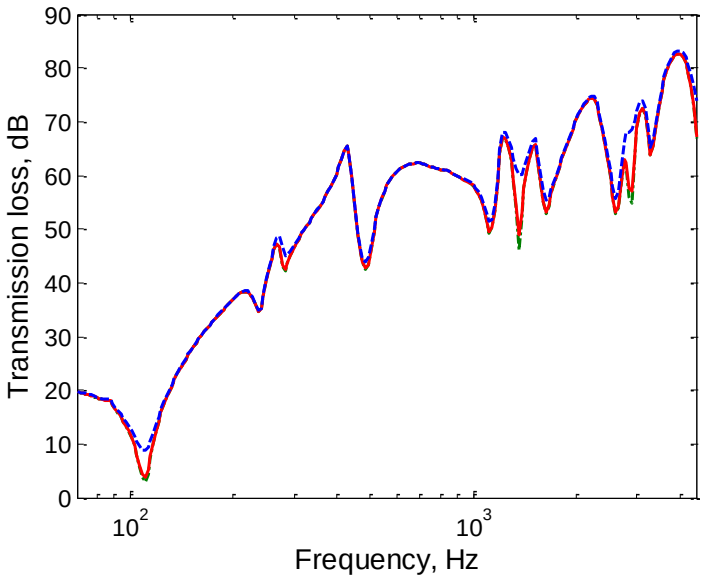

(b)

Figure 6.9. Effect of loss factor on TL of *in-vacuo* model for normal incidence: (a) E $= 2\times10^{11}$ N/m^2; (b) E $= 2\times10^{8}$ N/m^2 (- - - $\eta_{stud} = 0.1$; — $\eta_{stud} = 0.01$; •—• $\eta_{stud} = 0.001$).

Figure 6.9 presents the results. It is clear that the stud loss factor has negligible effect on the TL for all frequencies. This tendency remains even for a much less stiff stud as shown in Figure 6.9(b) in which a higher damping loss factor only affects particular

frequency regions. Hence, changing the stud material to have a higher damping loss factor will not be effective in obtaining better sound insulation unless the stiffness is considerably reduced.

6.6.4 Effect of stud geometric form

The geometric form of the stud affects its stiffness [2, 37, 44]. In practice, various stud geometries are used to achieve a higher sound transmission loss. In this section, the previous results which use the simplified stud, as shown in Figure 6.10(a) are compared with the full C-profile and an acoustic stud, as indicated in Figure 6.10(b) and (c), where the flange parts are now included. The perimeter of the stud is thus changed due to its modified shape. The length of the flange part is taken as the average length of the C-stud specification found in the market that is usually in the range 36 mm to 40 mm. For convenience, the length of the flange is kept the same for the C-stud and the acoustic stud. Hence the geometric detail of the acoustic stud may not exactly represent an actual industrial specification found in practice. Here, 4 plate elements are used to represent the simplified stud while 12 plate elements are considered for the C-stud and 23 plate elements are used for the acoustic stud due to the nature of its cross-section. In the numerical implementation, these studs are attached to each panel through a single node. For the case of the simplified stud, the coupling node exists on either tip of the web part while for the C-stud and the acoustic stud the node exists at the middle of the flange section. It should be noted that any contact between the rest of the flange and the plasterboard is neglected.

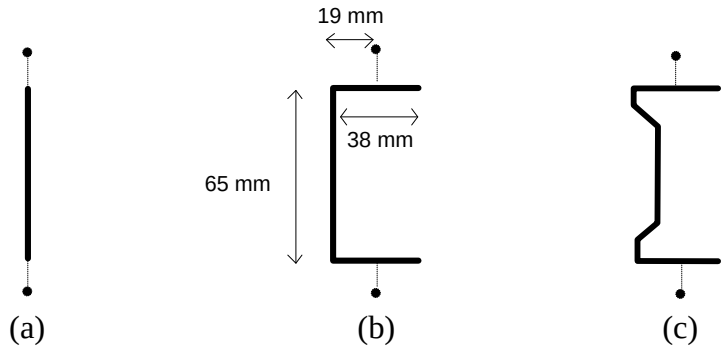

Figure 6.10. Cross-sectional shape of the studs: (a) simplified stud; (b) C-stud; (c) acoustic stud.

The effect of the cross-sectional shape of the studs on the TL can be observed from Figure 6.11. Clearly, the dips at low frequency shift to lower frequency when the simplified studs are replaced with the C-stud and the acoustic stud. From a stiffness point of view, as expected, the results indicate that the lowest stiffness is found for the acoustic stud, followed by the C-stud, while the simplified stud is the stiffest. Considering the results at mid and high frequency, the inclusion of the flange causes a higher TL. In this frequency region, however, the results for the C-studs and acoustic studs are not much different. This may be influenced by the flange length which is taken as identical for both the stud design. Apart from this, the pass-stop band behaviour becomes less apparent in the transmission loss curve for less stiff studs.

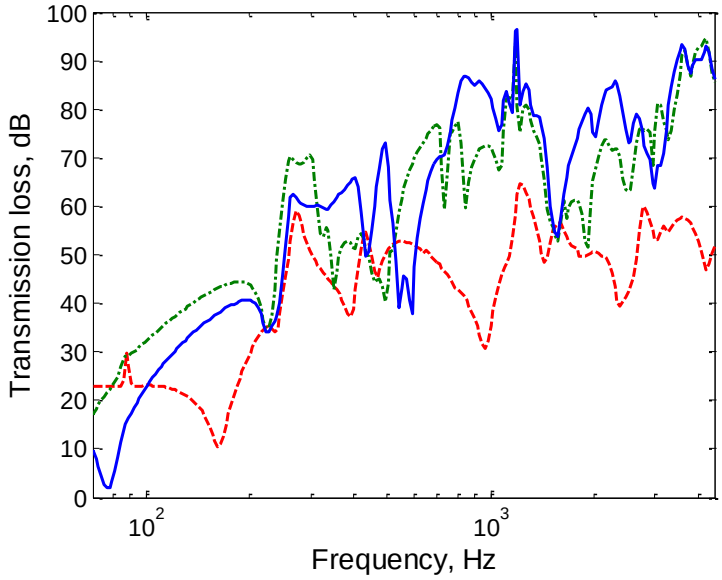

Figure 6.11. Effect of stud geometric form for normal incidence case (--- simplified C-stud; — C-stud; —•— acoustic stud).

Now the air is added again into the cavity to assess its contribution for the case of a less stiff stud. In the numerical model, the couplings of the stud and the fluid are only introduced at the web part of the studs while no coupling exists between the flange parts and the fluid. The *in-vacuo* and full model with C-studs are compared in Figure 6.12. This differs from the results corresponding to the simplified stud (see Figure 6.5), as the lateral cavity modes and internal coincidence effect are now more pronounced at high frequency. Again such cavity modes are present at higher frequency as the lateral cavity dimension is reduced due to existence of the studs. The less stiff stud is believed to support their

presence allowing fluid deformation to occur more easily. This fact also means that transmission through the cavity is not limited to below the bridge frequency. This has been observed for a double panel system with studs where sound absorbing material is present in the cavity [7, 37].

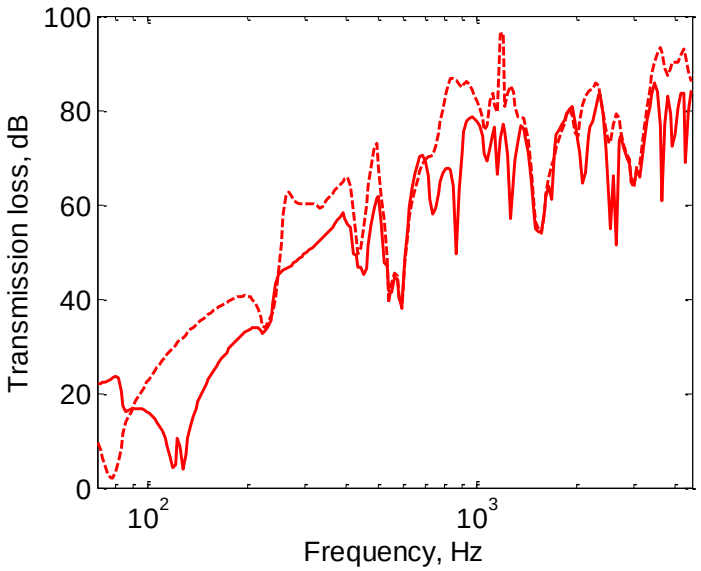

Figure 6.12. TL comparison between *in-vacuo* and full model with C-stud (— full model; --- *in-vacuo* model).

6.7 Diffuse sound field excitation: comparison with measurement

To demonstrate the validity of the model developed so far, the results for diffuse sound field excitation are compared with a measurement result from the literature (TL-93-057) [38]. This measurement data corresponds to a structure comprising a double-leaf gypsum wall with 16 mm plasterboard connected by steel C-studs at 406 mm spacing with 65 mm cavity depth. No geometric detail of the studs is available. Hence the length of flange part is assumed to be 38 mm as above. The total dimensions of the measured sample were 3.05×2.44 m^2 and no sound-absorbing material was present in the cavity. The diffuse sound field in the numerical model is calculated with the upper limit angle equal to 90° while the procedure for calculating it is the same as used in section 5.2.9.

6.7.1 Effect of cavity loss factor

Figure 6.13 presents TL comparisons of the full C-stud for different cavity loss factors η_{cav}. It is clear that the TL of the numerical model increases and becomes closer to

the measurement results as the loss factor is increased. For example, the numerical result is 7 dB lower on average than the measured one for frequencies between the first dip and the critical frequency when $\eta_{cav} = 10^{-2}$ is used. Compared with the results for $\eta_{cav} = 1\times10^{-3}$, a 4 dB improvement is obtained. This result gives R_w of 33 dB. However, little improvement is found at low frequency where the stiffness behaviour is dominant. It is clear that the cavity loss factor has a little effect on the TL in this region. Moreover, when the cavity loss factor is further increased to 10^{-1}, the TL is overestimated at high frequencies compared with the measured one although a good prediction is obtained at mid frequency. Consequently the numerical result has an R_w of 37 dB which is 1 dB higher than found in the measured result.

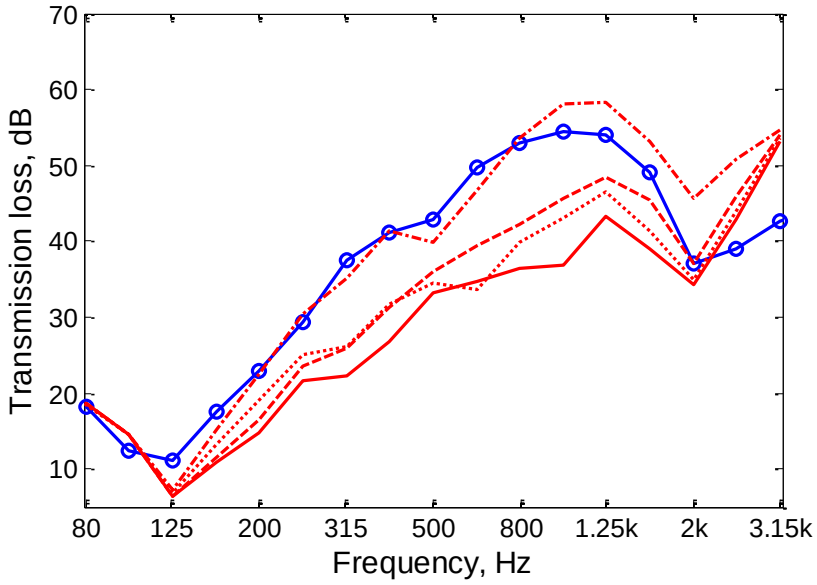

Figure 6.13. TL comparison of measured result and numerical results (WANDS) for different cavity loss factor η_{cav} (— $\eta_{cav} = 10^{-3}$; - - - $\eta_{cav} = 10^{-2}$; – • – $\eta_{cav} = 10^{-1}$; • • • frequency-dependent cavity loss factor; – ○ – measurement TL-93-057 [38]).

Alternatively, frequency-dependent cavity loss factors can be used in order to achieve better prediction results over a wider frequency range. Such an approach was used by Price and Crocker in [26] when predicting the TL of a double panel system using Statistical Energy Analysis. However, their results are not directly applicable to this case as no sound-absorbing material is present along the edges of the double panel system. An

equivalent sound absorption coefficient $\bar{\alpha}_0$ for the case of no edge absorption is required accordingly. According to Brekke [51], based on measurement results, $\bar{\alpha}_0 = 0.275$ can be used for 65 mm depth cavity. The calculation of the cavity loss factor based on a value of $\bar{\alpha}_0$ is provided in Appendix E. It should be noted that in such a model a constant value of $\bar{\alpha}_0$ leads to a frequency-dependent loss factor. From Figure 6.13, it can be seen that the use of the "frequency-dependent cavity loss factor" allows the TL behaviour of the numerical model to become closer to the measured one at low and mid frequencies without introducing overestimated results at high frequencies. The corresponding R_w is 33 dB. Nevertheless, this approach tends to be hard to realize and there is no strong physical basis for obtaining the loss factor except when the edge absorber is present in such a system.

6.7.2 Effect of simplified cross-section stud shape

It is clear that the simplified stud model leads to a considerable underestimate of the TL particularly at high frequencies as shown in Figure 6.14; for example at 1 kHz the results differ by 21 dB. Moreover, the dip at low frequency occurs at a higher frequency than in the measurement and a higher TL occurs at low frequency, below the frequency of the first dip, than in the experimental result. The numerical results are closer to the measured ones at mid and high frequencies when the full C-stud shape is implemented but there is still a discrepancy of up to 18 dB. Above the critical frequency, however, the TL of the numerical model tends to be higher than that of the measurement. Apart from this, the inclusion of the flange part in this current case allows the numerical model to have a more reasonable result at low frequency where the first dip is situated in the same frequency region as the measurement. Despite this, in terms of weighted sound reduction index R_w, the full C-stud has a slightly lower R_w of 30 dB, because of the reduced TL at 125 Hz and 160 Hz, while that of the simplied stud is 31 dB. Meanwhile, R_w of the measured one is 36 dB. Therefore, both the results are 5 to 6 dB lower in terms of R_w than found in the measured result. The result becomes closer to the measured one when using an average cavity loss factor of 2.7×10^{-2} from [26] which gives R_w of 34 dB.

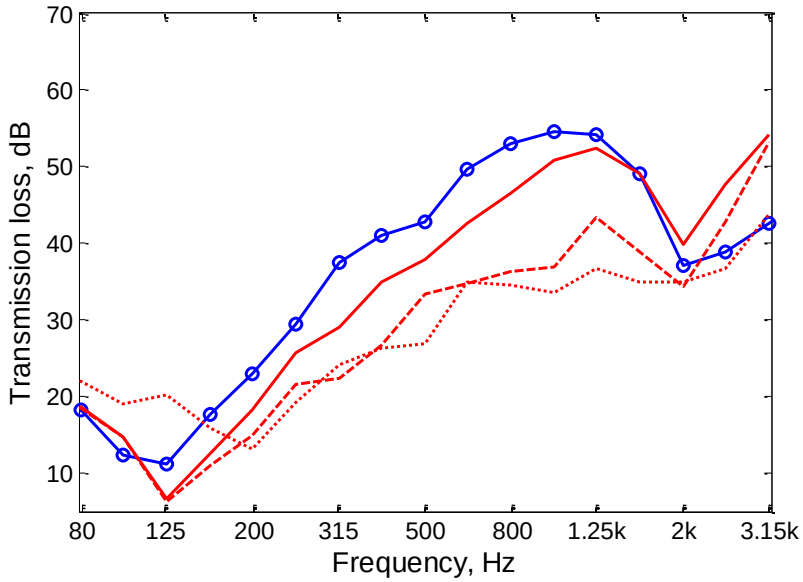

Figure 6.14. TL comparison of numerical results (WANDS) and measured one for the case of 65 mm cavity depth (C-stud: — $\eta_{cav}=2.7\times10^{-2}$, - - - $\eta_{cav}=10^{-3}$; • • • simplified stud with $\eta_{cav}=10^{-3}$; – ○ – measurement TL-93-057 [38]).

6.7.3 Effect of limiting angle

To see the effect of the upper limit angle $\theta_{\lim}$, this parameter is varied between 60° and 90°. The C-stud case with the cavity loss factor η_{cav} of 10^{-3} is selected to demonstrate the effect of the limiting angle. The results are presented in Figure 6.15. It is clear that reducing the limiting angle increases the TL at high frequency, e.g. 3 dB higher TL is obtained for $\theta_{\lim}=80^{\circ}$ around 1 kHz so that the R_w increases from 30 dB to 31 dB. This effect becomes significant down to lower frequency with reducing limiting angle and the results become closer to the measured ones, e.g an R_w of 35 dB is found where the upper limit angle is set to 60°. However, with reducing upper limit angle the results are overestimated at high frequency particularly around the critical frequency. Moreover the dip in the TL around the critical frequency becomes less apparent. At low frequency, negligible effect is found.

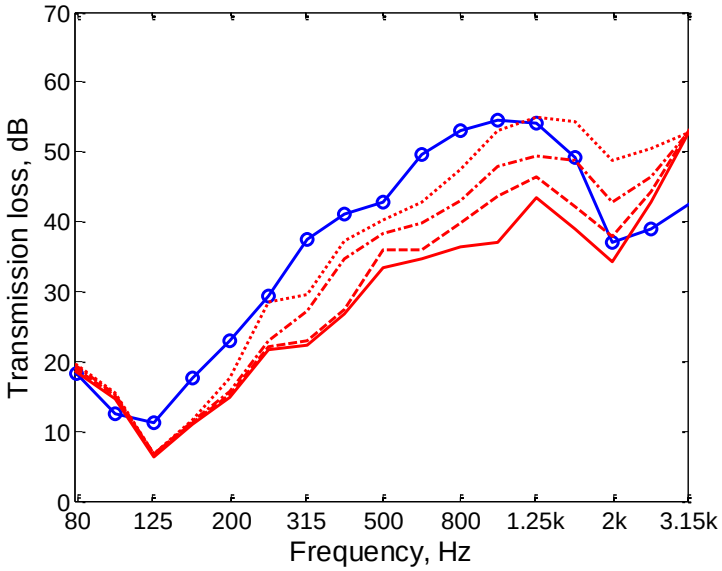

Figure 6.15. TL comparison of measured result and numerical results (WANDS) for different upper limit angle $\theta_{\lim}$ (— $\theta_{\lim}=90^{\circ}$; --- $\theta_{\lim}=80^{\circ}$; – • – $\theta_{\lim}=70^{\circ}$; • • • $\theta_{\lim}=60^{\circ}$; – ○ – measurement TL-93-057 [38]).

6.7.4 Effect of air stiffness

Regarding the TL behaviour at frequencies between the first dip and the critical frequency, it is instructive to investigate the role of the air stiffness in the cavity. Another motivating factor is that a discrepancy remains from the comparisons particularly around the first dip (or the "mass-air-mass" resonance) even when the cavity loss factor has been increased considerably. The air stiffness is proportional to the air density and inversely proportional to the cavity depth. Hence, in order to change the air stiffness in the model, the air density ρ_o is reduced to half of its original value in order to get a lower bulk modulus of the air $\left(\rho_0 c^2\right)$ while the cavity loss factor is kept at 10^{-2}. The results can be seen in Figure 6.16. Compared with the TL of the numerical model with the original air stiffness value, it can be seen that the reduced stiffness causes the TL of the numerical model to be higher at frequencies above the "mass-air-mass" resonance frequency hence the result becomes closer to the measured one. This produces a weighted sound reduction index $R_w = 35$ dB which is only 1 dB lower than the measured result, which has $R_w = 36$ dB. A distinct improvement can be observed at low frequency at which the cavity loss factor had a little effect. Moreover, the "mass-air-mass" resonance frequency shifts to a

lower frequency but it is still acceptable compared with the measured result. This improvement implies that the air behaviour in the cavity is not only influenced by dissipative mechanisms but also by processes affecting the air stiffness. One possible cause of this is the existence of holes commonly found in real steel studs. Hence the air in the cavity is not totally enclosed between two adjacent studs. This has been neglected in the numerical model. Moreover, the sample may not be completely air-tight as small leaks effectively lead to a reduction in stiffness. However, the use of the reduced air stiffness, by introducing ρ_{air} = 0.6 kg/m^{3,} should be used with caution while its mechanism requires further investigation.

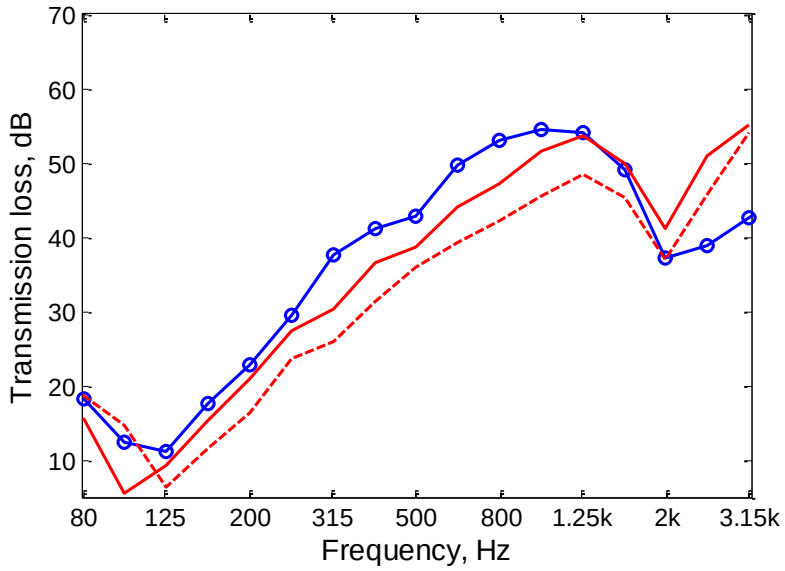

Figure 6.16. TL comparison of measured result and numerical results (WANDS) for different air stiffness with cavity loss factor of 10^{-2} (— ρ_{air} = 0.6 kg/m^3; --- ρ_{air} = 1.21 kg/m^3; – ○ – measurement TL-93-057 [38]).

It can be demonstrated that a better prediction result for the previous case, where $\rho_{air} = 0.6$ kg/m^3, can be obtained by combining this with an increased the cavity loss factor of 2.7×10^{-2} (previously 10^{-2}) as shown in Figure 6.17. The TL behaviour of the numerical model is now closer at low and mid frequencies but the results at high frequencies are overestimated. This result gives $R_w = 36$ dB which is equal to the measured one. Compared with the numerical result where $\eta_{cav} = 10^{-1}$ and $\rho_{air} = 1.2$ kg/m^3

are used, also shown, this approach improves the result in frequency range between 125 Hz and 200 Hz. Moreover, $\eta_{cav} = 10^{-1}$ cannot be justified in experimental results (cf. [51]).

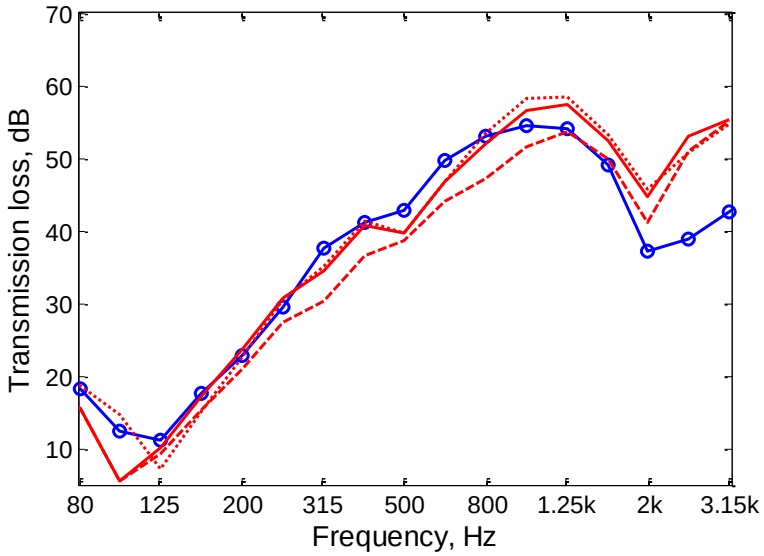

Figure 6.17. TL comparison of measured result and numerical results (WANDS) and for half air stiffness with different cavity loss factor (— $\eta_{cav} = 2.7\times10^{-2}$; --- $\eta_{cav} = 10^{-2}$; ••• $\eta_{cav} = 10^{-1}$ and $\rho_{air} = 1.21$ kg/m^3; – ○ – measurement TL-93-057 [38]).

The case of the same system with full C-stud and a larger 90 mm cavity depth is now considered. The cavity loss factor is set to 10^{-2} while the reduced air density of 0.6 kg/m^3 is assumed to give lower air stiffness. The upper limit angle is 90°. Figure 6.18 presents a comparison of the numerical model and the measurement result (TL-93-418) [38] under diffuse sound field excitation. At low frequency the numerical results show a good agreement compared with the measured one, including the dip found at 100 Hz. Some discrepancies are found between the frequency of the first dip and the critical frequency, where the numerical model results are 5 dB lower on average than those obtained by the measurement. This numerical result gives $R_w = 36$ dB compared with $R_w = 39$ dB as found in the measurement. This discrepancy reduces when $\eta_{cav} = 2.7\times10^{-2}$ is used. The improvement can be obtained particularly at frequencies below 1 kHz. The weighted sound reduction index is 39 dB from this curve. Above the critical frequency, however, the numerical model produces a higher TL than the measurement one.

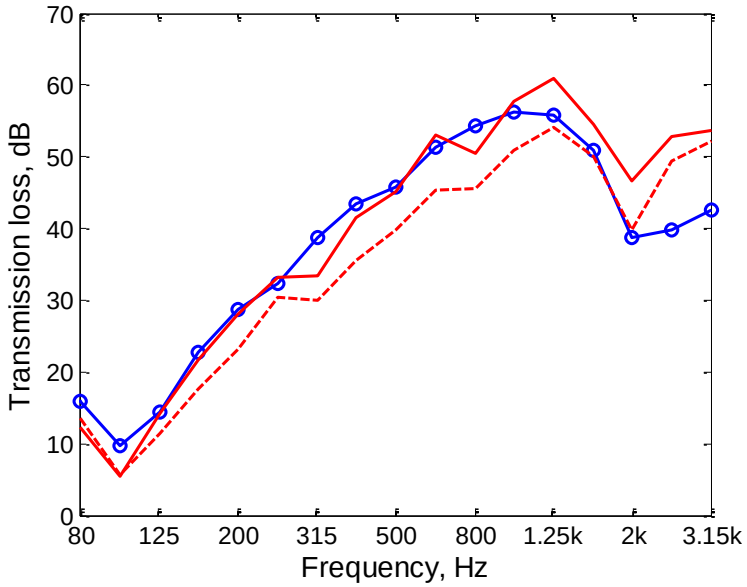

Figure 6.18 TL comparison of numerical result (WANDS) and measurement one for the case of 90 mm cavity depth (— Numerical result for $\rho_{air} = 0.6$ kg/m^3 and $\eta_{cav} = 2.7\times10^{-2}$; - - - Numerical result for $\rho_{air} = 0.6$ kg/m^3 and $\eta_{cav} = 10^{-2}$; - ○ - measurement TL-93-418 [38]).

6.8 Summary

In this chapter, the waveguide double panel system with studs has been modelled using the WFBE method. A finite width of panel is modelled with the studs placed a certain distance apart. The system is infinite in the other dimension. New features are found in the results compared with the existing analytical models, even though some of them take advantage of periodic structure theory to solve the vibro-acoustic problem for such a system. After introducing the studs into the system, a considerable reduction in performance of the waveguide double panel system is found at mid and high frequency. At lower frequencies, the response is a combination of the structural response and the air cavity one.

Regarding the stud behaviour, the results suggest that the stiffness of the stud is an important parameter in determining the total response of the double panel system, particularly in relation to the pass-stop band characteristic that is evident in the results. Such characteristics become less apparent as the stiffness of the studs is reduced. In practical terms, the stud cross-section shape has a critical role in affecting the behaviour of

the sound transmission loss, as it affects the stud stiffness. Conversely, the loss factor of the stud has negligible effect on the results, even for less stiff studs.

The effect of the air in the cavity becomes less significant with increasing frequency for the case of stiff studs so that the stud behaviour is predominant at high frequency. However, for less stiff studs lateral cavity modes and the internal coincidence effect are more significant and reduce the sound transmission loss. Therefore, for the case of an elastic steel stud both the transmission paths need to be handled carefully in order to achieve a good TL.

Comparisons of the numerical results and measurements from the literature suggest that inclusion of an appropriate cavity loss factor is required to achieve more accurate results. The use of a frequency-dependent cavity loss factor can be an alternative approach to optimize the result over a wider frequency range. A reduced air stiffness also needs to be considered to account for practical considerations. Moreover, it is of importance to include the detail in terms of elastic stud geometry. Meanwhile, the reducing of upper limit angle leads the results to be closer to the measured one but they are overestimated at high frequency. At low frequency, its effect is negligible. Further evidence of these phenomena will be seen in Chapter 7 in which the numerical model results are compared with measured ones.

Chapter 7. Experimental validation

In this chapter, measurement results are presented in order to validate the results, particularly in relation to the effect of the finite cavity on the transmission loss. To meet this objective, test specimens consisting of identical 9.5 mm thick plasterboards and a 30 mm cavity depth without sound absorbing material are used. The dimension of cavity has then been varied by adjusting the width or increasing the cavity depth. Subsequently, a mechanical connection in the form of a steel C-stud is introduced in the cavity to look further at its effect on the transmission loss of such systems, as well as to obtain further evidence of the validity of the numerical model developed based on the WFBE method.

7.1 Experimental setup and procedure

7.1.1 Reverberation chamber

The measurements were conducted in the ISVR transmission suite facility situated in building 15 of the University of Southampton. The transmission suite comprises a large reverberation chamber and a smaller one which have volumes of 348 m^3 and 131 m^3 respectively. An aperture size of 2.02 $\times$ 2.42 m^2 exists between the two reverberation chambers in which a test specimen can be fitted.

The source room is excited by broadband noise. The sound field approximates a difuse field above the Schroeder frequency f_s. This frequency ensures that on average at least three eigenmodes occur within the half-power bandwidth of one resonance. It is given by [115]

$$f_s \approx 2000\sqrt{\frac{T_{60}}{V}} \tag{7.1}$$

where T_{60} is the reverberation time of the room and V is the room volume. Considering the measured reveberation time and the room volume of each reverberation chamber, the Schroeder frequency of the large reverberation chamber is approximately 315 Hz while 400 Hz for the smaller reverberation chamber. Hence, above these frequencies, a diffuse

sound field can be assumed in each reverberation chamber. The newer standard ISO-10140 part 5 [116] requires a reverberation time between 1 s and $2(V/50)^{2/3}$ s where V is the room volume in order to get measurement results that are down to 100 Hz.

According to those values of the Schroeder frequency, evalution for the results in terms of weighted sound reduction index R_w in later sections will only incorporate 11 frequency bands starting from 315 Hz to 3150 Hz. Hence, the total of unfavourable deviations becomes 22 dB rather than 32 dB for 16 bands as described in ISO 717 part 1 [117]. Due to this different definition in R_w , the weighted sound reduction index throughout this section is denoted as $\bar{R}_w$.

7.1.2 Test specimen parameter

Four test specimens are considered for this experimental validation. For convenience, the test specimens are labelled TS1, TS2, TS3 and TS4 throughout this chapter. The parameters of each test specimen are listed in Table 7.1 with the dimensions of all specimens nominally 0.9×2.4 m$^{2.}$ They are chosen to be long and thin so that waveguide structural properties are expected to apply. Moreover, this is a typical dimension of the plasterboard found in the market so that the specimens could be easily constructed in practice. All the test specimens are shown in Figure 7.1. Timber section frames were placed on their perimeter to hold the plasterboard samples when they were fitted to the aperture. A cavity depth of 30 mm is considered here in order to ensure that f_{MAM} is not too low relative to the Schroeder frequency of the reverberation chambers as discussed in section 7.1.1. With this cavity depth, the mass-air-mass frequency is expected at around 273 Hz. Moreover, a 48 mm cavity depth is considered in TS3 and TS4 corresponding to the smallest steel stud thickness found in the market. A smaller cavity depth would be more suited to meeting the measurement objective as it leads to higher f_{MAM} which would ensure that the low frequency transmission loss behaviour could be clearly seen under the diffuse sound field. However, it is not further considered here due to technical constraints during construction. It should be noted that the use of the timber frames gives rise to potentially higher flanking transmission compared with steel and brick ones, as discussed in [118], so that the overall TL may be lower than the actual one particularly at high frequency. Despite this, timber frames are used for ease of construction

considering the aperture dimension. Moreover, this should not be a critical aspect in this measurement as all test specimens were treated in the same approach. Hence differences in the TL behaviour corresponding with the cavity dimension and steel stud are still expected to exist.

Table 7.1. Parameters of test specimens

TS	Plasterboard	Cavity (width × depth)	Mechanical link
1	Identical 9.5 mm	2020 mm × 30 mm	-
2	Identical 9.5 mm	900 mm × 30 mm	-
3	Identical 9.5 mm	900 mm × 48 mm	-
4	Identical 9.5 mm	900 mm × 48 mm	steel C-stud

For cases TS2-TS4, cavity blockers were put in the cavity in order to reduce the width of the air cavity to 0.9 m from its original dimension of 2.02 m as applied for TS1. These blockers, made of timber, were arranged in such a way so that they do not act as a "vibration bridge" for the section frames. To realize this, a silicone rubber sealant was put between the blocker edges and the timber frames (see Figure 7.2). For this measurement, a steel C-stud was only introduced in TS4 which basically has the same specification as TS3. The steel C-stud was attached to the panel using screws which were spaced on 300 mm.

As the test specimen has smaller dimension compared with the aperture size, filler walls were required so that the test specimen can be fitted into a 0.9×2.4 m^2 aperture. According to ISO 140 part 3 [119], 15 dB higher reduction is required compared with the test speciment. Therefore, four layers of 15 mm sound bloc with surface density of 12.6 kg/m^2 were used. They are expected to provide approximately 15 dB higher transmission loss.

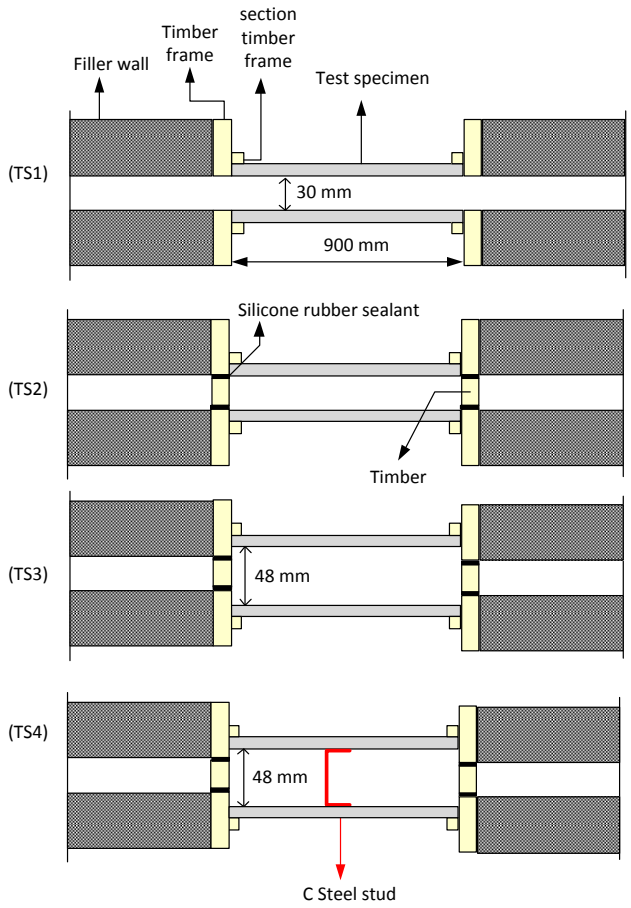

Figure 7.1. Sketch of test specimens considered in the measurement.

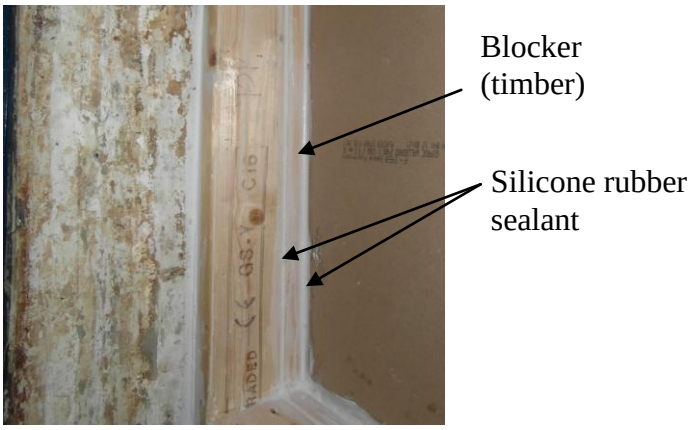

Figure 7.2. Timber cavity blocker

7.1.3 Measurement procedure

The measurement was conducted according to ISO 140 part 3 [119] which describes laboratory measurements of airborne transmission loss. The large reverberation chamber was designated as the source room while the smaller one was the receiver room. A random broadband sound source was used. Measurements were then performed at eight microphone different positions in order to get spatial averaging. The same number of measurement positions was also used in the receiver room. For each position, the measurement data was captured for a 30 s averaging time. Meanwhile, the measurement of reverberation time T_{60} was carried out in the small reverberation room following ISO 354 [120] in order to obtain the equivalent sound absorption A. For this, four different configurations of microphone and loudspeakers were used and the measurement was repeated five times for each configuration. Finally, T_{60} was obtained through an averaging a number of multispectral [121].

Figure 7.3 illutrates the measurement setup in the large reveberation chamber. During the measurement, four Brüel & Kjaer $1/2''$ free field microphones type 4165 were used to measure the acoustic pressure in the source and receiver rooms, with two microphones for each room. These microphones were connected to a Brüel & Kjaer front end PULSE type 3650C in the control room in order to capture the data in $1/3$ octave frequency bands with centre frequencies from 50 Hz to 10 kHz. This system was also used to generate broadband noise for the same frequency range through the loudspeaker which was located close to one corner of the room about 1 m from the wall. This loudspeaker was moved to an other corner for a different set of microphone positions. Before starting the transmission loss measurement, the microphones were calibrated using a Brüel & Kjaer piston calibrator type 4230.

Figure 7.3. Measurement setup in the reverberation chamber

The measured transmission loss TL is given by [119]

$$TL = L_{p1} - L_{p2} + 10\log_{10}\left(\frac{S}{A}\right) \quad \text{dB} \tag{7.2}$$

where L_{p1} is the average sound pressure level in the source room, L_{p2} is the average sound pressure level in the receiver room, S is the area of the test specimen and A is the equivalent sound absorption area in the receiver room. A is determined from the reverberation time of the receiver room using Sabine's formula

$$A = \frac{0.16\ V}{T_{60}} \tag{7.3}$$

A temperature of 19° C and humidity of 62% were measured in the reverberation chamber during the measurements.

7.2 Preliminary test

In order to comply with the standard ISO 140 Part 3 [119], a preliminary test was conducted first to ensure that the filler wall achieves a transmission loss at least 15 dB higher compared than that of the designated test specimens. For this test, the whole partition was constructed using the arrangement of the filler wall as shown in Figure 7.4.

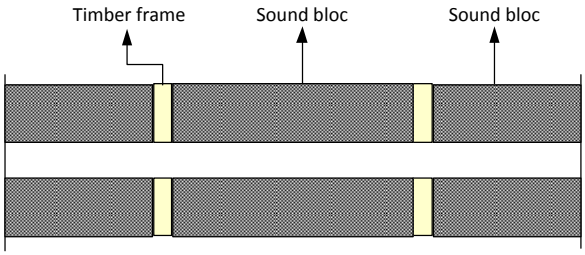

Figure 7.4. Sketch of filler wall during preliminary test.

Figure 7.5 presents the TL of the filler wall. Considering the sound pressure level obtained particularly in the receiver room L_{p2}, some corrections need to be applied to the measured sound pressure level as the level is comparable to that of background noise at high frequency as shown in Figure 7.6. It is clear that L_{p2} at 5 kHz is only 8 dB higher than the background noise. Hence, in accordance with ISO 140 [119], the following equation is used to apply such corrections:

$$L = 10\log\left(10^{L_{p2}/10} - 10^{L_b/10}\right) \quad \text{dB} \tag{7.4}$$

where L is the adjusted sound pressure level, L_{p2} is the measured sound pressure level combined with background noise and L_b is the level of background noise. At 6.3 kHz the level difference is less than 6 dB which is the limit allowed in the standard. Due to the background noise issue, no results related with frequencies above 5 kHz are considered further. For the case of TS1, TS2, TS3 and TS4, the measured sound pressure level shows a difference in level greater than 15 dB compared with the background noise in this frequency region as indicated in Figure 7.6. Hence, no correction is applied for those results.

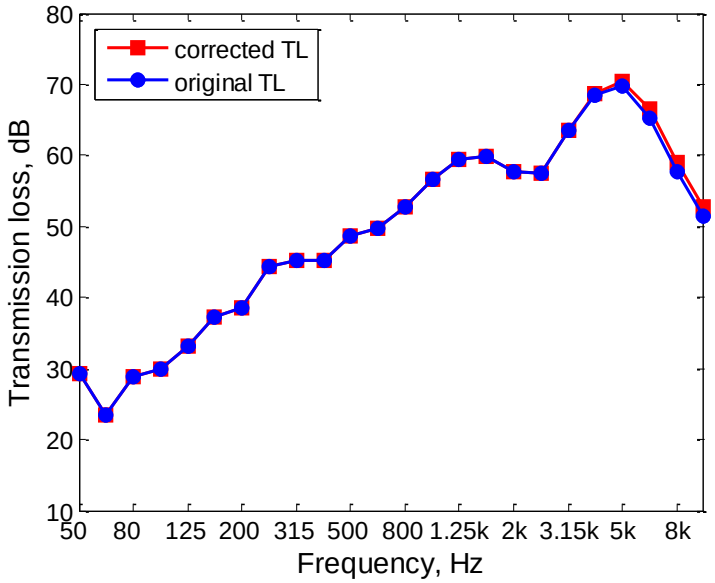

Figure 7.5. TL of filler wall.

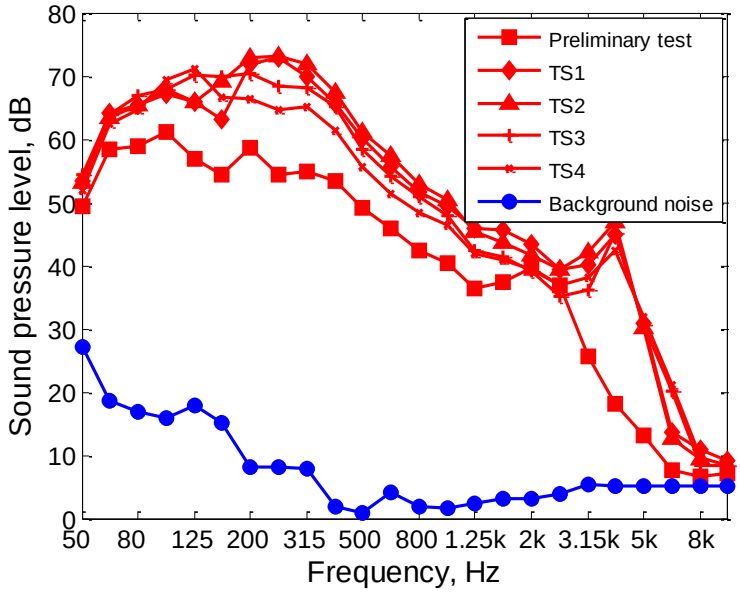

Figure 7.6. Sound pressure level at receiver room and compared with that of background noise when the filler wall or each test specimen fitted into the aperture.

Figure 7.7 presents the transmission loss of the filler wall compared with that of TS1. It can be seen that the transmission loss of the filler wall is between 14 dB and 23 dB greater than TS1 except below 125 Hz and around 2.5 kHz which are in the range of 8 to 10 dB. Consequently, it is expected that sound transmission through the filler wall can be disregarded, so that the measurement results of all test specimens are expected to be valid

for the frequency range of interest. From this figure, it can also be seen that there is a dip at 63 Hz in both the curves which may be due to the influence of room modes.

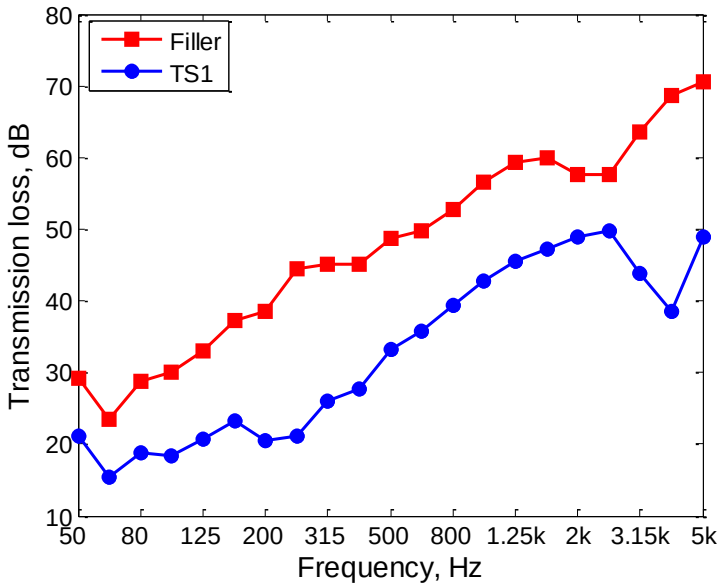

Figure 7.7. Transmission loss comparison between filler wall and TS1

7.3 Effect of air cavity dimensions

Changing the air cavity dimensions is expected to affect the transmission loss as discussed in Chapter 5. Such a tendency is evident in the measurement results as shown in Figure 7.8. It can be seen that the narrower cavity leads to a lower transmission loss below the coincidence dip at 4 kHz down to 160 Hz, although such a tendency is not seen at frequencies between 1.25 kHz and 2 kHz. Considering the frequency region, apparently this lower TL is not related with additional flanking transmission through the timber frame as indicated in [118]. Meanwhile, a larger cavity depth causes a higher transmission loss is evident for TS3, where the cavity depth was increased from 30 mm to 48 mm. For all configurations, the coincidence dip at high frequency is found around 4 kHz.

Numerical models for these structures were developed assuming a cavity loss factor of 2.7×10^{-2}. This is chosen based on the results in section 6.7 in which this value allows the numerical models to produce reasonable results compared with published experimental data. As mentioned before, it should be borne in mind that this value should be used with caution and can be considered as an ‘empirical fix’. Hence this may be different for different circumstances and modelling approach. Simply supported boundary conditions were assumed for all models. 48 elements are used to cover 0.9 m width plasterboard and

the boundary element mesh is extended by 0.675 m beyond the structure width on each side. Under such circumstances, the model is expected to be acceptable for a lowest frequency of around 76 Hz due to the width of the baffle and up to 4.5 kHz at high frequency at which the acoustic wavelength equals 0.076 m. The rest of the properties are the same as in the numerical model developed in section 5.2 except the cavity width was extended to 2.2 m beyond the structural width to model configuration TS1. For the TS1 model, the number of elements for the plasterboard is reduced to 22 elements in order to allow the air cavity, which is coupled to the plasterboard, to be modelled properly considering maximum number of nodes and elements that can be handled by WANDS. Hence, the result of this model is only acceptable up to 2.1 kHz while the lowest frequency limit is the same as the other models. Material properties used in the numerical model are listed in Table 7.2. They are obtained based on typical properties of plasterboard and steel rather than measurement.

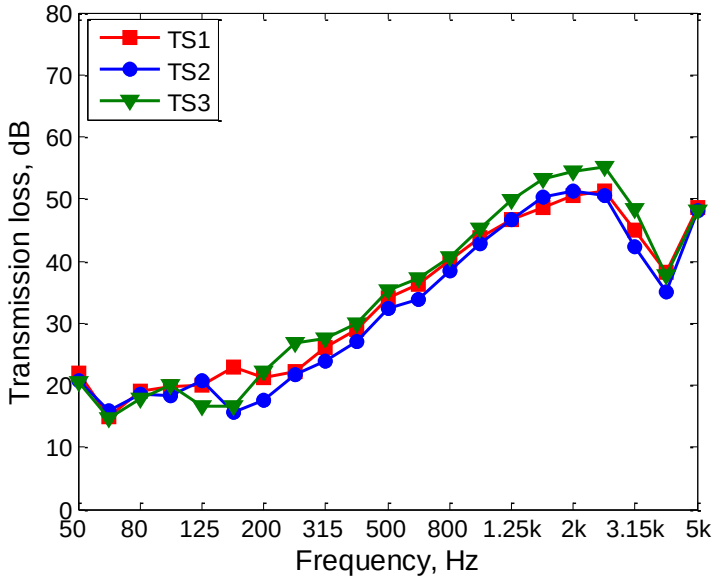

Figure 7.8. Transmission loss of TS1, TS2 and TS3

Table 7.2. Material properties used in numerical models (unless otherwise stated)

Properties	Plasterboard	Steel
Young's modulus, E (N/m^2)	2.5×10^9	2×10^{11}
Poisson's ratio, v_p	0.3	0.28
Density (kg/m^3)	663	7800
Thickness, h (mm)	9.5	0.5

The numerical results are compared with the experimental results in Figure 7.9 for TS1 and TS2. It can be seen that the same tendency is obtained between those configurations as the measurement results. The narrower cavity has a higher stiffness than the wider one, giving a higher f_{MAM}. Agreement between experiments and the numerical model is less good below 250 Hz; this is likely to be affected by modal room response in the experiments results where the diffuse sound field assumption is expected to be less well satisfied. In 1/3 octave bands, the dip occurs between the 3.15 kHz and 4 kHz and is less distinct than the measurement. This critical frequency can be more clearly seen when the results are presented in narrow band e.g. for the case of TS2 as shown in Figure 7.10. From this figure, the dip is found at around 3.6 kHz from the numerical results while it is 3.9 kHz from the measurement result. Therefore, those dip frequencies differ by 8%.

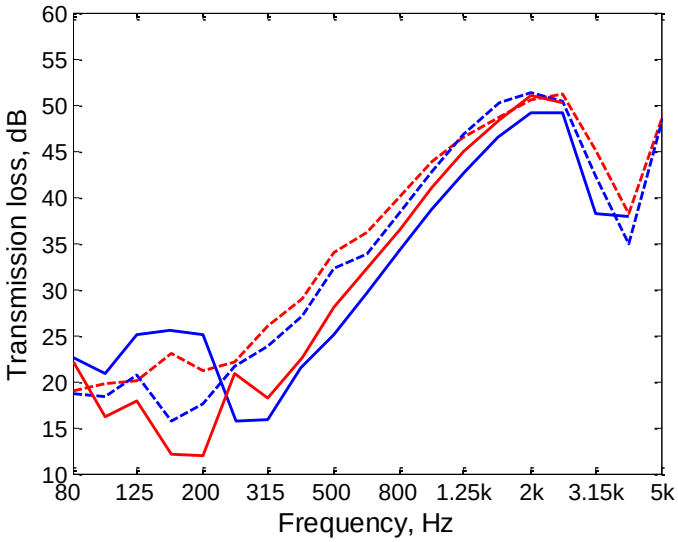

Figure 7.9. TL comparison of numerical results and measurements ones in 1/3 octave frequency bands (--- TS1; - - - TS2; — numerical model for TS1; — numerical model for TS2).

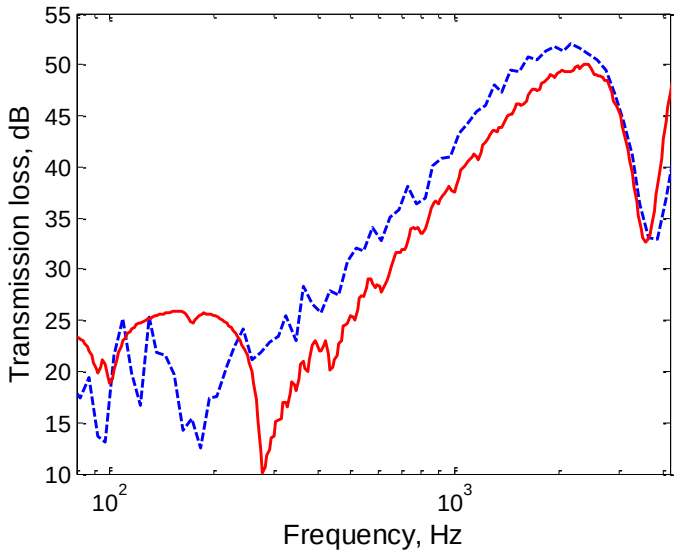

Figure 7.10. TL comparison of numerical result and measurements one for TS2 in narrow bands (--- measurement; — numerical model).

Figure 7.11 presents the TL differences between TS1 and TS2 for both the measurement and numerical results. The TL differences of 1 dB to 3 dB are found in the numerical results while the TL differences of 1.8 dB to 2.4 dB occur in the measurement results for frequencies between 250 Hz and 1.25 kHz. Beyond this frequency region, negative TL differences are found in the measurement results which indicate the TL of TS2 is higher than that of TS1.

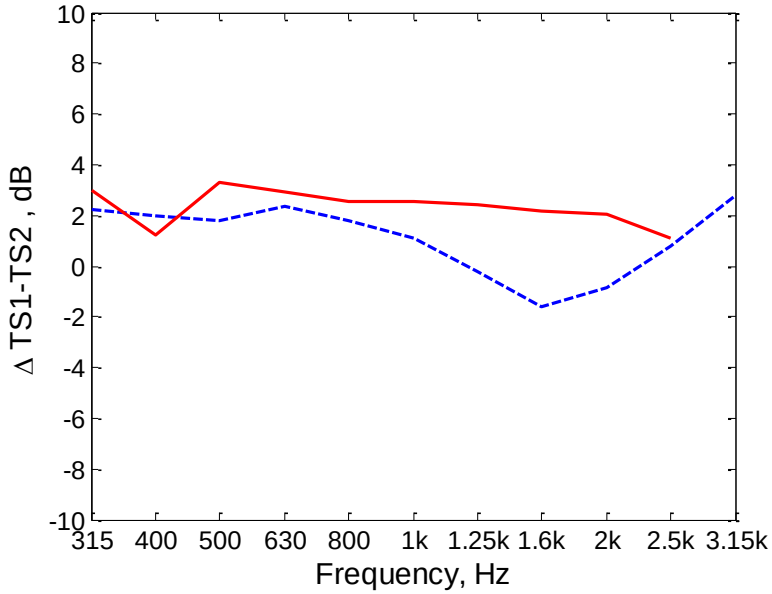

Figure 7.11. The difference in the transmission loss between TS1 and TS2 (— Numerical model; --- Measurement)

Figure 7.12 shows the results separately for each test specimen. It can be seen from Figure 7.12(a) that the numerical model results are 2 dB to 7 dB lower than the measured ones for the case of TS1, which causes $\bar{R}_w$ of the numerical result to be lower than that of the measurement result. For the current case, $\bar{R}_w$ of the numerical model result is 35 dB while that of the measured one is 41 dB. This tendency is also evident for the case of TS2 as shown in Figure 7.12(b) where the numerical model result is 4 dB to 7 dB lower than measurement result. It is found that $\bar{R}_w$ of the numerical model is 33 dB while $\bar{R}_w$ = 39 dB is found for the measured one. This may be caused by the non air tight nature of the air cavity of the test specimens. Such an indication can be seen from Figure 7.12(b), where the result for reduced air stiffness is included. It is clear that the numerical result becomes closer to the measured one after the air stiffness is reduced, giving $\bar{R}_w$ = 39 dB from the numerical result.

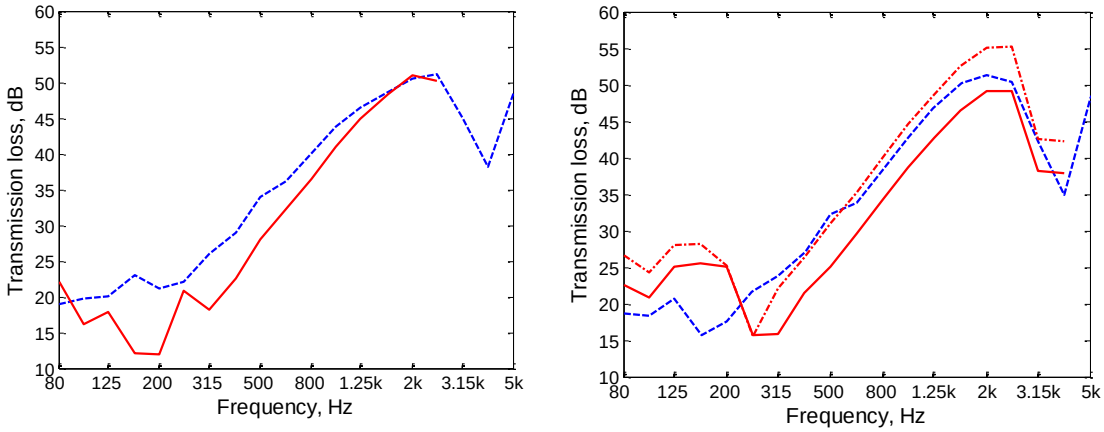

Figure 7.12. TL comparison of numerical results and measured ones: (a) TS1 (b) TS2 (--- measurement ; — numerical model ; – • – numerical model with ρ_o = 0.6 kg/m^3).

For the case of a finite cavity with a bigger cavity depth, the transmission loss increases compared with the narrower specimen, as expected. The numerical model of the same specification shows similar trends, as shown in Figure 7.13. From the measurements, it is found that TS3 gives $\bar{R}_w = 42$ dB while $\bar{R}_w$ of the numerical model for the same specification is 37 dB. Compared with TS2, the TL of TS3 is 2.9 dB to 4.9 dB higher according to the numerical results while it is 3.7 dB to 6 dB higher in the measurement results, as indicated in Figure 7.14. This TL difference leads to a difference of $\bar{R}_w$ by 3 to 4

dB. Despite this, the results of TS2 and TS3 in the measurement results and the numerical ones indicate a similar trend.

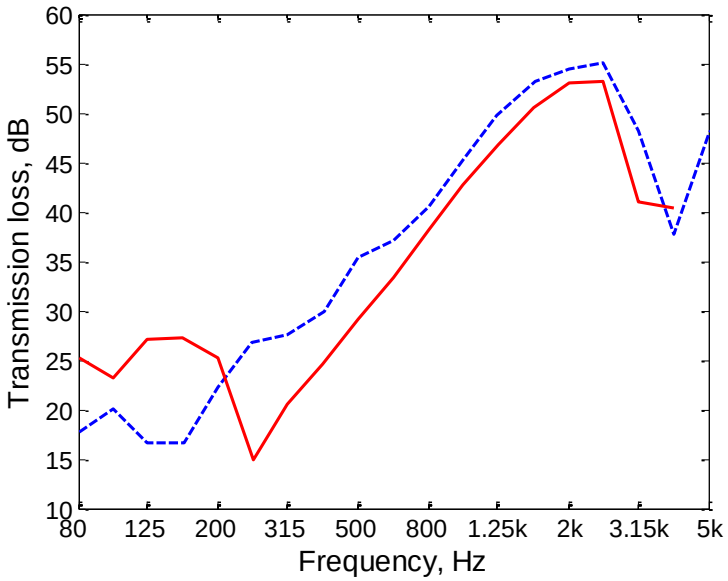

Figure 7.13. TL comparison of numerical results and measured ones for the case of TS3 (— numerical model ; - - - measurement).

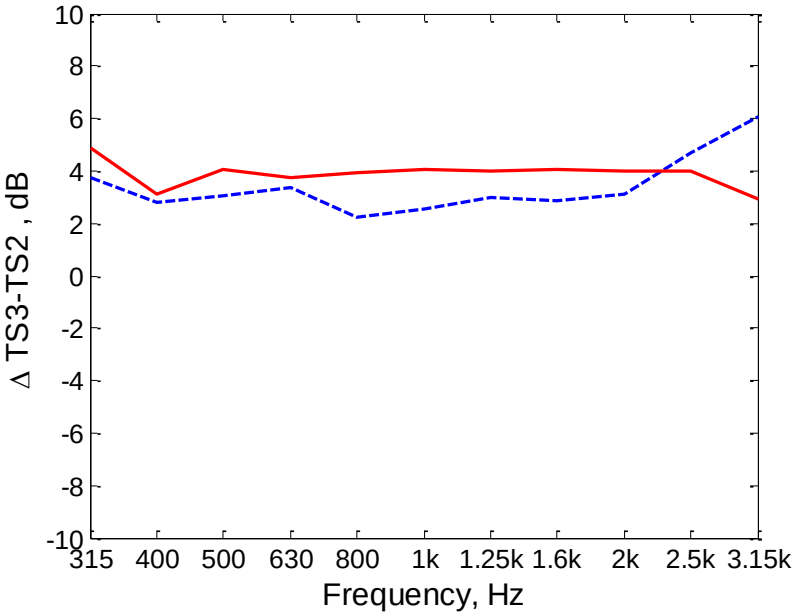

Figure 7.14. The difference in the transmission loss between TS2 and TS3 (— Numerical model; - - - Measurement).

7.4 Effect of steel stud

Figure 7.15 presents measurement results of TS4 compared with that of TS3 showing the effect of adding a steel stud. It is clear that the steel stud reduces the TL by 3 dB at high frequency. At low frequency, particularly around 315 Hz, TS4 has a slightly higher TL than that measured from TS3.

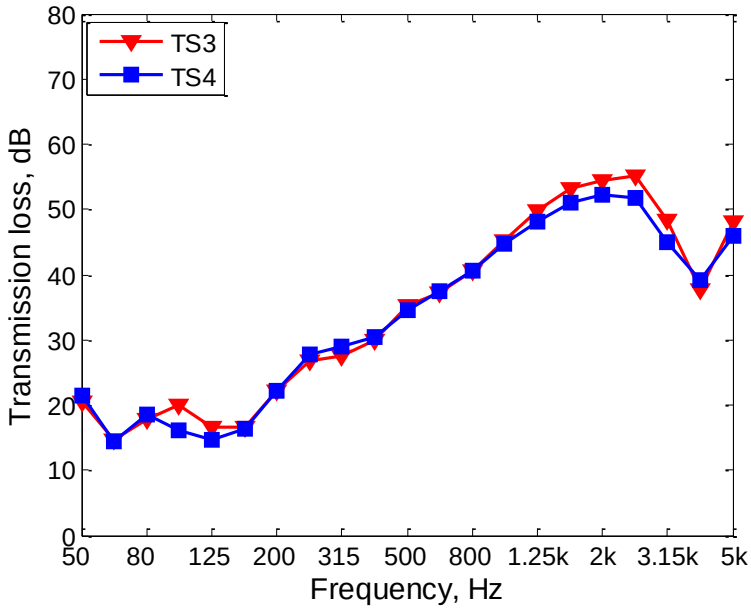

Figure 7.15. Effect of steel stud on transmission loss

The numerical model results also show the same tendency as shown in Figure 7.16 although the dip around 250 Hz in both the predicted curves is not evident in the measurement results. However, the difference between the TL of the double panel system with and without the steel C-stud tends to be bigger than in the measurement results. It is found that the steel C-stud causes a difference of up to 4.7 dB at high frequency while that of the measurement results is up to 3.4 dB as shown in Figure 7.17. Below 500 Hz, both the results have negative differences that mean the TL of TS4 is higher than TS3 in this frequency region.

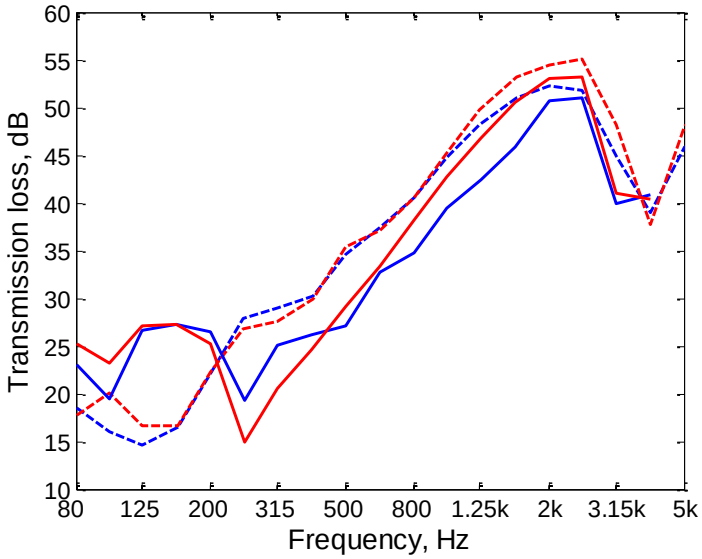

Figure 7.16. TL comparison of numerical results and measurements ones (--- TS3; --- TS4; — numerical model for TS3; — numerical model for TS4).

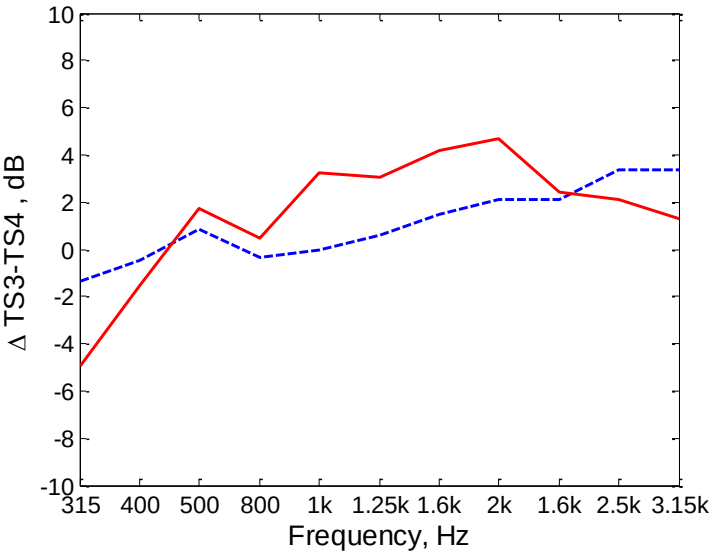

Figure 7.17. The difference in the transmission loss between TS3 and TS4 (— Numerical model; --- Measurement)

It is clear from Figure 7.18 that there are differences between the numerical results and the measured ones for the case of TS4. $\bar{R}_w$ = 43 dB is found from the measured result while $\bar{R}_w$ = 38 dB from the numerical model result for the same case. Better prediction results can be obtained by reducing the air stiffness, particularly for the current case. Using

this approach, $\bar{R}_w$ of the numerical model result increases to 41 dB which is only 2 dB lower than that of the measured result.

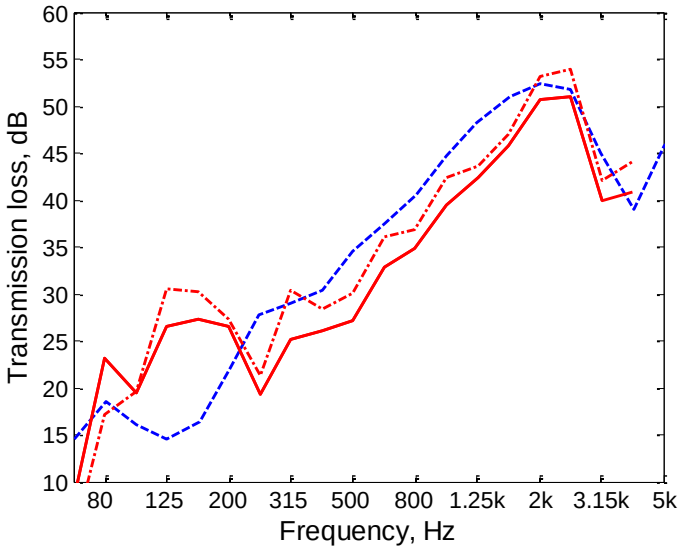

Figure 7.18. TL comparison of numerical results and measured one for TS4 (measurement ; numerical model; numerical model with ρ_o = 0.6 kg/m^3).

7.5 Summary

Transmission loss measurements were conducted by following standard ISO 140 [119] rather than the more recent ISO-10140 [116] hence the results must be used with caution. The use of timber frames may lead to higher flanking transmission. Moreover, a totally enclosed cavity system of the specimens, as assumed in the numerical model, may not be completely air-tight. Regarding the numerical model, empirical adjustment were used in order to get the results closer to measured ones. Hence these values may be different for different cirucumstances and modelling approach.

Despite some detail differences, the measurement results generally validate the findings of the numerical model. However, the mass-air-mass resonance frequency is not observable from the measurement results. Theoretically, it should also be affected by the air stiffness in the finite cavity due to the presence of lateral cavity modes.

For the case of the double panel system with a steel C stud, the measurement results indicate that the numerical model can show the effect of the stud on TL with a reasonable result. The results can be improved by introducing a lower air stiffness in calculation which may be justified by a lack of air tightness in the cavity. This can further confirm the comparison results in section 6.7.

Chapter 8. Conclusions

8.1 Infinite plate strip

A study of the vibro-acoustic behaviour of a plate strip has been presented. An analytical model has been developed in order to investigate the plate strip behaviour in terms of its mobility, its sound radiation and its sound transmission loss. Some concluding remarks can be made as follows:

1. The mobility of the plate strip due to a point force excitation is stiffness-controlled at low frequency while it tends to be similar to that of an infinite plate at high frequencies. Peaks occur at the cut-on frequencies with magnitudes that depend on the location of the excitation point. Damping has an effect only around the cut-on frequencies.
2. It is clear that the plate strip still radiates sound below the critical frequency even if it is less than above the critical frequency. This sound is produced by nearfield waves in the vicinity of the forcing point and by 'edge modes', that is waves with an axial wavenumber smaller than the acoustic wavenumber while the transverse wavenumber is greater than the acoustic wavenumber. Therefore, it is clear that the finite width and the point force excitation influence the sound power radiation below the critical frequency.
3. The sound transmission loss of the plate strip for normal incidence converges to the mass-law result at high frequencies. At low frequency, below the first cut-on frequency, a stiffness-controlled region appears, while the mass-controlled region exists above the first cut-on frequency. The slope at low frequencies is modified from the result for an infinite plate when the width is less than half the acoustic wavelength. Some dips or ripples in the curve are related to various cut-on frequencies. Such features are not present in an infinite model.

The results presented here can be used as benchmark solutions for validating numerical methods such as waveguide FE/BE.

8.2 Waveguide Finite Element-Boundary Element

The waveguide FE/BE method has been applied to a plate strip. Comparisons of the numerical results and analytical ones were conducted to validate the WFBE method

applied in this study and to determine under what circumstances the numerical model can be used to give accurate results. In terms of the mobility calculation a suitable wavenumber range and step size are determined in order to ensure errors are less than a certain value. This is expressed in terms of the maximum wavenumber ratio, relative to the associated free bending wavenumber of the plate. This study shows that the maximum wavenumber ratio decreases as frequency increases; e.g. for 1 Hz $\kappa_{\max}/\mathrm{Re}(k_B) =$ 18 while $\kappa_{\max}/\mathrm{Re}(k_B) =$ 1.5 for 3 kHz in order to get results with an error of less than 0.1 dB.

Some practical aspects of implementing this method using the WANDS software have been highlighted in order to obtain correct results. Firstly, the Waveguide Boundary Element (WBE) should have a closed boundary rather than an open one. The thickness of the mesh should be determined carefully to avoid the jump phenomenon which causes misleading results. Secondly, to simulate a baffled situation a finite rigid baffle should be included in the model by extending the width of the WBE fluid model beyond the width of the structure. The width of the finite rigid baffle is important in determining accuracy of the numerical model results in comparison with the analytical ones which are for an infinite baffle. The lowest frequency at which the numerical model results are still valid depends on the total width of baffle at the radiating side which should be at least half the acoustic wavelength. Thirdly, care should be taken in choosing the element type in the WANDS software. For the case of the waveguide structure considered in this study, the plate element type along with its coupling element to acoustic BE fails to calculate accurately the vibro-acoustic response of the plate strip although it gives good results for the mobility. It is found that the radiated sound power is incorrect in the critical frequency region and the sound transmission loss is incorrect around and above the coincidence frequency. Alternatively, solid elements can be used to obtain the results although a higher element density is required. These problems are believed to be due to errors in the WANDS software and not a fundamental limitation of the WFBE method.

All in all, the WFBE method is applicable for the cases considered in this study. Moreover, the WANDS software can be used to develop numerical models of structures and the structure-fluid interaction provided that suitable precautions are taken. The problems associated with plate-fluid coupling require further attention in the WANDS software which is beyond the scope of the present study.

8.3 Waveguide double panel system

The sound transmission of a double panel system has been studied using the WFBE approach. Finite extent and non-uniformity of the pressure distribution introduced in the waveguide double panel system with enclosed cavity cause some features to emerge in the sound transmission compared with the infinite system. Under such conditions, lateral cavity modes are evident along with cavity modes across the cavity depth. Hence, the total response in the cavity of such a system is the superposition of the air-stiffness dependent response across the depth and the cross-section modal response. This causes the mass-air-mass frequency of the waveguide double panel system to be modified. As a consequence, a stronger acoustical coupling is found which reduces the sound transmission loss in a wide frequency region. Moreover, the presence of coupled system resonances in which internal coincidence in the cavity occurs also cause the sound transmission loss to be reduced. The cavity loss factor has a large effect on the TL behaviour. The results obtained also show that the dissipative mechanism behaviour found in the real structure originates from the cavity rather than from the panel as postulated by London [15].

The finite width of the waveguide structure limits the radiation efficiency for larger angles of incidence. Consequently, a higher TL is found in the waveguide double panel partition as the finite width system radiates less compared with the infinite plate model.

After introducing studs into the system, a considerable reduction in performance of the waveguide double panel system was found at mid and high frequency. At lower frequencies, the response is a combination of the structural response and that of the air in the cavity. Moreover, pass-stop band characteristics typical of periodic structures are evident in the results.

Regarding the stud behaviour, the results suggest that the stiffness of the stud is an important parameter in determining the total response of the double panel system. In practical terms, the stud cross-section shape has a critical role in affecting the sound transmission loss as it determines the stud stiffness. However, for a less stiff stud the presence of lateral cavity modes and internal coincidence becomes more significant and limits the TL. Therefore, for the case of an elastic steel stud both air-borne and structure-borne transmission paths need to be handled carefully in order to achieve a good TL prediction.

Measurement results generally validate the findings of the numerical model with regard to the air cavity dimension. Without the presence of sound absorbing material in the cavity, this affects the overall TL of the double panel system.

8.4 Recommendations for further work

Numerical models have been developed using the WFBE method. As a consequence, the model is only able to represent the structure as a two-dimensional problem although the results obtained from the current approach show a good agreement compared with the experimental results. Further work is required to extend the model to predict the transmission loss of fully bounded structures as found in practice. This could be achieved e.g. by applying spatial windowing to modify the two dimensional structural problem to become a three dimensional one. Another concept that may be considered is to use particular set of wavenumbers in the x direction which are associated with natural frequencies of modes in the length direction e.g. $\kappa = n\pi / l_x$ for simply supported boundary conditions.

In a more general sense, the errors found in coupling plate-FE and acoustic-BE implies that it is required to have further analytical models of simple cases to validate the results of WANDS. It is particularly useful for testing the cases incorporating coupling models before proceeding to handle multi-domain models in which more than two sub-models are used. The results obtained can then be used to update WANDS to resolve the errors found.

Sound-absorbing material needs to be considered to make the model more versatile to cover various double panel systems found in practice. Although it can be included by using a suitable loss factor in the cavity, this should be frequency dependent. Moreover, the wavespeed is also frequency dependent. For this, therefore, a new sub-model is required which implements poroelastic material.

The findings in this thesis related to the stiffness of air in the cavity need to be examined further for different double panel systems, e.g. double glazing in order to get further comfirmation.

Finally, approximate formulae can be derived from the numerical models in order to have efficient and simple models particularly for practical purposes. Such an effort can be carried out by introducing some parameters related with material and geometrical

properties of a particular double panel system which can approximate the numerical results for the same system.

Appendix A. Out-of plane displacement of a plate strip due to a point force

The out-of plane displacement of the infinite plate strip vibrating in order m contained in Eq. (2.2) can be written as

$$\begin{aligned} w_m(x \le 0) &= A_{1,m} e^{ik_{x1,m}x} + A_{2,m} e^{ik_{x2,m}x} \\ w_m(x \ge 0) &= A_{3,m} e^{-ik_{x1,m}x} + A_{4,m} e^{-ik_{x2,m}x} \end{aligned} \tag{A.1}$$

where $k_{x1,m}$ and $k_{x2,m}$ are given in Eq. (2.6).

The generalized force acting on the m^{th} order motion is given by

$$F_m = F \sin\left(\frac{m\pi y_0}{l_y}\right) \qquad (x = 0) \tag{A.2}$$

The boundary conditions for such structures evaluated at $x = 0$ are as follows

1. Continuity equation ; equal displacement

$$w_m(0)_- = w_m(0)_+$$

$$\left.\begin{aligned} w_m(0,y)_- &= (A_{1,m} + A_{2,m}) \\ w_m(0,y)_+ &= (A_{3,m} + A_{4,m}) \end{aligned}\right\} A_{1,m} + A_{2,m} = A_{3,m} + A_{4,m} \tag{A.3}$$

2. Continuity of rotation

$$\frac{\partial w_m(x)_-}{\partial x} = \left.\frac{\partial w_m(x)_+}{\partial x}\right|_{x=0} \rightarrow A_{1,m}(ik_{x1,m}) + A_{2,m}(ik_{x2,m}) = -iA_{3,m}k_{x1,m} - iA_{4,m}k_{x2,m} \tag{A.4}$$

3. Continuity of bending moment

$$\frac{\partial^2 w_m}{\partial x^2}(x)_- = \left.\frac{\partial^2 w_m}{\partial x^2}(x)_+\right|_{x=0} \rightarrow -A_{1,m}k_{x1,m}^2 - A_{2,m}k_{x2,m}^2 = -A_{3,m}k_{x1,m}^2 - A_{4,m}k_{x2,m}^2 \tag{A.5}$$

Appendix A

4. Force equilibrium condition

$$S_m(0,y)_+ - S_m(0,y)_- = F_m \tag{A.6}$$

$$\left([A_{3,m}(ik_{x1,m}^3)+A_{4,m}(ik_{x2,m}^3)]-\left[(2-\nu)\left[A_{3,m}(-ik_{x1,m})+A_{4,m}(-ik_{x2,m})\right]\left(\frac{m\pi}{l}\right)^2\right]\right)-$$
$$\left([A_{1,m}(-ik_{x1,m}^3)+A_{2,m}(-ik_{x2,m}^3)]-\left[(2-\nu)\left[A_{1,m}(ik_{x1,m})+A_{2,m}(ik_{x2,m})\right]\left(\frac{m\pi}{l}\right)^2\right]\right)=\frac{F_m}{D'}$$

Using the relation from (A.4)

$$-A_{3,m}k_{x1,m}^3 - A_{4,m}k_{x2,m}^3 - A_{1,m}k_{x1,m}^3 - A_{2,m}k_{x2,m}^3 = \frac{F_m}{D'} \tag{A.7}$$

From Eq. (A.3) and Eq. (A.5) the following relations are obtained

$$A_{1,m} = A_{3,m} \;;\; A_{2,m} = A_{4,m}$$
$$A_{4,m} = -\frac{k_{x1,m}}{k_{x2,m}}A_{3,m} \tag{A.8}$$

By substituting Eq. (A.8) into Eq. (A.7) this yields

$$iA_{3,m}\left(k_{x1,m}^3 - k_{x2,m}^3\frac{k_{x1,m}}{k_{x2,m}} + k_{x1,m}^3 - k_{x2,m}^3\frac{k_{x1,m}}{k_{x2,m}}\right)=\frac{F_m}{D'}$$
$$A_{3,m} = \frac{-iF_m}{2D'k_{x1,m}\left(k_{x1,m}^2 - k_{x2,m}^2\right)}$$

The other coefficients will be

$$A_{1,m} = \frac{-iF_m}{2D'k_{x1,m}\left(k_{x1,m}^2 - k_{x2,m}^2\right)}$$

$$A_{2,m} = \left(-\frac{k_{x1,m}}{k_{x2,m}}\right)\frac{-iF_m}{2D'k_{x1,m}\left(k_{x1,m}^2 - k_{x2,m}^2\right)}$$
$$A_{4,m} = \left(-\frac{k_{x1,m}}{k_{x2,m}}\right)\frac{-iF_m}{2D'k_{x1,m}\left(k_{x1,m}^2 - k_{x2,m}^2\right)}$$

Based on these coefficients, the solution may be written as follows

$$w_m(x \le 0) = \frac{-iF_m}{2D'k_{x1,m}\left(k_{x1,m}^2 - k_{x2,m}^2\right)}\left[e^{ik_{x1,m}x} - \frac{k_{x1,m}}{k_{x2,m}}e^{ik_{x2,m}x}\right]$$
$$w_m(x \ge 0) = \frac{-iF_m}{2D'k_{x1,m}\left(k_{x1,m}^2 - k_{x2,m}^2\right)}\left[e^{-ik_{x1,m}x} - \frac{k_{x1,m}}{k_{x2,m}}e^{-ik_{x2,m}x}\right] \quad \text{(A.9 a,b)}$$

The complete solution is given by

$$w(x \le 0, y) = \sum_{m=1}^{\infty} \frac{-iF_m}{2D'k_{x1,m}\left(k_{x1,m}^2 - k_{x2,m}^2\right)}\left[e^{ik_{x1,m}x} - \frac{k_{x1,m}}{k_{x2,m}}e^{ik_{x2,m}x}\right]\sin\left(\frac{m\pi y}{l_y}\right)$$
$$w(x \ge 0, y) = \sum_{m=1}^{\infty} \frac{-iF_m}{2D'k_{x1,m}\left(k_{x1,m}^2 - k_{x2,m}^2\right)}\left[e^{-ik_{x1,m}x} - \frac{k_{x1,m}}{k_{x2,m}}e^{-ik_{x2,m}x}\right]\sin\left(\frac{m\pi y}{l_y}\right) \quad \text{(A.10)}$$

Appendix B. Modulus squared of plate velocity in wavenumber domain

The plate velocity in the wavenumber domain for a single mode m is given by Eq. (2.20) as follows

$$\tilde{V}(k_x,k_y)=\frac{\omega F_m}{2D'k_{x1,m}\left(k_{x1,m}^2-k_{x2,m}^2\right)}\left[\int_{-\infty}^{0}\left(e^{i(k_{x1,m}+k_x)x}-\frac{k_{x1,m}}{k_{x2,m}}e^{i(k_{x2,m}+k_x)x}\right)dx+\left(\int_{0}^{\infty}e^{-i(k_{x1,m}-k_x)x}-\frac{k_{x1,m}}{k_{x2,m}}e^{-i(k_{x2,m}-k_x)x}\right)dx\right]\left[\int_{0}^{l_y}\left(\frac{e^{i(m\pi/l_y+k_y)y}-e^{-i(m\pi/l_y-k_y)y}}{2i}\right)dy\right] \tag{B.1}$$

From Eq. (B.1), the plate velocity in the wavenumber domain in the $x-$direction is

$$\begin{aligned}\tilde{V}_x(k_x)&=\frac{\omega F_n}{2D'k_{x1}\left(k_{x1}^2-k_{x2}^2\right)}\left(\left[\frac{1}{i(k_{x1}+k_x)}-\frac{k_{x1}}{k_{x2}}\frac{1}{i(k_{x2}+k_x)}\right]+\left[\frac{1}{i(k_{x1}-k_x)}-\frac{k_{x1}}{k_{x2}}\frac{1}{i(k_{x2}-k_x)}\right]\right)\\&=\frac{\omega F_n}{2D'k_{x1}\left(k_{x1}^2-k_{x2}^2\right)}\left(-\frac{2ik_{x1}}{\left(k_{x1}^2-k_x^2\right)}+\frac{2ik_{x1}}{k_{x2}}\left(\frac{k_{x2}}{k_{x2}^2-k_x^2}\right)\right)\\&=\frac{i\omega F_n}{D'\left(k_{x1}^2-k_{x2}^2\right)}\left(\frac{1}{\left(k_{x2}^2-k_x^2\right)}-\frac{1}{\left(k_{x1}^2-k_x^2\right)}\right)\\&=\frac{i\omega F_n}{D'\left(k_{x1}^2-k_x^2\right)\left(k_{x2}^2-k_x^2\right)}\end{aligned} \tag{B.2}$$

while that of the y dependent plate velocity in the wavenumber domain is

$$\tilde{V}_y(k_y)=\left(\frac{m\pi/l_y}{k_y^2-(m\pi/l_y)^2}\right)\left[(-1)^m e^{ik_y l_y}-1\right] \tag{B.3}$$

The absolute value of Eq. (B.3) is

Appendix B

$$\left|\tilde{V}_y(k_y)\right| = \left|\frac{m\pi/l_y}{k_y^2-(m\pi/l_y)^2}\right|\left|e^{i(k_y l_y - m\pi)}-1\right|$$

$$= \left|\frac{m\pi/l_y}{k_y^2-(m\pi/l_y)^2}\right|\left|\cos(k_y l_y - m\pi)+i\sin(k_y l_y - m\pi)-1\right|$$

$$= \left|\frac{m\pi/l_y}{k_y^2-(m\pi/l_y)^2}\right|\sqrt{2(1-\cos(k_y l_y - m\pi))} \qquad \text{(B.4)}$$

$$= \left|\frac{m\pi/l_y}{k_y^2-(n\pi/l_y)^2}\right|\sqrt{4\sin^2\left(\frac{k_y l_y - m\pi}{2}\right)}$$

The plate velocity in x and y directions may be written as

$$\tilde{V}(k_x,k_y) = \tilde{V}_x(k_x)\tilde{V}_y(k_y) \qquad \text{(B.5)}$$

Hence the modulus of $\tilde{V}(k_x,k_y)$ can be written as combination of Eq. (B.2) and (B.4) as

$$\left|\tilde{V}(k_x,k_y)\right| = \left|\frac{\omega F_n}{D'\left(k_{x1}^2-k_x^2\right)\left(k_{x2}^2-k_x^2\right)}\right|\left|\frac{m\pi/l_y}{k_y^2-(m\pi/l_y)^2}\right|\sqrt{4\sin^2\left(\frac{k_y l_y - m\pi}{2}\right)} \qquad \text{(B.5)}$$

Thus the modulus squared of $\tilde{V}(k_x,k_y)$ is

$$\left|\tilde{V}(k_x,k_y)\right|^2 = \left|\frac{\omega F_n}{D'\left(k_{x1}^2-k_x^2\right)\left(k_{x2}^2-k_x^2\right)}\right|^2\left[\frac{2\pi m/l_y}{k_y^2-(m\pi/l_y)^2}\right]^2\sin^2\left(\frac{k_y l_y - m\pi}{2}\right) \qquad \text{(B.6)}$$

Appendix C. Stiffness and mass matrices of WFE method

C.1 Plate elements

For a structure assembled of a number of elements, the overall equation can be written in the form

$$\left[\mathbf{K}_4\frac{\partial^4}{\partial x^4}+\mathbf{K}_2\frac{\partial^2}{\partial x^2}+\mathbf{K}_1\frac{\partial}{\partial x}+\mathbf{K}_0-\omega^2\mathbf{M}\right]\mathbf{W}(x)=\mathbf{F}(x) \tag{C.1}$$

where $\mathbf{K_0}=\mathbf{a_{00}}$, $\mathbf{K_1}=\mathbf{a_{01}}-\mathbf{a_{10}}$, $\mathbf{K_2}=\mathbf{a_{02}}+\mathbf{a_{21}}-\mathbf{a_{11}}$ and $\mathbf{K_4}=\mathbf{a_{22}}$. The matrices $\mathbf{a}_{ij}$ and $\mathbf{M}$ are calculated as follows

$$\mathbf{a}_{ij}=\int\left[\mathbf{B}_i\mathbf{\Psi}\right]^{\mathbf{T}}\left[\mathbf{D}\right]\left[\mathbf{B}_j\mathbf{\Psi}\right]dy \tag{C.2}$$

$$\mathbf{M}=\int\rho h\mathbf{\Psi}^{\mathbf{T}}\mathbf{\Psi}dy \tag{C.3}$$

where $\mathbf{D}$ is the material stiffness matrix, ρ is the material density, h is the plate thickness . $\mathbf{B}_0\mathbf{\Psi}$, $\mathbf{B}_1\mathbf{\Psi}$ and $\mathbf{B}_2\mathbf{\Psi}$ in Eq. (C.2) are defined as

$$\left[\mathbf{B}_0\mathbf{\Psi}\right]=\begin{bmatrix}0&0&0&0&0&0&0&0\\0&\frac{\partial N_{1ip}}{\partial y}&0&0&0&\frac{\partial N_{2ip}}{\partial y}&0&0\\\frac{\partial N_{1ip}}{\partial y}&0&0&0&\frac{\partial N_{2ip}}{\partial y}&0&0&0\\0&0&0&0&0&0&0&0\\0&0&\frac{\partial^2 N_{1b}}{\partial y^2}&\frac{\partial^2 N_{2b}}{\partial y^2}&0&0&\frac{\partial^2 N_{3b}}{\partial y^2}&\frac{\partial^2 N_{4b}}{\partial y^2}\\0&0&0&0&0&0&0&0\end{bmatrix} \tag{C.4}$$

Appendix C

$$\left[\mathbf{B_1}\boldsymbol{\Psi}\right]=\begin{bmatrix} N_{1ip} & 0 & 0 & 0 & N_{2ip} & 0 & 0 & 0 \\ 0 & 0 & 0 & 0 & 0 & 0 & 0 & 0 \\ 0 & N_{1ip} & 0 & 0 & 0 & N_{2ip} & 0 & 0 \\ 0 & 0 & 0 & 0 & 0 & 0 & 0 & 0 \\ 0 & 0 & 0 & 0 & 0 & 0 & 0 & 0 \\ 0 & 0 & \dfrac{\partial N_{1b}}{\partial y} & \dfrac{\partial N_{2b}}{\partial y} & 0 & 0 & \dfrac{\partial N_{3b}}{\partial y} & \dfrac{\partial N_{4b}}{\partial y} \end{bmatrix} \tag{C.5}$$

$$\left[\mathbf{B_2}\boldsymbol{\Psi}\right]=\begin{bmatrix} 0 & 0 & 0 & 0 & 0 & 0 & 0 & 0 \\ 0 & 0 & 0 & 0 & 0 & 0 & 0 & 0 \\ 0 & 0 & 0 & 0 & 0 & 0 & 0 & 0 \\ 0 & 0 & N_{1b} & N_{2b} & 0 & 0 & N_{3b} & N_{4b} \\ 0 & 0 & 0 & 0 & 0 & 0 & 0 & 0 \\ 0 & 0 & 0 & 0 & 0 & 0 & 0 & 0 \end{bmatrix} \tag{C.6}$$

where $\mathbf{B_0}$, $\mathbf{B_1}$ and $\mathbf{B_2}$ are given by

$$\mathbf{B_0}=\begin{bmatrix} 0 & 0 & 0 \\ 0 & \dfrac{\partial}{\partial y} & 0 \\ \dfrac{\partial}{\partial y} & 0 & 0 \\ 0 & 0 & 0 \\ 0 & 0 & \dfrac{\partial^2}{\partial y^2} \\ 0 & 0 & 0 \end{bmatrix}, \quad \mathbf{B_1}=\begin{bmatrix} 1 & 0 & 0 \\ 0 & 0 & 0 \\ 0 & 1 & 0 \\ 0 & 0 & 0 \\ 0 & 0 & 0 \\ 0 & 0 & \dfrac{\partial}{\partial y} \end{bmatrix}, \quad \mathbf{B_2}=\begin{bmatrix} 0 & 0 & 0 \\ 0 & 0 & 0 \\ 0 & 0 & 0 \\ 0 & 0 & 1 \\ 0 & 0 & 0 \\ 0 & 0 & 0 \end{bmatrix} \tag{C.7}$$

and $\boldsymbol{\Psi}$ is the shape function and is defined as

$$\boldsymbol{\Psi}=\begin{bmatrix} N_{1ip} & 0 & 0 & 0 & N_{2ip} & 0 & 0 & 0 \\ 0 & N_{1ip} & 0 & 0 & 0 & N_{2ip} & 0 & 0 \\ 0 & 0 & N_{1b} & N_{2b} & 0 & 0 & N_{3b} & N_{3b} \end{bmatrix} \tag{C.8}$$

$$N_{1ip}=\frac{1}{2}(1-\xi) \tag{C.9}$$

$$N_{2ip}=\frac{1}{2}(1+\xi) \tag{C.10}$$

$$N_{1b} = \frac{1}{4}\left(2 - 3\xi + \xi^3\right) \tag{C.11}$$

$$N_{2b} = \frac{L}{8}\left(1 - \xi - \xi^2 + \xi^3\right) \tag{C.12}$$

$$N_{1b} = \frac{1}{4}\left(2 + 3\xi - \xi^3\right) \tag{C.13}$$

$$N_{2b} = \frac{L}{8}\left(-1 - \xi + \xi^2 + \xi^3\right) \tag{C.14}$$

where $\xi = \frac{y - y_m}{L/2}$ with y_m the mid $y-$coordinate of element and L the width of element.

C.2 Solid elements

The overall motion of a structure built up of solid elements can be written as follows [78]

$$\left[\mathbf{K}_2 \frac{\partial^2}{\partial x^2} + \mathbf{K}_1 \frac{\partial}{\partial x} + \mathbf{K}_0 - \omega^2 \mathbf{M}\right] \mathbf{W}(x) = \mathbf{F}(x) \tag{C.15}$$

where $\mathbf{K}_0 = \mathbf{a}_{00}$, $\mathbf{K}_1 = \mathbf{a}_{01} - \mathbf{a}_{10}$ and $\mathbf{K}_2 = -\mathbf{a}_{11}$. In this method, $\mathbf{a}_{ij}$ and $\mathbf{M}$ are given by

$$\mathbf{a}_{ij} = \int_A \left[\mathbf{B}_i \mathbf{N}\right]^{\mathbf{T}} \left[\mathbf{D}\right] \left[\mathbf{B}_j \mathbf{N}\right] dA \tag{C.16}$$

$$\mathbf{M} = \int_A \rho_s \mathbf{N}^{\mathbf{T}} \mathbf{N} dA \tag{C.17}$$

where $\mathbf{D}$ is the material stiffness matrix, ρ_s is the material stiffness, A is the cross-sectional area of element and $\mathbf{N}_s$ is the shape function as defined as

$$\mathbf{N} = \begin{bmatrix} \mathbf{N_s^T} & 0 & 0 \\ 0 & \mathbf{N_s^T} & 0 \\ 0 & 0 & \mathbf{N_s^T} \end{bmatrix} \tag{C.18}$$

C.3 Fluid elements

The assembling of the fluid elements can be formulated [78]

$$\mathbf{K_2}\frac{\partial^2\hat{\boldsymbol{\psi}}}{\partial x^2}+\mathbf{K_0}\hat{\boldsymbol{\psi}}-\omega^2\mathbf{M_f}\hat{\boldsymbol{\psi}}=0 \tag{C.19}$$

where $\hat{\boldsymbol{\psi}}$ is the velocity potential while $\mathbf{K}_0$, $\mathbf{K}_2$ and $\mathbf{M_f}$ are defined as

$$\mathbf{K}_0=\int_A \mathbf{N}_f\mathbf{N}_f^{\mathbf{T}}dA \tag{C.20}$$

$$\mathbf{K}_2=-A\mathbf{B}\mathbf{B}^{\mathbf{T}} \tag{C.21}$$

$$\mathbf{M_f}=\frac{\mathbf{K}_0}{c^2} \tag{C.22}$$

where $\mathbf{B}=\left[\partial\mathbf{N}_f/\partial z \quad \partial\mathbf{N}_f/\partial y\right]$, A is the cross-sectional area of element and c is the sound speed in fluid.

Appendix D. Mobility of single panel system and double panel system with steel studs

D.1 Mobility of steel stud-panel

The behaviour of stud-panel connections in lightweight structures is investigated here particularly the effect of screw spacing in order to give insights into its overall effect as to the role of screws along a steel stud and the spacing between respective screws.

To achieve this objective, measurements of transfer mobility of stud-panel systems were performed. In general, test specimen consists of the stud attached to a single piece of plasterboard by screws. Free-free boundary conditions are considered for all configurations. Such boundary conditions are less relevant in practice but easy to set up without requiring a specific arrangement to apply constraints.

D.2 Test specimen parameters

The test specimen consists of a steel stud and a single piece of plasterboard as shown in Figure D.1. The plasterboard dimensions nominally 600 × 450 × 12.5 mm (length × width × thickness) while the steel stud was 600 × 70 × 0.5 mm (length × depth × thickness). For this configuration, three variants are considered owing to different screw spacing, i.e. 600 mm, 300 mm and 150 mm spacing. The stud-plasterboard connection is situated at the middle of the plasterboard or 225 mm from the edges.

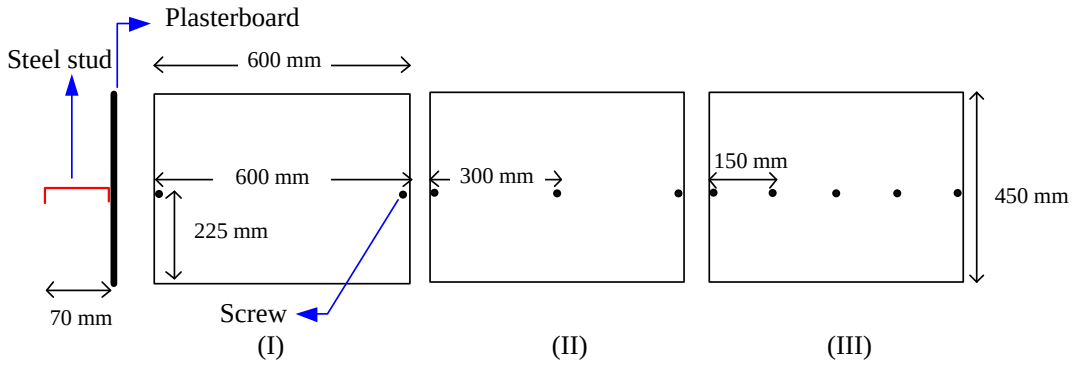

Figure D.1. Test specimen for the first configuration

D.3 Experimental setup and procedure

The measurement setup is shown in Figure D.2. The test specimens were laid on pieces of soft foam at each corner to approximate free-free boundary conditions. Small PCB accelerometers were attached at two different positions to capture the mobility at the

stud and plasterboard simultaneously. Accelerometer 1 is at the lower flange and accelerometer 2 is on plasterboard. For each measurement point, the stud was excited by an impact hammer at its upper flange. The excitation was repeated 3-5 times to get a consistent result. By using a Data Physics DP240 analyser, the FRF and the coherence were calculated. This procedure was then repeated for other measurement points. As the weight of the accelerometer is less than 2 gram, which is about 1/1500 times the weight of the stud and 1/1000 times the weight of the plasterboard, the total impedance before and after the accelerometer attached on the stud and plasterboard is not much different. Hence the mass loading effect in this measurement is expected to be neglible.

The frequency range of interest was up to 4 kHz. The set of measurement positions selected for the single panel and double panel system are indicated in Figure D.3. At selected measurement points, where the square and dot symbols coincide, correspond with measurements were made at the screw area; otherwise the measurement was taken at a location at which the stud and the plasterboard are not directly connected. To get a clear representation, the data is presented in 1/3 octave frequency bands.

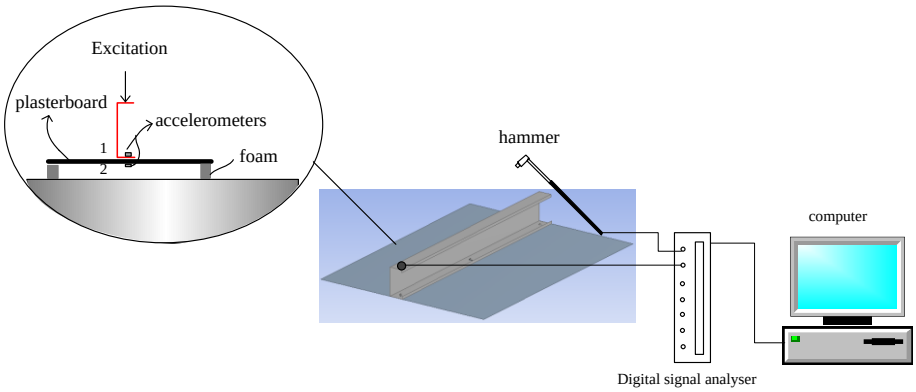

Figure D.2. Experimental setup for mobility measurement and accelerometer arrangement of the single panel system.

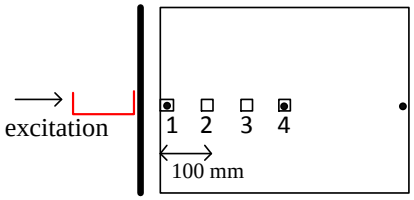

Figure D.3. Measurement point positions of single panel system (● screw; □ measurement points).

D.4 Mobility results for single panel sytem

Figure D.4 presents transfer mobility results on the plasterboard for each screw spacing at all measurement points, taken from accelerometer 2 for excitation at the upper flange as indicated in Figure D.2. It can be seen that the results are not much different particularly for 300 mm and 600 mm screw spacings while the mobility tends to be higher for the case of the 150 mm stud spacing case although it is only 5 dB higher which can be considered small. Moreover, the overall behaviour of all cases considered here is similar as shown in the measurement point 1, 2, 3 and 4. Compared with the point mobility of infinite plasterboard, indicated by the black dashed line, the mobility of each case is evident around that of the infinite plasterboard particularly above 250 Hz. At measurement point 1 and 4, which coincide with the screw positions, the mobility of the plasterboard with stud is higher than that of the infinite plasterboard. This only gives 3 dB differences on average compared with the measurement points where the screws are absent. Hence, this would not give rise to significant implications.

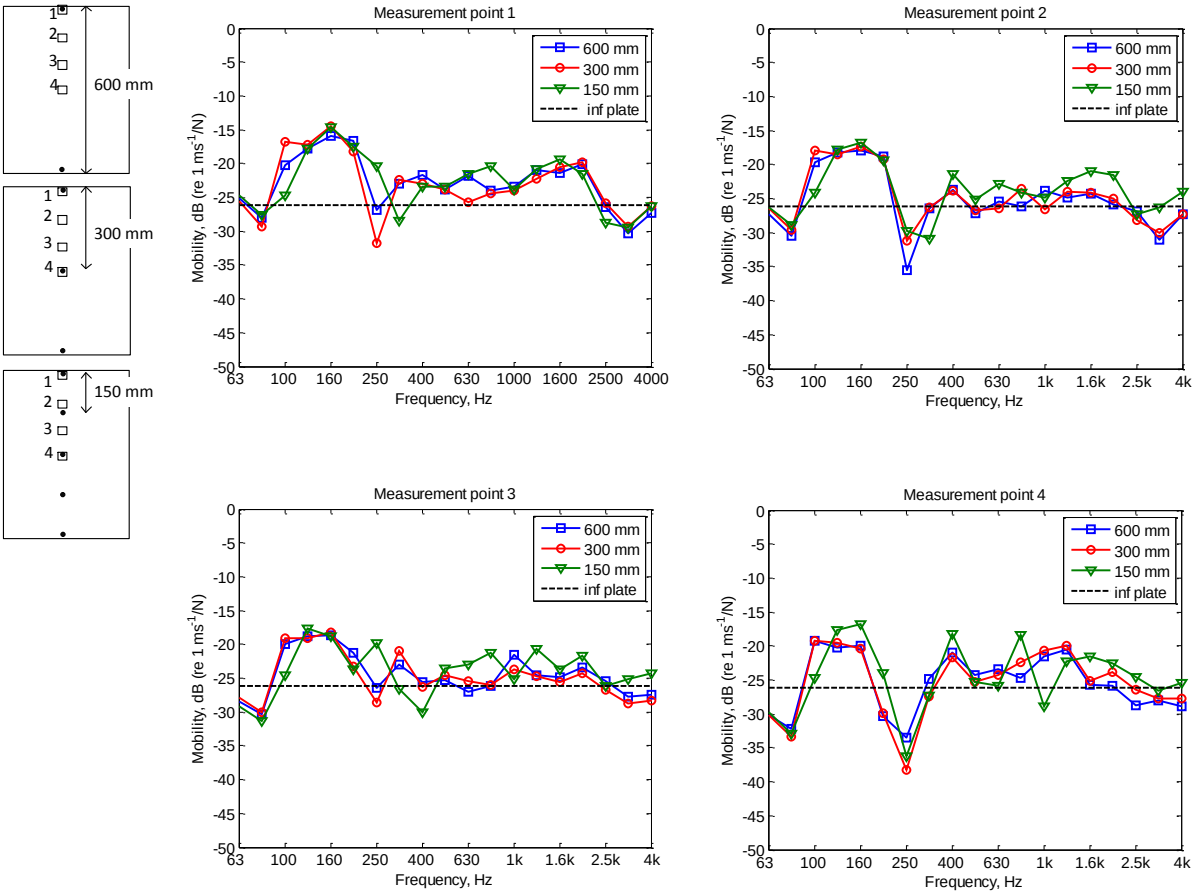

Figure D.4. Mobility comparison on plasterboard for different screw spacings.

Appendix E. Cavity loss factor

It is difficult to obtain an appropriate cavity loss factor to be included in the prediction model when no absorbing material is present in the cavity. Price and Crocker [26] estimated this value based on normal-incidence sound absorption coefficient α_0 of sound-absorbing material at edges. The cavity loss factor is thus formulated as

$$\eta_{cav} = \frac{cS\alpha_0}{4\omega V} \tag{E.1}$$

where c is the sound velocity , $S = 2\left(l_x l_z + l_y l_z\right)$ with l_x, l_y and l_z cavity dimension in x, y and z directions respectively is the surface area of sound absorption at the edge of cavity, ω is the angular frequency and V is the cavity volume. As the waveguide is infinite in one dimension, l_x can be assigned as a large value so that Eq. (E.1) becomes

$$\eta_{cav} = \frac{c\alpha_0}{2\omega l_y} \tag{E.2}$$

For the case of double panel system where the edge sound-absorber is absent, an equivalent normal-incidence sound absorption coefficient $\bar{\alpha}_0$ can be used. For this, from measurement results Brekke [51] found $\bar{\alpha}_0 \approx 0.1$ for $d \geq 0.1$ m and $\bar{\alpha}_0 \approx 0.5$ for $d \leq 0.02$ m, with d cavity depth, and interpolation can be made for cavity depths between these values. The interpolation is given as

$$\bar{\alpha}_0 = -5d + 0.6 \tag{E.3}$$

hence $\bar{\alpha}_0 = 0.275$ can be found for 0.065 m cavity depth used in this thesis.

By inserting $\bar{\alpha}_0 = 0.275$ into Eq.(E.2), the frequency-dependent cavity loss factors for 0.065 m cavity depth and 1.218 m width are found as given in Table E.1

Appendix E

Table E.1. Cavity loss factor for 65 mm cavity depth and 1.218 m width

Frequency, Hz	η_{cav}
80	0.077
100	0.062
125	0.049
160	0.039
200	0.031
250	0.025
315	0.020
400	0.015
500	0.012
630	0.010
800	0.008
1000	0.006
1250	0.005
1600	0.004
2000	0.003
2500	0.002
3150	0.002
4000	0.002

References

1. *Building Regulations 2010 Approved document E, Resistance to the passage of sound*, HM Government
2. Fahy, F. and P. Gardonio, *Sound and Structural Vibration: Radiation, Transmission and Response*. 2nd ed. 2006, London: Academic Press.
3. Fahy, F., *Foundations of Engineering Acoustics*. 2001: Academic Press.
4. Cremer, L., M. Heckl, and B.A.T. Petersson, *Structure-Borne Sound*. 3rd edition ed. 2005, Berlin: Springer.
5. London, A., *Transmission of reverberant sound through single walls.* Research Nat. Bur. of Standard, 1949. **42**(605).
6. Sewell, E.C., *Two-dimensional solution for transmission of reverberant sound through a double partition.* Journal of Sound and Vibration, 1970. **12**(1): p. 33-57.
7. Sharp, B.H., *Prediction methods for the sound transmission of building elements.* Noise Control Engineering, 1978. **11**: p. 53–63.
8. Hongisto, V., *Sound Insulation of Double Panels - Comparison of Existing Prediction Models.* Acta Acustica united with Acustica, 2006. **92**: p. 61-78.
9. Nilsson, C.-M., *Waveguide Finite Elements Applied on a Car Tyre*. 2004, MWL KTH: Stockholm.
10. Beranek, L.L., *Noise and Vibration Control* 1971, New York: McGraw-Hill
11. Cremer, L., *Theorie der Schalldammung dunner Wande bei schragen Einfall.* Akustica Zeitschrift, 1942. **7**: p. 81-103.
12. Sewell, E.C., *Transmission of reverberant sound through a single-leaf partition surrounded by an infinite rigid baffle.* Journal of Sound and Vibration, 1970. **12**(1): p. 21-32.
13. Leppington, F.G., et al., *Resonant and Non-Resonant Acoustic Properties of Elastic Panels. II. The Transmission Problem.* Proceedings of the Royal Society of London. A. Mathematical and Physical Sciences, 1987. **412**(1843): p. 309-337.
14. Beranek, L.L. and G.A. Work, *Sound transmission through multiple structures containing flexible blankets.* The Journal of the Acoustical Society of America, 1949. **21**(4): p. 419-428.
15. London, A., *Transmission of reverberant sound through double walls.* The Journal of the Acoustical Society of America, 1950. **22**(2): p. 270-279.

16. Jones, R.E., *Intercomparisons of laboratory determinations of airborne sound transmission loss.* The Journal of the Acoustical Society of America, 1979. **66**(1): p. 148-164.
17. Mulholland, K.A., H.D. Parbrook, and A. Cummings, *The transmission loss of double panels.* Journal of Sound and Vibration, 1967. **6**(3): p. 324-334.
18. Hopkins, C., *Sound Insulation*. 2007, Oxford, UK: Elsevier.
19. Vinokur, R., *Mechanism and calculation of the niche effect in airborne sound transmission.* J. Acoust. Soc. Am., 2006. **119**(4): p. 2211-2219.
20. Kang, H.-J., et al., *Prediction of sound transmission loss through multilayered panels by using Gaussian distribution of directional incident energy.* Journal of the Acoustical Society of America, 2000. **107**(3): p. 1413-1420.
21. Cummings, A. and K.A. Mulholland, *The transmission loss of finite sized double panels in a random incidence sound field.* Journal of Sound and Vibration, 1968. **8**(1): p. 126-133.
22. Xin, F.X., T.J. Lu, and C.Q. Chen, *Vibroacoustic behavior of clamp mounted double-panel partition with enclosure air cavity.* The Journal of the Acoustical Society of America, 2008. **124**(6): p. 3604-3612.
23. Villot, M., C. Guigou, and L. Gagliardini, *Predicting the acoustical radiation of finite size multi-layered structures by applying spatial windowing on infinite structures.* Journal of Sound and Vibration, 2001. **245**(3): p. 433-455.
24. Atalla, N., F. Sgard, and C.K. Amedin, *On the modeling of sound radiation from poroelastic materials.* The Journal of the Acoustical Society of America, 2006. **120**(4): p. 1990-1995.
25. Vigran, T.E., *Predicting the sound reduction index of finite size specimen by a simplified spatial windowing technique.* Journal of Sound and Vibration, 2009. **325**(3): p. 507-512.
26. Price, A.J. and M.J. Crocker, *Sound Transmission through Double Panels Using Statistical Energy Analysis.* The Journal of the Acoustical Society of America, 1970. **47**(3A): p. 683-693.
27. Panneton, R. and N. Atalla, *Numerical prediction of sound transmission through finite multilayer systems with poroelastic materials.* Journal of the Acoustical Society of America, 1996. **100**(1): p. 346-354.

28. Sgard, F.C., N. Atalla, and J. Nicolas, *A numerical model for the low frequency diffuse field sound transmission loss of double-wall sound barriers with elastic porous linings.* The Journal of the Acoustical Society of America, 2000. **108**(6): p. 2865-2872.
29. Gu, Q. and J. Wang, *Effect of resilient connection on sound transmission loss of metal stud double panel partitions.* Chinese Journal of Acoustics, 1983. **2**: p. 113-116.
30. Davy, J.L., *The improvement of a simple theoretical model for the prediction of the sound insulation of double leaf walls.* The Journal of the Acoustical Society of America, 2010. **127**(2): p. 841-849.
31. Davy, J.L., *Predicting the Sound Insulation of Walls.* Building Acoustics, 2009. **16**(1): p. 1-20.
32. Sato, H., *On the mechanism of outdoor noise transmission through walls and windows - A modification of infinite wall theory with respect to radiation of transmitted wave.* The Journal of the Acoustical Society of Japan, 1973. **29**(9): p. 509-516.
33. Legault, J. and N. Atalla, *Numerical and experimental investigation of the effect of structural links on the sound transmission of a lightweight double panel structure.* Journal of Sound and Vibration, 2009. **324**(3-5): p. 712-732.
34. Brunskog, J., *The influence of finite cavities on the sound insulation of double-plate structures.* The Journal of the Acoustical Society of America, 2005. **117**(6): p. 3727-3739.
35. Leppington, F.G., K.H. Heron, and E.G. Broadbent, *Resonant and Non-Resonant Transmission of Random Noise through Complex Plates.* Proceedings: Mathematical, Physical and Engineering Sciences, 2002. **458**(2019): p. 683-704.
36. Nakanishi, S., M. Yairi, and A. Minemura, *Estimation method for parameters of construction on predicting transmission loss of double leaf dry partition.* Applied Acoustics, 2011. **72**(6): p. 364-371.
37. Hongisto, V., M. Lindgren, and R. Helenius, *Sound Insulation of Double Walls An Experimental Parametric Study.* Acta Acustica united with Acustica, 2002. **88**(6): p. 904-923.

38. Halliwell, R., et al., *Gypsum board walls: transmission loss data. Internal report IRC-IR-761*. 1998, Institute for Research in Construction, National Research Council of Canada.
39. Lin, G.-F. and J.M. Garrelick, *Sound transmission through periodically framed parallel plates.* The Journal of the Acoustical Society of America, 1977. **61**(4): p. 1014-1018.
40. Urusovskii, I.A., *Sound transmission through two periodically framed parallel plates.* Journal of Soviet Physics Acoustics, 1992. **38**(4): p. 411-413.
41. Wang, J., et al., *Sound transmission through lightweight double-leaf partitions: theoretical modelling.* Journal of Sound and Vibration, 2005. **286**(4-5): p. 817-847.
42. Mead, D.J., *Free wave propagation in periodically supported, infinite beams.* Journal of Sound and Vibration, 1970. **11**(2): p. 181-197.
43. Mead, D.J. and K.K. Pujara, *Space-harmonic analysis of periodically supported beams: response to convected random loading.* Journal of Sound and Vibration, 1971. **14**(4): p. 525-532, IN9, 533-541.
44. Poblet-Puig, J., et al., *The Role of Studs in the Sound Transmission of Double Walls.* Acta Acustica united with Acustica, 2009. **95**: p. 555-567.
45. Vigran, T.E., *Sound insulation of double-leaf walls - Allowing for studs of finite stiffness in a transfer matrix scheme.* Applied Acoustics, 2010. **71**(7): p. 616-621.
46. Davy, J.L., C. Guigou-Carter, and M. Villot, *An empirical model for the equivalent translational compliance of steel studs.* The Journal of the Acoustical Society of America, 2012. **131**(6): p. 4615-4624.
47. Li, S., T. Wang, and S.R. Nutt, *Transmission loss assessments of sandwich structures by using a combination of finite element and boundary element methods.* The Journal of the Acoustical Society of America, 2005. **118**(3): p. 1847-1848.
48. Crocker, M.J. and A.J. Price, *Sound transmission using statistical energy analysis.* Journal of Sound and Vibration, 1969. **9**(3): p. 469-486.
49. Elmallawany, A., *Criticism of statistical energy analysis for the calculation of sound insulation—Part 1: Single partitions.* Applied Acoustics, 1978. **11**(4): p. 305-312.
50. Elmallawany, A., *Criticism of statistical energy analysis for the calculation of sound insulation: Part 2-double partitions.* Applied Acoustics, 1980. **13**(1): p. 33-41.
51. Brekke, A., *Calculation methods for the transmission loss of single, double and triple partitions.* Applied Acoustics, 1981. **14**(3): p. 225-240.

52. Craik, R.J.M. and R.S. Smith, *Sound transmission through double leaf lightweight partitions part I: airborne sound.* Applied Acoustics, 2000. **61**(2): p. 223-245.
53. Craik, R.J.M. and R. Wilson, *Sound transmission through masonry cavity walls.* Journal of Sound and Vibration, 1995. **179**(1): p. 79-96.
54. Wang, T., et al., *Predicting the sound transmission loss of sandwich panels by Statistical Energy Analysis approach.* Journal of Vibration and Acoustics, 2010. **132**(1): p. 011004-1 - 011004-7.
55. Finnveden, S., *Spectral finite element analysis of the vibration of straight fluid-filled pipes with flanges.* Journal of Sound and Vibration, 1997. **199**(1): p. 125-154.
56. Bartoli, I., et al., *Modeling wave propagation in damped waveguides of arbitrary cross-section.* Journal of Sound and Vibration, 2006. **295**(3-5): p. 685-707.
57. Gavric, L., *Computation of propagative waves in free rail using a finite element technique.* Journal of Sound and Vibration, 1995. **185**(3): p. 531-543.
58. Nilsson, C.M., et al., *A waveguide finite element and boundary element approach to calculating the sound radiated by railway and tram rails.* Journal of Sound and Vibration, 2009. **321**(3-5): p. 813-836.
59. Ryue, J., *A waveguide finite element and boundary element approach applied on submerged fluid-filled cylindrical shells*, in *RASD2010*. 2010: Southampton, UK.
60. Waki, Y., B.R. Mace, and M.J. Brennan, *Free and forced vibrations of a tyre using a wave/finite element approach.* Journal of Sound and Vibration, 2009. **323**(3-5): p. 737-756.
61. Nilsson, C.-M., et al. *A coupled waveguide finite and boundary element for calculating the sound transmission through complex panel structure*. in *IX International Conference on Recent Advances in Structural Dynamics*. 2006. University of Southampton UK.
62. Thompson, D.J., *Wheel-rail noise generation, Part III: Rail vibration.* Journal of Sound and Vibration, 1993. **161**(3): p. 421-446.
63. Mace, B.R., et al., *Finite element prediction of wave motion in structural waveguides.* The Journal of the Acoustical Society of America, 2005. **117**(5): p. 2835-2843.
64. Waki, Y., B.R. Mace, and M.J. Brennan, *Numerical issues concerning the wave and finite element method for free and forced vibrations of waveguides.* Journal of Sound and Vibration, 2009. **327**(1–2): p. 92-108.

65. Wu, T.W., ed. *Boundary Element Acoustics: Fundamentals and Computer Codes*. 2000, WIT Press: Southampton.
66. Cremer, L., M. Heckl, and E.E. Ungar, *Structure-borne Sound (second ed.)*. 1988, Berlin: Springer.
67. Gardonio, P. and M.J. Brennan, *Mobility and Impedance Method in Structural Dynamics*. chapter 9 in Advanced Applications in Acoustics, Noise and Vibration, ed. F.J. Fahy and J.G. Walker. 2004: Spon Press.
68. Williams, E., *Fourier Acoustics: Sound Radiation and Nearfield Acoustical Holography*. 1999: Academic Press.
69. Junger, M.C. and D. Feit, *Sound, structures, and their interaction* 1972, Cambridge, Mass.: MIT Press.
70. Sakagami, K., et al., *Sound radiation from a baffled elastic plate strip of infinite length with various concentrated excitation forces.* Applied Acoustics, 1998. **55**(3): p. 181-202.
71. Maidanik, G., *Response of Ribbed Panels to Reverberant Acoustic Fields.* J. Acoust. Soc. Am., 1962. **34**(6): p. 809.
72. Wallace, C., *Radiation Resistance of a Rectangular Panel.* J. Acoust. Soc. Am., 1972. **51**(3B): p. 946.
73. Li, W.L. and H.J. Gibeling, *Determination of the mutual radiation resistance of a rectangular plate and their impact on the radiated sound power.* Journal of Sound and Vibration, 2000. **229**(5): p. 1213-1233.
74. Davies, H.G., *Low frequency random excitation of water-loaded rectangular plates.* Journal of Sound and Vibration, 1971. **15**(1): p. 107-126.
75. Stepanishen, P.R., *Modal coupling in the vibration of fluid-loaded cylindrical shells.* The Journal of the Acoustical Society of America, 1982. **71**(4): p. 813-823.
76. Thompson, D.J., P. Gardonio, and J. Rohlfing, *Can a transmission coefficient be greater than unity?* Applied Acoustics, 2009. **70**(5): p. 681-688.
77. Villot, M., C. Guigou, and L. Gagliardini, *Predicting the acoustical radiation of finite size multi-layered structures by applying spatial windowing of infinite structures.* Journal of Sound and Vibration, 2001. **245**(3): p. 433-455.
78. Nilsson, C.-M. and C.J.C. Jones, *Theory manual for WANDS 2.1, ISVR technical memorandum No.975*. 2007, University of Southampton: UK.
79. Doyle, J.F., *Wave Propagation in Structures*. 1997, New York: Springer.

80. Gavric, L., *Finite element computation of dispersion properties of thin-walled waveguides.* Journal of Sound and Vibration, 1994. **173**(1): p. 113-124.
81. Karasalo, I., *Exact finite elements for wave propagation in range-independent fluid-solid media.* Journal of Sound and Vibration, 1994. **172**(5): p. 671-688.
82. Temkin, S., *Element of Acoustics*. 1981, New York: John Wiley & Sons.
83. Nilsson, C.M. and S. Finnveden, *Input power to waveguides calculated by a finite element method.* Journal of Sound and Vibration, 2007. **305**(4-5): p. 641-658.
84. Kreyszig, E., *Advanced Engineering Mathematics*. 7th ed. 1993, Canada: John Wiley & Sons.
85. Stroud, A. and D. Secrest, *Gaussian Quadrature Formulas*. 1966, New York: Prentice-Hall.
86. Kuttruff, H., *Room acoustics*. 2000, London: Spon Press.
87. Nilsson, C.-M. and C.J.C. Jones, *Manual for WANDS 2.1, ISVR technical memorandum No.976*. 2007, University of Southampton: UK.
88. Petyt, M., *Introduction to Finite Element Vibration Analysis*. 1990, Cambridge: Cambridge University Press.
89. Filippi, P.J.T., *Layer potentials and acoustic diffraction.* Journal of Sound and Vibration, 1977. **54**(4): p. 473-500.
90. Vlahopoulos, N. and S.T. Raveendra, *Formulation, implementation and validation of multiple connection and free edge constraint in an indirect boundary element formulation.* Journal of Sound and Vibration, 1998. **210**(1): p. 137-152.
91. Ih, K.D. and D.J. Lee, *Development of the direct Boundary Element method for thin bodies with general boundary conditions* Journal of Sound and Vibration, 1997. **202**(3): p. 361-373.
92. Ver, I.L. and L.L. Beranek, *Noise and Vibration Control Engineering - Principles and Applications*. 2006: John Wiley & Sons.
93. Quirt, J.D., *Sound transmission through windows II. Double and triple glazing.* The Journal of the Acoustical Society of America, 1983. **74**(2): p. 534-542.
94. Basten, T.G.H., et al., *On the acousto-elastic behaviour of double-wall panels with a viscothermal air layer.* Journal of Sound and Vibration, 2001. **243**(4): p. 699-719.
95. Grosveld, F.W., *Field-incidence noise transmission loss of general aviation aircraft double-wall configurations.* Journal of Aircraft, 1985. **22**: p. 117-123.

96. Xin, F.X., T.J. Lu, and C.Q. Chen, *Sound Transmission Through Simply Supported Finite Double-Panel Partitions With Enclosed Air Cavity.* Journal of Vibration and Acoustics, 2010. **132**(1): p. 011008-1 - 011008-11.
97. Gösele, K. and U. Gösele, *The influence of cavity-volume damping on the stiffness of air layers in double walls.* Acustica, 1977. **38**(3): p. 159 -166.
98. Dowell, E.H. and H.M. Voss, *The effect of a cavity on panel vibration.* AIAA, 1963. **1**(476).
99. Pretlove, A.J., *Free vibrations of a rectangular panel backed by a closed rectangular cavity by a closed rectangular cavity.* Journal of Sound and Vibration, 1965. **2**(3): p. 197-209.
100. Nightingale, T. and J.D. Quirt, *Preliminary results of a systematic study of sound transmission through a cavity wall assembly*. 1999, Institute for Research in Construction, National Research Council of Canada.
101. Quirt, J.D. and A. Warnock. *Influence of sound-absorbing material, stud type and spacing, and screw spacing on sound transmision through a double panel wall specimen*. in *Inter-noise93*. 1993. Leuven, Belgium.
102. Utley, W.A., A. Cummings, and H.D. Parbrook, *The use of absorbent material in double-leaf wall constructions.* Journal of Sound and Vibration, 1969. **9**(1): p. 90-96.
103. Bhattacharya, M.C., R.W. Guy, and M.J. Crocker, *Coincidence effect with sound waves in a finite plate.* Journal of Sound and Vibration, 1971. **18**(2): p. 157-169.
104. Dijckmans, A., G. Vermeir, and W. Lauriks, *Sound transmission through finite lightweight multilayered structures with thin air layers.* The Journal of the Acoustical Society of America, 2010. **128**(6): p. 3513-3524.
105. Gomperts, M.C., *Radiation from rigid baffled, rectangular plates with general boundary conditions.* Acustica, 1974. **30**: p. 320-327.
106. Li, W.L., *Vibroacoustic analysis of rectangular plates with elastic rotational edge restraints.* J. Acoust. Soc. Am., 2006. **120**(2): p. 769-779.
107. Utley, W.A. and B.L. Fletcher, *The effect of edge conditions on the sound insulation of double windows.* Journal of Sound and Vibration, 1973. **26**(1): p. 63-72.
108. Ljunggren, S., *Airborne sound insulation of thin walls.* J. Acoust. Soc. Am., 1991. **89**(5): p. 2324-2337.
109. Craik, R.J.M. and R.S. Smith, *Sound transmission through lightweight parallel plates. Part II: structure-borne sound.* Applied Acoustics, 2000. **61**(2): p. 247-269.

110. Smith, R.S., *Sound transmission through lighweight parallel plates*. 1997, University of Heriot-Watt.
111. Mead, D.J., *Wave propagation in continuous periodic structures: Research contributions from Southampton, 1964 - 1995.* Journal of Sound and Vibration, 1996. **190**(3): p. 495-524.
112. Dowell, E.H., G.F. Gorman III, and D.A. Smith, *Acoustoelasticity: General theory, acoustic natural modes and forced response to sinusoidal excitation, including comparisons with experiment.* Journal of Sound and Vibration, 1977. **52**(4): p. 519-542.
113. Lyon, R.H., *Noise Reduction of Rectangular Enclosures with One Flexible Wall.* The Journal of the Acoustical Society of America, 1963. **35**(11): p. 1791-1797.
114. Bradley, J.S. and J.A. Birta, *On the sound insulation of wood stud exterior walls.* The Journal of the Acoustical Society of America, 2001. **110**(6): p. 3086-3096.
115. Schroeder, M.R., *The ``Schroeder frequency'' revisited.* The Journal of the Acoustical Society of America, 1996. **99**(5): p. 3240-3241.
116. ISO10140, *Acoustics-Laboratory measurement of sound insulation of building elements* 2010.
117. ISO717, *Acoustics rating of sound insulation in buildings and of building elements*, in *Part 1: Airborne sound insulation*. 1997.
118. Smith, R.S., R. Pompoli, and P. Fausti, *An investigation into the reproducibility values of the europe inter-laboratoy test for lightweigh walls.* Building Acoustics, 1999. **6**(3-4): p. 187-210.
119. ISO140, *Acoustics - Measurement of sound insulation in buildings and of building elements* 1995.
120. ISO354, *Measurement of sound absorption in a reveberation room*. 2003.
121. Højlberg, K., *Measurement of reverberation time with the single/dual channel real-time analyzer 2123/33*. 1988, Brüel & Kjaer: Denmark.